Measurements of the Isotopic Composition of Solar Energetic Particles with the MAST Instrument aboard the SAMPEX Spacecraft

Thesis by

Daniel LeRoy Williams

In Partial Fulfillment of the Requirements

for the Degree of

Doctor of Philosophy

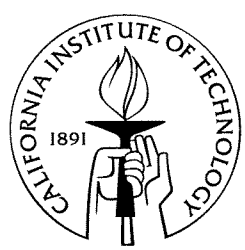

California Institute of Technology

Pasadena, California

1998

(Submitted 30 April 1998)

© 1998
Daniel LeRoy Williams
All rights reserved

Acknowledgements

When I first began to write these acknowledgments, I was quickly lost in the remembrance of so many friends and colleagues who have passed through over the years. Such unfocused reverie could have prevented me from actually finishing this document, but fortunately I have had Richard Mewaldt as an advisor. One thing which he has endeavored to teach me over the years is to not get sidetracked by the details, but to know when to move on. In what can often be a dry field, Dick has the ability to see beyond cobblestones to the larger path of cosmic ray research. His ability to juggle several projects at once is impressive, and is intricately linked to the fact that he knows where to set his priorities. I cannot say with confidence that I have mastered this ability yet, but Dick has at least set the yardstick high.

I would secondly like to thank Rick Leske. He has a most impressive dedication to getting at the truth, no matter how strange or convoluted the data. The hours he and I spent hashing out the basics of this research, from data anomalies in the DPU, to the orbital mechanics of SAMPEX, have been an invaluable lesson in the power of sheer persistence. I thank him mostly because I have never felt I could not ask him naive questions such as "how do we know the spacecraft is really pointing up?" or "how can we be certain that random bit-errors can't mimic a real particle in MAST?" Such basic questions are the heart of education, and I thank him for helping me to answer them.

I would like to thank the members of the MAST/PET team at SRL who worked long hours to get MAST and PET ready on time: Alan Cummings, Tom Garrard, Rick Cook, Branislav Kecman, Ed Stone, Jay Cummings, Richard Selesnick, Brownlee Gauld, Glen Albritton and Kirk Hargreaves. Alan has taught me the benefits of an organized schedule, from "no between-meal snacks" to the weekly lunchtime Caltech bird watching expeditions. Tom Garrard taught me the benefits of organizing material and ideas, from keeping a clean desk, to developing a filing system. And his example of always telling people how much they are appreciated is a lesson I should never forget (hence this long acknowledgments section).

The SAMPEX project has been fun to work on. Its small size and broad objectives have allowed the team to be familiar and dynamic. Thanks to the SAMPEX principal investigator, Glenn Mason of the University of Maryland. Thanks also go to the other scientists who have worked on SAMPEX: Dan Baker, Tycho von Rosenvinge, Berndt Klecker, Dietrich Hovestadt, Joe Mazur, Lin Callis, Berne Blake, Doug Hamilton, Mark Looper, and Shri Kanekal. Great thanks also to the people who are responsible for obtaining and processing the SAMPEX data, and communicating with the spacecraft: Larry Bleau, Mike Lennard, Bob Boughner, Peter Walpole, Tim Coulter and John Nagy.

Besides learning physics and astronomy at Caltech, I have been able to indulge my fascination with computers. For keeping the computers up and running, but mostly for teaching me to understand the systems, sincere thanks to Minerva Calderon, Laura Carriere, Bruce Sears and Andrew Davis.

For aiding me in the battle against bureaucracy and paperwork, I thank Frances Spalding. Thanks for helping me meet all those proposal deadlines.

For keeping me supplied with pens, pencils and lab notebooks; for feeding me cookies, cakes and apple crisps; for being a good secretary, reliable house mate and caring friend, I thank Debby Kubly.

I owe a debt of gratitude to all my office mates who have provided hours of amusement, plenty distractions, and every so often a little assistance: Biff Heindl, Deepto Chakrabarty, Mark Looper, Song Wang, Ah San Wong, Stéphane Corbel, Rachael Kubly, Evren Tumer, Luke Sollitt, and Aaron Eichelberger. I might have been able to finish my PhD sooner without them, but I certainly would not have enjoyed it so. Thanks also to my friends in the lab: Mike Thayer, Brian Vaughn, Christina Cohen, Mark Wiedenbeck, Danny Koh, Brian Matthews, Peter Mao, Alan Labrador and Jill Burnham.

Thanks to Ali Rahbar, whose "Physics with Calculus" class senior year of high school first revealed to me the crazy and exciting world of experimental physics. To my undergraduate advisor Greg Guzik, who first put me to work in cosmic rays. To Bob Svoboda who sent me to work in the salt mines to aid a failing neutrino detector, and who taught me that you don't have to be a nerd to think astrophysics

is cool.

Thanks to my mom and dad. They never pushed me to become a physicist, and they are still probably not sure why I do what I do, or even what it is that I do. But their steadfast love for each other, for myself, and for my siblings has been a rock of comfort to me through the years, and will continue to be so for years to come.

Thanks to John Hartman for giving me physics problems other than astrophysics to think about, and for asking me tough questions about my research. Thanks to him, John Elwood and Quentin Turchette for the good times living at 1987 North El Molino and exploring the San Gabriels.

I reserve ante-penultimate thanks for Rebecca Meyers. Thank you for the sushi, the movies, the plays, the poems, the coffee, your listening ear and your wise advice. Through thick and thin we shall always be friends.

Penultimate thanks to my oldest friend, Patrick, whose earful of complaints about grad school from me over the phone is simply a return for the long hours of complaints about law school and the bar exam I had to suffer five years ago. Thanks for the support. And if you ever want to drop out of the legal profession and become a computer programmer in California...

Ultimate thanks go to the memory of Eric M. Candell. Back in high school when I wanted to become a poet, he opened me to the challenge of mastering matter and energy and space and time by convincing me to take advanced physics. He also convinced me to apply to Caltech, something I would not have had the confidence to do myself. We shall never meet as planned, years hence as retired professors, sitting in a dusty library in leather chairs, drinking Scotch and smoking cigars to reflect on the times and to discuss the philosophy of physics and metaphysics. For that I am greatly sad. But for the unique perspective on the world he has given me, for the courage and boldness to attempt the impossible, I thank him with all my heart.

This research was funded by a NASA Graduate Student Researchers Program fellowship, grant number NGT-51156, and by NASA grant NAG5-2963.

Measurements of the Isotopic Composition of Solar Energetic Particles with the MAST Instrument aboard the SAMPEX Spacecraft

Daniel LeRoy Williams

California Institute of Technology

Abstract

We report measurements of the isotopic composition of solar energetic particles (SEP) as observed in two gradual solar energetic particle events which began on 30 October and 2 November of 1992. These measurements were taken by the Mass Spectrometer Telescope (MAST), a charged-particle telescope on board the SAMPEX satellite in a polar, low-Earth orbit. The elements measured are carbon, nitrogen, oxygen, neon, magnesium and silicon, which are observed over an energy interval of $\sim$15 to 70 MeV per nucleon. These are the first isotopic measurements of silicon, and only the second measurements of the other elements in individual SEP events.

SAMPEX has access to interplanetary fluxes of energetic particles during the high latitude portions of its orbit. This access depends on the rigidity of the particles and therefore on their charge to mass ratio. Fortunately, the polar orbit of SAMPEX allows measurement of SEP charge states using the geomagnetic filtering technique, and a previous study reported measurements of the ionic charge states in the same two SEP events studied in this work. This was the first time that charge states of SEPs at these high energies have been measured, and it allows rigidity-dependent biases in the elemental and isotopic composition to be investigated in the present study. This is particularly important since acceleration/transport processes depend on rigidity, and because the observed composition is also affected by the Earth's magnetic field.

The MAST instrument measures both elemental and isotopic composition using the $\frac{dE}{dx}$-E' technique, which resulted in a typical mass resolution of $\sim$0.24 amu. It was found that during times of high counting rates, the measured mass distributions exhibited high-mass tails. Through computer simulation of the instrument and its particle environment, it was found that these tails are caused by $\gtrsim$4 MeV protons which hit the instrument hodoscope in coincidence with the heavy ions of interest. By choosing only data which occurred during periods of low to moderate counting

rates, the probability of such coincidences could be reduced, and these tails could be effectively removed. The elemental composition was used to find and correct for the bias introduced by these restrictions.

The energy spectra of the elements in each SEP event could be fit with exponentials in energy per nucleon, with a single, characteristic e-folding energy for each event. Such well-behaved spectra allowed elemental abundances to be calculated. These abundances exhibited a fractionation due to acceleration and propagation of the SEP source material, which could be ordered as a function of the charge to mass ratio of each element. The SEP source abundances exhibited a depletion of elements with a high first-ionization potential as compared to the composition of the solar photosphere, a phenomena which has been well-observed in SEP composition for many years. The depletion factor varied by a factor of $\sim$2 between the two SEP events.

The isotopic ratios of $^{22}Ne/^{20}Ne$, $^{25}Mg/^{24}Mg$, $^{26}Mg/^{24}Mg$, $^{29}Si/^{28}Si$ and $^{30}Si/^{28}Si$ were found to be in generally good agreement with the solar system values of isotopic composition as tabulated by Anders and Grevesse (1989) based on terrestrial and meteoritic measurements. Earlier measurements of SEP isotopes found a $^{22}Ne/^{20}Ne$ ratio which was $\sim$80% higher than the $^{22}Ne/^{20}Ne$ ratio measured in the solar wind, but close to the neon-A component found in meteorites, which had been adopted as the solar system standard by Cameron (1982). Our measurements of $^{22}Ne/^{20}Ne$, however, are consistent with the $^{22}Ne/^{20}Ne$ ratio found in the solar wind. This leads us to conclude that the underlying isotopic composition of the SEP source material is closer to that of the solar wind.

There are only two cases in which the measured isotope ratios differ significantly from the Anders and Grevesse (1989) values, the $^{13}C/^{12}C$ and the $^{18}O/^{16}O$ ratio in the second SEP event, both of which are a factor of $\sim$2 higher than the solar system value. There is no apparent pattern to these overabundances.

While the isotopic ratios measured in the two SEP events generally support the assumption that SEPs and solar wind come from the same reservoir of material, and that SEP composition is consistent with the standard solar system abundances compiled by Anders and Grevesse (1989), SEP isotope measurements are still at an ex-

ploratory stage. The limited number of observations prevent us from making definite conclusions about the nature of event-to-event variations in SEP isotopic composition, or about possible differences between the coronal and solar system abundances.

Thesis supervisor: Richard A. Mewaldt, Senior Research Associate

Contents

List of Figures

List of Tables

Chapter 1

Introduction

In this thesis measurements of the isotopic composition of heavy (Z>5) solar energetic particles in the energy interval from ~15 to 250 MeV per nucleon are presented. These measurements were made during two large solar particle events in 1992 using a silicon solid-state charged particle telescope on board the SAMPEX spacecraft in polar orbit about the Earth.

Solar energetic particles (SEP) originate at the Sun, where a sudden release of magnetic energy occasionally causes solar material to be accelerated to energies in excess of 100 MeV per nucleon. Measurement of SEPs thus provides an opportunity to sample the composition of the Sun. Since the Sun contains 99.9% of the material in the solar system, SEP composition is related to the composition of the solar system as a whole. Planetary scientists use measurements of solar system composition to infer the properties of the proto-solar nebula from which our solar system was formed, and to aid in interpreting the contributions that solar wind and solar particles make to other bodies in the solar system. Nuclear astrophysicists test their understanding and modeling of nuclear processes by comparing their calculations of elemental and isotopic abundances to the observed composition of solar material, which was produced through previous generations of stellar nucleosynthesis. Space physicists examine SEP composition to understand the source of the particles, the environment where they originated, and the processes which accelerate them. The study of solar energetic particles is thus relevant to many fields of research.

1.1 Layout of This Thesis

This thesis is divided into six chapters, including this introduction. Chapter 1 introduces energetic particles in space, and discusses how solar energetic particles differ from galactic cosmic rays (GCR) and anomalous cosmic rays (ACR). Solar structure and composition are then briefly discussed. A short history of scientific understanding of SEPs is given, including the developments in detector technology which make SEP isotopic measurements possible. Isotopic composition measurements from solar wind, from implanted particles, and from spectroscopic investigations are then presented. Finally, the relationship between SEP measurements and the bulk composition of the solar system is discussed.

Chapters 2 and 3 describe the MAST instrument and the analysis of MAST data. They are very detailed and are intended to serve as a guide to future users of MAST. The techniques described may also be of help to designers and users of similar instruments on future missions. Chapter 2 explains how the MAST instrument works. It gives the theory behind its operation, describes its calibration, and explains its limitations. Chapter 3 discusses how the MAST data is obtained from the SAMPEX spacecraft. It also discusses the algorithms used to determine the charge, mass, and kinetic energy of the heavy ions measured. It then describes how the instrument counting rates are used to obtain fluxes of particles, and finally shows plots of fluxes of interplanetary particles.

Chapter 4 describes the specific observations made of the solar particle events, one which began on 30 October 1992 and another which began on 2 November 1992. An introduction to the magnetospheric environment is given, so that the reader can appreciate the nuances involved in observing charged particles from low-Earth orbit. The characteristics of the two SEP events are given, including observations at optical, X-ray and radio wavelengths of the solar activity associated with these events. The method for obtaining elemental composition are described. The spectra and abundances of the elements are then given, and discussed in the light of current theories of SEP composition.

Chapter 5 is dedicated to measurements of the SEP isotopes. It first dis-

cusses the techniques used to measure the isotopic abundances. Next the data analysis and selection criteria necessary to obtain particle mass are described. Then limits are placed on the possible sources of contamination in the instrument, and the instrument bias due to range sampling is discussed. Next the final selection criteria are discussed, a table of the isotopic ratios is given, and there is a brief discussion of how the isotopic ratios vary with energy and time. The chapter ends with a discussion of how the isotopic composition of the SEP source material is obtained, based on the observed fractionation of the elements.

Chapter 6 discusses how our isotopic ratios compare with measurements from previous missions and with the isotopic composition of the solar wind. Following that is a statistical analysis of our results, addressing the question of whether the measurements are statistically consistent. Then our measurements are compared to the standard isotopic ratios of the bulk solar system. Finally, past, present and future experiments for measuring SEP isotopic composition are discussed.

Chapter 7 presents a brief summary of this work and of the interpretation of the results.

1.2 Energetic Particles in Space

In the 15-250 MeV per nucleon energy range there are three dominant populations of energetic particles in interplanetary space near Earth: galactic cosmic rays (GCR), anomalous cosmic rays (ACR), and solar energetic particles (SEP). The intensities of each population of particles are not constant over time. The galactic and anomalous cosmic rays have their peak intensity during solar "quiet" times, the periods of minimal activity in the 11-year solar cycle. Since high-energy GCRs produce showers of particles, including neutrons, when they collide with the Earth's atmosphere, the level of GCR activity can be measured by ground-based neutron monitors. Thus, changes in the intensity of GCRs are reflected by changes in neutron monitor counting rates, as illustrated in Figure 1.1 (Pyle 1998). The change in ACR intensity roughly follows that of GCRs, but the variations are much greater.

SEPs occur primarily during "active" times of the solar cycle. Such times

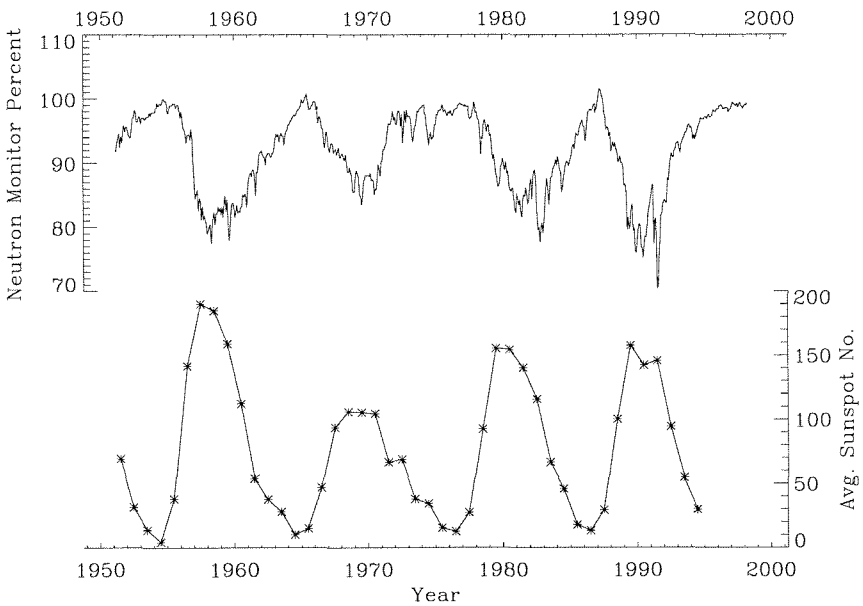

Figure 1.1: The solar activity cycle. *Top*: The Climax Neutron Monitor Average rate, normalized as a percentage of the maximum signal seen in 1954, showing the variation of $\gtrsim$3GeV galactic cosmic rays (Data from K. Roger Pyle and John A. Simpson at the University of Chicago, National Science Foundation Grant ATM-9613963). *Bottom*: The yearly average sunspot number, indicating solar activity (from the National Geophysical Data Center in Boulder, USA).

are indicated by increases in the number of sunspots, also shown in Figure 1.1. A summary of SEP activity over the past three solar cycles is given in Shea and Smart (1990). SEPs occur as brief outbursts of particles, and are observed over a few hours to a few days. Figure 1.2 shows the counting rate of a detector on MAST instrument on SAMPEX for a period of a few days, which included a large SEP event which began on 30 October 1992. Figure 1.3 shows the overall frequency of large SEP events as observed over the past 23 years by instruments aboard the IMP-8 spacecraft. SEP events appear as spikes in the flux of > 30 MeV protons.

The energy spectra for each population of particles is not the same, as illustrated in Figure 1.4. The flux of ACR oxygen at one astronomical unit (AU), for instance, changes by about a factor of 100 over the solar cycle (Mewaldt et al. 1992; Klecker 1995). In the galactic cosmic rays, the intensity of particles below 1000 MeV per nucleon can vary by a factor of $\sim$10 (Webber and Lezniak 1974). The time scale for the variation of SEP intensity is much shorter than that of the ACR and GCR. Solar energetic particle fluxes can rise from below ACR and GCR background levels in a few hours, as shown in Figure 1.2. The intensity, spectral shape, and composition can vary greatly from one SEP event to the next (Cook et al. 1984). Occasionally, the flux of SEPs can be as much as six orders of magnitude above background levels, and dominate the interplanetary energetic particle population up to 100 MeV/nucleon. Such events last only a few days, however, before the intensity of SEPs drops once again below the ACR and GCR background levels.

The composition of each of these three energetic particle populations is unique. For example, galactic cosmic rays contain high abundances of rare elements such as lithium, beryllium and boron, as well as radioactive isotopes such as ^{26}Al and ^{10}Be. They also contain a high fraction of rare isotopes as compared to normal solar system of interstellar material. This unusual composition can be obtained if the source of galactic cosmic rays is composed of matter which is similar to that found in the solar system, yet which has been accelerated, and then has traveled through 5-10 g cm^{-2} of hydrogen. The rare elements and isotopes are produced when the original particles collide with interstellar hydrogen nuclei and fragment into lighter products. Detailed analyses of the radioactive isotopes indicate that the lifetime of galactic cos-

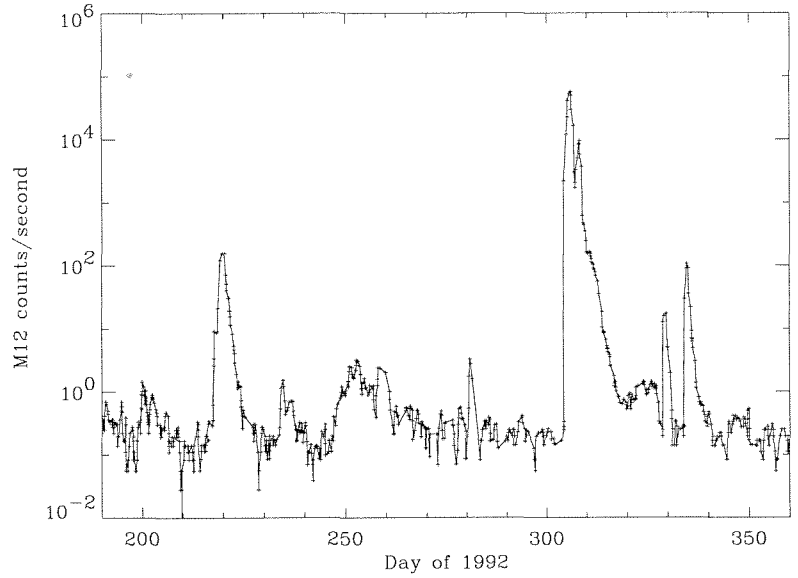

Figure 1.2: Count rate for coincidences between the M1 and M2 detectors on SAMPEX. The spike structures are periods of solar energetic particle activity, showing how this activity varies over the course of a few days. The fairly constant background rates are due to ACR and GCR nuclei.

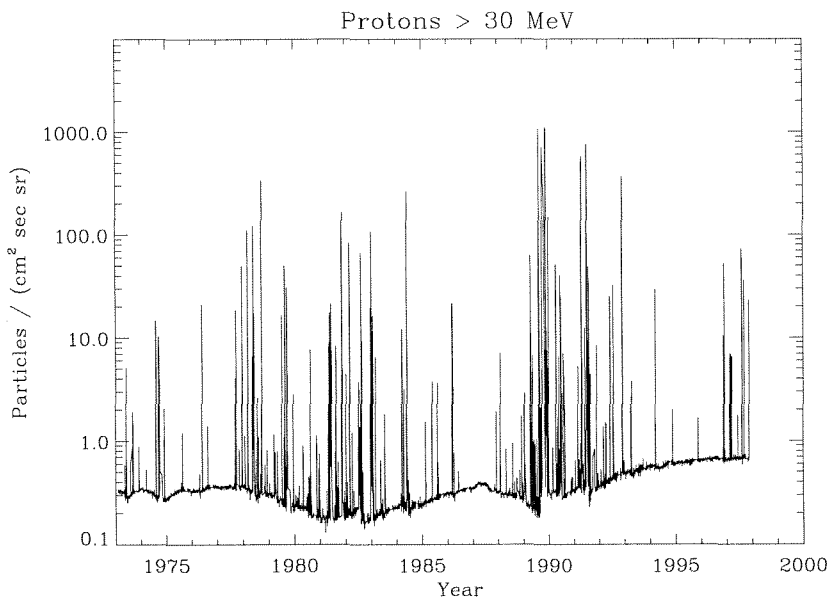

Figure 1.3: The daily average flux of >30 MeV protons, in particles per cm^2sr per sec, as measured by an instrument aboard the IMP-8 spacecraft. Large SEP events appear as spikes above the smoothly varying GCR background.

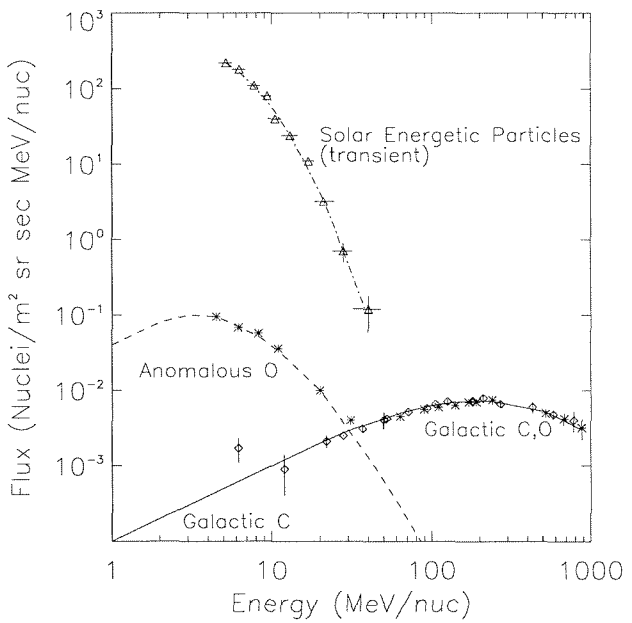

Figure 1.4: The spectra of energetic oxygen and carbon nuclei in the energy range of MAST, as measured by ISEE-3. The galactic cosmic ray (GCR) and anomalous cosmic ray (ACR) fluxes are fairly constant over periods of months to years, but vary over the solar cycle. Solar energetic particles (SEP) are more transient, typically present for only a few days at a time.

mic rays is approximately 10 million years (Wiedenbeck and Greiner 1980). For a review of galactic cosmic ray composition, see Mewaldt (1994) or Simpson (1983).

The anomalous cosmic rays were not discovered until the early 1970s, when instruments which measure composition which had energy thresholds below ~10 MeV/nucleon were flown into space. The composition of ACR particles is dominated by elements such as helium, oxygen, and neon, all of which have a high first-ionization potential. Studies of the isotopic composition of these cosmic rays also reveal that the abundances of ACR isotopes are similar to that of the solar system, and not contaminated with rare isotopes like the galactic cosmic rays (see Leske et al. 1996). Strong evidence indicates that ACRs originate as interstellar neutral particles which have been ionized and then accelerated at the solar wind termination shock. The ACRs are primarily composed of hydrogen, helium, carbon, nitrogen, oxygen, neon, and argon (Cummings and Stone 1990). For recent reviews of the anomalous cosmic rays, the reader is referred to Klecker (1995) or Simpson (1995).

It is not at first obvious how any individual energetic charged particle can be classified as being GCR, ACR, or SEP. At energies of 10-100s of MeV per nucleon, the paths of charged particles are altered greatly by the magnetic fields in interstellar and interplanetary space, so that the direction they come from often bears little relation to their source. Two simple ways to distinguish the particles are energy and time.

At energies below 200 MeV/nucleon, the flux of GCRs falls linearly with kinetic energy for the majority of the elements. However, for elements which are present in ACRs, there is a "bump" on the low-energy GCR spectrum. For the heavy ($Z \geq 6$) elements, the peak flux is at a few MeV/nucleon. For elements which are less abundant in the ACRs, such as argon, it can be difficult to distinguish this bump above the GCR spectrum. However, for elements such as oxygen and neon, it is clear that the vast majority of particles observed in the 1-20 MeV/nucleon range are anomalous cosmic rays. By taking an element without an ACR component, such as silicon, and scaling its GCR flux, one can determine the flux of particles which are ACRs for the elements which have an ACR contribution. Above about 10 MeV per nucleon the ACR spectrum falls roughly exponentially. As the energy increases, the number of ACRs drops, and the number of GCRs increases, until there is no longer

a significant contribution of ACRs.

The energies of SEPs overlap those of ACRs and GCRs. However, SEPs are seen as transient increases in the flux of energetic particles which last from a few hours to a few days. While the fluxes of ACRs and GCRs change slowly over the course of 11 years, the flux of SEPs can rise suddenly to as much as six orders of magnitude above the background GCR and ACR fluxes (see Figure 1.3). Thus, while an SEP event is occurring, the vast majority of particles observed are SEPs. The number of ACR and GCR particles contaminating a particular SEP observation can be easily calculated by measuring the fluxes of ACR and GCR before or after the SEP event.

What can we learn from the composition of these particles? From GCR composition we learn about the acceleration and sources of GCRs, and about the interactions and the lifetime of GCRs in the galaxy. From the anomalous cosmic rays we learn about the local interstellar medium, and the interaction of the solar wind with that medium. From the solar energetic particles we learn about five broad areas: the phenomenon of particle acceleration, the fractionation of the SEP source material, the transport of particles through the interplanetary medium, the structure of the solar atmosphere, and the composition of the Sun.

1.3 Solar Structure, Composition, and Dynamics

1.3.1 Regions and Characteristics of the Sun

The Sun comprises 99.9% of the mass of the solar system. Some features of the Sun are shown in Figure 1.5. In the inner 30% of the radius lies the Sun's core, where hydrogen nuclei are fused into helium through nuclear interactions, providing the source of the Sun's energy. The density at the very center is $\sim$150 $\mathrm{g\,cm^{-3}}$ and the temperature is 15 million Kelvin. Beyond the core is the radiative zone, where the photons released in the nuclear reactions are scattered and attenuated by the surrounding material, leading to a thermalization of the core energy into an approximately blackbody spectrum. At $\sim$0.75 solar radii, the radiative heat loss becomes

larger than the adiabatic heat loss, and convection occurs. For recent textbooks on the Sun, see Zirin (1989) and Foukal (1990).

An important property of the material in the solar convective zone is that the gas is partially ionized, and thus a plasma. This plasma carries magnetic fields as it convects, so not only do the convection cells bring heat to the surface, but they also entwine the magnetic field lines dragged with the plasma. Furthermore, the rotational velocity of the Sun depends on latitude, so that while the rotation period at the equator is 25 days, the period at the poles is greater than 30 days. This differential rotation also serves as a powerful driver of magnetic activity.

The solar surface, or photosphere, is defined as the point where the density of scatterers drops sufficiently so that photons may escape the Sun without further collisions. The temperature of the photosphere corresponds to a blackbody at 5800 K. It might be expected that the temperature of material above the photosphere should decrease with distance from the hot solar surface. However, as shown in Figure 1.6, this is not quite what happens.

The chromosphere is a region extending to approximately 2000 km above the photosphere. In the chromosphere the temperature drops to a minimum of ~4500 K, before beginning a slow rise with height until the transition region is reached. The name "chromosphere" comes from the Greek for "color-sphere," because it was first observed during solar eclipses as a bright red ring around the eclipsed Sun. This redness is due to strong H-α emission by chromospheric gas heated by the underlying photosphere. The chromosphere is riddled with many fine bristle-like structures which are called spicules when seen on the solar limb in H-α emission lines, and which are called mottles when viewed as H-α absorption features against the brighter photosphere. Another feature seen in the chromosphere are prominences, large filaments of material suspended above the photosphere which last for many days. When these structures are seen above the photosphere, they are seen as dark lines, and called filaments. Prominences are large, extending thousands of kilometers in length, and rising thousands of kilometers above the photosphere. Theories of prominence formation (Priest et al. 1996) suggest that prominences actively lift photospheric material to coronal heights, and may thus be the source of coronal material.

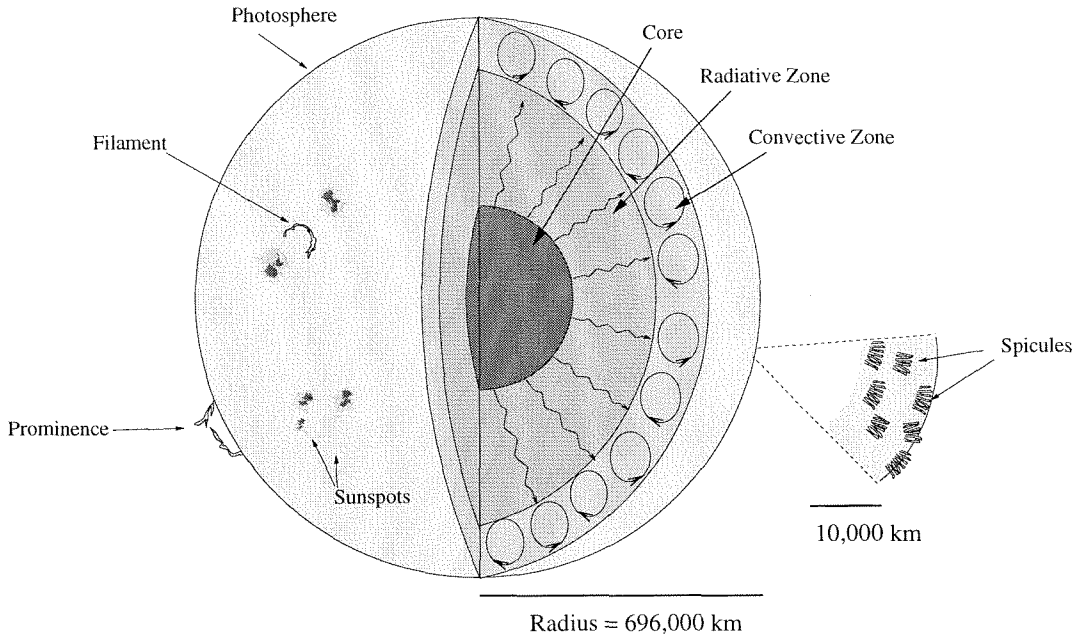

Figure 1.5: Prominent features of the Sun.

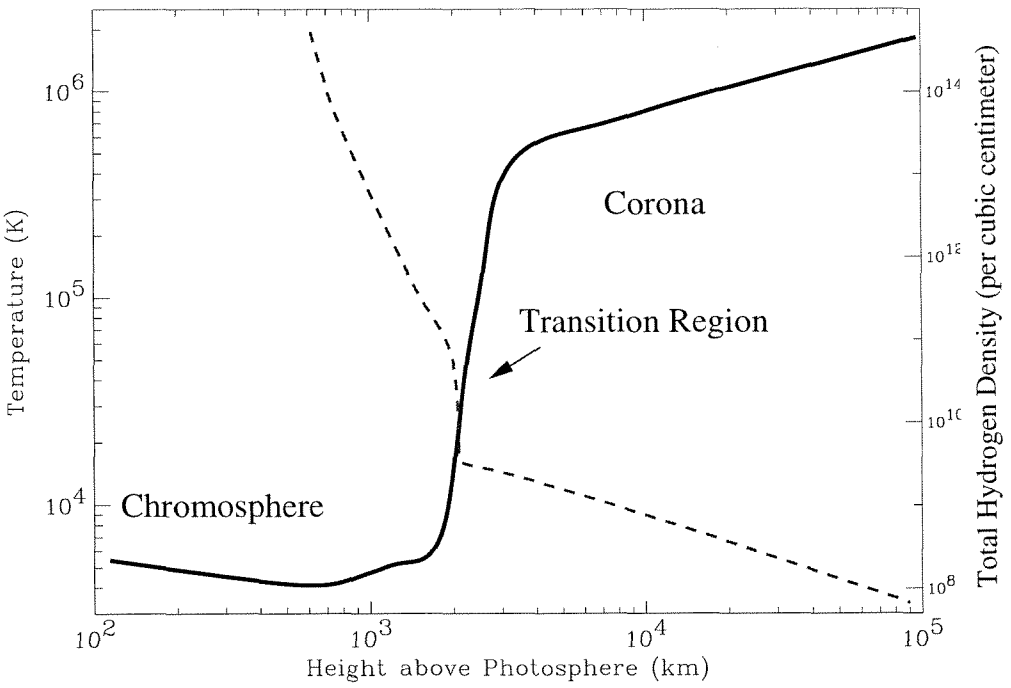

Figure 1.6: Solar temperature and hydrogen density profile as a function of height above the photosphere. The solid line corresponds to temperature, and the dashed line corresponds to the total hydrogen density. Adapted from Foukal (1990).

In the solar corona, the density of particles is very low, yet the temperature is an astonishing 1.5 million Kelvin. This is measured using coronagraphs, which observe the emission-lines of heavy, multiply-ionized atoms. The mechanism which heats the corona is not exactly understood. It could not be heated by radiation, convection, or conduction by the photosphere beneath it, since that material is at a temperature of only 5800 K. Solving the mystery of coronal heating is one of the great tasks before solar physics.

1.3.2 Solar Composition

The composition of the Sun has been studied for years using spectroscopy. William Wollaston in 1802 was the first to notice dark lines in the solar spectrum, due to absorption by cool material in the outer layers of the photosphere. Ten years later Joseph Fraunhofer studied the lines in detail, discovering that the absorption lines corresponded to many elements commonly found on Earth. In the mid 1800s, unknown emission lines observed in the corona were attributed to an element which had not been observed on Earth, and so this element was named "helium" after the Greek word for Sun.

Spectroscopy remains the primary tool for measuring solar composition. Such measurements are presently limited by 1) thermal broadening of lines, which causes strong lines to obscure weaker ones, 2) uncertainty in the local thermodynamic conditions where the lines are produced, and 3) an incomplete understanding of certain line transition rates. In the photosphere lines are usually observed as absorption lines in the continuum. In the corona, lines are observed as emission lines, often in the X-ray and UV region of the spectrum.

It was not until the early 1980s that X-ray and UV observations of coronal abundances found that the composition of the solar corona differed from that of the photosphere. Measurements of solar energetic particles had found that SEPs were depleted in elements with a high ($\gtrsim$10 eV) *first-ionization potential*[1] (Hovestadt 1974; Cook et al. 1980). It had been suggested that these measurements indicated that the composition of the corona and the photosphere were different (Mewaldt 1980; Meyer

1981). Yet until UV observations began to return results confirming this hypothesis it was not widely accepted by the solar physics community (Veck and Parkinson 1981; Meyer 1985).

The evidence for a compositional difference between the photosphere and the corona is that elements with a first ionization potential (FIP) above ~10 eV are depleted in the corona, as compared to the photosphere, by a factor of ~4. Recent observations of coronal emission lines (Spicer et al. 1998) and of solar wind (von Steiger et al. 1997) find that the depletion factor varies from ~1.5 to ~5 in different kinds of solar wind, and so the ~4 depletion factor is likely an average value. Furthermore, theories of coronal fractionation suggest that the depletion is better organized by *first ionization time* (FIT), rather than FIP (Geiss and Bochsler 1985; Marsch et al. 1995). The FIT is the time it takes for a neutral atom to be ionized in the solar corona.

The composition of the Sun can also be measured through particles which are emitted from the Sun, in particular solar energetic particles, solar wind, and in solar wind and energetic particles which are embedded in the surfaces of lunar material and meteorites. These three samples of material provide complimentary information for determining the composition of the Sun.

1.4 Solar Energetic Particles

The association of energetic particles with flares on the Sun was first observed using ground-based ionization chambers in the 1940s. A network for rapid-notification of particle activity was established in the early 1950s. This allowed scientists to launch detectors aboard balloons and sounding rockets, which would collect energetic particles using nuclear emulsions, whenever particle events were in progress.

Early satellites in the 1960s often carried solid-state detectors which measured particle activity at lower flux levels than could be observed from Earth. These were silicon solid-state detectors which measure energy deposited in them by ener-

[1]The FIP is the amount of energy required to remove a single electron from a neutral atom.

getic nuclei. At first the electronics of such instruments simply measured the rate of particles which deposited energy above some threshold in these detectors. As both these instruments and balloon-borne emulsion experiments improved, it was realized that the heavy SEP elements did not contain the enhanced abundance of rare elements as seen in the galactic cosmic rays. Rather, their composition was more akin to that of the solar photosphere (Fichtel and McDonald 1967).

In the late 1960s and early 1970s solid-state detectors were built which could identify the charge of energetic nuclei, rather than just the integral flux of all particles above a certain energy. With this ability came the necessity to develop electronic priority systems, since the flux of protons and alpha particles can be 10^4 times greater than the flux of the heavier nuclei. With the ability to measure elemental composition in detail, observations soon revealed that although the SEP composition was similar to solar photospheric composition, there were large variations in composition from event to event, particularly in the Fe/O ratios (Mogro-Campero and Simpson 1972a, 1972b; Teegarden et al. 1973).

With the advent of multi-element solid-state telescopes in the mid-1970s, particularly the Goddard instrument on IMP-8 (McGuire and von Rosenvinge 1986), and the Caltech instruments aboard Voyagers 1 and 2 (Stone et al. 1977), a detailed study of the heavy element composition in individual SEP events became possible (Cook et al. 1984; McGuire and von Rosenvinge 1986). It was found that the overall abundances of the heavy elements, compared to photospheric composition, showed a depletion of high-FIP elements. Shortly later UV spectroscopic observations confirmed that this effect was characteristic of coronal material, suggesting that the source of SEPs was coronal material. Yet these studies also found that not only the ratio of iron to oxygen (Fe/O), but other ratios, such as that of helium to oxygen (He/O) also varied between SEP events. They also found that the enhancement of heavy ions was related to atomic number.

Instruments with lower thresholds also revealed that certain SEP events had curious composition, almost appearing to be a separate class of SEP event. Specifically, Hsieh and Simpson (1970) found that some SEP events had an anomalously high abundance of ^{3}He. The ratio of ^{3}He/^{4}He in these events was up to four orders

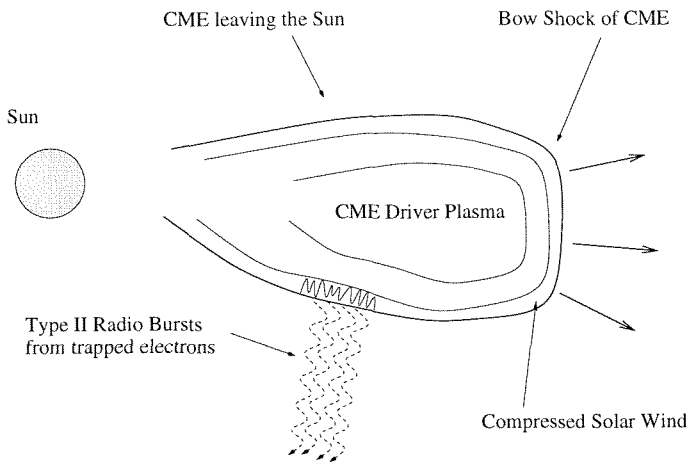

Figure 1.7: Gradual SEP events are associated with radio emission from electrons high in the corona (Type II bursts), X-rays from large coronal loops, and coronal mass ejections. Particles from such events can be observed on field lines which are far separated from the site of the X-ray flare in the lower coronal regions. These particles also have an ionization temperature representative of coronal material.

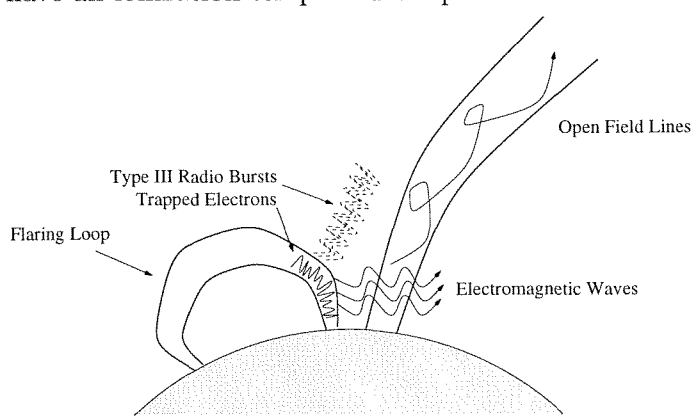

Figure 1.8: Impulsive SEP events are associated with radio emission from electrons low down in the corona (Type III bursts), and X-rays from small magnetic loops. The particles are observed only when they are connected to the Earth or to interplanetary spacecraft through open magnetic field lines. Their ionization temperature is that of a hot flare plasma. Adapted from Reames (1990).

TABLE 1.1

Characteristics of gradual and impulsive SEP events. (Data from Klecker et al. 1984; Luhn et at. 1987; Klecker 1991; and Gosling 1993).

	Gradual	Impulsive
Frequency at Solar Maximum	10 yr^{-1}	1000 yr^{-1}
Rise Time from Onset to Maximum	12 hr	2.5 hr
Cone of Connection	$\sim$180°	$\lesssim$60°
Associated Radio Emission	Type II and IV	Type III
CME Present?	yes	no
X-ray Loop Spatial Scale	4×10^4 km	10^4 km
Soft X-ray Duration	>1 hr	$\sim$1 hr
p/α Ratio	$\sim$100	$\sim$10
e/p Ratio (at 10 MeV)	< 0.1	$\gtrsim$0.1
Fe/O Ratio (at 10 MeV/nuc.)	$\sim$0.1	$\sim$1
^{3}He/^{4}He	$\sim 5\times10^{-4}$	$\sim$1
Charge State Temperature	$\sim 10^6$ K	$\sim 10^7$ K
Si Charge State	+11	+14
Fe Charge State	+15	+20

of magnitude higher than the photospheric ratio of 10^{-4}. Although it was initially speculated that the ^{3}He was due to nuclear interactions of ^{4}He in the solar atmosphere (Ramaty and Kozlovsky 1974), this idea proved to be inadequate when no corresponding enhancements in ^{2}H or ^{3}H were observed (Garrard, Stone, and Vogt 1973).

Over the years evidence accumulated which suggested that there are two general classes of SEP events (see Table 1.1). The ^{3}He-rich events were found to be associated with impulsive bursts of X-ray activity on the Sun, and came to be referred to as *impulsive* events, in contrast to the *gradual* SEP events, in which the intensity of associated X-rays decays more slowly. Impulsive events were also found to have enhancements of heavy ions relative to gradual events, and to be associated with high fluxes of electrons and the presence of type III radio bursts (Reames 1990). The energetic particles in these events are thought to be accelerated deep in the solar corona, near the footprints of coronal loops. These impulsive events occur at lower energies and contain lower intensities of particles, and so their presence had not been discovered until instruments with sufficient sensitivity and low enough energy thresholds were flown. In contrast, the flux of particles in gradual events is generally one to three orders of magnitude greater than that in impulsive events.

The acceleration mechanism in the two classes of events appears to be quite different. In impulsive events, the enhancements of ^{3}He and certain heavy ions are thought to be due to gyro-resonant absorption of waves produced by streaming electrons near the base of coronal loops (Fisk 1978; Temerin and Roth 1992). The acceleration mechanism of the particles is thought to be due to stochastic Fermi acceleration from plasma-wave turbulence (Moebius et al. 1982). In contrast, particles in gradual events appear to be accelerated by CME-driven shocks in the corona (Lee and Ryan 1986; Reames 1990).

The understanding of impulsive and gradual events was greatly assisted by observations of the ionic charge states of solar energetic particles. Measurements of the mean charge states for many abundant elements were reported in 1984 (Luhn et al. 1984) for particles at energies around 1 MeV/nucleon. The charge states found indicated that the ions from gradual events had an ionization equilibrium temper-

ature of 1-4$\times 10^6$ K, characteristic of material in the solar corona. In contrast, the charge states observed for particles in impulsive SEP events were higher, representing material at equilibrium temperatures of $\sim 10^7$ K, too hot for the corona, but not for the plasma near the base of coronal loops where flaring is occurring (Klecker et al. 1984; Luhn et al. 1987). Charge states for SEPs in gradual events were also measured by three of the instruments on SAMPEX (see Mason et al. 1995, Leske et al. 1995 and Oetliker et al. 1997). The charge state measurements of Luhn et al. and those from the LICA instrument (Mason et al. 1995) and the MAST instrument (Leske et al. 1995) aboard SAMPEX are given in Table 1.2.

Although the source of SEPs continues to be a subject of debate, a consensus appears to be emerging. It was once thought that all SEPs originated from low in the corona, near the source of energy release in an X-ray flare. However, SEPs from gradual events have been observed which are traveling on field lines which are not connected to the flare site at all. Also, charge state measurements show that gradual SEP particles could not have been accelerated at the flare site, then transported to other heliolongitudes low in the corona. If that had occurred, they would have been further stripped of electrons (Ruffolo 1997). Thus, SEPs observed in impulsive events are accelerated near the site of solar flares, while SEPs in gradual events must originate from shocks higher in the corona. Furthermore, Kahler (1984) found a 96% correlation between coronal mass ejections (CMEs) and gradual events. The current consensus is that particles from gradual events are accelerated by shocks in the corona driven by CMEs (Gosling 1993; Reames et al. 1997).

1.4.1 Gradual SEP Composition

The elemental composition of gradual SEPs was first studied in detail in the late 1970s (Cook et al. 1979, 1980, 1984; McGuire and von Rosenvinge 1986). Systematic variations in the elemental abundances were observed; in particular, enhancements of elements appeared to be correlated with the charge of the elements. Abundances of elements close together on the periodic table varied little with respect to one another, while elements far separated, such as iron and oxygen, showed wide

TABLE 1.2

Mean charge states of solar energetic particles from gradual SEP events. The values from Luhn are averages over 6 to 12 SEP events (depending on the element), while those from Leske and Mason are averages over the two SEP events of October and November 1992.

Element	Luhn (1985) 0.4-4.0 MeV/n	Mason (1995) 0.5-5 MeV/n	Leske (1995) 15-70 Mev/n
C	5.70± 0.05	5.63± 0.11	5.70-6.00 (assumed)
N	6.37± 0.04	6.52± 0.16	6.47± 0.20
O	7.00± 0.02	7.21± 0.15	6.95± 0.20
Ne	9.05± 0.07	9.38± 0.16	8.53± 0.27
Na	n/a	n/a	9.11± 0.36
Mg	10.7± 0.07	10.62± 0.55	10.30± 0.34
Al	11.0± 0.10	n/a	11.09± 0.58
Si	11.0± 0.10	10.98± 0.23	10.54± 0.37
S	10.9± 0.24	11.91± 0.25	10.84± 0.44
Ar	n/a	n/a	10.08± 0.91
Ca	n/a	11.83± 0.21	11.46± 0.49
Fe	14.9± 0.09	11.04± 0.22	15.18± 0.73
Ni	n/a	n/a	12.62± 1.30

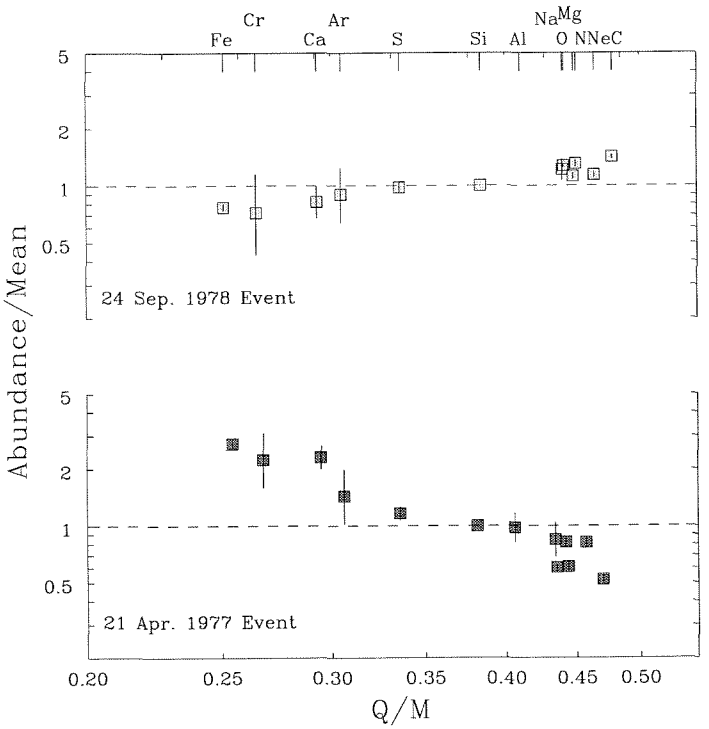

Figure 1.9: Abundances relative to the average SEP abundances as a function of ionic charge to mass ratio for two SEP events, showing how the event-to-event variation depends on Q/M. Reproduced from Brenneman and Stone (1985).

variation in their relative abundances. However, the variations appeared to arise from an event-dependent mechanism, the strength of which varied from event to event.

Breneman and Stone (1985) hypothesized that the variation in abundances were due to acceleration or interplanetary propagation of the particles, and thus the variation should be a function of the magnetic rigidity of the particles, which is proportional to their charge-to-mass ratio, Q/M. They used the measurements of SEP charge states at ~1 MeV/nucleon (Luhn et al. 1984), and combined these with Voyager observations of elemental abundances at 5-15 MeV/nucleon. They found that the abundance variations in gradual events could be organized by Q/M, the ratio of an element's charge to its mass (see Figure 1.9). The overall composition of SEPs was consistent with coronal composition, but each SEP event had a unique power-law index which they attributed to acceleration and/or propagation effects. By correct-

ing for this effect, it was found that SEP abundances matched the available coronal abundances extremely well. Thus, it became feasible to relate SEP composition to coronal composition (Breneman and Stone 1985; Garrard and Stone 1994). Taking into account the FIP-dependent fractionation between the coronal and photospheric compositions, the SEP measurements could then also be used to augment other measures of solar composition.

1.4.2 SEP Isotopes

In the late 1970s instruments were developed which could not only separate elements, but which could also resolve isotopes of heavy nuclei. These were similar to the solid-state detector telescopes used to identify elements. In such instruments, the charged particle penetrates one or more solid-state detectors before coming to rest in the instrument. The charge is measured using the range-energy relationships for the various nuclei. This requires a measurement of the ionization rate of the nuclei, approximated by the amount of energy deposited in a silicon detector, divided by the thickness of that detector, called "$\frac{dE}{dx}$". In earlier instruments, measurements of mass were not possible because particles could penetrate the detector at a variety of angles, and so the thickness penetrated (the "dx") was smeared out. If the $\frac{dE}{dx}$ could be measured more accurately, then mass, as well as charge, could be resolved.

There are two ways to improve the measurement of $\frac{dE}{dx}$. One way is to limit the angle of incidence of particles, so that the variations in angle are small, as was done with the Chicago instrument on IMP-8. This method has the limitation that the geometry factor in such an instrument is small. Another approach, which has proven better in the long term, has been to use position-sensitive devices to measure particle trajectory. This allows one to determine the angle of incidence of the particles. In addition, the thickness of each silicon detector is mapped before flight. The trajectory of each particle is then used to determine where each particle penetrates each detector, yielding a measurement of Δx which is as accurate as the detector thickness maps. By measuring the penetration pathlength to an accuracy of a few tenths of a percent, such instruments can obtain excellent mass resolution, as demonstrated in Figure 1.10.

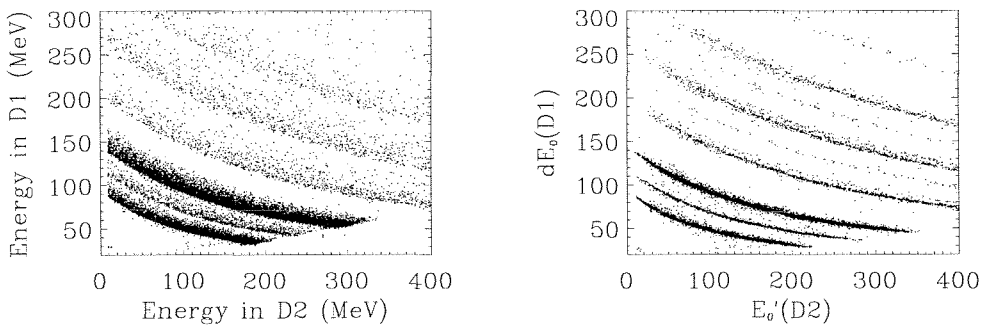

Figure 1.10: Illustration of the difference between having trajectory information and not having it. The figure on the left shows data without any correction for the angle of incidence, while that on the right shows the same data which have been corrected to zero degrees incidence using the measured incidence angle. This simple correction improves the resolution to the point where mass resolution of the heavy elements becomes possible.

The first such instrument which could measure particle trajectories was the Caltech HIST experiment, flown on ISEE-3 (Althouse et al. 1978).

In 1979 both the Chicago and the Caltech teams reported measurements of the isotopic abundance ratio $^{22}Ne/^{20}Ne$ in SEPs (Mewaldt et al. 1979; Dietrich and Simpson 1981). Further analysis of the HIST data provided isotopic ratios for a number of elements (Mewaldt et al. 1984). An experiment on the S81-1 spacecraft made additional measurements of isotopic composition in 1984, though the instrument was greatly limited by troubles with its position-sensitive detectors at high counting rates. The heavy-ion isotopic composition has also been measured in ^{3}He-rich SEP events (Mason et al. 1994). Such observations find evidence that heavy isotopes are enhanced, though not nearly as much as the ^{3}He. The uncertainties on all of these measurements are rather large, and the results are given in Table 1.3.

All these measurements of isotopic composition were limited mainly by the number of particles measured. From an engineering standpoint, the number of particles is limited by the size of the telescope, the efficiency of the electronics, the energy threshold of the instrument, and the quality of the data taken. The quality of the data can be compromised by the instrument not performing well during periods of high

TABLE 1.3

Previous studies of solar energetic particle isotopic composition.

Isotope Ratio	Ratio (percent) 8-23-78 Event[a]	7-10 Event Avg.	4 Event Avg.[d]	^{3}He-rich Event[e]
$^3He/^4He$	$\leq 2.6 \times 10^{-3}$	-	-	65± 8
$^{13}C/^{12}C$	$.95^{+0.42}_{-0.29}$	-	$1.6^{+1.4}_{-0.6}$	<11
$^{14}C/^{12}C$	< 0.14	-	-	-
$^{15}N/^{14}N$	$0.8^{+1.0}_{-0.5}$	-	< 4.5	<13
$^{17}O/^{16}O$	≤ 0.21	-	< 0.6	<1.5
$^{18}O/^{16}O$	$0.15^{+0.11}_{-0.07}$	-	< 0.31	<1.5
$^{21}Ne/^{20}Ne$	≤ 1.4	-	< 3.0	<4
$^{22}Ne/^{20}Ne$	$10.9^{+2.6}_{-1.9}$	13.0± 4.0[b]	$6.0^{+4.5}_{-2.3}$	29± 10
$^{25}Mg/^{24}Mg$	$14.8^{+4.6}_{-2.6}$	-	24^{+26}_{-10}	25± 19
$^{26}Mg/^{24}Mg$	$14.8^{+4.3}_{-2.5}$	22.0± 7.0[c]	14^{+7}_{-6}	36± 21
$^{29}Si/^{28}Si$	-	<10[b]	16^{+21}_{-11}	-
$^{30}Si/^{28}Si$	-	<10[b]	< 9	-

a) Mewaldt, Spalding, and Stone (1984)

b) Average over 7 SEP events, Dietrich and Simpson (1979)

c) Average over 10 SEP events, Dietrich and Simpson (1981)

d) Simpson, Wefel, and Zamow (1984)

e) Mason et al. (1994)

particle flux. However, the solar cycle also affects the number of particles measured, in that during solar minimum few SEP events occur.

While the composition of SEPs was being studied, a parallel effort was happening at lower energies in the study of solar wind. Since both SEPs and solar wind come from coronal material, comparison of the two is of fundamental importance.

1.5 Solar Wind

The idea of a wind of particles streaming outward from the Sun was put into formal theory by Eugene Parker in the 1950s (Parker 1963). He was attempting to explain why comets appear to have two tails. One tail is gas and dust blown off the nucleus by photon pressure. The other tail is composed of particles which have been ionized by a fast plasma streaming by the comet. In 1962 the US Mariner II spacecraft found the first conclusive evidence of this plasma, the "solar wind." It measured the density and velocity of these particles, as well as the magnetic fields in interplanetary space (Neugebauer and Snyder 1966). It was found that this wind travels at about 400 km/second, and has a density of about 7 particles per cubic centimeter. Later studies found that there are at least two varieties of solar wind: the "slow" solar wind, which travels at speeds from ~300 to 600 km/s, and "fast" solar wind, which travels at speeds from ~600 to 800 km/s. For a recent review of the solar wind, see, e.g., von Steiger et al. (1997).

During the Apollo program in the 1970s, a team lead by Johannes Geiss of the University of Bern sent clean aluminum and platinum foils to the moon with the Apollo astronauts. The foils were placed on the moon's surface and left open for a few days. Since the moon has no magnetic field to deflect the particles, nor atmosphere to absorb them, the solar wind, traveling at 400 km/second, could penetrate a few angstroms into the foil material, becoming trapped. At the end of the mission, the foils were rolled back up and sealed. Back on Earth the composition of the captured solar wind was analyzed. This yielded measurements of the relative abundances of helium, neon, and argon and also provided measurements of the isotopic composition of those elements (see Table 1.4).

In the 1970s spacecraft were launched carrying electrostatic analyzers designed to study the solar wind. Such devices could measure the ratio E/q, the energy per charge of ions. In slow solar wind all of the ion species travel with the same velocity. The the kinetic energy of these ions is $\frac{1}{2}mv^2$, and so E/q is proportional to the mass per charge, m/q. This measurement could yield abundances and charge states of H, He, and a few elements. It was limited, due the ambiguity in separating

TABLE 1.4

In-situ measurements of solar wind isotopic composition.

Ratio	Value (percent)	Reference
$^{18}O/^{16}O$	0.222± 0.064	Collier et al. (1998)
$^{21}Ne/^{20}Ne$	0.24 ± 0.03	Geiss et al. (1972)
	0.23 ± 0.06	Kallenbach et al. (1997)
$^{22}Ne/^{20}Ne$	7.30 ± 0.16	Geiss et al. (1972)
	7.25 ± 0.37	Kallenbach et al. (1997)
$^{25}Mg/^{24}Mg$	12.0 ± 0.6	Bochsler et al. (1996)
$^{26}Mg/^{24}Mg$	14.2 ± 0.6	Bochsler et al. (1996)
$^{54}Fe/^{56}Fe$	$8.5^{+0.5}_{-2.2}$	Oetliker et al. (1997)
$^{57}Fe/^{56}Fe$	≤ 5	Oetliker et al. (1997)

different elements which have the similar E/q ratio, which meant that for instance, certain charge states of carbon and iron were obscured by helium. Thermal broadening of the helium peak also prevented studies of all but the coldest solar wind, so that it was not possible to study shock regions or the driver plasma in coronal mass ejections.

In the late 1980s instruments were developed which measured particle composition using time-of-flight analyzers (Gloeckler 1990). These instruments offered better mass resolution and lower background. The SWICS instrument on Ulysses made the first measurements of the abundances of C, N and Mg in the solar wind, and allowed much improved measurements of O, Si and Fe.

Solar wind experiments aboard WIND, SOHO and ACE have begun to measure the isotopic composition of the solar wind. Thus far, the isotopic composition of oxygen, neon, magnesium and iron have been reported. These measurements, along with the results from the lunar foils, are listed in Table 1.4.

TABLE 1.5

Isotopic abundances of particles implanted in lunar material.

Ratio	Value (percent)	Source
$^{13}C/^{12}C$	1.11± 0.2	Lunar soils and breccia (Becker 1980)
$^{15}N/^{14}N$	0.37± 0.03	Lunar soils and breccia (ibid.)
$^{21}Ne/^{20}Ne$	<0.26	Lunar soils "SEP" (Wieler et al. 1986)
$^{22}Ne/^{20}Ne$	8.85± 0.23	(ibid.)

1.6 Implanted Particles

Around the same time that the Apollo missions were returning the solar-wind collection foils from the moon, scientists discovered more clues to the solar wind composition in meteorites and lunar samples. Like the foils, the rocks and soils on the moon's surface and meteoroids in interplanetary space are also exposed to interplanetary particles. Solar wind, SEPs, and galactic cosmic rays are implanted into such material, and over millions of years of exposure, measurable quantities of material are trapped. The only elements which can be reliably studied in these samples are those which do not occur naturally in the exposed materials. This includes the noble gases, and also includes nitrogen in lunar materials. Values of the isotopic ratios in such materials are listed in Table 1.5.

Black and Pepin first investigated the isotopic composition of noble gases in meteorites in the late 1960s (Pepin 1967; Black and Pepin 1969). The source of the gases was not clear at the time. It was thought that this gas could be primordial trapped gas, or implanted solar wind, or implanted solar energetic particles. Yet with the return of lunar rocks and soils from the Apollo program, scientists had a wealth of material for investigation.

Meteoritic and lunar surveys found that there appeared to be a number of different populations of neon, each with a distinct isotopic composition. Two of these populations may be related to energetic particles: neon-B, which has $^{20}Ne/^{22}Ne$=12-

13, and neon-C, which has $^{20}Ne/^{22}Ne=10.6\pm0.3$ (Black 1983). Another component, neon-A, with $^{20}Ne/^{22}Ne=8.2\pm0.4$, was thought to be primordial neon trapped in the meteorites. (Note that the ratios are $^{20}Ne/^{22}Ne$, not $^{22}Ne/^{20}Ne$, as in the SEP and Solar Wind ratios previously mentioned. This is a matter of convention). The sources of these populations has been a matter of great debate. The initial method of studying these gases was to heat a sample of material, and to observe the composition of neon as it outgassed. Different populations of neon outgassed at different times and temperatures. Neon-B outgassed first, and so it was thought that this material occurred only in the outer few angstroms of the samples. Neon-C outgassed after neon-B, suggesting that perhaps it occurred only in the first few microns of the samples. Such behavior suggested that neon B and C could be particles implanted in the samples over long periods of time. The isotopic composition of neon-B was consistent with solar wind, and its implantation depths were consistent with particles at solar wind energies.

It was thought that neon-C component could be due to implanted solar energetic particles. The $^{20}Ne/^{22}Ne$ ratio in neon-C was lower that that of neon-B, and measurements of SEP neon isotopes by the Chicago and Caltech groups found ratios of $^{20}Ne/^{22}Ne$ which were also lower than solar wind values. At the time this result supported the suggestion that the neon-C component was due to implanted SEPs, and also supported the suggestion (Cameron 1982) that the neon-A component represented the bulk abundance of neon in the solar system.

Since there are three isotopes of neon, the various isotopic components can be represented in a "three-isotope" plot. Such a plot is shown in Figure 1.11, which is a simplified version illustrating the major points. Plots with real data can be found in Black and Pepin (1969), Black (1983), and Wieler et al. (1986). This plot shows the ratio of $^{21}Ne/^{22}Ne$ versus $^{20}Ne/^{22}Ne$ for different samples of material. When samples are heated, the first component to be released is neon-B. The $^{20}Ne/^{22}Ne$ ratio then decreases until the neon-C component is reached. As the temperature increases, the two ratios approach the point labeled "GCR spallation," which represents neon produced by high-energy GCR protons fragmenting the material in the rock.

A major breakthrough in the understanding of these neon components came

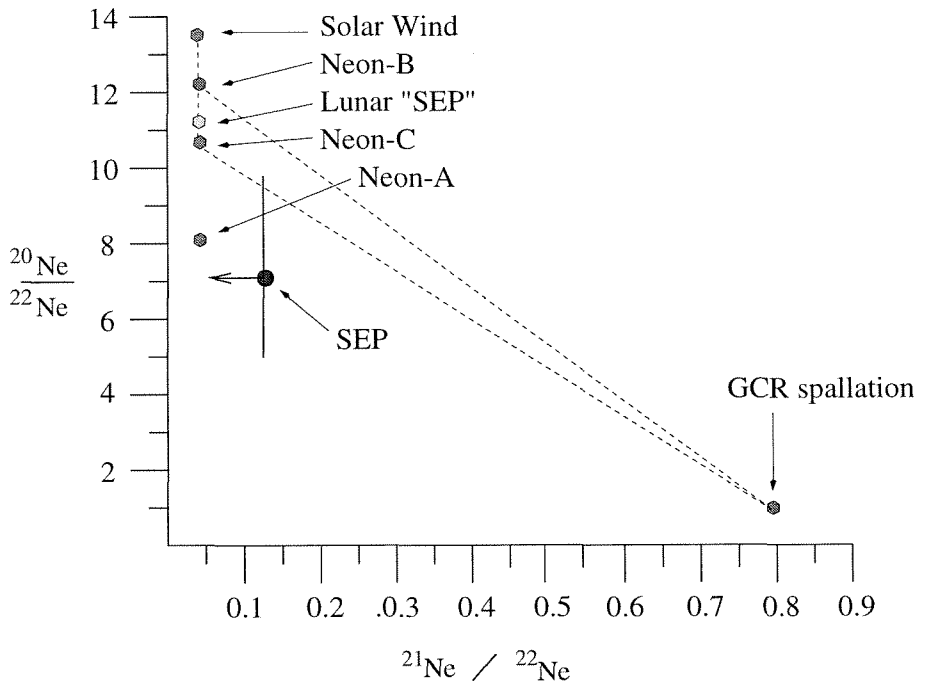

Figure 1.11: Three-isotope plot for neon, showing the neon A, B, and C components found in analysis of meteorites, adapted from Black (1983). Also shown for comparison are the ratio of "energetic particle" neon found in Lunar soils (Wieler et al., 1986), the neon ratios in the solar wind (Geiss et al., 1972), and the neon ratios in solar energetic particles (Mewaldt and Stone, 1989). The dotted lines drawn to the "GCR spallation" point show mixing of a few of the implanted components with neon which has been produced as the result GCR protons causing fragmentation of the material in the meteorites and/or lunar samples.

with new analyses of lunar materials. Two major approaches are used: closed system stepwise etching of soil grain surfaces (Wieler et al. 1986), and laser vaporization of individual grains (Nichols et al. 1994). Such studies find that there are at least two components of neon trapped in these lunar materials. In the first several hundred of angstroms, where particles with energies of a few hundred eV/nucleon can penetrate, there is a component of neon which has isotopic ratios virtually identical to the solar wind measurements of Geiss et al. (1972), and thus the same as the neon-B observed in meteorites. Deeper into the samples, where particles with energies $\geq$ 1MeV/nucleon could have been implanted, there exists an isotopically heavier component, similar to neon-C. This component has been referred to as "solar energetic particle" neon,

TABLE 1.6

Isotope abundance ratios observed in solar spectra.

Isotope Ratio	Ratio (percent)	Reference
$^{13}C/^{12}C$	1.06± 0.15	Hall (1973)
$^{18}O/^{16}O$	0.22± 0.07	""
$^{25}Mg/^{24}Mg$	12.5± 0.56	Boyer et al. (1971)
$^{26}Mg/^{24}Mg$	12.5± 0.56	""

since those depths are appropriate for implantation of ions at solar-flare energies. However, Wieler et al. (1986) note that the fluences required to produce the observed concentration of implanted material are much higher than the fluence of solar energetic particles as measured by spacecraft, and so the true source of neon-C has not been confidently identified.

1.7 Spectroscopic Observations of Solar Isotopes

The isotopic composition of solar material can be observed spectroscopically for a few elements by observing molecular absorption lines in sunspots and umbrae. The rotational-vibrational bands of molecules such as MgH and CO depend on the masses of their atomic constituents, and so the absorption lines from different isotopic species can be measured. Such measurements are problematic, however, since strength of the measured lines depends strongly on the local thermodynamic conditions in the region observed, and on the model of the radiation being absorbed. Results of these observations are given in Table 1.6.

1.8 Seeking Solar System Standards

The solar system formed ~4.6 billion years ago out of an interstellar cloud of gas and dust, often referred to as the proto-solar nebula. The present composition of the many bodies of the solar system derives from this initial source of material. Scientists have attempted over the years to determine the composition of this material, using observations of the photosphere, the corona, meteorites, terrestrial matter, and other sources. (Brown 1949; Suess and Urey 1956; Cameron 1982; Anders and Ebihara 1982; Anders and Grevesse 1989). The first tabulation of abundances combining solar, meteoritic, and stellar sources was compiled by Brown (1949), and the most recent listing of solar system abundances was compiled by Anders and Grevesse (1989). These tabulations is intended to provide scientists with a standard for the bulk composition of the solar system both at present and at the formation of the solar system.

For the purposes of this thesis, the tabulation by Anders and Grevesse (1989) is in comparing our results with the solar system composition. Henceforth, that paper and the data contained in it, will be referred to as "AG89." A list of isotopic ratios from AG89 is given in Table 1.7.

Such a table has many uses. The proto-solar abundances can be compared to the present composition of the interstellar medium, both nearby and in other parts of the galaxy. This can be used to test theories of the evolution of elements in the galaxy, or even of the birthplace of the Sun (Wielen and Wilson 1997). In studying the formation of planets and meteoroids, the primordial composition can also be used to study how these bodies evolved into their present state (Larimer 1988). Present-day solar composition can be compared to measurements of ancient trapped materials to see whether the composition of the Sun has changed over the lifetime of the solar system (Wieler and Baur 1995).

Some of the most precise measurements of elemental abundances come from meteorites. There are variations in the composition of meteorites, and such variations tell about their origins. However, one class of meteorites, the carbonaceous chondrites, show very little sign that they have been chemically altered since the formation of the

TABLE 1.7

Isotope abundance ratios adopted by Anders and Grevesse (1989). These values are used throughout the text, and are referred to as the "AG89" values, for brevity.

Isotope Ratio	Ratio (percent)
$^{13}C/^{12}C$	1.11
$^{14}C/^{12}C$	0 (extinct)
$^{15}N/^{14}N$	3.69
$^{17}O/^{16}O$	0.0381
$^{18}O/^{16}O$	0.201
$^{21}Ne/^{20}Ne$	0.243
$^{22}Ne/^{20}Ne$	7.31
$^{25}Mg/^{24}Mg$	12.6
$^{26}Mg/^{24}Mg$	13.9
$^{29}Si/^{28}Si$	5.07
$^{30}Si/^{28}Si$	3.36

solar system (Cameron 1982; Grevesse 1984). The relative abundances of the non-volatile heavy elements in these meteorites closely match those of the photosphere, which reinforces the concept that a set of abundances representative of the primordial solar nebula can be found through such comparisons.

The sources used to establish the isotopic composition of the solar system are less democratic. The majority of isotopic abundances tabulated by Anders and Grevesse come from analysis of terrestrial material, with the exceptions of hydrogen and the noble gases.

The noble gases are volatile, and so not well trapped by meteoroids. The processes which led to the loss of these gases also likely altered the isotopic composition of the remaining gas, and so Anders and Grevesse chose to base their measurements of Ne, Kr, Xe isotopic composition on solar wind measurements (Geiss and Bochsler 1985). The ratio $^{38}Ar/^{36}Ar$ in the solar wind is consistent with the ratio found in Earth's atmosphere, and so they use terrestrial measurements for this ratio. However, the abundance of ^{40}Ar is dominated by the decay product of ^{40}K, an abundant isotope in the Earth's crust. Since meteoritic argon appears to be less affected by ^{40}K decay, the lowest measured value of $^{40}Ar/^{36}Ar$ found in meteorites is taken to be representative of the pre-solar value.

The abundance of ^{2}H (deuterium) and ^{3}He are linked. Deuterium is destroyed in all forms of stellar burning and processed into ^{3}He. Thus, most of the deuterium in the universe was created in the Big Bang, and has only been depleted since. In order to calculate the pre-solar $^{2}H/^{1}H$ ratio, Anders and Grevesse calculated the difference between the abundance of ^{3}He trapped in meteorites and the present abundances of ^{3}He measured in the solar wind. The excess ^{3}He in the solar wind is then attributed to processed deuterium.

Nitrogen is a special case in that it does not occur in the lunar regolith, and so nitrogen found in lunar materials has most likely been implanted. Ancient samples of nitrogen taken from lunar soils of different ages suggest that the $^{15}N/^{14}N$ ratio in this material has increased as much as 40% over the past 2.5 Gy (Kim et al. 1995). Recent analysis of lunar soils, however, indicates that the nitrogen component is not from the solar wind, but has some as-yet unknown origin (Humbert et al. 1998).

For most elements, the isotope abundances are inferred from terrestrial materials. New measurements of solar wind and solar energetic particles are currently being made, however, and although the uncertainties in both kinds of particle measurements are currently much greater than those of terrestrial and meteoritic sources, the accuracy of particle measurements is improving with every new generation of detectors.

1.9 Chapter Summary

The SEP data investigated in this thesis was taken by the Mass Spectrometer Telescope (MAST) on SAMPEX. The overall aim of this study is to analyze the elemental and isotopic composition from two SEP events which occurred in 1992, and to compare the isotopic composition to measurements of solar wind, meteoritic material, and the photosphere. Both the satellite and the instrument are described in the next chapter.

Chapter 2

Experiment

2.1 The SAMPEX Mission

The Solar, Anomalous, and Magnetospheric Particle Explorer (SAMPEX) is a NASA mission dedicated to studying the composition of solar energetic particles, anomalous and galactic cosmic rays, and magnetospheric particles. The SAMPEX team is a collaboration between a number of institutions, with the University of Maryland at College Park as its principle institution. It was the first mission of NASA's Small Explorer (SMEX) program. Its international designation is 1992-038A, and is also designated Explorer 68. A description of the SAMPEX mission, and of each scientific instrument aboard SAMPEX, is given in volume 31 of the *IEEE Transactions in Geosciences and Remote Sensing* (Baker et al. 1993). A recent review of the current status of the mission is given in Mason et al. (1997).

There are four instruments aboard SAMPEX: the Heavy Ion Large Telescope (HILT), the Low Energy Ion Composition Analyzer (LICA), the Mass Spectrometer Telescope (MAST), and the Proton/Electron Telescope (PET). The abilities of these instruments are briefly described in Table 2.1. The suite of instruments together can measure particle composition at energies from hundreds of keV per nucleon up to several hundred MeV per nucleon. They are sensitive to atomic nuclei from hydrogen through nickel, as well as to electrons.

SAMPEX was launched on a Scout Rocket from the Western Space and

TABLE 2.1

Scientific instruments aboard SAMPEX.

	LICA	HILT	MAST	PET
Energy Range for:				
Electrons	-	-	-	0.4-30 MeV
H	0.76-6.1	-	-	18-250 MeV
He	0.45-6.1	4.3-38	7-20	18-350 MeV/nuc.
C	0.44-11.4	7.2-160	14-135	34-120 MeV/nuc.*
Si	0.33-5.5	9.6-177	21-210	54-195 MeV/nuc.*
Fe	0.21-3.1	11 -90	27-290	70-270 MeV/nuc.*
Charge range for Elements	1-25	2-28	2-28	1-2 (1-28)*
Charge range for Isotopes	2-16	2	2-28	1-2 (1-10)*
Geometry Factor (cm^2sr)	0.8	60	7-14	0.3-1.6
Field of View (deg, full angle)	24×20	68×68	101	58
Mass (kg)	7.4	22.8	7.5	(incl. with MAST)
Power (W)	4.9	5.6	5.3	(incl. with MAST)
Telemetry (kbps)	1.3	0.9	1.4	0.5

* - When PET is commanded to run in low-gain mode.

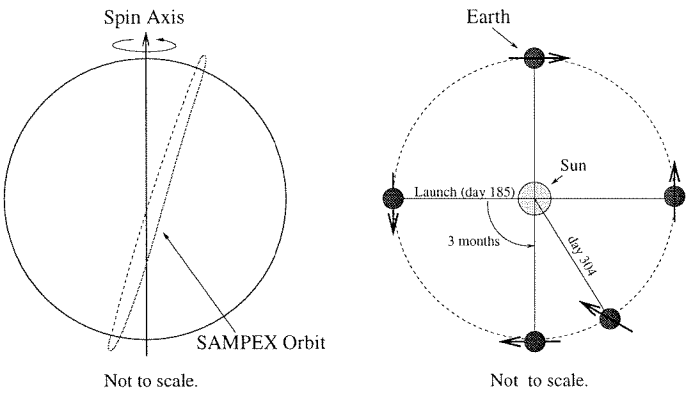

Figure 2.1: *Left*: The polar orbit of SAMPEX about the Earth. *Right*: As seen from above the northern poles of the Sun and Earth, the orbital plane of SAMPEX rotates clockwise by 90° every three months. The arrows over the Earth show the direction of SAMPEX as it crosses Earth's north pole. SAMPEX was launched into a dawn-dusk orbit on July 3, 1992 (day 185). On October 30th (day 304) SAMPEX was approaching a noon-midnight orbit.

Missile Center at Vandenberg Air Force Base in California on July 3, 1992 at 14:19UT. Its trajectory sent it roughly south over the Pacific ocean, placing it into a polar orbit inclined 82° with respect to the Earth's equator. The orbit is slightly elliptical, with apogee and perigee of 675 km and 512 km, respectively, above the Earth.

The spacecraft completes one orbit every 96 minutes. From a perspective sitting on Earth's equator, the spacecraft appears to cross the sky 24 degrees further westward with every orbit. So each day the spacecraft passes over the whole surface of the Earth twice. The orbital plane of SAMPEX rotates in space, with a period of about one year. Approximately every three months the spacecraft moves into a "dawn-dusk" orbit, meaning that its orbital axis is at a minimum angle with respect to the Earth-Sun line, and so the spacecraft is in full sunlight over its whole orbit. During such orbits the temperature of the spacecraft increases by ~9° centigrade. For example, the typical operating temperature of MAST is 16° C, but during dawn-dusk orbits the temperature can increase to 25° C.

2.1.1 MAST and PET

The Mass Spectrometer Telescope (MAST) shares a common electronics housing with the Proton-Electron Telescope (PET). Together, MAST, PET, and their housing make up the MAST/PET instrument. The two telescopes were designed and most of their parts were procured from 1979 through 1982 in a collaboration between Caltech and the Goddard Space Flight Center. The pair of instruments were to fly as part of the COMPAS experiment on board the U.S. spacecraft of the International Solar-Polar Mission. This was a joint mission between NASA and ESA, the European Space Agency. The mission was to consist of two spacecraft, which would fly out of the ecliptic plane and simultaneously explore the interplanetary environment on opposite poles of the Sun. The ESA spacecraft was eventually renamed Ulysses and launched in 1990. However, plans for the U.S. spacecraft were cancelled in late 1981, although the MAST and PET instruments were then at an advanced stage of development.

In 1988 NASA released an announcement of opportunity for the Small Explorer (SMEX) program. The goal of the SMEX program is described as follows:

> *NASA's Small Explorer (SMEX) Program provides frequent flight opportunities for highly focused and relatively inexpensive space science missions. SMEX spacecraft are 180 to 250 kg with orbit-average power consumption of 50 to 200 watts. Each mission is expected to cost approximately $35 million for design, development, and operations through the first 30 days in orbit.* (see `http://sunland.gsfc.nasa.gov/smex/smexhomepage.html`)

A requirement for the program was that the missions accepted had to be ready for launch within three years of acceptance. The MAST and PET instruments were in a good position to be prepared for flight within that short time. When SAMPEX was accepted as the first SMEX mission, work was begun to complete the construction of MAST and PET.

In 1990 a number of detectors were purchased to complete MAST. The individual detectors of MAST were calibrated in 1990 using heavy ion beams at the Lawrence Berkeley Laboratory Bevalac Facility. The new detectors and those purchased originally for COMPAS were further characterized, and the MAST and PET telescopes were assembled, at the Space Radiation Laboratory at Caltech in 1990 and

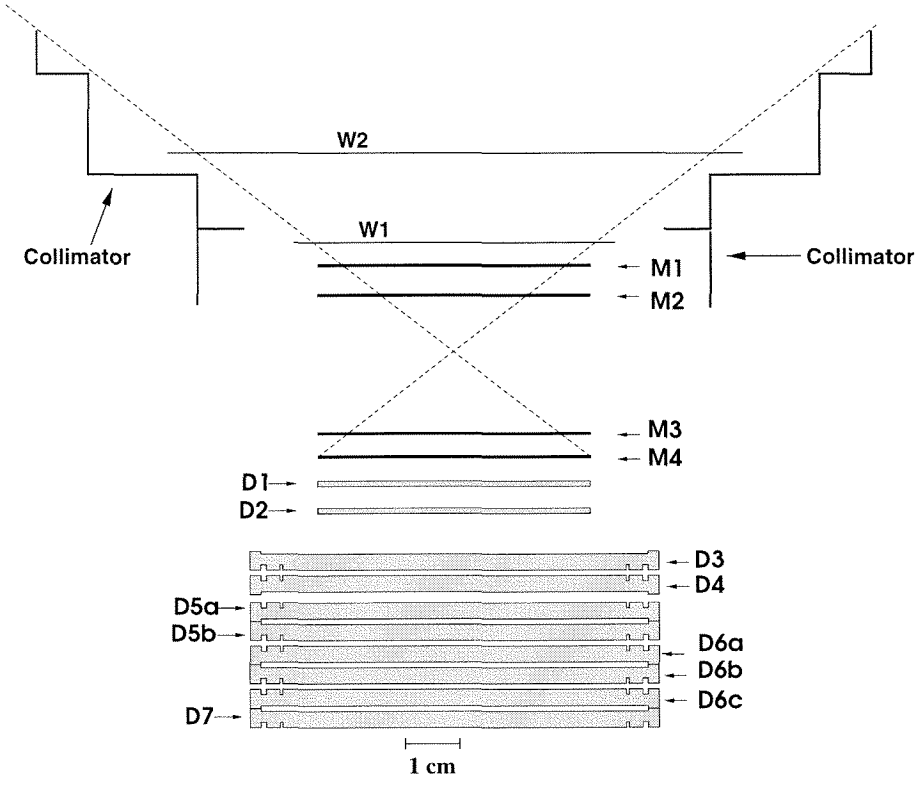

Figure 2.2: The Mass Spectrometer Telescope (MAST).

1991. The PET instrument was calibrated using electron beams at EG&G Ortec in Santa Barbara, CA, in 1991. In 1992 the assembled MAST/PET instrument was taken to the Bevalac for further calibration of MAST using energetic silicon and iron nuclei. The instrument electronics were assembled and tested, and the telescopes were integrated into their common housing at the Perkin-Elmer Corporation in Pomona, CA, from 1991 through 1992. Further calibrations of the instrument were performed at Goddard Space Flight Center, where the instrument was integrated onto the SAMPEX spacecraft.

2.2 The Mass Spectrometer Telescope

The MAST telescope is composed of a stack of silicon solid-state charged-particle detectors (see Figure 2.2). The detectors are protected from sunlight and

micrometeoroids by two Kapton windows, the outer window 1 mil thick and the inner window 3 mils thick. A collimator helps to limit the single-detector counting rates in the outer detectors so that they do not saturate the electronics. Each detector measures the energy deposited by energetic charged particles passing through it. The first four detectors also each measure a one-dimensional position of the particles, yielding trajectory. The detectors are ~115 μm thick at the front of the telescope, and increase in thickness to ~3000 μm at the back, as listed in Table 2.2. This enables MAST to measure the charge, mass and kinetic energy of energetic nuclei from Z=2 (helium) through Z=28 (nickel), in the energy range from ~15 to ~250 MeV per nucleon. Measurements of charge and mass are made using the $\frac{dE}{dx}$ versus E' technique, which will be described in Section 2.5. A description of the MAST instrument is also given in Cook et al. (1993). For a general discussion of solid-state detectors, see *Radiation Detection and Measurement* (Knoll 1989).

2.2.1 Surface Barrier Detectors: D1 and D2

The detectors D1 and D2 are n-type silicon surface barrier detectors (Ortec Incorporated 1980; Knoll 1989), purchased from EG&G Ortec in 1990. As specified by the manufacturer, the average thickness of D1 is 163 μm, and the average thickness of D2 is 495 μm (see Table 2.3). Both are nominally 2.526 cm in radius. The electrode ground side is made of aluminum, while the other bias contact is made of gold. The mass thickness of each contact is 40 $\mu g/cm^2$, for a total thickness of 0.02 μm of gold, and 0.15 μm of aluminum. Negative bias voltage is applied to the contacts through thin gold wires (see Table 2.7).

2.2.2 Lithium-Drifted Detectors: D3 through D7

The maximum possible depletion depth of a surface barrier detector is 1-2 mm. In order to measure higher-energy particles deeper in the MAST stack, the detectors D3 through D7 are made through the lithium-drift process, which can produce detectors with depletion depths up to 5-10 mm thick. These detectors are p-type silicon which have had one side exposed to a hot (~40° C) lithium vapor. The lithium,

TABLE 2.2

Detectors and windows in the MAST instrument.

Name	Center Thickness (μm)	Vertical* Distance (cm)	Radius (cm)	Description
W2	25.4	-1.616	5.240	Kapton® Window
W1	76.2	-0.422	2.940	Kapton® Window
M1	130	0.0	2.526	Silicon Matrix Surf. Barrier
M2	108	0.638	2.526	"
M3	114	3.180	2.526	"
M4	113	3.655	2.526	"
D1	164	4.224	2.526	Silicon Surface Barrier
D2	496	4.646	2.526	"
D3	1767	5.364	3.065	Silicon Lithium-Drifted
D4	3057	5.679	3.070	"
D5a	3113	6.167	3.070	"
D5b	3113	6.507	3.065	"
D6a	3082	6.927	3.070	"
D6b	3074	7.262	3.065	"
D6c	3136	7.673	3.075	"
D7	3134	8.016	3.070	"

*Measured from the top of M1 to the top of the detector.

TABLE 2.3

Thickness measurements of surface-barrier detectors, as specified by EG&G Ortec.

Detector Name	Manufacturer's Serial No.	Average Thickness (μm)	Center Thickness (μm)
D1	30-473B	163	164
D2	30-071D	495	496

an electron donor, drifts into the material, compensating the p-type material in the interior of the detector, and leaving an n-type layer near the diffusion surface. The far surface remains p-type, and the detector thus has a p-i-n junction across it. The p-type surface is not active and forms a "dead layer." In the MAST 3000 μm detectors this layer is typically $\sim$30 μm thick, and is on the grooved side of the detector (see Figure 2.2).

The lithium drifted detectors (henceforth the LiDs) were purchased from Lawrence Berkeley Labs in 1980. Coarse maps of the detector thicknesses, made using appropriately calibrated non-contacting ADE thickness gauges, were supplied by the manufacturer. Some parameters from these thickness maps are given in Table 2.4.

The LiDs are wider than the M1 through D2 detectors, as listed in Table 2.5. A negative reverse bias is applied across the detectors to fully deplete the active regions, as listed in Table 2.7.

The lithium LiDs have two grooves cut into their electrodes, creating an inner detector of radius $\sim$3 cm, and a guard ring of width $\sim$0.24 cm. Particle identification by MAST requires that a particle passes into and stops within the detector stack, so the guard rings indicate whether a particle enters or leaves through the sides of the stack. Such particles cannot be used for charge and mass measurements.

TABLE 2.4

Thickness measurements of the lithium-drifted detectors were made using a non-contacting ADE thickness gauge at about 30 points across the detector, yielding the measurements listed below. The depths of the dead layers were measured using alpha particles.

Detector	Manufacturer's	Thickness (μm)			Avg. Dead Layer
Name	Serial No.	Average	at Center	Variance	Thickness (μm)
D3	4003	1747	1767	13.3	35
D4	4181	3064	3057	6.5	31
D5a	4184	3101	3113	9.5	33
D5b	4067	3100	3113	8.2	28
D6a	4183	3070	3082	7.5	33
D6b	4185	3068	3074	7.2	31
D6c	4186	3125	3136	6.7	35
D7	4062	3125	3134	7.0	27

TABLE 2.5

Diameters of the lithium-drifted detectors, and widths of their guard rings.

Detector Name	Wafer Diameter (cm)	Inner Region Diameter (cm)	Guard Width (mm)
D3	7.51	6.13	2.48
D4	7.50	6.14	2.40
D5a	7.50	6.14	2.46
D5b	7.51	6.13	2.41
D6a	7.50	6.14	2.37
D6b	7.50	6.13	2.29
D6c	7.50	6.15	2.35
D7	7.51	6.14	2.35

2.2.3 Matrix Surface Barrier Detectors: M1 through M4

The detectors M1 through M4 are surface barrier detectors, 2.526 cm in radius and ~115 μm thick (see Table 2.6). They were all purchased from EG&G Ortec. M2 was purchased in the early 1980s for the COMPAS instrument on the International Solar Polar Mission, while M1, M3, and M4 were purchased for MAST in 1990 and 1992.

The contact on the ground side of each matrix detector is 40 $\mu g/cm^2$ of gold. The biased side is 120 $\mu g/cm^2$ of aluminum, deposited in 93 parallel strips of 0.5 mm pitch. These strips range in length from 2.17 to 5.05 cm, and are connected by 19 Ω resistors in series (see Figure 2.3 and Figure 2.4). Electron-hole pairs are liberated by the passing ion, and the holes are collected on both sides of this resistive divider. The charge collected from one side of the resistive divider is defined as Q1, and the charge collected on the other side is defined as Q2. Charge-sensitive preamplifiers amplify those charges into voltage signals, designated V_1 and V_2. The MAST electronics then

TABLE 2.6

Thickness measurements of matrix detectors. The thicknesses of M1, M3 and M4 are from the manufacturer, while the thickness of M2 was calculated from calibrations of the instrument.

Detector Name	Manufacturer's Serial No.	Average Thickness (μm)
M1	30-192C	125
M2	20-848C	114
M3	31-174C	113
M4	31-155C	115

sums V_1 and V_2, amplifies the signal, and then digitizes that voltage to form V_{sum}. The V1 voltage is also amplified and then digitized. To a good approximation, the position, X, of a particle which hits a matrix detector is given by

$$X \propto \frac{V_1}{V_{sum}}$$

Detectors M1 and M3 measure particle position in the X direction, while M2 and M4 measure in the Y direction. This provides two (X,Y) coordinate pairs which can be used to determine particle trajectories through the telescope.

The design using a resistive divider to determine particle position is very efficient in terms of reducing the electronic complexity of the trajectory system, and hence the weight of the instrument. However, it does introduce a complication to the analysis of the signals from the matrix detectors.

The 19 Ω resistors combine with the capacitance of the strips to introduce RC time constants into the circuit. This causes the signal to be stretched out in time depending on how many strips it had to cross. The signal pulse received thus has a duration which is not much less than the shaping time of the preamplifier, leading to a nonlinear response by the preamplifier. This "ballistic deficit" was measured

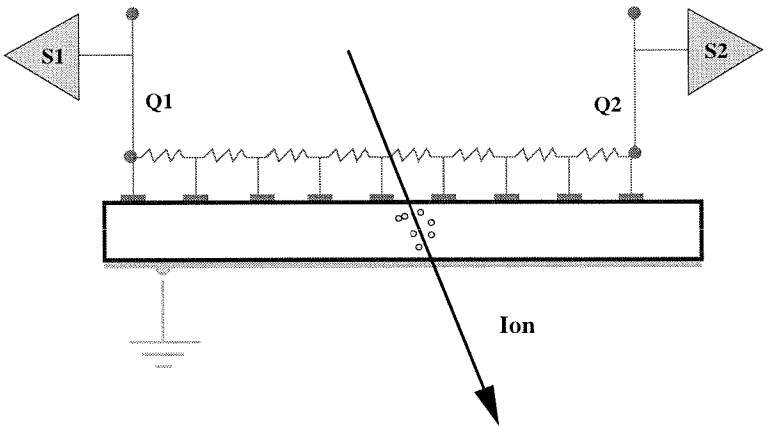

Figure 2.3: Illustration of the operation of a matrix detector, using only 9 strips in this example. The strips are connected to one another by resistors. Electron-hole pairs are liberated by a passing ion, and the holes are collected on either side of this chain, and designated "Q1" and "Q2." S1 and S2 are preamplifiers which convert the charges to voltage levels. The voltage outputs of S1 and S2 are summed to form V_{sum}, and the voltage output of S1 is converted to the voltage V_1. Both V_{sum} and V_1 are digitized and stored.

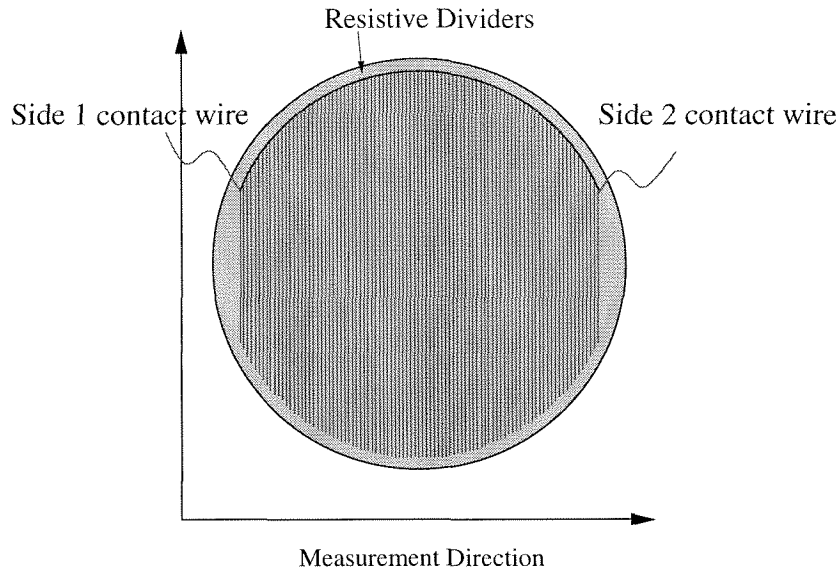

Figure 2.4: Top view of a matrix detector. The conducting strips are connected at one end through resistors, and the measurement direction is perpendicular to the orientation of the strips.

in the laboratory, and has been successfully modeled (Selesnick 1992). This effect is discussed more fully in Chapter 3.

2.3 MAST Electronics

This section explains how the detectors on MAST are electronically connected, and how the instrument electronics uses the signals from the detectors. A diagram of the MAST electronics is shown in Figure 2.5.

A voltage bias is applied across each of detectors M1 through D7, opposite to the direction of the p-n junctions. The voltage is regulated by the MAST/PET High Voltage Power Supply (HVPS), located in the MAST/PET housing. Voltage levels are listed in Table 2.7.

Detectors D5a and D5b are electronically connected to the same readout electronics to form the "D5" detector. Detectors D6a, D6b, and D6c are connected to form the "D6" detector. This allows the instrument to measure a wide range of

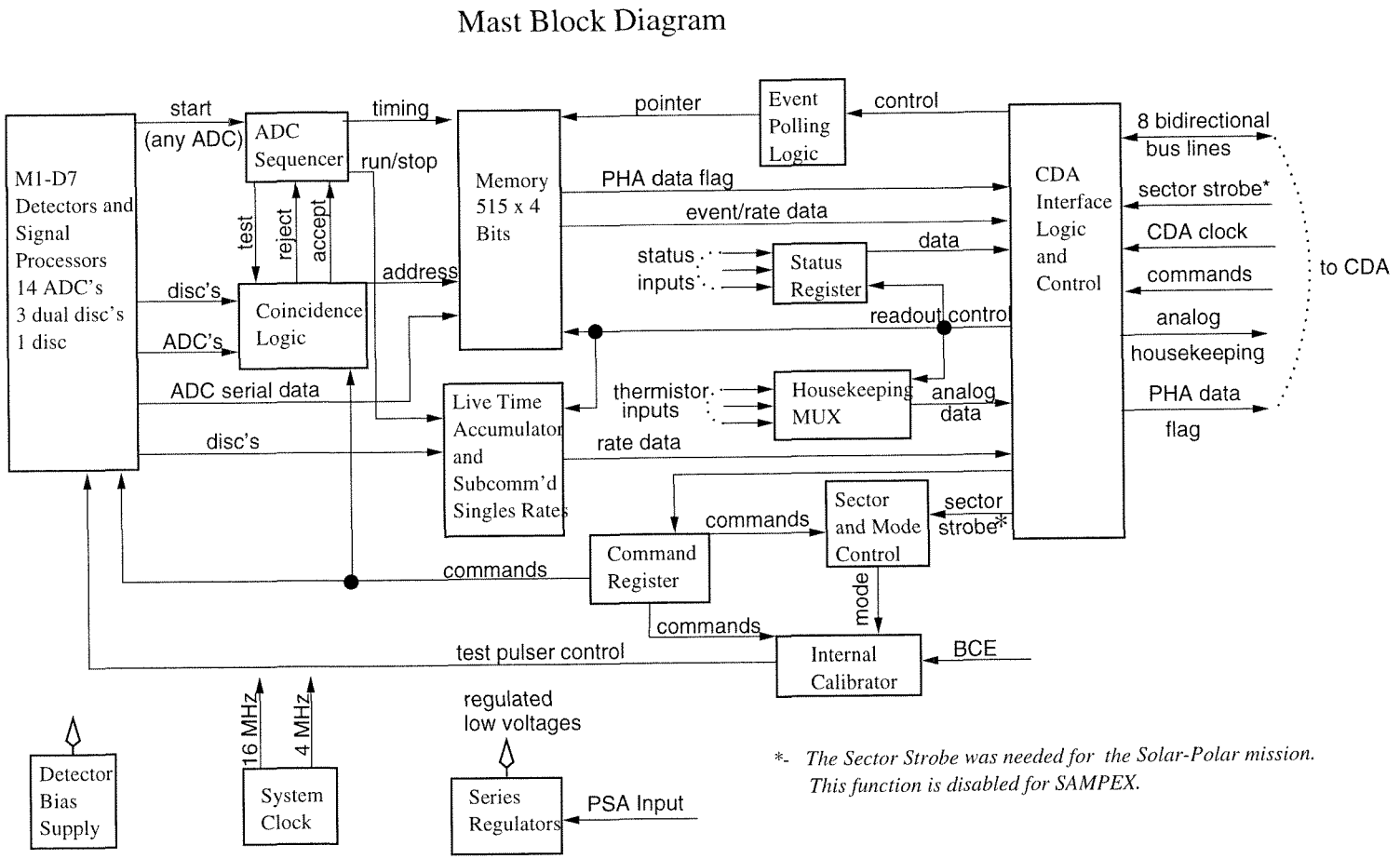

Figure 2.5: MAST Block Diagram.

TABLE 2.7
Bias voltages of the MAST detectors.

Detector	Bias Voltage (volts)
M1-D1	-40
D2	-200
D3	-300
D4-D7	-500

particle energies with a minimum of electronic complexity. For similar reasons, guard rings G3, G5a, and G5b are connected to form "G35," rings G4 and G7 are connected to form "G47," and guard rings G6a, G6b, and G6c are connected to form "G6."

The readout electronics of each MAST detector element begins with a charge-sensitive preamplifier. The output voltage of each preamplifier is AC-coupled to a post-amplifier which shapes the pulse for use by further electronics. There are a total of 18 of these "pre/post" amplifiers in MAST. The outputs of 14 of the pre/posts are connected to analog-to-digital converters, and the outputs of the remaining 4 are sent to discriminator circuits, as shown in Table 2.8.

The guards G35, G47 and G6 are connected to dual-level discriminators. The lower threshold of each discriminator is called the "low guard," and the higher one is the "high guard." The low guards are sensitive to singly-ionizing radiation and are used in the coincidence requirements for $Z<3$ nuclei. However, heavy ions passing through the detector stack may result in knock-on electrons or cross talk signals which could trigger the low-level guards. To avoid rejecting the heavy ions because of this, the high guards have higher thresholds, and are used for the $Z\geq 3$ coincidence equations.

The last detector, D7, is connected to a single discriminator. D7 is used to determine whether a high-energy particle penetrates through the detector stack. The trigger levels of these discriminators are given in Table 2.8.

TABLE 2.8

MAST detector electronics and threshold levels.

Electronic Element	Detectors Involved	Threshold(s) MeV		
ADC		Trigger	A	B
M1X1	M1(S1)	1.78	-	-
M1XS	M1(S1+S2)	2.20	6.6	22.0
M2Y1	M2(S1)	1.66	-	-
M2YS	M2(S1+S2)	1.65	6.3	21.3
M3X1	M3(S1)	1.26	-	-
M3XS	M3(S1+S2)	1.30	7.8	24.8
M4Y1	M4(S1)	2.59	-	-
M4YS	M4(S1+S2)	3.15	8.1	25.0
D1	D1	1.46	7.2	26.6
D2	D2	2.94	12.3	45.3
D3	D3	5.68	25.6	82.4
D4	D4	8.97	33.8	125
D5	D5a+D5b	13.31	48.7	179
D6	D6a+D6b+D6c	19.77	69.4	256
Dual Discriminators		Low	High	
G35	G3+G5a+G5b	0.49	4.95	
G47	G4+G7	0.42	4.35	
G6	G6a+G6b+G6c	0.38	3.96	
Single Discriminator				
D7	D7	0.35		

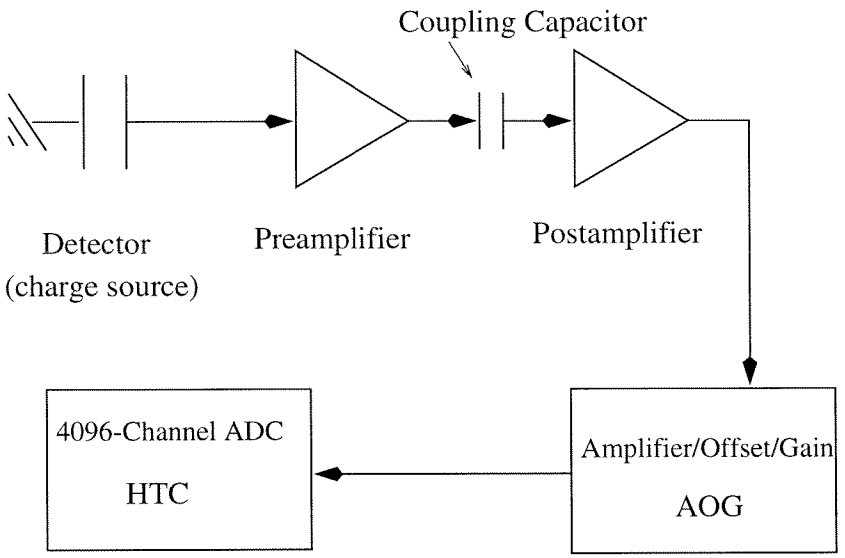

Figure 2.6: Illustration of the pulse-height analysis electronics. The post-amplifier is AC-coupled to the post-amplifier through a capacitor.

A flowchart illustrating the electronic elements in the pulse-height analysis chain is shown in Figure 2.6. The detector itself is a current source, and the preamplifier converts this to a voltage, which is then capacitively coupled to the post-amplifier, which shapes the signal. The Amplifier Offset Gain (AOG) then amplifies the signal, and sends it to the 4096-channel ADC, which digitizes the signal using a height-to-time converter (HTC).

Each ADC also has two additional commandable discriminators, designated A and B, which are used to classify events. The threshold of each A-level discriminator is set just above the maximum energy which a proton could deposit in that detector, at the maximum angle of incidence for a given detector. Likewise, the threshold of each B-level discriminator is set just above the maximum energy which an alpha particle could deposit in that detector.

Particles which trigger one or more of the B discriminators are labeled as Z3 events ($Z \geq 3$), and are nominally identified as heavy ions. Particles which trigger one or more of the A-level discriminators and none of the B-levels are labeled as Z2 events and are nominally helium. Those which trigger neither A nor B are classified as Z1 and are nominally protons. The trigger level of each A and B discriminator, as

well as that of each ADC, is given in Table 2.8.

2.3.1 Instrument Livetime

MAST has an internal clock which signals the MAST electronics every 8.192 ms. If the electronics are not otherwise busy, this signal causes the logic to increment the MAST livetime counter by one. However, if the instrument is busy processing another signal when the livetime clock signals, that count is not added to the livetime rate. In a six-second interval during which the instrument is not otherwise occupied, the total number of livetime counts will be 732. If there are N livetime counts in a six-second interval, then the time, τ, over which the instrument was live to real events is

$$\tau = \frac{N - N_{min}}{732 - N_{min}} \times 6sec \tag{2.1}$$

An extensive analysis of MAST livetime has been made by Richard Leske (Leske 1995), who finds that for solar energetic particle observations, the best value for the offset is $N_{min} = 92.7$.

2.3.2 Event Timing

A MAST "event" occurs whenever any of the 14 ADC discriminators listed in Table 2.8 is triggered, or when the livetime clock signals. Instrument dead time is introduced whenever such an event occurs, as illustrated in Figure 2.7. During this time MAST cannot respond to new events, as the instrument polls its logic, increments the appropriate rate counters, and writes information to rate memory. Further dead time may be introduced if the instrument logic dictates that the event is to be pulse-height analyzed and written to the PHA event memory. The simplest event happens when only the rates are incremented. This can last from 34-40 μs, depending on how many rates need to be incremented. The longest dead time is introduced when the event is pulse height analyzed. This kind of event requires rundown time for the height-to-time converter, and also requires 375 μs to write the

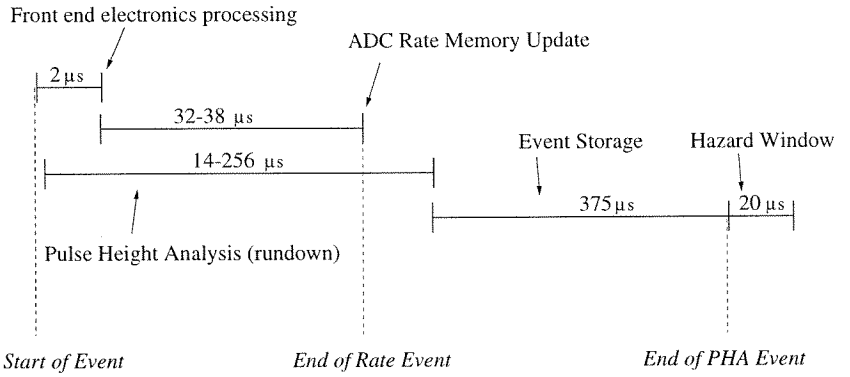

Figure 2.7: Timing of the MAST Electronic Logic (not to scale).

digital signals to memory. The hazard window is open for 20 μs after an event is finished. If an event occurs in this time and is pulse-height analyzed, it is flagged as a hazard, and the HAZ rate is updated. The lower limit on the event duration means that the maximum rate that MAST can register is $\sim 29 \times 10^3$ counts per second.

The "front end processing" begins when a discriminator is triggered, or the livetime clock signals. The instrument waits 2 μs in order that all of the ADC signals, presumably from a valid particle, can reach their maximum. Triggers are accumulated during this time for use in the logic processing.

After the front end processing, the instrument spends from 32-38 μs performing logic tests and incrementing rate equations. The logical tests and some of the rate equations are listed in Table 2.9. The low-resolution rates are described in Table 2.11.

A number of these rates could be incremented for one particular event trigger, and the instrument dead time depends on how many rates are to be updated. For example, if the event is simply a livetime trigger, then the only rate which will be updated is the livetime rate, LIVE.

If the logic determines that the event should be written to PHA event memory, then an event rundown time is introduced. When the first HTC detects that the peak of a pulse has been reached, a linear gate in each of the AOGs is closed so that no new signals can get through. This begins the rundown. The height of each signal is converted to a time, and the time is converted into digital channel number.

The duration of the rundown can be from 14 to 256 μs, depending on the amount of energy deposited in each detector. While the event rundown is happening, the rate memory is updated as mentioned above. A further fixed interval of 375 μs is required for writing the event to memory once it has been analyzed.

Events which deposit a large amount of energy in the telescope may cause certain baseline voltages in the electronics to dip below normal levels. For this reason, there is a 20 μs gate called the "hazard window" which opens right after MAST finishes processing an event. If another MAST event occurs within this window, the event is flagged as a hazard, and classified as a "HAZ" event, which goes into its own separate buffer. The hazard flag indicates that the detector electronics may not have had sufficient time to return to baseline levels, and so the quality of the event may be suspect. In the data discussed in this thesis, HAZ events were vetoed by the instrument, and so they were not written out in the data.

2.3.3 Event Logic

The triggers that are received during the front-end electronics processing are used to classify the event. A set of logic equations is applied to the event, as given in Table 2.9. The results of the logic test determine how the instrument will treat the event. If an event does not satisfy any of the PHA Event equations, then only the instrument rates will be incremented. When the instrument is in nominal operation mode, if the event does satisfy one of the PHA Event equations, and if it is not tagged as a hazard event, then it will be pulse-height analyzed and stored in a PHA event buffer. The instrument can be commanded, however, to allow pulse-height analysis of hazard events.

2.3.4 Event Rate Data

A given MAST event can satisfy one or more of the logic equations. Every event causes one or more rate counters to be incremented. The rates stored by MAST are listed in Table 2.11. Some rates correspond to the discriminators listed in Table 2.8 and some correspond to equations listed in Table 2.9. The rate counters are stored

TABLE 2.9

MAST Sub-equations. These equations are used to define MAST PHA and Rate events. Logical elements which are discriminator triggers (as given in Table 2.8) are written in italics. The symbol "!" is logical NOT, "• " is logical AND, and "+" is logical OR.

MAST Sub-Equations

	Name	Equation
1	M12	*M1XS* • *M2YS*
2	M34	*M3XS* • *M4YS*
3	EVENT	M12 • M34
4	R6	*D6*
5	R5	*D5* • !R6
6	R4	*D4* • !R6 • !R5
7	R3	*D3* • !R6 • !R5 • !R4
8	R2	*D2* • !R6 • !R5 • !R4 • !R3
9	R1	*D1* • !R6 • !R5 • !R4 • !R3 • !R2
10	R0	!R6 • !R5 • !R4 • !R3 • !R2 • !R1
11	L	*M1XSA + M2YSA + M3XSA + M4YSA + D1A + D2A + D3A + D4A + D5A + D6A*
12	H	*M1XSB + M2YSB + M3XSB + M4YSB + D1B + D2B + D3B + D4B + D5B + D6B*
13	G1	G35L + G47L + G6L
14	G2	G35H + G47H + G6H
15	HIZ	EVENT • !*D7* • !G2 • H

TABLE 2.10

MAST PHA Event Equations.

MAST PHA Event Equations		
	Name	Equation
1	HIZR0	HIZ • R0
2	HIZR1	HIZ • R1
3	HIZR2	HIZ • R2
4	HIZR3	HIZ • R3
5	HIZR4	HIZ • R4
6	HIZR5	HIZ • R5
7	HIZR6	HIZ • R6
8	Z1	EVENT • !*D7* • !G1 • !H • !L
9	Z2	EVENT • !*D7* • !G1 • !H • L
10	PEN	EVENT • *D7* • !G2

TABLE 2.11

MAST Low-Resolution Rates.

Rate Name	Description
Z1SEC	Z = 1 events, Ranges 0, 1, and 2
ADCOR	OR of all ADC triggers
LIVE	Livetime pulser rate; no dead time = 732
PEN	Events which satisfy the EVENT equation and trigger D7, but do not trigger the high-level guards (G2)
Z1	Z=1 event rate
Z2	Z=2 event rate
HIZR0	Z>2 events; only matrix detectors triggered
HIZR1	Z>2 events; D1 last triggered detector
HIZR2	Z>2 events; D2 last triggered detector
HIZR3	Z>2 events; D3 last triggered detector
HIZR4	Z>2 events; D4 last triggered detector
HIZR5	Z>2 events; D5 last triggered detector
HIZR6	Z>2 events; D6 triggered
RATE17	Subcommutated rate 17*
RATE16	Subcommutated rate 16*
RATE18	Subcommutated rate 18*
Z1RX	Subcommutated Z = 1 events*
Z2RX	Subcommutated Z = 2 events*

* See Table 2.12.

in instrument rate memory. They are accumulated over 6 seconds and then reset to zero.

A portion of the MAST rates are stored in the same area of memory at different times, in a process called subcommutating, which saves on telemetry at

TABLE 2.12

Subcommutated Rate Description.

Subcom	Subcom Rate				
1	M1XSA	M1X1	D7	Z1R0	Z1R0
2	M1XSB	M1XS	G35L	Z1R1	Z1R1
3	M2YSA	M2Y1	G35H	Z1R2	Z1R2
4	M2YSB	M2YS	G47L	Z1R3	Z1R3
5	M3XSA	M3X1	G47H	Z1R4	Z1R4
6	M3XSB	M3XS	G6L	Z1R5	Z1R5
7	M4YSA	M4Y1	G6H	Z1R6	Z1R6
8	M4YSB	M4YS	HAZ	Z1R0	Z1R0
9	D1A	D1	D5A	Z1R0	Z1R0
10	D1B	D2	D5B	Z1R1	Z1R1
11	D2A	D3	D6A	Z1R2	Z1R2
12	D2B	D4	D6B	Z1R3	Z1R3
13	D3A	D5	M12	Z1R4	Z1R4
14	D3B	D6	M34	Z1R5	Z1R5
15	D4A	G1	L	Z1R6	Z1R6
16	D4B	G2	H	Z1R0	Z1R0

the cost of obtaining only a regular sampling of the subcommutated rates, instead of continuous coverage. Five of the MAST rates are subcommutated, and each one measures a different rate every 6 seconds over 16 cycles. This way the same buffer can store many different rates at different times. The subcommutated rates are described in Table 2.12.

A key rate which will be mentioned in the next chapter is the ADCOR rate. The ADCOR counter is incremented every time any of the MAST ADC discriminators is triggered. During solar particle events the ADCOR rate is dominated by low-energy

TABLE 2.13

MAST status bytes.

Name	Bit	Name	Comment	Name	Bit	Name	Comment
DTFLG	7	Range	Last det. fired	EVFLG	7	not HIZ	Event-type flags
	6	"	"		6	not PEN	"
	5	"	"		5	not Z2	"
	4	G2	High guard flag		4	not Z1	"
	3	G1	Low guard flag		3	not Cal	"
	2	Spare	Spare		2	not HAZ	"
	1	-	"		1	Spare	Spare
	0	-	"		0	"	"

(~5 MeV) protons triggering the M1 detector.

2.3.5 Event PHA Data

Events which are pulse-height analyzed ("PHA events") are stored in the PHA event memory as two status bytes and 14 12-bit ADC channel numbers. The two status bytes contain information describing which guards have been triggered, identifying the deepest detector triggered, and describing the class of the event. These data bytes are described in Table 2.13. The ADC channel numbers encode the amount of energy deposited in each of the pulse-height analyzed detectors (M1 through M4, and D1 through D6).

MAST PHA events fall into five classes: Z1, Z2, HIZ ($Z \geq 3$), PEN, and CAL. These are described in Table 2.14, and the logic equations defining them are given in Table 2.9. The Z1, Z2, and HIZ events correspond to particles which stop within the detector stack, and thus require anti-coincidence with D7 and the guards. The PEN events go through the telescope and trigger D7. CAL events are created when the instrument goes into a self-calibration mode approximately once every month. In calibration mode, voltage pulses are sent to the detector electronics at eight different

TABLE 2.14

MAST Event buffers.

Name	Buffer	Description
CAL	1	Internal Calibrator
HIZR456	2	Z≥3 Ranges 4, 5, and 6
HIZR3	3	Z≥3 Range 3
HIZR2	4	Z≥3 Range 2
HIZR1	5	Z≥3 Range 1
HIZR0	6	Z≥3 Range 0
PEN	7	Penetrating Events
Z2	8	Z=2 Ranges 0-6
Z1	9	Z=1 Ranges 0-6

voltage levels. The pulse-heights thus generated are stored as an ordinary MAST PHA Event.

Particles are also classified by the detector in which they stop. The stopping detector is the last ADC which was triggered for that particle. Particles which stop in M4 are called Range 0, those stopping in D1 are called Range 1, and so on to Range 6, as described in Table 2.9. During solar particle events the MAST electronics can be saturated with event triggers. Since particles which penetrate deep into the detector stack are rarer than short-range particles, they are given a higher priority in the readout of PHA Events.

MAST has nine memory buffers in which it stores PHA Events, as shown in Table 2.14. The SAMPEX Data Processing Unit (DPU) takes data from these buffers, and places them in spacecraft memory for telemetry to the ground. The format of these events is shown in Table 2.15. The DPU has a limit on the number of events of each type that it can read out. For the time periods discussed in this thesis, the quota is 12 events per second for HIZ, Z2, Z1, and PEN events. Because the DPU begins reading from the first buffer, events with lower buffer number have

TABLE 2.15

Format of MAST Event data as sent to the SAMPEX DPU.

Name	Size	Description
DTFLG	8 bits	Range and Guard status byte
EVFLG	8 bits	Event-type status byte
M1X1 ADC	12 bits	Matrix 1, Side 1 energy
M1XS ADC	12 bits	Matrix 1, Sum energy
M2Y1 ADC	12 bits	Matrix 2, Side 1 energy
M2YS ADC	12 bits	Matrix 2, Sum energy
M3X1 ADC	12 bits	Matrix 3, Side 1 energy
M3XS ADC	12 bits	Matrix 3, Sum energy
M4Y1 ADC	12 bits	Matrix 4, Side 1 energy
M4YS ADC	12 bits	Matrix 4, Sum energy
D1 ADC	12 bits	Detector 1 energy
D2 ADC	12 bits	Detector 2 energy
D3 ADC	12 bits	Detector 3 energy
D4 ADC	12 bits	Detector 4 energy
D5 ADC	12 bits	Detector 5 energy
D6 ADC	12 bits	Detector 6 energy

higher priority.

The DPU adds some data to the MAST event. First is the spacecraft time, or STIME, which is updated every 256 seconds. Each MAST event also has a time assigned to it, the ETIME, which is the number of seconds since the last STIME. These two numbers are used to identify when each MAST event occurred. Each event is also tagged with an event sequence number which counts the number of events stored by the DPU, which is reset to zero at the beginning of each day.

2.3.6 Other Data Types

There are two other data types associated with the analysis of MAST PHA Events. The first is the MAST status byte. This indicates whether MAST is in calibration mode and whether the ADCs are enabled. The other data are the MAST housekeeping parameters. Among these parameters are the voltages across a number of thermistors located throughout the MAST/PET housing and within the telescopes themselves. These data are taken by the spacecraft, stored, and written out independently of the MAST Rate or PHA Event data.

2.4 Instrument Calibration

During and after the assembly of MAST, a number of calibrations were performed in order to verify that the instrument was working properly, and so that a set of instrument parameters would exist for the analysis of the instrument data during the mission.

2.4.1 Discriminator Thresholds and ADC Response

The MAST preamplifiers, and all their following electronics, can be tested by sending charge pulses to the preamplifier inputs. The electronics chains were tested and calibrated by two methods. In one method an external capacitor is connected to the preamp input, and voltage pulses are sent to the test capacitor. The other method is to send test pulses to the internal test capacitor which is built in to every preamp. Knowing the input voltages and the capacitor values, it is possible to send known charge pulses to the electronics, and thus characterize the system response.

The relationship between input voltage, V, and charge, Q, sent to the preamplifier is given by $Q = C_T V$, where C_T is the capacitance of either the internal or external test capacitor. The capacitances of the internal test capacitors are given in Table 2.16.

The signal from a silicon detector is a charge pulse. It takes 3.62 eV to liberate an electron-hole pair in silicon, which means that one pico-Coulomb of charge

TABLE 2.16

Capacitances of the internal test capacitors used for ground and in-flight pulser calibrations of MAST.

Detector	Test Capacitor (pF)	Detector	Test Capacitor (pF)	Detector	Test Capacitor (pF)
M1	2.71	D1	3.83	D5	28.9
M2	2.61	D2	7.06	D6	39.5
M3	3.33	D3	12.2		
M4	2.75	D4	20.0		

corresponds to 22.6 MeV of energy deposited in a detector. The relation between input voltage and equivalent energy given to the detector is:

$$E = 22.6 C_T V \tag{2.2}$$

where E is in MeV, C is the capacitance of the test capacitor in picofarads and V is the input voltage in volts.

Discriminator thresholds were calibrated by sending a set of voltage pulses to the test capacitor inputs and observing how the number of triggers depended on the input voltage level. Plots of trigger rate versus equivalent energy were fit with the error function to determine the mean and the width of the response of each discriminator, as demonstrated in Figure 2.8.

A similar technique was used to calibrate the ADC channels. Pulser voltage levels were ramped through the voltage range of each ADC to map the relation between channels and voltage. This relation is linear to better than a tenth of a percent. Systematic deviations from linearity below the 0.1% level were mapped out, as illustrated in Figure 2.9, to increase the accuracy. The deviations of the fits from linearity were fit with piecewise linear functions, each of the form $E = A \times (N - B)$ where E is the energy in keV, N is the channel number, A is the energy per channel in keV, and B is a channel offset. The fits to this function and the boundaries for

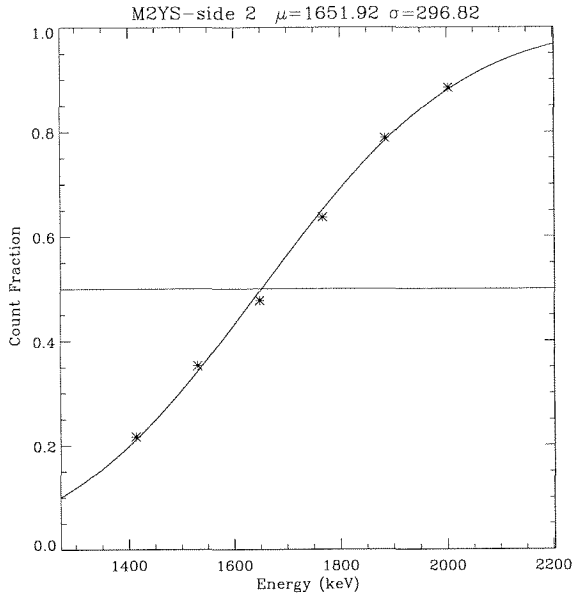

Figure 2.8: Calibration of the M2YS ADC discriminator, with the pulser attached to side 2 of the matrix detector. μ is the mean energy, and σ is the noise, both in keV.

the different fit regions are given in Table 2.17. Note that the linearity maps were only made from the offset channel up to about channel 3000. However, the size of the deviations is about the same over all channels, and so the fractional deviation of the channel-energy relationship above channel 3000 is extremely small.

The electronics are also sensitive to temperature changes. Calibrations were made with the instrument in a thermal vacuum chamber over a range of temperatures from -30 to +40°C. The temperature was measured by thermistors on the MAST electronics boards. Unlike with the fine-scale calibrations, data were taken at only ten voltage levels. A single linear fit was made at each temperature, and the fit coefficients were then plotted as a function of temperature. It was found that both the "A" and "B" coefficient of these fits were linear functions of temperature. The coefficients describing the change in "A" and "B" coefficients as a function of temperature are listed in Table 2.18.

The variations in the coefficients were $\sim$0.1% over the total 70° temperature range of the calibrations. Note that the mobility of the charge carriers in the silicon

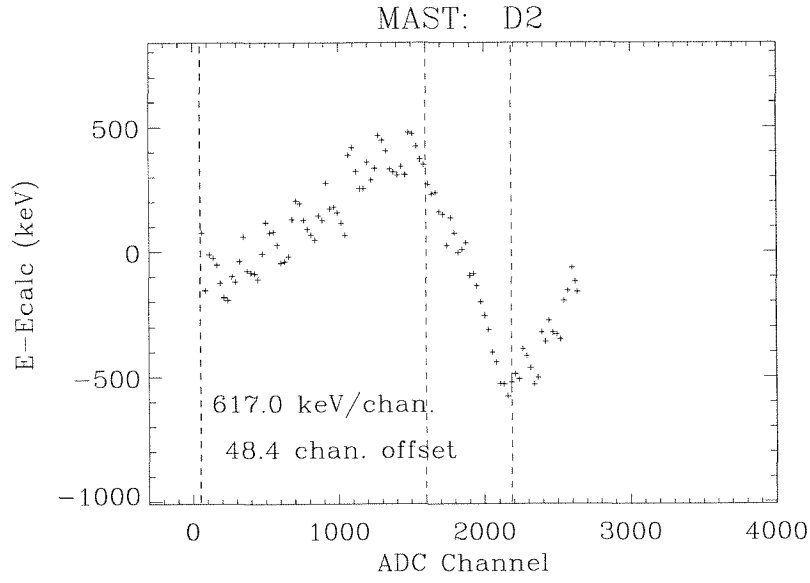

Figure 2.9: A set of channel-energy pairs are fit to a linear form, whose coefficients are listed on the figure. The deviations from this linear fit are then plotted as a function of channel number, showing that different regions require slightly different linear fits. The regions are marked by dashed lines. Each region is then fit separately, making a piecewise linear map for the full channel-energy relation.

TABLE 2.17

Fine-scale maps of the channel-energy relations, as described in the text.

Detector	Region #1	A	B	Region #2	A	B	Region #3	A	B
M1X1	55- 274	191.77	49.46	274-1932	190.78	48.58	1932-4096	190.25	43.52
M1XS	51- 280	187.33	49.95	280-1822	186.37	48.84	1822-2917	185.91	44.40
M2Y1	55- 270	186.31	47.36	270-1912	185.01	46.07	1912-2659	184.38	39.90
M2YS	51- 269	185.78	45.73	269-1840	184.61	44.56	1840-4096	184.09	39.62
M3X1	56- 209	188.56	50.01	209-1090	187.18	48.90	1090-1971	187.29	49.39
M3XS	51- 287	189.56	49.80	287-1798	188.63	48.68	1798-2593	188.24	45.04
M4Y1	63- 210	183.36	51.26	210-1972	182.08	50.23	1972-2773	181.48	43.88
M4YS	51- 200	184.34	52.56	200-1968	182.67	51.26	1968-4096	182.06	44.91
D1	52-1700	327.29	48.03	1700-4096	326.22	42.79	-	-	-
D2	52-1601	617.01	48.68	1601-2184	615.10	44.01	2184-4096	617.58	52.59
D3	52-1468	1216.29	50.17	1468-4096	1212.44	45.77	-	-	-
D4	52-1663	1822.30	48.82	1663-4096	1816.30	43.91	-	-	-
D5	52- 537	2679.27	49.17	537-1514	2682.02	49.62	1514-4096	2673.03	44.85
D6	52-1474	3913.46	49.07	1474-4096	3901.31	44.85	-	-	-

Detector	Region #4	A	B	Region #5	A	B
M1X1	-	-	-	-	-	-
M1XS	2917-4096	186.84	58.66	-	-	-
M2Y1	2659-4096	184.80	45.69	-	-	-
M2YS	-	-	-	-	-	-
M3X1	1971-2451	186.89	45.31	2451-4096	187.79	56.71
M3XS	2593-4096	188.90	54.01	-	-	-
M4Y1	2773-3093	181.83	49.02	3093-4096	182.80	65.14
M4YS	-	-	-	-	-	-

detectors also increases with temperature, but this effect is much smaller, on the order of 0.05%. In all cases the energy per channel increases with increasing temperature. The temperature range studied was more than adequate for modeling the response of the detector electronics in space on SAMPEX, where the temperature ranges from +15 to +25°C.

The energy for a given channel is obtained as follows: given a detector and a channel number, the appropriate coefficients for that linearity region, designated A_{fs} and B_{fs}, are found from Table 2.17.

The temperature of the instrument, T, is then taken from thermistor measurements in the housekeeping data. The relations between the linear coefficients and temperature for the coarse-scale fits are given in Table 2.18. It is assumed that the fine-scale linearity coefficients scale with temperature the same as the coarse-scale coefficients. We then calculate the ratio of the coarse-scale coefficients at temperature T to those coefficients at the temperature, T_c, at which the fine-scale calibrations were made ($T_c = 24$).

$$A = A_{fs}\frac{a_0 + a_1 T}{a_0 + a_1 T_c} \tag{2.3}$$

$$B = B_{fs}\frac{b_0 + b_1 T}{b_0 + b_1 T_c} \tag{2.4}$$

where A_{fs} and B_{fs} are the coefficients from the fine-scale fits, and T is the temperature in Celsius. The coefficients a_0, a_1, b_0, and b_1 are given in Table 2.18. The energy is then solved as $E = A \times (N - B)$, where N is the channel number, and A and B are calculated as above.

2.4.2 Matrix Positions

The matrix detectors can locate the one-dimensional position of a particle to within 0.5mm, the pitch of the strips. Thus, the precise location of the matrix detector and the location of the strips is of primary importance in making use of matrix position information.

TABLE 2.18

Temperature dependence of the coarse-scale channel-energy relations. These coefficients express the dependence of the channel-to-energy relations on temperature. The channel-to-energy relation is $E = A(N - B)$. At temperature T, the coefficients A and B are fit by the equations $A = a_0 + a_1 T$ and $B = b_0 + b_1 T$.

	a_0	a_1	b_0	b_1
Detector	keV/chan.	keV/chan./°C	chan.	chan./°C
M1X1	190.625	0.0296	48.6074	-0.00662
M1XS	191.659	0.0242	49.0532	-0.01426
M2Y1	184.534	0.0231	46.6209	-0.01511
M2YS	191.298	0.0157	43.9208	-0.00733
M3X1	186.551	0.0228	49.2592	-0.01284
M3XS	207.732	0.0321	48.7721	-0.01610
M4Y1	180.729	0.0356	50.4246	-0.01382
M4YS	186.676	0.0247	51.4425	-0.01836
D1	325.823	0.0624	47.9762	-0.01397
D2	614.300	0.1032	48.6009	-0.01304
D3	1210.57	0.2172	50.0367	-0.01229
D4	1815.07	0.2428	48.5815	-0.00958
D5	2670.29	0.5766	48.9895	-0.00595
D6	3901.34	0.3923	48.7864	-0.00648

The ballistic deficit mentioned earlier can alter the apparent positions by ~10%. In the laboratory, an alpha particle source was used to map out the response of each matrix detector with position, showing the ballistic deficit. This calibration was then modeled by simulation of the readout electronics, which yielded good agreement with the observed deficit (Selesnick 1992).

If there were no charge deficit in the matrix detectors, the position of a particle would be related to E_1 and $E_{\rm sum}$ by the simple relation

$$x = w \times E_{\rm S1}/E_{\rm sum} - c \tag{2.5}$$

where w is the physical width from the first to the last strip of the matrix detector and c is an offset. The offset is nominally the half-width of the detector for a coordinate system which places the center of each matrix detector at origin, which lies along the symmetry axis of the telescope.

As a result of the ballistic deficit, the charge collected from the sides of the detector is less than the actual amount of charge liberated by a passing ion. This deficit has been solved for analytically taking into account the capacitance of each individual strip in each matrix detector which depends on both the strip length, and the thickness of the detector (Selesnick 1992). The fraction of the total charge which is measured by the E_1 and $E_{\rm sum}$ are shown in Figure 2.10 as a function of strip number.

The measured position, x_m, is obtained by using the measured energies in Equation 2.5, while the true position, x_t, is the actual position of the particle along the matrix strips. There is a one-to-one correspondence between x_m and x_t. The results from Selesnick (1992) were used to construct a table of x_t versus x_m. This allows one to interpolate along the table to convert "measured" position to true position.

Likewise, a tabulation of the fraction of the charge measured as a function of measured position allows one to find the true amount of energy deposited in the detector. After conversion of ADC channel to energy is done for the matrix signals, the $E_{\rm sum}$ energies are corrected for the ballistic deficit so that they may be used as ΔE values in the $\frac{dE}{dx}$ versus E' analysis.

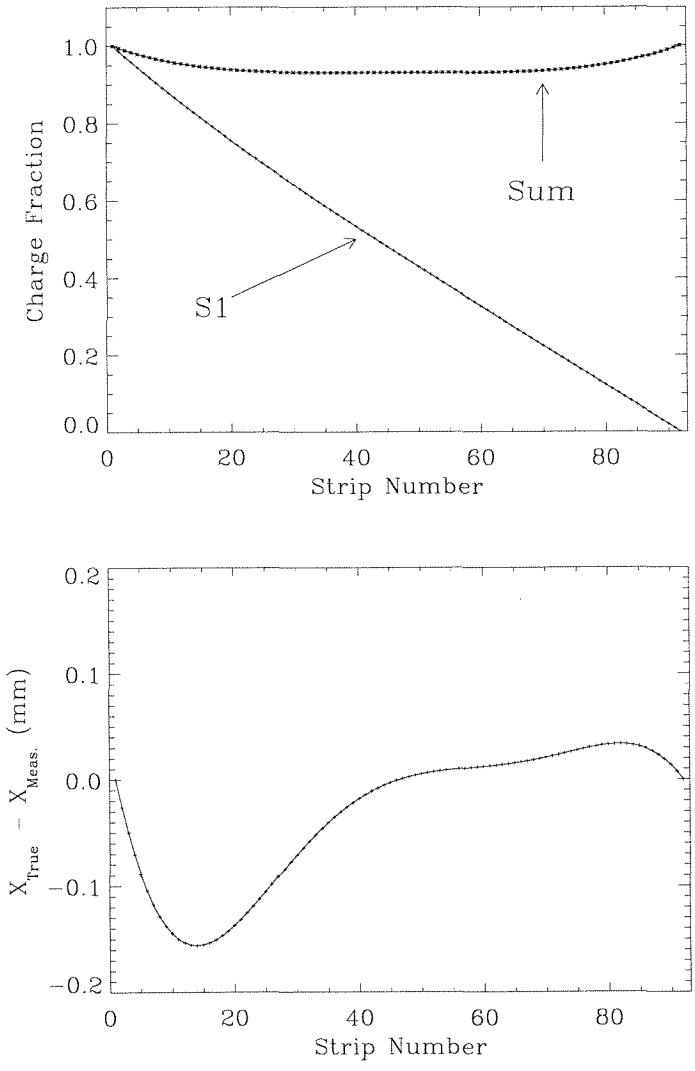

Figure 2.10: Ballistic deficit in the M1 matrix detector, representative of the effects seen in each matrix detector. The top figure shows the efficiency of charge collection for the S1 and Sum signals, which also reflects the fraction of the total energy measured in the ADC. The lower plot shows the difference between the true position and the measured position. There are 93 strips on each matrix detector.

2.4.3 Detector Thicknesses

The $\frac{dE}{dx}$ vs E' technique requires maps of each detector accurate to a few tenths of a percent in order to achieve the desired mass resolution. Rough maps of detector thicknesses were provided by the manufacturers. However, these were not precise enough for our purposes.

To map out thickness variations in the detectors on a finer scale, the assembled MAST instrument was taken to the Lawrence Berkeley Laboratory Bevalac and exposed to a beam of ^{28}Si at 280 MeV per nucleon, and ^{56}Fe at 410 MeV per nucleon. Absorbing material was used to alter the incident energy of the ion beam so that particles could be stopped within each detector in the instrument. A movable platform allowed the instrument to be placed at a number of angles with respect to the beam.

In this calibration, the charge, mass, and angle of incidence of the dominant beam particles (^{28}Si or ^{56}Fe) are known. We used the instrument calibrations and the nominal average thickness of each detector to calculate the charge using the ΔE-E' technique. Small deviations of the calculated charge from the actual charge were then attributed to differences in the detector thickness. Using the positions of the particles from the MAST trajectory system, M1-M4, these deviations were mapped out in 4mm by 4mm cells.

Maps were made of each ΔE detector and of the dead layers in the stack found on the grooved sides of the LiD detectors. The MAST detector maps are shown in Figure 2.11, and the average thicknesses are given in Table 2.19.

2.5 Identifying Particles

2.5.1 Theory

The energetic particles which MAST is designed to study are charged ions. The particles are sub-relativistic, with a velocity parameter of β<0.65c. When such particles pass through neutral matter they are slowed down primarily through Coulomb collisions with atomic electrons. The stopping power of an ion in a given

TABLE 2.19

Summary of the thicknesses of the MAST detectors, as measured through Bevalac calibrations, along with the typical size of thickness variations in each detector.

Detector	Average Thickness (μm)	Thickness Variation (percent)
M1	119.3	10
M2	108.1	4
M3	115.1	2
M4	113.3	3
D1	163.4	5
D2	491.9	7
D3	1723.7	3
D4	3000.7	6
D5	6195.6	7
Dead Layers		
D3/D4	102.2	15
D4/D5	34.4	15
D5/D6	101.2	20

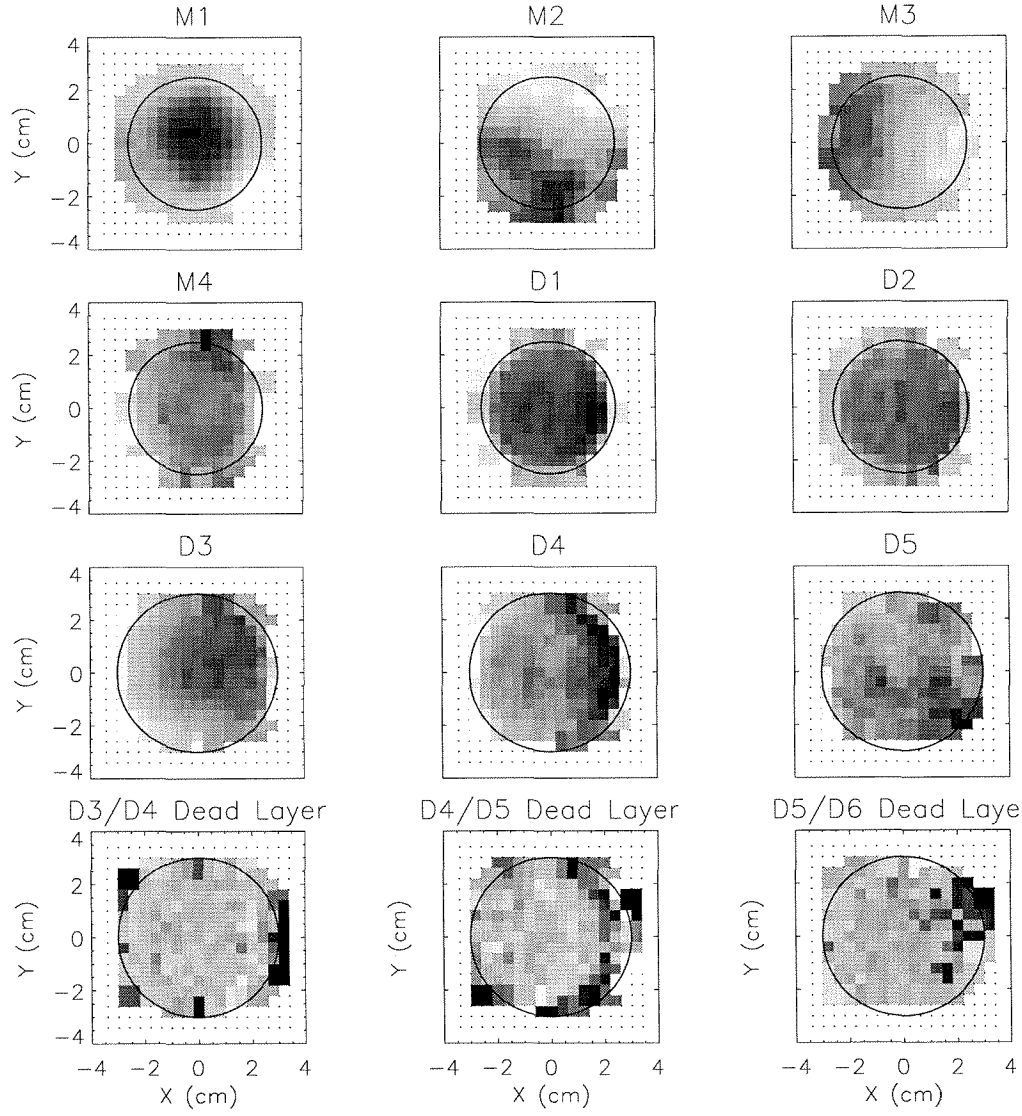

Figure 2.11: MAST detector maps. The thicknesses are represented as a linear grey scale, with the shade corresponding to the deviation from the average thickness. Black represents maximum positive deviation, and white represents maximum negative deviation. The sizes of thickness variations are listed in Table 2.19.

medium depends on the charge and velocity of the ion. The total kinetic energy of the ion depends on the velocity and the mass of the ion. MAST measures the energy which an ion deposits in each of its detectors as the ion slows down and comes to rest in the instrument, as well as the trajectory of the ion through the detectors. By measuring the energy an ion deposits and the amount of material it penetrates in each detector as it slows down, along with the particle's total kinetic energy when it enters the instrument, we can identify the charge, mass and kinetic energy of each particle which comes to rest in the instrument.

This method of identifying particle charge and mass is often referred to as the $\frac{dE}{dx}$ versus E' technique. Figure 2.12 shows the range over which MAST can resolve isotopes. The elements range from helium through zinc ($2 \leq Z \leq 30$), and the kinetic energy ranges from ~15-250 MeV per nucleon, depending on the element.

An important aspect of the $\frac{dE}{dx}$ versus E' technique is that at MAST energies the dominant process of energy exchange between the nucleus and the detector material is in Coulomb collisions between the nucleus and the atomic electrons in the detector material. For such energies the number of electronic collisions is very large, since each collision can deliver at most $2\beta\gamma$ times the electron rest mass energy to any single atomic electron, where β and γ are the velocity parameter and the Lorentz parameter of the nucleus. This large number of collisions means that at a given kinetic energy there is a well-determined average distance, or range, which particles of a given charge and mass will travel before they stop. The relationship between the kinetic energy and the average range of a particle in a given material can be approximated by:

$$R(Z, M, E) = k \frac{M}{Z^2} \left(\frac{E}{M} \right)^{\alpha} \tag{2.6}$$

R - Particle range, in microns

E - Kinetic energy in MeV

Z - Particle charge

M - Number of nucleons

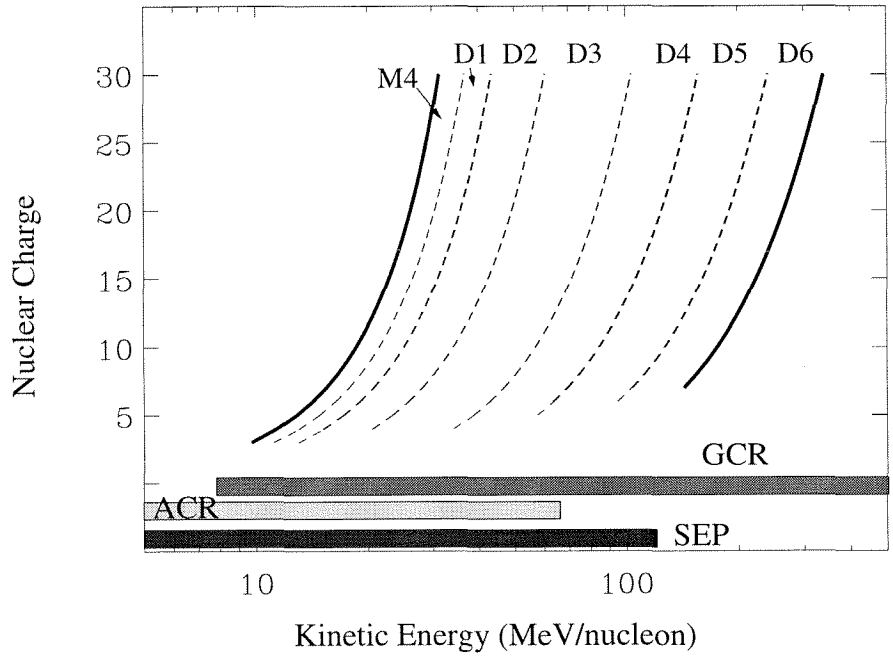

Figure 2.12: The range of nuclear charge and energy/nucleon over which MAST can resolve isotopes is shown by the solid curves. The dotted lines denote roughly the energy range for each detector. The bars along the bottom represent typical energies of the three main particle populations (ACR, SEP, and GCR) measured by MAST.

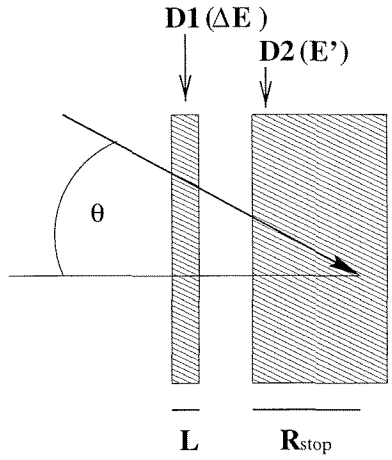

Figure 2.13: Basics of the ΔE-E' technique. A particle passes through an amount of material $L \sec\theta$ in detector D1, depositing an energy ΔE. It then stops in detector D2, depositing energy E'. Knowing the relation between $L \sec\theta$, ΔE, and E' allows identification of particle charge and mass.

k = 11.9 microns in silicon

α = 1.77

The parameters k and α are empirical quantities (see, e.g., Skryme 1967). The listed values are a fair approximation over much of the MAST energy and particle range. For much of the following discussion we will use this approximation to the range-energy relation, though a more accurate range energy relation is used in the actual data analysis.

The principle of $\frac{dE}{dx}$ versus E' is illustrated in Figures 2.13 and 2.14. As shown, a particle passes through detector D1 at an angle θ, depositing energy ΔE. It then stops in detector D2, depositing energy E'. The particle initially had a total kinetic energy of $E_{total} = \Delta E + E'$. The range-energy relationship tells us that the range of the particle at that time was:

$$R_o \sec\theta = R(Z, M, \Delta E + E') \tag{2.7}$$

After passing through the D1 detector and depositing energy ΔE, the particle was left with kinetic energy E'. Since it passed through $L \sec\theta$ of material in

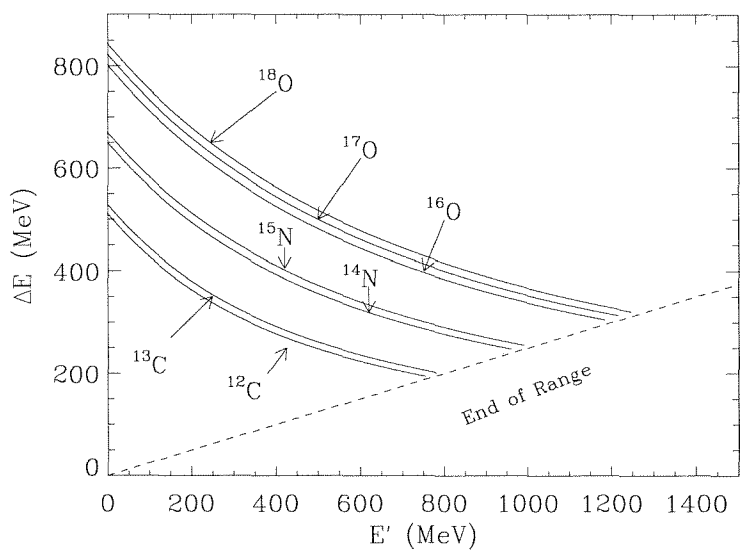

Figure 2.14: Theoretical locations of isotope tracks in ΔE versus E' for particles at normal incidence. In this example the ΔE detector is $3000\mu m$ thick, and the E' detector is $6000\mu m$ thick. The right end of the particle tracks indicates where particles stop at the end of the E' detector.

D1, the range of the particle entering D2 is given by:

$$R_{stop} \sec\theta = R_o \sec\theta - L \sec\theta = R(Z, M, E') \tag{2.8}$$

This pair of equations can be used to eliminate R_o, yielding the relation

$$L \sec\theta = R(Z, M, \Delta E + E') - R(Z, M, E') \tag{2.9}$$

The matrix detectors measure the trajectory of the particle, which yields the angle of incidence, θ, as well as the (x, y) location where the particle penetrated D1, which gives the thickness L. The silicon detectors measure ΔE and E', so the only remaining unknowns in Equation 2.9 are Z and M.

A useful method for gaining an intuitive understanding of the range-energy technique is to substitute Equation 2.6 into the above expression. If the mass is substituted in that equation as $M = 2Z$, the charge can be solved for, yielding,

$$Z(L, \theta, \Delta E, E'; \alpha, k) = \left(\frac{2^{1-\alpha} k}{L \sec\theta} \left[(\Delta E + E')^{\alpha} - E'^{\alpha} \right] \right)^{\frac{1}{\alpha+1}} \tag{2.10}$$

This equation is not exact, since the values of α and k depend weakly on the nuclear charge. Even for a single nuclide, the values are not the same at all energies. However, this approximation will yield values of charge which are, at the very extreme, off by approximately 0.5 charge units.

If the value of M inserted into Equation 2.6 were $2Z \pm 1$ instead of $2Z$, then the resulting charge will differ from the value in Equation 2.10 by approximately ± 0.14 charge units for most values of α and k. Likewise, if the charge is calculated for an isotope which has mass $2Z + \Delta M$, then the value of the charge calculated using Equation 2.10 will be $Z + 0.14\Delta M$ charge units, where ΔM is the difference between the isotope mass and the quantity $2Z$. Thus, neutron-rich isotopes will have a higher calculated charge, and neutron poor isotopes will have a lower calculated charge.

If the charge of a nucleus is known, then the algebraic approximation can likewise yield a useful formula for mass,

$$M(L,\theta,\Delta E,E';\alpha,k,Z)=\left(\frac{k}{L\sec\theta Z^2}\left[(\Delta E+E')^{\alpha}-E'^{\alpha}\right]\right)^{\frac{1}{\alpha-1}} \tag{2.11}$$

This equation is useful when the charge is known exactly, as is often the case in the calibration data using mono-isotopic heavy-ion beams. Yet because the range-energy relation for heavy ions cannot be described by a simple power law, the preferred method for finding particle charge and mass is to find the values of M and Z which minimize f in the following equation:

$$f(L,\theta,\Delta E,E')=R(Z,M,\Delta E+E')-R(Z,M,E')-L\sec\theta \tag{2.12}$$

The value of f should be zero for a perfectly measured particle. Note that there is a degeneracy in solving for Z and M. In practice, the charge is first found by assuming that the mass is a monotonic function of the charge. With the resulting charge set to an integer, the equation is then solved for mass. This will be described in more detail further on.

Let us assume that we have two detectors as in Figure 2.13, and that the amount of material traversed, $L\sec\theta$, is kept constant as the kinetic energy (and hence the range) of the particle varies. As shown in Figure 2.14, a particle with charge Z and mass M will trace out a unique path in plots of ΔE versus E' for a given angle of incidence. The traces of the different elements are separated in a roughly quadratic fashion, and the sub-traces of isotopes of a given charge are separated from each other by roughly 0.14 times the charge separation distance. The range-energy relation dictates the location of these traces, and so we identify the charge and mass of particles by finding their location on this ΔE versus E' map. An example of such particle tracks is shown in Figure 2.15, where ΔE versus E' is plotted. Since the angle of incidence is fixed, $L\sec\theta$ is approximately the same for all of the particles.

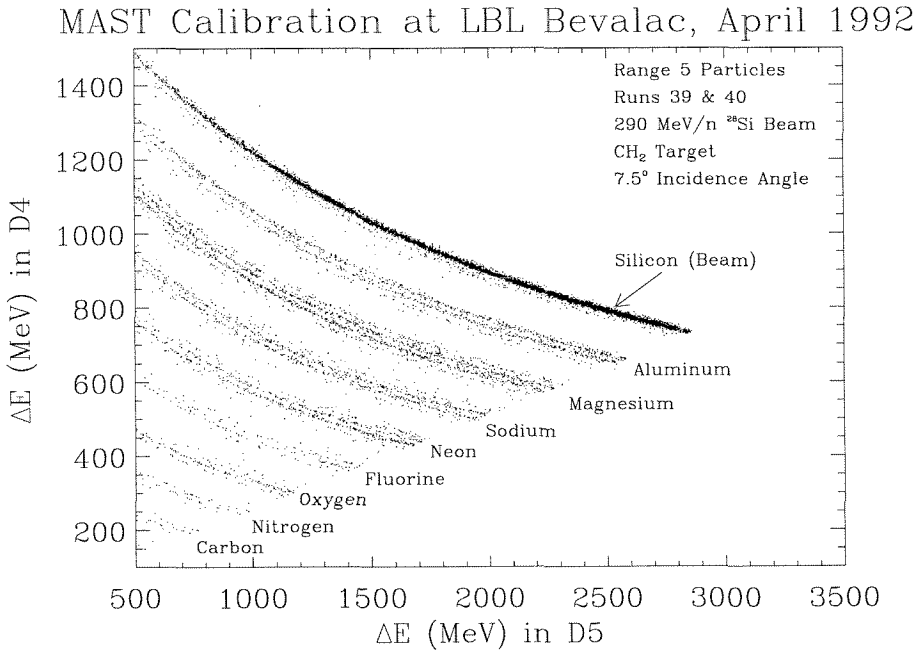

Figure 2.15: Nuclear fragments measured in MAST during calibration at the LBL Bevalac heavy-ion accelerator. The plot shows the energy deposited in D4 and D5 by particles stopping in D5 at an incidence angle of 7.5° (the thickness of D4 is $\sim 3000 \mu m$). The broad bands are elemental tracks, and the sub-bands within these are the isotopes produced by fragmentation of the silicon beam upstream.

2.5.2 Range-Energy Relation

Equation 2.6 is only an approximation, based on scaling the stopping power of protons to heavier nuclei. In particular it does not take into account the fact that as a heavy ion slows down, it picks up electrons. A traditional way to approximate the range energy relation is to begin with the range-energy relation for protons, scaled for heavier nuclei:

$$R(Z, M, E) = \frac{M}{Z^2} R_p(E/M) \tag{2.13}$$

where R_p is the range-energy relation for protons. This equation does not take charge pickup into account, but it represents the range-energy relation better than the power law approximation of Equation 2.6. The proton range-energy relation is taken from a set of standard tables which list the ranges of protons in silicon and a number of other materials at energies from 0.1 to 1000 MeV (Janni 1966). To compensate for charge pickup, we add a "range extension" term onto the equation, which is then written as (see Cook (1981)),

$$R(Z, M, E) = \frac{M}{Z^2} R_p \left(\frac{E}{M} \right) + M Z^{\frac{2}{3}} C(\frac{137\beta}{Z}) \tag{2.14}$$

The function C(x) is found empirically, and is a velocity-dependent function of the form

$$C(x) = A_3 A_2 \left[\exp(-\frac{x}{A_3} - 1.0) \right] + A_1 \left[A_4 - A_5 \ln \left(1 + \exp(-\frac{x - A_4}{A_5}) \right) \right] \tag{2.15}$$

where the constants A_1 through A_5 can be found by fitting data. In this technique, we use Ziegler's semi-empirical stopping formulae (Ziegler 1985) to fit this function. Ziegler has collected data describing the stopping power of many ions as a function of energy and has created a semi-empirical formula for the stopping power. These formulae take into account the electronic shell structure of the ion. To use his results,

we integrate Ziegler's $\frac{dE}{dx}$ formula for each element to get a particle range. The function $C(x)$ is then the difference between this range, and the range based scaling Janni's proton ranges by $\frac{M}{Z^2}$. We find $C(x)$ and fit values of A_i for each individual element. The values used are given in Table 2.20.

Thus, we have a range-energy relation which takes into account the unique stopping properties of each element.

2.5.3 Solving for Charge and Mass

As mentioned, the relation 2.12 depends on both Z and M. To first find charge, we set the mass to be a continuous and monotonic function of the charge. The function traces the dominant isotope of each element with the formula,

$$M = \begin{cases} 2Z & Z \leq 20 \\ 40 + 4.772(Z - 20) & 20 < Z \leq 21 \\ 2.132Z & Z > 21 \end{cases} \tag{2.16}$$

Setting the mass in this fashion yields charge values which are centered on integers for the dominant isotopes. Non-dominant isotopes are off of this integer value by an amount $\Delta Z \simeq 0.14\Delta M$, where $\Delta M = M_{\text{true}} - 2Z$. For example, ^{16}O would be centered at charge 8, while ^{18}O would lie at charge 8.28.

Because the isotopes involved in this study are all near the valley of stability, the isotopes of a particular charge lie within ± 0.5 charge units of the integer charge. After the charge is calculated, it is set to an integer. Then Equation 2.12 is solved for mass. The application of the technique to real MAST data is discussed in Chapter 3.

2.5.4 Multiple Mass Estimators

The MAST instrument allows more than one determination of mass for each particle. A subset of these determinations which use a single detector for the ΔE measurements are to a large degree independent and can be combined to form an improved measure of the mass. Consider a set of three detectors as depicted in

TABLE 2.20

Coefficients for the range-extension formula from Ziegler's semi-empirical stopping powers.

Z	A_1	A_2	A_3	A_4	A_5
2	1.50	1.77	0.37	1.75	0.247
3	3.48	3.27	0.57	1.39	0.26
4	2.80181	0.83932	0.75693	2.30754	1.02056
5	2.63512	0.94120	0.85390	2.29603	0.91939
6	2.50655	1.01797	0.83166	2.27197	0.84339
7	2.43397	1.08272	0.80991	2.23272	0.78490
8	2.39104	1.13931	0.78695	2.18812	0.73864
9	2.36208	1.18688	0.76129	2.14313	0.70063
10	2.34292	1.22784	0.73665	2.09932	0.66866
11	2.33071	1.26374	0.71419	2.05742	0.64126
12	2.32310	1.29542	0.69374	2.01778	0.61737
13	2.31930	1.32388	0.67570	1.98032	0.59630
14	2.31694	1.34903	0.65861	1.94523	0.57744
15	2.31816	1.37262	0.64468	1.91185	0.56053
16	2.31700	1.39238	0.62909	1.88105	0.54496
17	2.32265	1.41327	0.61945	1.85092	0.53106
18	2.32003	1.42816	0.60391	1.82399	0.51774
19	2.33007	1.44792	0.59846	1.79636	0.50612
20	2.32425	1.45818	0.58196	1.77291	0.49439
21	2.33883	1.47795	0.58051	1.74715	0.48461
22	2.32937	1.48335	0.56337	1.72692	0.47418
23	2.35771	1.51086	0.57002	1.70037	0.46630
24	2.37301	1.53002	0.56888	1.67756	0.45821
25	2.44664	1.58681	0.60039	1.64590	0.45380
26	2.32334	1.51544	0.52237	1.64970	0.43929
27	2.29164	1.50325	0.49666	1.63862	0.43020
28	2.32001	1.52792	0.50474	1.61581	0.42438
29	2.33718	1.54560	0.50645	1.59605	0.41843
30	2.34813	1.55914	0.50494	1.57819	0.41246

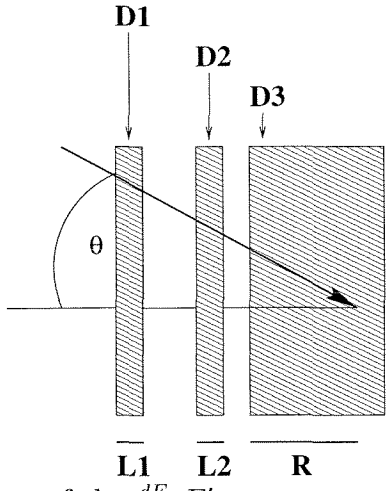

Figure 2.16: Illustration of the $\frac{dE}{dx}$-E' measurements for three detectors.

Figure 2.16. The signal in D1, E_1, can be used as the ΔE detector. The E' energy can then be obtained by adding the D2 and D3 energies, $E'= E_2 + E_1$, to yield the equation:

$$L_1 \sec\theta = R(Z, M, E_1 + E_2 + E_3) - R(Z, M, E_2 + E_3) \tag{2.17}$$

This can be solved for Z, and subsequently for M. As discussed in the next section, the uncertainty in the measurement M is dominated by energy straggling and thickness variations in the D1 detector. Because of this, the calculation of M is to a great extent independent of the mass measurement which uses D2 to measure ΔE and D3 to measure E'.

In the MAST instrument, every valid particle must trigger all four of the matrix detectors. If a particle stops in the r^{th} detector in the stack, then let us designate M_1 as the mass measurement using the first detector (M1) as the ΔE measurement, and all of the other detectors, (M2 through r) as the E' measurement. Likewise, let M_2 be the mass measurement using the second detector as the ΔE detector, and the detectors M3 through r for the E' measurement, and so on. A Range 0 particle must pass through M1, M2 and M3, and stop in M4. Likewise, a Range R particle must pass into R+4 detectors, providing R+3 independent measurements of the mass. Each of these *mass estimators* will have a characteristic width to its mass

distribution. If the width of the i^{th} mass estimator is designated σ_{M_i}, then all of the mass measurements can be combined to form a weighted average mass,

$$\overline{M} = \sum_{i=1}^{R+3} M_i/\sigma_{M_i}^2 \times \left(\sum \frac{1}{\sigma_{M_i}^2}\right)^{-1} \tag{2.18}$$

If the mass estimators are independent and Gaussian, the width of the distribution of $\overline{M}$ will be

$$\sigma_M^2 = \left(\sum_{i=1}^{R+3} \frac{1}{\sigma_{M_i}^2}\right)^{-1} \tag{2.19}$$

For example, if all of the σ_{M_i} are the same and equal to σ_{M_1}, then the weighted average mass will have a mass resolution of

$$\sigma_M = \frac{\sigma_{M_1}}{\sqrt{R+3}}$$

which greatly improves the mass resolution over any single ΔE versus E' measurement.

With this multitude of mass estimators, the notation can get rather confusing, and the following standard is used. A mass estimator is called $M(\text{"Detector"})$, where "Detector" is the name of the detector used for the ΔE measurement. For example, if a particle stops in the D1 detector, then $M(M4)$ is the mass estimator which uses M4 as the ΔE detector and D1 as the E' detector. Similarly, $M(M3)$ is the mass estimator which uses M3 as the ΔE detector, and the sum of the signals in M4 and D1 as the E' measurement.

The measurement of charge is also important, and this notation is also used to label the charge estimators. Take for example a particle which stops in D6. The charge estimator which uses the D2 detector for the measurement of ΔE and the sum of the energies measured in D3 through D6 as the E' measurement is called $Z(D2)$. The detectors which are used for ΔE measurements in each Range are listed in Table 2.21.

TABLE 2.21

The detectors which can be used as the ΔE measurement for each range in the MAST instrument.

Range	ΔE detectors								
0	M1	M2	M3						
1	M1	M2	M3	M4					
2	M1	M2	M3	M4	D1				
3	M1	M2	M3	M4	D1	D2			
4	M1	M2	M3	M4	D1	D2	D3		
5	M1	M2	M3	M4	D1	D2	D3	D4	
6	M1	M2	M3	M4	D1	D2	D3	D4	D5

2.6 Mass Resolution

The limitations to the precision of the $\frac{dE}{dx}$ vs E' technique arise from a number of sources. Some are due to the physical phenomena involved in the slowing down of an ion in a material, while others are due to engineering constraints. Each of the measured quantities, ΔE, E', L and θ, are affected by both kinds of limitations. A list of the dominant sources of mass uncertainty is given in Table 2.22.

In the exploration of how each of these sources contributes to the overall mass resolution, we shall use the power-law approximation to solve for mass. This is obtained by taking Equation 2.12 and inserting the power-law approximation to the range-energy relation, as given by Equation 2.6, which yields

$$M(L,\theta,\Delta E,E';\alpha,k,Z) = \left(\frac{k}{L\sec\theta Z^2}\left[(\Delta E+E')^{\alpha}-E'^{\alpha}\right]\right)^{\frac{1}{\alpha-1}} \tag{2.20}$$

The dependence of mass on each of the measured quantities can be obtained by taking the partial derivatives of this equation with respect to each quantity, giving

TABLE 2.22

Contributions to the mass resolution of MAST.

Physical Processes
• Energy Loss Fluctuations
• Multiple Coulomb Scattering
• Charge State Fluctuations
Instrumental Design
• Detector Thickness Variations
• Hodoscope Position and Angle Uncertainty
• Electronic Noise and Signal Digitization

$$\sigma_M{}^2 = \left(\frac{\delta M}{\delta L}\right)^2 \sigma_L{}^2 + \left(\frac{\delta M}{\delta \theta}\right)^2 \sigma_\theta{}^2 + \left(\frac{\delta M}{\delta E'}\right)^2 \sigma_{E'}{}^2 + \left(\frac{\delta M}{\delta \Delta E}\right)^2 \sigma_{\Delta E}{}^2 \tag{2.21}$$

Each of the leading terms of Equation 2.21 relates how the mass resolution couples to the measurement uncertainty in each measured quantity. Each of the leading terms is also proportional to particle mass, and thus the total mass resolution is proportional to mass in this approximation. The individual terms of this equation will be discussed in more detail below.

2.6.1 Energy Loss Fluctuations

Energy loss fluctuations are caused by variations in the energy deposited in the ΔE detector due to the statistical nature of the ion-electron collision process. In each collision the ion can transfer from zero to $2\gamma m_e c^2$ of energy to the electron, depending on the impact parameter of the collision. This leads to a distribution in the amount of energy which otherwise identical ions will deposit in the ΔE detector. The shape of this distribution can be characterized by the parameter κ, which is

the ratio of the average total energy deposited in the ΔE detector to the maximum energy which can be exchanged in a single collision (Seltzer and Berger 1964).

$$\kappa = \frac{\overline{\Delta E}}{\Delta E_{\max}} \tag{2.22}$$

where $\overline{\Delta E}$ is the mean total energy deposited in the detector, and $\Delta E_{\max}$ is the maximum energy exchanged in any single ion-electron collision.

When κ is small, the number of collisions is small and the distribution of ΔE has a skewed shape with a high-end tail due to rare collisions with large energy transfer. For $\kappa \gg 1$, the distribution of ΔE is Gaussian. For the MAST experiment, heavy ions undergo a large number of collisions in every detector, κ is very large, and the Gaussian approximation is appropriate.

The width of the energy loss distribution is obtained by integrating the equation (see, e.g., Spalding 1981)

$$\sigma_{\Delta E} = \sqrt{\int_{\mathcal{E}_i}^{\mathcal{E}_f} \frac{(\frac{dE}{dx})^2_{\mathcal{E}_f}}{(\frac{dE}{dx})^3_{\mathcal{E}}} \sigma_0^2(\mathcal{E}) M d\mathcal{E}} \tag{2.23}$$

where

$$\sigma_0^2(\mathcal{E}) = (0.396 \frac{MeV}{\sqrt{\mu m}})^2 Z^2 \frac{Z_T}{A_T} \frac{\gamma^2 + 1}{2} \tag{2.24}$$

Z,M - charge and mass of the ion

Z_T,A_T - charge and mass number of detector material

$\mathcal{E}_i$ - initial energy per nucleon of ion

$\mathcal{E}_f$ - energy per nucleon of ion after penetrating the detector

γ - Lorentz factor of ion

$(\frac{dE}{dx})_{\mathcal{E}}$ - specific ionization at energy per nucleon $\mathcal{E}$

For a more complete discussion and derivation of these formulae, see Spalding (1983) and Spalding (1981).

Using the power-law approximation to the range-energy relation (Equation 2.6), and assuming that the variation in $\frac{\gamma^2+1}{2}$ is small enough so that the term can be taken out of the integral, Equation 2.23 can be reduced to

$$\sigma_{\Delta E} = \sigma_0 D \sqrt{L} \gamma^2 (1 - \beta^2/2) \tag{2.25}$$

where the "deceleration factor" D is given by

$$D = \sqrt{\frac{\alpha}{3\alpha - 2} \frac{1}{L/R} [(1 - L/R)^{(2/\alpha)-2} - (1 - L/R)]} \tag{2.26}$$

where L is the thickness of the ΔE detector, R is the range of the ion before it enters the ΔE detector, and α is the exponent of the range energy relation (Equation 2.6).

Consider identical particles which each have a constant total energy, $E_T = \Delta E + E'$. Energy loss fluctuations alter the amount of energy which a given particle deposits in the ΔE detector, and so the variation in the mass measurement due to energy loss fluctuations can be written:

$$\frac{\partial M}{\partial \Delta E} = \frac{\alpha}{\alpha - 1} \frac{M}{[E_T^\alpha - (E_T - \Delta E)^\alpha]} (E_T - \Delta E)^{\alpha - 1} \tag{2.27}$$

The quantities ΔE and E_T vary greatly for different elements, yet the instrument configuration remains the same. For this reason, it is quite useful to rewrite Equation 2.27 in terms of detector thickness, L, and particle range, R, using Equations 2.6, 2.7, and 2.8.

$$\frac{\partial M}{\partial \Delta E} = \frac{\alpha}{\alpha - 1} \left(\frac{kM}{Z^2} \right)^{1/\alpha} \frac{R^{\frac{\alpha-1}{\alpha}}}{L} \left[1 - (1 - L/R)^{\frac{\alpha-1}{\alpha}} \right]$$

In terms of the width of the mass resolution, this yields

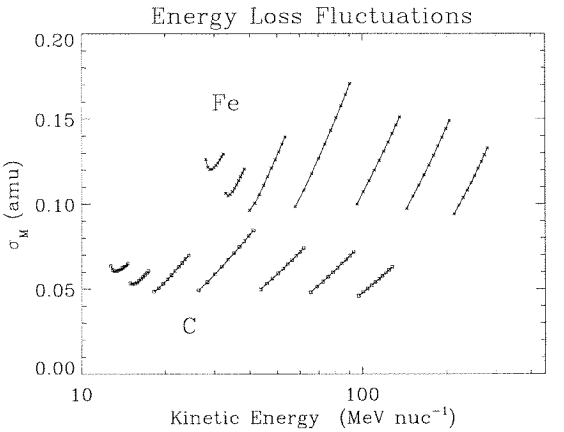

Figure 2.17: Estimation of the mass resolution due to energy loss fluctuations for ions at normal incidence. The upper traces (×'s) are for iron, and the lower traces (□'s) are for carbon. Each trace represents one range in the MAST detector, from Range 0 through Range 6. The mass resolution plotted is the quadratic sum of the contributions from each ΔE-E' combination.

$$\sigma_{M,\varepsilon} = \frac{\alpha}{\alpha - 1} \left(\frac{kM}{Z^2} \right)^{1/\alpha} \frac{R^{\frac{\alpha-1}{\alpha}}}{L} \left[1 - (1 - L/R)^{\frac{\alpha-1}{\alpha}} \right] \sigma_{\Delta E} \tag{2.28}$$

where $\sigma_{\Delta E}$ is the root mean square size of the energy fluctuations, as given in Equation 2.23.

Figure 2.17 shows the size of this contribution to the mass resolution. Note the steep rise in the mass resolution with increasing energy. This is due to the strong dependence of $\sigma_{\Delta E}$ on $\frac{R}{L}$, which illustrates the importance of using detectors of graduated thickness in $\frac{dE}{dx}$ versus E' telescopes.

2.6.2 Multiple Coulomb Scattering

The angle of incidence is measured by the hodoscope. However, the particle can suffer small angle deflections in each detector. Zumberge has found an expression for the mean scattering angle which takes into account the slowing down of the ion in the detector medium (Zumberge 1981). Derivation of the expression begins with the scattering formula from the Particle Data Group (Aguilar-Benitz et al. 1992),

$$\sigma_\theta = \frac{13.6MeV}{\beta cp} Z \sqrt{\frac{x}{X_0}} \left[1 + 0.038 \ln(\frac{x}{X_0})\right] \tag{2.29}$$

Here βc, p, and Z, are the velocity, momentum, and charge of the incident ion, and x/X_0 is the thickness of the scattering medium in radiation lengths. The radiation length, X_0, is given by:

$$X_0 = \frac{716.4 A_T}{Z_T(Z_T+1)\ln(287/\sqrt{Z_T})} \frac{g}{cm^2} \tag{2.30}$$

where Z_T and A_T are the charge and mass of the target nuclei. This formula, however, applies to particles which do not significantly slow down in the material. Zumberge had worked out a formula which takes deceleration into account:

$$\sigma_\theta^2 = \frac{\kappa k \alpha (m_u c^2)^\alpha}{2M} \frac{\gamma^2}{(\gamma-1)^{2-\alpha}(\gamma+1)} \ln\left[\frac{1}{\gamma+1}\left(\frac{2}{(1-L/R)^{1/\alpha}} + \gamma - 1\right)\right] \tag{2.31}$$

where

$$m_u = 931.5 \text{ MeV/c}^2, \text{ the atomic mass unit}$$

$$\kappa = (13.6/m_u)^2/Xo$$

$$\text{k} = 3.2 \times 10^{-3} \frac{g}{cm^2}$$

The partial derivatives of Equation 2.11 are taken with respect to $\sec\theta$ to obtain,

$$\sigma_{M,\text{scat}} = \frac{1}{\alpha - 1} M \tan\theta \, \sigma_\theta \tag{2.32}$$

The quantity σ_θ is the rms change in the angle of incidence. This angle can affect measurements in two ways. If the particle scatters in an earlier detector, then the angle of incidence used in calculating the pathlength is incorrect. If the particle scatters in the detector itself, then the pathlength through the detector is altered.

In the first case the scattering angle is the projection of σ_θ onto the normal plane, and so the scattering is

$$\sigma_\theta^{scat} = \frac{\sigma_\theta}{\sqrt{2}} \tag{2.33}$$

In the second case the scattering angle is based upon the change in the pathlength through the material, which is

$$\sigma_\theta^{path} = \frac{\sigma_\theta}{\sqrt{6}} \tag{2.34}$$

So for each ΔE-E' combination, the mass resolution from multiple Coulomb scattering has one component due to the alteration of the angle of incidence by scattering in previous detectors, and another element due to the the change in pathlength due to scattering in the ΔE detector itself.

An illustration of the multiple Coulomb scattering contribution to the mass resolution is given in Figure 2.18. The scattering angle is calculated for each detector from M3 onwards. The angles are added in quadrature for each ΔE-E' combination. The contribution to the mass resolution scales with mass, as shown in Equation 2.32.

2.6.3 Charge-State Fluctuations

Another physical process which can contribute to the mass resolution is that due to fluctuations in the charge state of an ion as it slows down in the detector material. As an ion slows down, it picks up and loses electrons in a stochastic manner, with the effect that its average charge decreases (see Figure 2.19). Since the energy deposited depends on the effective charge of the ion, fluctuations in the charge will alter the amount of energy deposited in a detector. This effect is not very significant for particles at high energies, which are essentially fully stripped of electrons, nor for very thick detectors, where the variation in ΔE is much less than the total amount of energy deposited in the detectors. However, for instruments which use detectors thinner than $\sim 200 \mu m$, this process can be important. Such instruments include

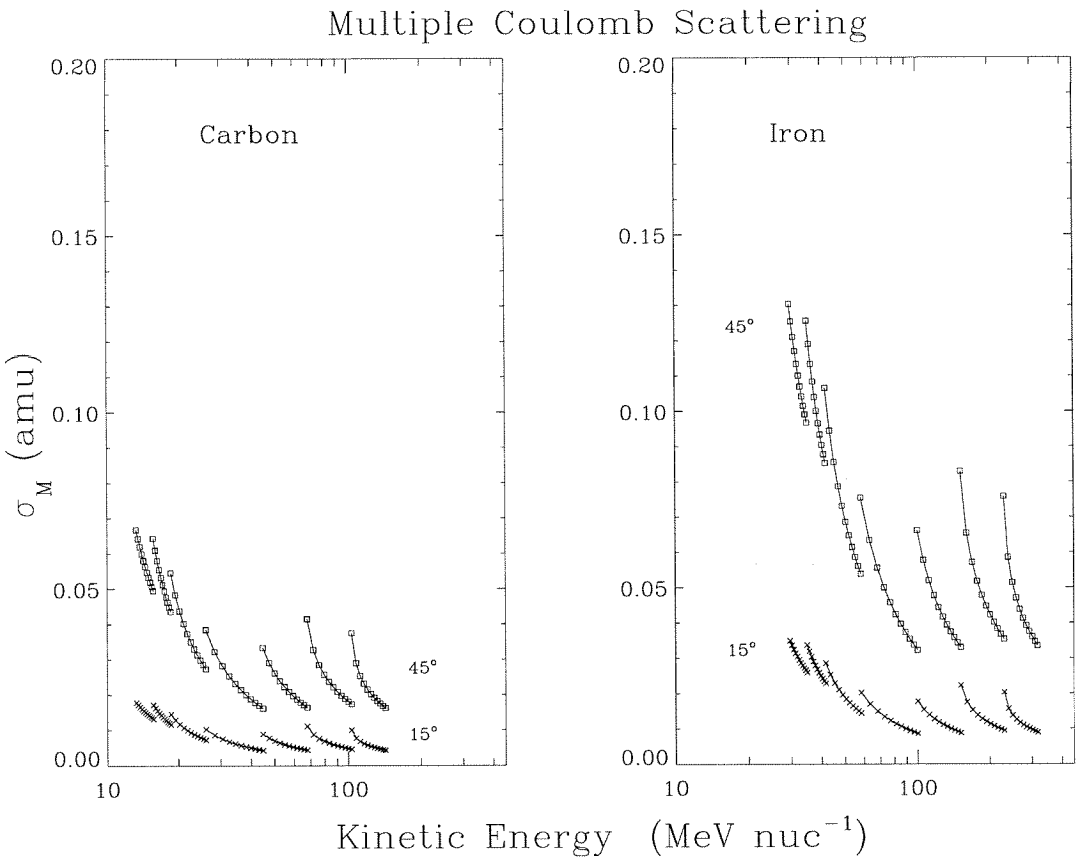

Figure 2.18: Estimation of the mass resolution due to multiple coulomb scattering in the instrument for carbon and iron. Scattering is considered to begin in the M3 detector, and to affect the mass resolution up to the final ΔE detector. Upper lines are calculated at 45°, lower lines at 15°.

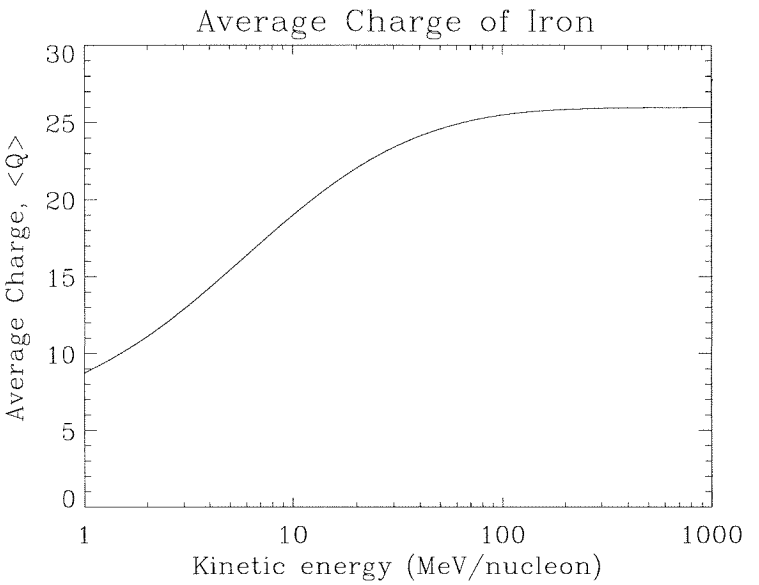

Figure 2.19: The effective charge of iron as a function of kinetic energy, based on the Ziegler (1985) stopping-power formulae.

MAST on SAMPEX and the Solar Isotope Spectrometer (SIS) on the Advanced Composition Explorer (ACE).

To investigate this phenomenon, a computer program was built which simulates the passage of particles through a detector. It uses code obtained from LBL which calculates the electron pick up and loss cross sections for ions of $Z = 25$ and higher (Pope 1990). The cross sections are converted to mean free pathlengths in silicon. The program calculates the probability that the ion could pickup or lose an electron in step sizes 1/50th of the shorter of either the electron pickup mean free path or the electron loss mean free path. The mean free paths for electron capture and loss for iron nuclei are shown in Figure 2.20.

The simulation works as follows: The particle of charge q is allowed to travel 1/50th of its mean free path through the detector. At each step the probability of loosing or capturing an electron is calculated. When the charge state changes, the amount of energy that the particle deposited before arriving at that step is calculated using its charge q. If an electron is picked up, the new charge is $q' = q - 1$; if the

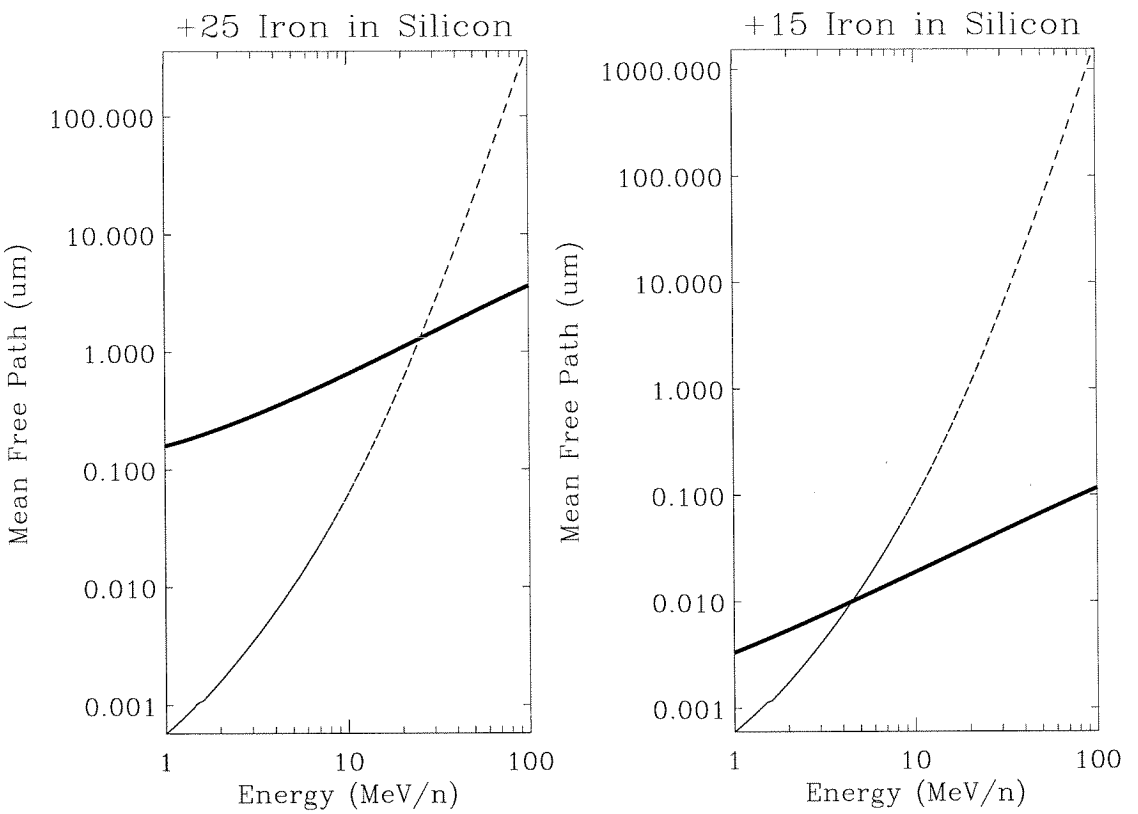

Figure 2.20: Electron pickup and loss cross sections for iron for the +25 and +15 iron charge states. Thick solid line: the mean free path for radiative and nonradiative electron capture. Thin dashed line: the mean free path for electron loss.

ion loses an electron, the new charge is $q' = q + 1$. The particle then travels through the detector with charge q' until its charge changes again, and its energy deposited is calculated using q'. This allows the particle to travel farther through the material than it would if the particle were stripped of all its electrons.

Simulations were run on 2000 particles for a given detector thickness and for particles with energies sufficient to penetrate the detector. The resulting distribution of ΔE is Gaussian. The width of ΔE is found for a number of energies. The shape of $\frac{\sigma_{\Delta E}}{\Delta E}$ as a function of R/L is shown for a number of detectors in Figure 2.21.

For a fixed total energy, the change in ΔE is equal and opposite to the change in E', just as in energy loss fluctuations due to electron-ion collisions. The relation to the variation in ΔE and the mass resolution is then given by:

$$\sigma_M = \frac{\alpha}{\alpha - 1}\frac{M}{E'}\left(\frac{R}{L} - 1\right)\sigma_{\Delta E,<Q>} \tag{2.35}$$

In MAST there are 115, 175 and 500μm thick detectors for which the charge-state fluctuations contribute significantly to the mass resolution. The mass resolution for MAST due to charge state fluctuations is shown in Figure 2.22. This plot shows the mass resolution using only the last two detectors as the ΔE-E' pair. For the detector combinations with higher R/L, the energy of the particle in the ΔE detector is higher, and consequently the charge state fluctuations are no longer significant. Thus, charge state fluctuations are primarily important when there is only a single combination of ΔE and E' available.

2.6.4 Thickness Variations

Thickness variations in the detectors are another limitation to the MAST mass resolution. The dependence of the mass on the ΔE detector thickness, L, is obtained by taking the partial derivative of Equation 2.11 with respect to L, which yields the equation

$$\sigma_M = \frac{M}{\alpha - 1}\frac{\sigma_L}{L} \approx 1.3M\frac{\sigma_L}{L} \tag{2.36}$$

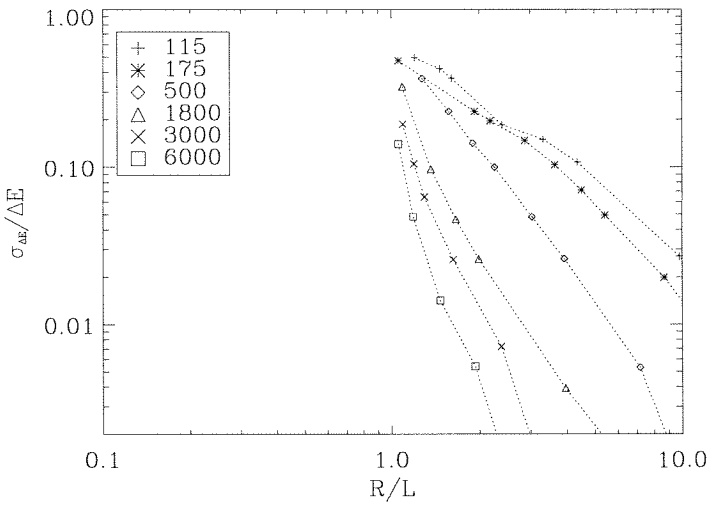

Figure 2.21: Monte Carlo calculations of the fractional variation in ΔE for iron ions due to charge state fluctuations in ΔE detectors of various thicknesses. The thickness values in microns are given in the legend.

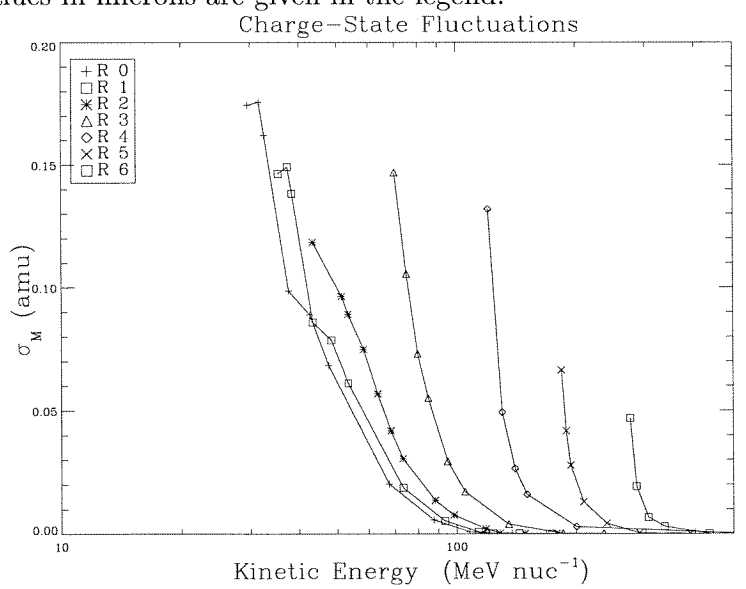

Figure 2.22: Mass resolution contribution due to charge state fluctuations for iron nuclei in MAST at normal incidence.

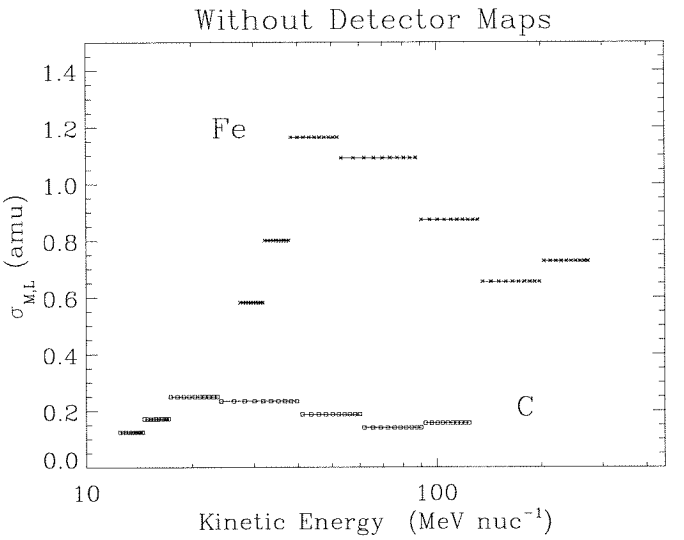

Figure 2.23: Demonstration of the MAST mass resolution due to variations in detector thickness if no detector maps are used. Use of the maps reduces this contribution by a factor of ~10.

The mass resolution is thus proportional to the accuracy of the detector maps. Without detector maps, the isotopes of heavy ions cannot be accurately measured (see Figure 2.23).

For example, measurements of the ratio $^{13}C/^{12}C$ requires that $\frac{\sigma_M}{M}$ be less than 1%, which in turn requires that the mass resolution be better than ~1%. The detector maps made with the Bevalac calibration data have allowed us to achieve an accuracy of approximately 0.2 percent.

2.6.5 Hodoscope Angle Uncertainty

An uncertainty in the detector thickness also arises from the measurement of the trajectory. The angle of incidence can only be measured to a certain accuracy, due to three main limitations of the hodoscope: 1) finite size of the matrix strips, 2) digitization of the measured energies, and 3) noise in the detector electronics. All of these uncertainties are expressed through Equation 2.36, which becomes,

$$\sigma_M = \frac{1.3M}{L}\frac{dL}{d\theta}\sigma_\theta \tag{2.37}$$

If the thickness penetrated in the ΔE detector is $L = L_0 \sec\theta$, then the mass resolution can be written

$$\sigma_M = 1.3M \tan\theta\, \sigma_\theta \tag{2.38}$$

If the measurement of one coordinate, for example the measurement of ΔX, has an uncertainty σ_x, then the uncertainty in the measured angle is

$$\sigma_\theta = \frac{\cos^2\theta\, \sigma_x}{D_0} \tag{2.39}$$

where D_0 is the separation of the matrix detectors, approximately 3.1 cm. If the uncertainty in the Y coordinate is the same size as that of the X coordinate, then the total uncertainty in the angle is simply multiplied by a factor of $\sqrt{2}$.

$$\sigma_M = 1.3M \tan\theta \frac{\sqrt{2}\cos^2\theta\, \sigma_x}{D_0} = 1.3M\sqrt{2}\sin\theta\cos\theta\frac{\sigma_x}{D_0} \tag{2.40}$$

The matrix strips have a pitch of 0.5 mm, which means that the rms uncertainty in particle position is $\frac{0.5mm}{\sqrt{12}}$. This leads to an uncertainty in the angle of incidence, which also leads to an uncertainty in the thickness penetrated in a given ΔE detector. The mass resolution due to a strip size of s is thus given by

$$\sigma_{M,\text{strip}} = \frac{1.3M}{\sqrt{6}}\sin\theta\cos\theta\frac{s}{D_0} \tag{2.41}$$

The measurement of angle is also affected by uncertainties in the measured position which arise from finite channel width and noise in the preamplifiers. Recalling Equation 2.5, we find that the relationship between uncertainty in energy and uncertainty in measured position is given by

$$\sigma_x = w \times \frac{\sigma_{E_{\rm S1}}}{E_{\rm sum}} \tag{2.42}$$

where w is the width of the matrix detector. In this calculation we take $E_{\rm S1}$ to be much less than $E_{\rm sum}$. Note that for particles which penetrate deep into the detector stack, the formula can overestimate the contribution of the angle uncertainty to the mass resolution. This is because the actual range of ΔX values is limited by the geometry of the telescope. Rather than using the full width of the matrix detectors, w, we should use the maximum possible value of ΔX or ΔY for a particle in a given range. This value is designated $X_{\rm max}$.

The rms uncertainty in the energy due to digitization is $\frac{c}{\sqrt{12}}$, where c is the size of the channel for a given detector, as given in Table 2.23. This leads to a mass resolution of

$$\sigma_{M,\rm chan.} = \frac{1.3M}{\sqrt{6}} \sin\theta \cos\theta \frac{X_{max}}{D_0} \frac{c}{\Delta E} \tag{2.43}$$

where ΔE is the amount of energy deposited in the matrix detectors.

The preamplifier circuits in MAST have intrinsic noise levels which depend on the detector capacitance and leakage currents, which also affect the mass resolution. Measurements of these noise levels were made prior to launch, and are given in Table 2.23. The mass resolution due to preamplifier noise is given by

$$\sigma_{M,\rm preamp} = 1.3M\sqrt{2} \sin\theta \cos\theta \frac{X_{max}}{D_0} \frac{\sigma_{\rm preamp}}{\Delta E} \tag{2.44}$$

where $\sigma_{\rm preamp}$ is the noise in the preamplifier circuits.

The mass resolution due to the three terms discussed in this section is shown in Figure 2.24. Light elements such as carbon are particularly affected by digitization and preamplifier noise when they penetrate deep into the detector stack. At deep ranges the energy which these ions deposit in the matrix detectors is so low that the matrix detectors no longer trigger at both ends, and so they cannot accurately

TABLE 2.23

Channel widths and preamplifier rms noise levels in MAST.

Detector Detector	Channel Width (keV)	Preamp Noise (keV)	Detector Detector	Channel Width (keV)	Preamp Noise (keV)
M1X1	191	150	D1	326	236
M1XS	192	150	D2	614	254
M2Y1	185	190	D3	1211	233
M2YS	191	270	D4	1815	440
M3X1	187	150	D5	2670	493
M3XS	208	150	D6	3901	907
M4Y1	181	130			
M4YS	187	150			

measure the positions of such particles. Such particles cannot be used in the isotope analysis. This effect is seen in the calculation of the instrument geometry factors, which is discussed in the next chapter.

2.6.6 Total Mass Resolution

The total mass resolution of MAST can be calculated using all the previously given formulae. Figure 2.25 shows the total mass resolution of MAST for particles which stop midway through the stopping detector in each range, at the average angle for particles stopping in that range (The average angle for each range is listed in Table 3.4).

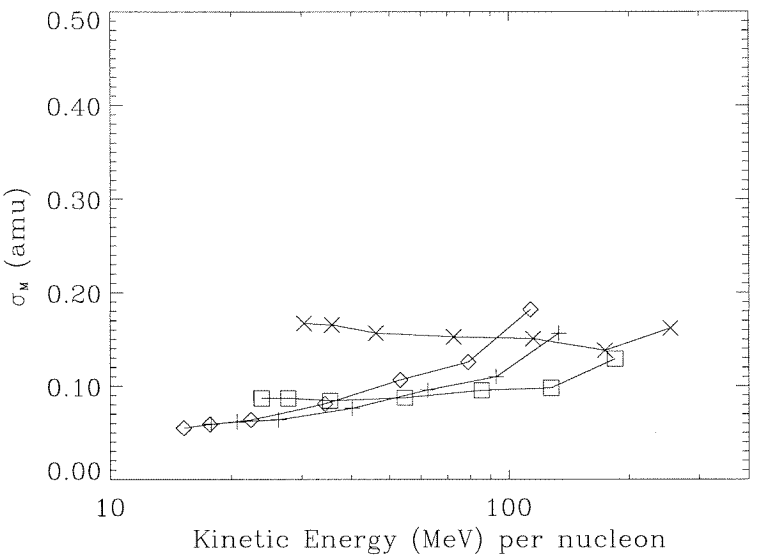

Figure 2.24: The mass resolution due to finite strip size in the matrix detectors, and also due to preamplifier noise and energy digitization. Calculations for four elements are shown: ×-iron, □-silicon, +- oxygen, and ◊-carbon.

2.7 Chapter Summary

We have endeavored in this chapter to describe how the MAST instrument works. MAST is designed to measure the charge, mass, and kinetic energy of heavy ($3 \geq Z \leq 30$) atomic nuclei in the energy range of 15-250 MeV per nucleon. The electronic logic should allow it to do this efficiently even when the intensity of lighter protons and alpha particles is high. Prior to the flight of SAMPEX, the response of the instrument was extensively tested using electronic stimuli, and also using heavy-ion beams at an accelerator. Relying on experience from earlier instruments, and from theories of how the physics of the measurement works, we have estimated the mass resolution of MAST.

Once the instrument was integrated onto SAMPEX, and once the spacecraft was in orbit about the Earth, how did the performance of the instrument match our expectations? This is discussed in the following chapter.

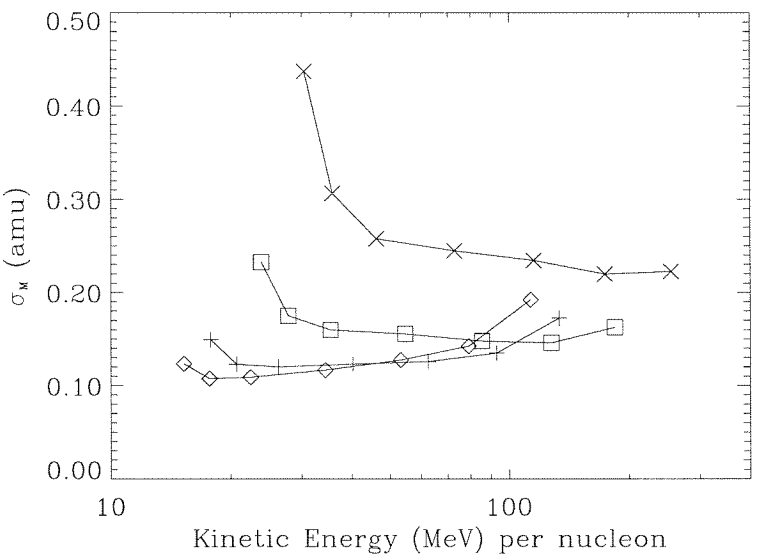

Figure 2.25: Total estimated mass resolution of MAST. The mass resolution is calculated for particles at average incidence angles which stop half-way through the stopping detector in each range. Calculations for four elements are shown: $\times$-iron, $\square$-silicon, +- oxygen, and $\Diamond$-carbon.

Chapter 3

Data Analysis

This chapter discusses the performance of MAST after the launch of SAMPEX in July, 1992. We begin by discussing how MAST data are obtained, and how those data are converted into measurements of the charge, mass, and kinetic energy of energetic particles. The set of particle data which is used in this section includes days 304 through 335 of 1992 (30 October through 30 November). This data set is dominated by particles which occurred during two large solar energetic particle events lasting from 31 October through 7 November, 1992.

3.1 Data Acquisition and Format

3.1.1 Spacecraft Data Processing

The SAMPEX DPU, built by Aerospace Corporation, serves as the interface between the four instruments on SAMPEX and the Small Explorer Data System (SEDS) (Mabry et al. 1993). It takes data from each instrument and gives it to the SEDS for placement in the spacecraft's memory. From one to three times a day the spacecraft transmits its data to the Wallops Flight Facility (WFF) Orbital Tracking Station at Wallops Island, Virginia.

3.1.2 SAMPEX Data Processing Stream

As shown in Figure 3.1, the data are sent directly from WFF to the Packet Processor facility (PACOR) at Goddard Space Flight Center (GSFC). PACOR extracts a subset of instrument data from the last orbit, called "history" packets, places the data into ASCII form and sends them via email to the SAMPEX co-investigators at the University of Maryland, Langley Research Center, California Institute of Technology, Aerospace Corporation, Goddard Space Flight Center, and the Max-Planck Institute. This allows the co-investigators to make quick evaluations of instrument status and of the particle environment. PACOR also takes the full data set and passes it on to the University of Maryland for processing.

A full set of the data are sent from PACOR to the University of Maryland Science Operations Center (UMSOC) where the orbital parameters are calculated and added to the data stream. The data are sorted into 24 hour periods, and placed into the Tennis Standard Data Format (Garrard 1994) to form the SAMPEX Master Data Files (MDF), also referred to as "Level One" data (Mazur et al. 1998). Each MDF corresponds to one day of data, and is typically from 25-50 Megabytes long. Sets of data are placed onto magneto-optical disks, which hold from five to ten days (500 MB) per side. The filled disks, containing perhaps ten days of data, are then sent to the SAMPEX co-investigators.

At Caltech the optical disk data are translated from VMS/Vax format to UNIX/Sun format, then a reduced set of the data is produced in order to make it smaller and thus more manageable. This includes removing LICA and HILT data, and removing some of the other data not needed in our analysis.

3.1.3 Relevant Data Sets

In the Tennis data format, the data are arranged in "sets," which are written sequentially onto the storage medium. The data sets relevant to the MAST analysis are listed in Table 3.1.

The "MAST Event," or "EM" sets have been described in Chapter 2, Section 2.3.5. These sets contain pulse-height information and time signatures for single

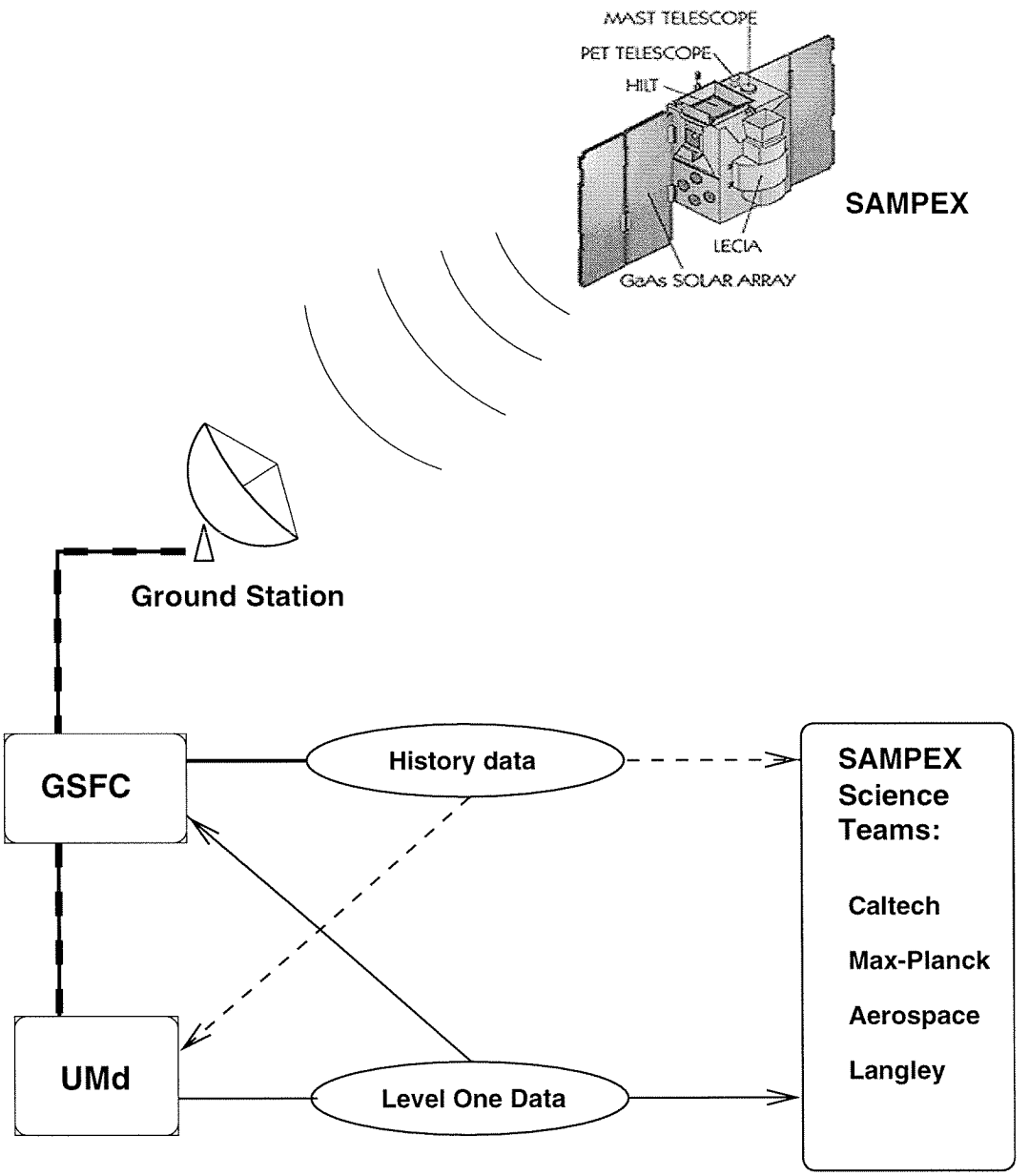

Figure 3.1: Data from the SAMPEX DPU are transmitted to ground stations, and then sent via dedicated lines to Goddard Space Flight Center, where history data is extracted and sent via email to the SAMPEX collaborators. The full compressed data is sent to the University of Maryland for processing into Level One data, which is then shipped via magneto-optical disks to the SAMPEX science teams.

TABLE 3.1

Data sets relevant to MAST data analysis.

Set	Name	Frequency	Description
EM	MAST Event	varies	MAST pulse-height analysis of a single particle
PS	SAMPEX Position	6 sec	Spacecraft location, orientation, and magnetic field
RS	Low-Resolution Rates	6 sec	Particle detection rates
HS	Housekeeping	60 sec	Instrument temperatures and detector voltages
DS	Digital Status	60 sec	MAST status and command bytes
PD	DPU Parameter Dump	1-2 per day	Instrument quotas for the DPU

particle measurements.

The "SAMPEX Rate", or "RS" sets contain rate information for all four of the SAMPEX instruments. When the reduced data sets are made at Caltech, the LICA and HILT rates are removed from this set, leaving only the MAST and PET rates.

The "DS" data set contains the command state of the instruments. MAST is flexible in its programming. Detectors can be added or removed from event equations, and the equations can be altered to some extent. The "PD" data set contains the quotas set by the DPU on the five different kinds of MAST PHA events which can be stored.

Some important items in the RS data are: 1) the HiZ rates by range, 2) the ADCOR rate, and 3) the instrument livetime. The HiZ rate is the instrument counting rate for events which satisfy the HiZ event equation for a particular range. The ADCOR rate is the OR of all 14 of the ADC triggers. The instrument livetime counter was discussed in Chapter 2.

Another relevant Tennis set is the "Housekeeping," or HS, set, which contains instrument housekeeping data. This contains, among other things, readings from the each of the eight thermistors on MAST, which measure temperature. These temperatures are used to correct for the temperature dependence of the channel-energy relations.

The "SAMPEX Position," or "PS" data set, contains orbital information such as spacecraft altitude, longitude and latitude. It also contains magnetic field information such as the invariant latitude of the spacecraft and the magnetic field strength and direction. The orbital and magnetic field parameters are calculated on the ground after the data are acquired from SAMPEX, based on orbital tracking calculations and magnetic field models. They are added to the data during Level-One processing into Master Data Files.

3.2 PHA Data Analysis

3.2.1 Energy

Each MAST event contains fourteen 12-bit channel numbers which encode the energy deposited in each of the MAST detectors, as listed in Table 2.15. Each channel number, N, is converted to an energy through the equation $E = A \times (N - B)$, where A and B take into account both the piecewise linearity and the temperature dependence of the channel-energy relation, as described in Section 2.4.1.

The temperature is measured by thermistors located at a number of locations on MAST. There is some temperature dependence in the channel-energy relations, and the temperature measured by a thermistor on one of the MAST electronics boards where the analog-to-digital circuits are found is used to calculate the effect of temperature on the channel-energy relations.

In-Flight Calibrations

During flight an automatic calibration is run on the MAST instrument roughly once per month. Periods of calibration are indicated in the SAMPEX Digital

TABLE 3.2

In-flight calibration responses of the matrix detectors taken on September 3, 1992. Voltage levels which are outside of the range of the ADCs return channel zero. Pulsing side 1 of the matrix detectors sends a signal to both the single and the sum side of each detector, while pulsing side 2 only activates the sum side, causing the single side to register a pedestal, near channel 50, as indicated by italics.

	Channel							
Voltage	M1X1	M1XS	M2Y1	M2YS	M3X1*	M3XS*	M4Y1	M4YS
-0.070	72	69	71	69	*52*	79	76	73
-0.212	*52*	117	*53*	114	121	120	*53*	103
-0.494	203	208	200	198	*52*	238	216	221
-1.059	*50*	369	*52*	357	394	391	*54*	386
-2.188	716	734	708	708	*52*	861	761	755
-4.445	*51*	1396	*50*	1396	1493	1483	*59*	1463
-8.965	2781	2850	2758	2762	*51*	3373	2965	2957
-18.0	*53*	0	*59*	0	0	0	*54*	0

*—The pulse order of the M3 detector is reversed, so that when side 1 is pulsed for the other detectors, side 2 is pulsed for M3.

TABLE 3.3

In-flight calibration responses of detectors D1 through D6 taken on September 3, 1992. At the highest calibration voltage, some of the responses are off scale, and so are returned as zeros.

	Channel					
Voltage	D1	D2	D3	D4	D5	D6
-0.070	67	67	67	67	66	65
-0.212	101	102	97	100	98	96
-0.494	171	170	157	165	163	156
-1.059	304	303	273	292	287	273
-2.188	576	574	511	551	543	512
-4.445	1120	1116	986	1069	1053	990
-8.965	2210	2201	1937	2107	2074	1946
-18.0	0	0	3858	0	0	3850

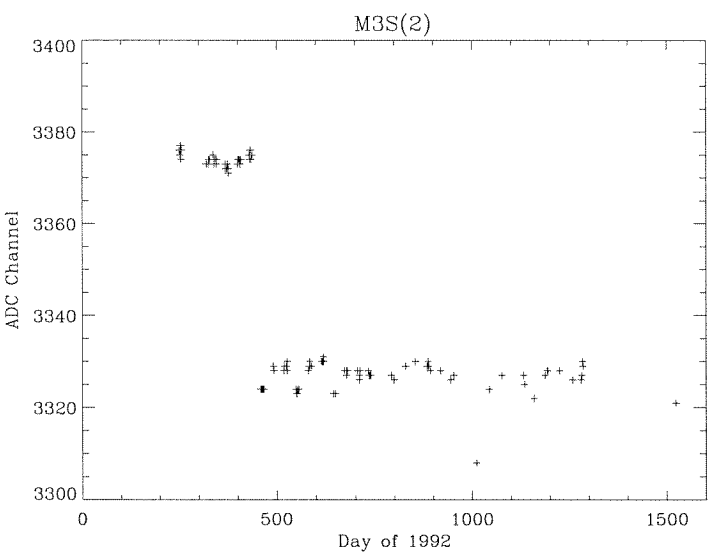

Figure 3.2: M3 Sum response to the -8.965 volt calibration pulse. Note the shift in the M3 Sum gain around day 435.

Status (DS) sets, which occur every 60 seconds and contain information pertaining to the status of the instruments. The calibration lasts 32 seconds, during which time eight voltage levels are sent to the test pulsers of the MAST ADCs. The voltage levels are ordered from -0.070 Volts to -18 volts. By observing the ADC response to these test voltages, it is possible to detect any change in the electronics during the mission. Such calibrations have been used to verify that the electronics which sum the signals from both sides of the M3 matrix detector (the M3XS signal) experienced a permanent gain decrease of 1.4% sometime near March 10, 1993.

The D1-D6 detectors receive pulses at all eight voltage levels. For matrix detectors, however, the odd-numbered voltage pulses are sent to side one of the detector, and the even-numbered pulses are sent to side two (the "S1" and "S2" preamplifiers shown in Figure 2.3). On the M3 detector, however, the order is reversed. Typical values of the ADC channels from the calibrations are given in Tables 3.2 and 3.3.

The voltage scale used by the pulser is not absolute, so that conversion to energies is not meaningful. However, the stability of the in-flight response for each detector can be studied over many months, to look for changes in the electronic response. Such data are shown in Figure 3.2, which shows the gain shift which occurred in the M3XS signal. For the time period that includes the data used in this thesis, the in-flight calibrations indicate no changes in the electronics response.

3.2.2 Particle Trajectory

As discussed in Chapter 2, each matrix detector provides two measurements of energy. The first, E_{S1}, is based on the pulse-height analysis of the signal from one side of the matrix detector, while the second, E_{sum}, is based on pulse-height analysis of the sum of the signals from either side. The first 8 ADC channels in a MAST Event Set contain pairs of energies for each of the four matrix detectors, corresponding to E_{S1} and E_{sum}.

Position Requirements

Isotopic resolution requires that the full trajectory of a particle be measured, which requires valid position measurements in every matrix detector. However, there are two reasons why events may not have valid position measurements. First, the triggering of a MAST event requires only that the Sum signal of each matrix detector be triggered, as indicated in Table 2.9. Depending on the energy deposited in the detector and on the position in the detector, a particle can trigger the Sum discriminator yet not provide enough energy to the S1 preamplifier to place the signal above its ADC pedestal. Thus, the area of the detector over which both sides of a matrix detector receive valid signals depends on the energy loss, and the location of the particle in the detector.

The second reason that an event may not have a valid position measurement arises because changes were introduced in the MAST event equations a few months after launch. The M4 detector had become noisy, and in order that the instrument not receive too many false triggers from M4, that detector was taken out of the event equation. This allows particles which stop in M3 to register as valid events, classified as Range 0. Since the particle spectrum falls with energy, this means that Range 0 is largely composed of events which stop in M3, rather than in M4. To discriminate between events which stop in M3 and those which stop in M4, we require that the Sum signal in M4 be above pedestal.

Trajectory Coordinates

Each matrix detector measures a one-dimensional position. Detectors M1 and M3 measure position in what is defined to be the X direction. Detectors M2 and M4 are aligned perpendicular to M1 and M3 and so measure particle position in the Y direction. M1 and M2 form one (X,Y) pair, and M3 and M4 form a second. This is illustrated in Figure 3.3.

The zero point along the vertical, Z, axis is the front of the M1 detector. Positive Z points into the detector stack. The location of the top of each matrix detector in the vertical direction is designated as Z_{M1}, Z_{M2}, Z_{M3}, and Z_{M4}. The

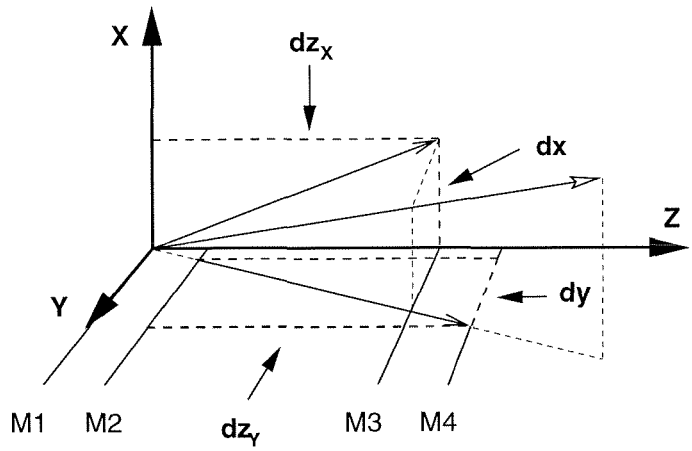

Figure 3.3: Calculation of particle trajectory using the four matrix detectors.

position measurements in the X direction are X_{M1} and X_{M3}, and the positions in the Y direction are Y_{M2} and Y_{M4}. The motion of the ion along a straight path in the Z direction can then be broken into its X and Y components,

$$X(Z) = Z\frac{\Delta X}{\Delta Z_X} + X_{M1}; \qquad Y(Z) = Z\frac{\Delta Y}{\Delta Z_Y} + Y_{M2} \tag{3.1}$$

with

$$\frac{\Delta X}{\Delta Z_X} = \frac{X_{M3} - X_{M1}}{Z_{M3} - Z_{M1}}; \qquad \frac{\Delta Y}{\Delta Z_Y} = \frac{Y_{M4} - Y_{M2}}{Z_{M4} - Z_{M2}}. \tag{3.2}$$

The angle of the particle's trajectory normal to the detector plane, θ, is then given by

$$\theta = \arctan\sqrt{\left(\frac{\Delta X}{\Delta Z_X}\right)^2 + \left(\frac{\Delta Y}{\Delta Z_Y}\right)^2} \tag{3.3}$$

The particle's position at any point in the telescope can be calculated using $X(Z)$ and $Y(Z)$. The detector thickness maps give the thickness at each ΔE detector at a given (X,Y), and so combining the trajectory with the maps yields $L(X,Y)$, the thickness penetrated in each ΔE detector. As described in the previous chapter, the change in θ due to multiple coulomb scattering is small, on the order of $\sim$10 mrad.

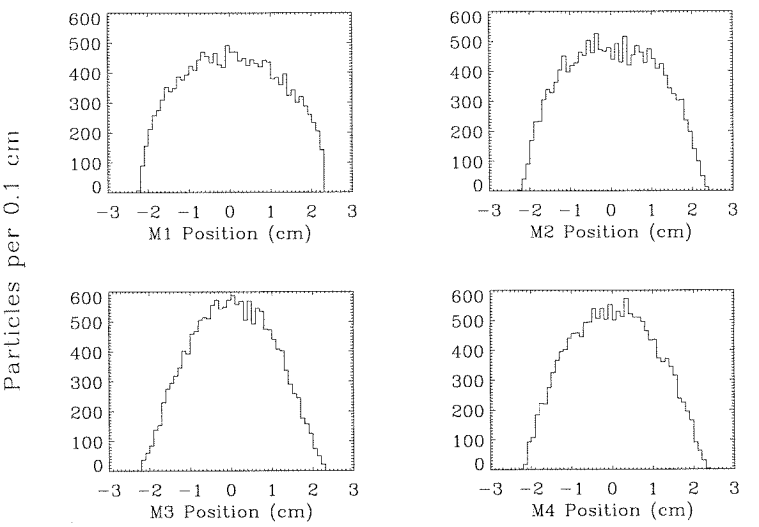

Figure 3.4: Histogram of the positions calculated in each matrix detector for Range 1 particles.

Trajectory Verification

Figure 3.4 shows the distribution of measured positions in each matrix detector for particles stopping in D1. The left-hand plot in Figure 3.5 is a close up of the position distribution for valid particles in M3. On this finer scale, the strips in M1 are visible. This is because the distribution of charge liberated by a passing ion is small compared to the strip size. All the charge is collected on a single strip, and since the strips are conducting surfaces, the electronics cannot determine position more accurately than the width of a single strip.

This is further illustrated by the right-hand plot in Figure 3.6, which shows X_{M1} and Y_{M2} for particles stopping in D1. The digitization in the X and Y directions give the data a pixelated look. Also visible are the edges of the M1 detector, corresponding to the first and last strips.

The distribution of θ is slightly different for each Range, since the geometry becomes more restricted deeper into the detector stack. A computer simulation of MAST was written to produce a distribution of trajectories for particles in each Range, and thus yield the angle average of incidence for an isotropic distribution of

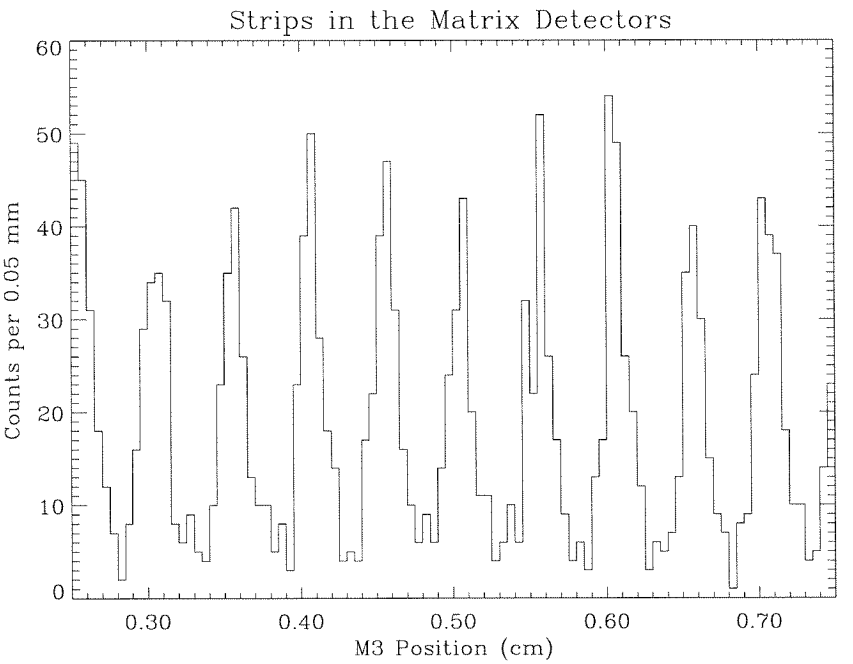

Figure 3.5: The histogram shows evidence of the matrix strips in the positions as measured in the M3 detector for Range 1 oxygen particles.

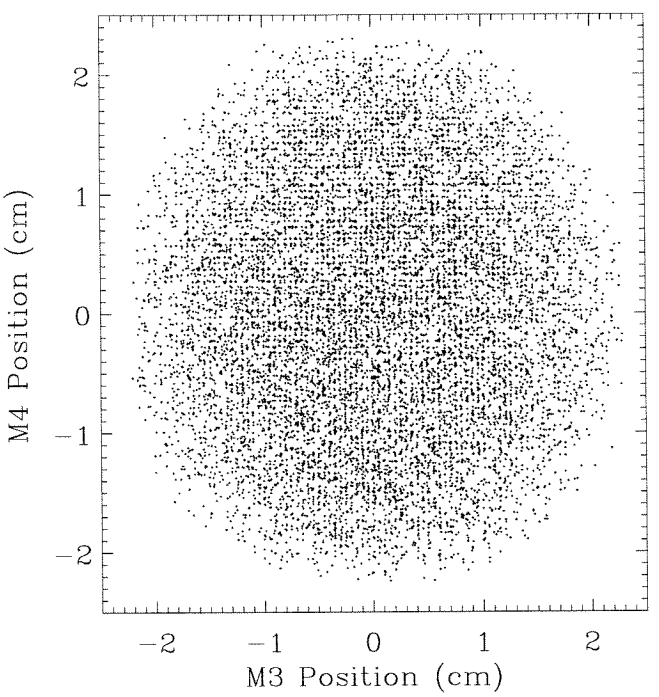

Figure 3.6: A plot of M3 (X-aligned) positions versus M4 (Y-aligned) positions, showing the pixel-like effect of the strips for Range 1 oxygen particles.

TABLE 3.4

The average angle incidence for particles in each Range.

Range	Average Angle (deg)
0	22.7
1	22.2
2	21.9
3	21.4
4	20.2
5	17.8
6	16.2

particles. The resulting average angles are listed in Table 3.4.

3.2.3 Charge Calculation

After the energies and trajectories are calculated for a particular particle, the charge and the mass of the particle are calculated using the $\frac{dE}{dx}$ versus E' technique. A useful way of displaying the data is to normalize ΔE and E' to $\theta = 0°$. This is done using the power-law approximation to the range-energy relation, as given in Equation 2.6, to solve for ΔE_0 and E'_0.

Figure 3.7 shows in detail a plot of ΔE_0 versus E'_0 for Range 2 particles. The plots in Figure 3.8 are similar plots for all ranges of particles. Only data for the last ΔE versus E' detector combination is shown for each range. This detector combination generally provides the best estimate of charge and mass. Note that for particles in range R, there are a total of R+3 such combinations of ΔE versus E'.

In each plot, the lowest three bands are the tracks of carbon, nitrogen, and oxygen particles. The three thick bands above that are neon, magnesium, and silicon. The uppermost thick band in each plot corresponds to iron.

To unfold particle charge from this data, we solve Equation 2.12 for particle

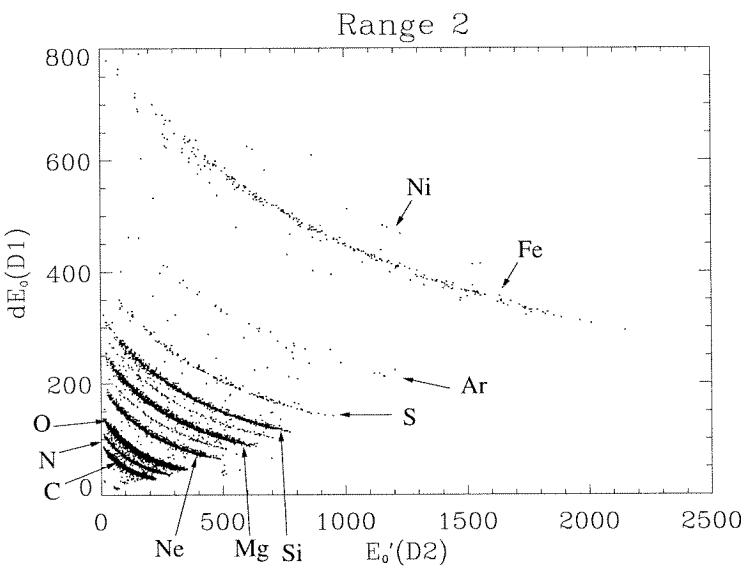

Figure 3.7: ΔE_0 versus E'_0 plot for the MAST SEP data for Range 2, showing the tracks of the abundant elements. The ΔE and E' measurements are corrected to zero degrees incidence angle using the algebraic approximation to the range-energy relation. The three dense lowest tracks, starting from the bottom to top, are carbon, nitrogen, and oxygen. Above them are neon, magnesium, and silicon. The uppermost track is from iron. The data shown was obtained from day 304 through day 335 of 1992.

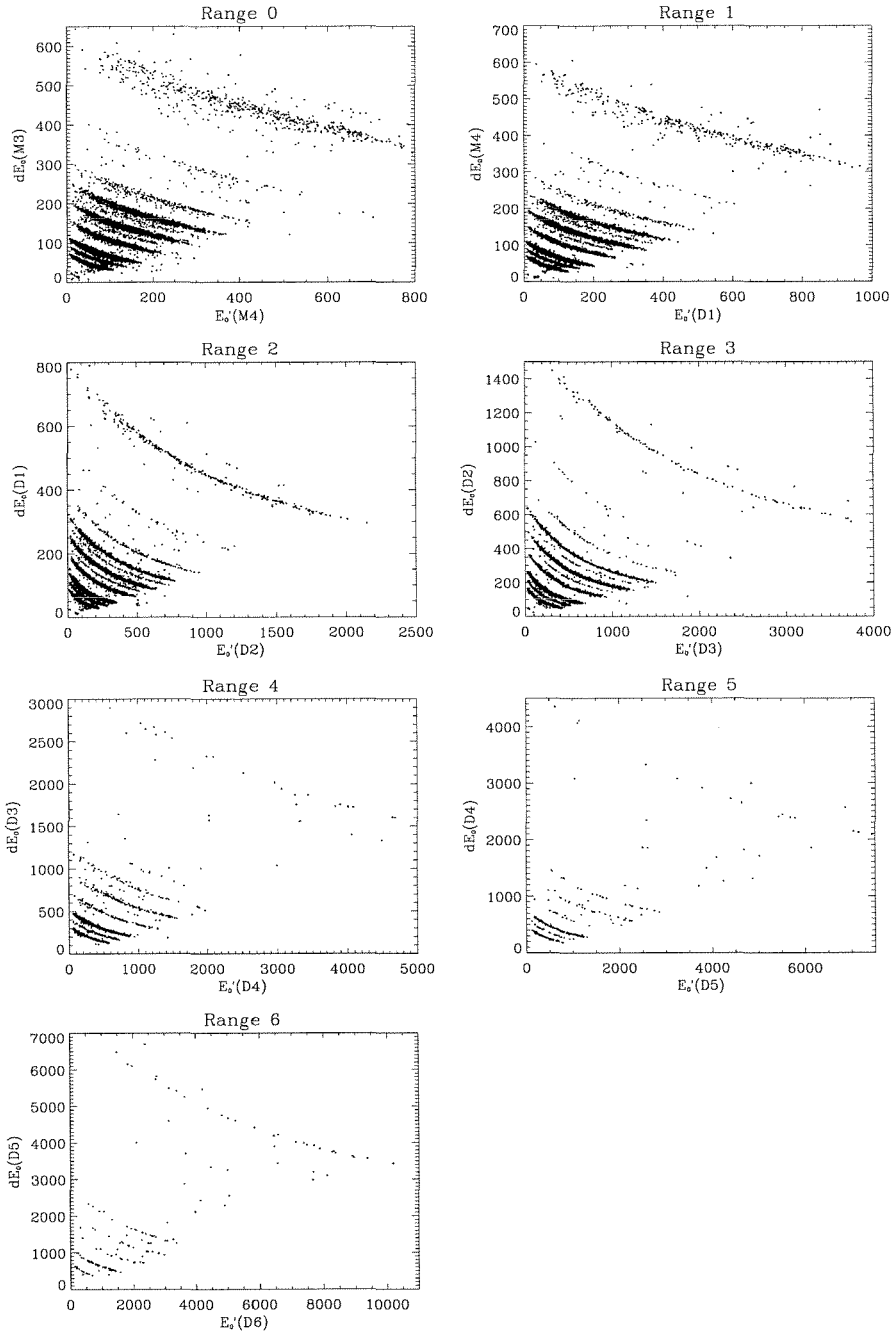

Figure 3.8: ΔE_0 versus E'_0 plots of the MAST SEP for all ranges. Both ΔE and E' have been normalized to zero degrees, as in the previous figure. The predominant element tracks are due to C, N, O, Ne, Mg, Si, and Fe, as shown in the previous figure. The data shown was obtained from day 304 through day 335 of 1992.

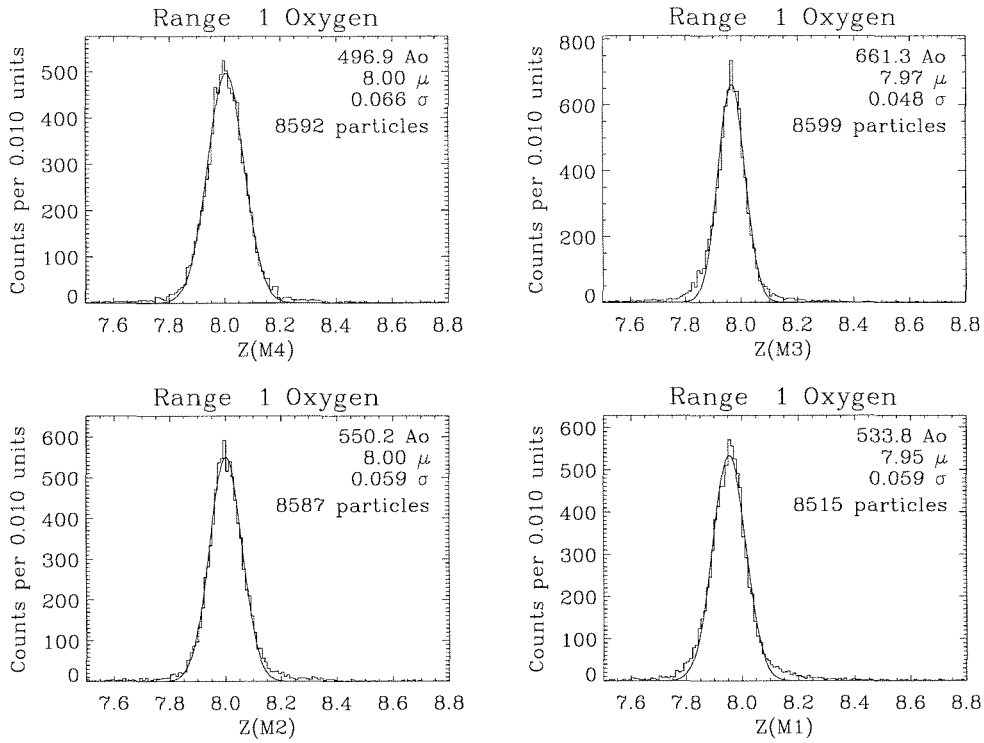

Figure 3.9: Histograms of the charge measurements of oxygen for each $\frac{dE}{dx}$-E' combination in Range 1. The distributions are fit with Gaussian shapes, where A_0 is the height, μ is the mean, and σ is the standard deviation of the Gaussian. The data shown was obtained from day 304 through day 335 of 1992.

charge, Z, for each $\frac{dE}{dx}$-E' combination available in a given range. This is done by numerically minimizing Equation 2.12 with respect to Z. For the i^{th} $\frac{dE}{dx}$-E' combination we obtain one measure of charge, Z_i. For oxygen particles, histograms of the calculated charges are shown for Range 1 particles in Figure 3.9. The notation for the charge estimators is explained in Section 2.5.4.

To make optimal use of all the charge estimators, an average charge is computed from the weighted average of all the estimators as explained in Section 2.5.4. In order to make this weighted average, the mean of each estimator is normalized to the integer value of the charge. This is done by adjusting each individual charge measurement so that the whole distribution of charge measurements for each mass estimator is centered at an integer value, Z_I. If the center of the distribution of the

i^{th} charge estimator is μ_i, then the "corrected" charge estimator for the element Z_I is given by

$$Z_i' = Z_i \times \frac{Z_I}{\mu_i} \tag{3.4}$$

where $Z_I = 8$ for oxygen. The charge peaks are now centered about the same value, and a weighted average charge, $\overline{Z}$, can be calculated using the width, σ_i, of each mass distribution,

$$\overline{Z} = \frac{\sum_{i=1}^{R+3} \frac{Z_i'}{\sigma_i^2}}{\sum_{i=1}^{R+3} \frac{1}{\sigma_i^2}} \tag{3.5}$$

The result of such an average is shown in Figure 3.10. Note that if the distribution of charge estimators were completely independent and distributed in a Gaussian manner, then the width of the weighted average should be ~0.028 charge units, rather than the 0.042 charge units shown in the figure. Although the measurements are not entirely independent, the uncertainties are dominated by fluctuations in the ΔE measurement, for example, unmapped variations in the thickness of the ΔE detector or energy loss fluctuations in the ΔE detector. The reason that the width of the weighted average charge is not as small as expected is due primarily to systematic deviations in the charge measurement. Such deviations are not large enough to make one charge appear to be another, and so are not of concern for measurements of particle charge. They are of concern in measurements of mass, and so are discussed in the next section.

The weighted average charge estimators for all particles in the October and November 1992 SEP events are shown in Figure 3.11. This plot also shows roughly the number of events available for data analysis for each element.

3.2.4 Mass Calculation

The charge of a particle can be measured quite unambiguously with MAST, and so the weighted charge estimator is rounded to the nearest integer for the purpose

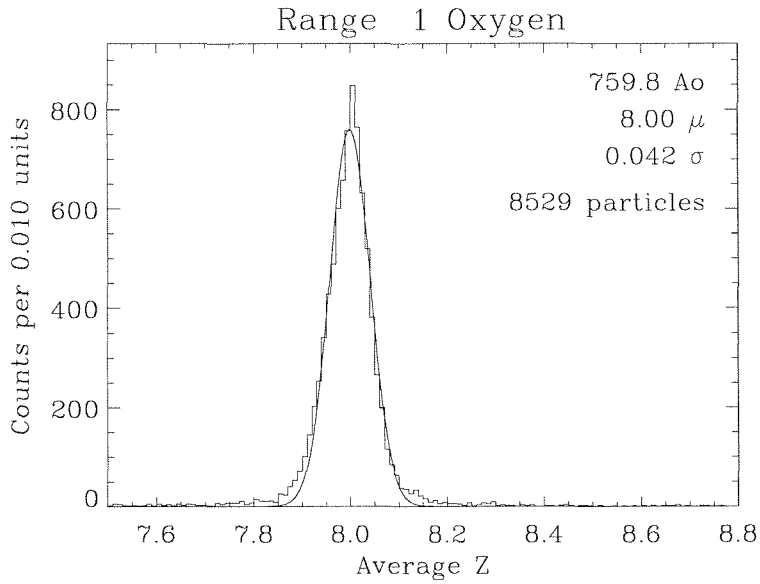

Figure 3.10: Histogram of the weighted average charge of all the charge measurements in Range 1 for oxygen particles shown in Figure 3.9.

of finding mass. Equation 2.12 is then minimized with respect to mass, M, for each mass estimator. As with charge, each ΔE-E' combination yields one measurement of mass, so that each range has Range+3 estimates of the mass. An example of these mass estimators is shown in Figure 3.12. Recall from Chapter 2 that it is predicted that the last ΔE-E' combination, in this case $M(M4)$, should yield the best mass resolution. In practice, the M4 detector is noisy, causing its mass estimate to be poorer than expected. Each mass estimator has been fit with a Gaussian shape, which locates the mean and standard deviation of each estimator.

The weighted average mass is calculated for each range in a similar fashion as the weighted average charge is calculated. However, for the mass estimators, the mean of the Gaussian is set equal to the integer mass of the most abundant isotope. The distribution of $\overline{M}$ for oxygen particles in each range is shown in Figure 3.13. The mass resolution of each range is indicated by the width, σ, of the fitted Gaussian function. These numbers are greater than 0.12 amu, the theoretical mass resolution calculated in Chapter 2.

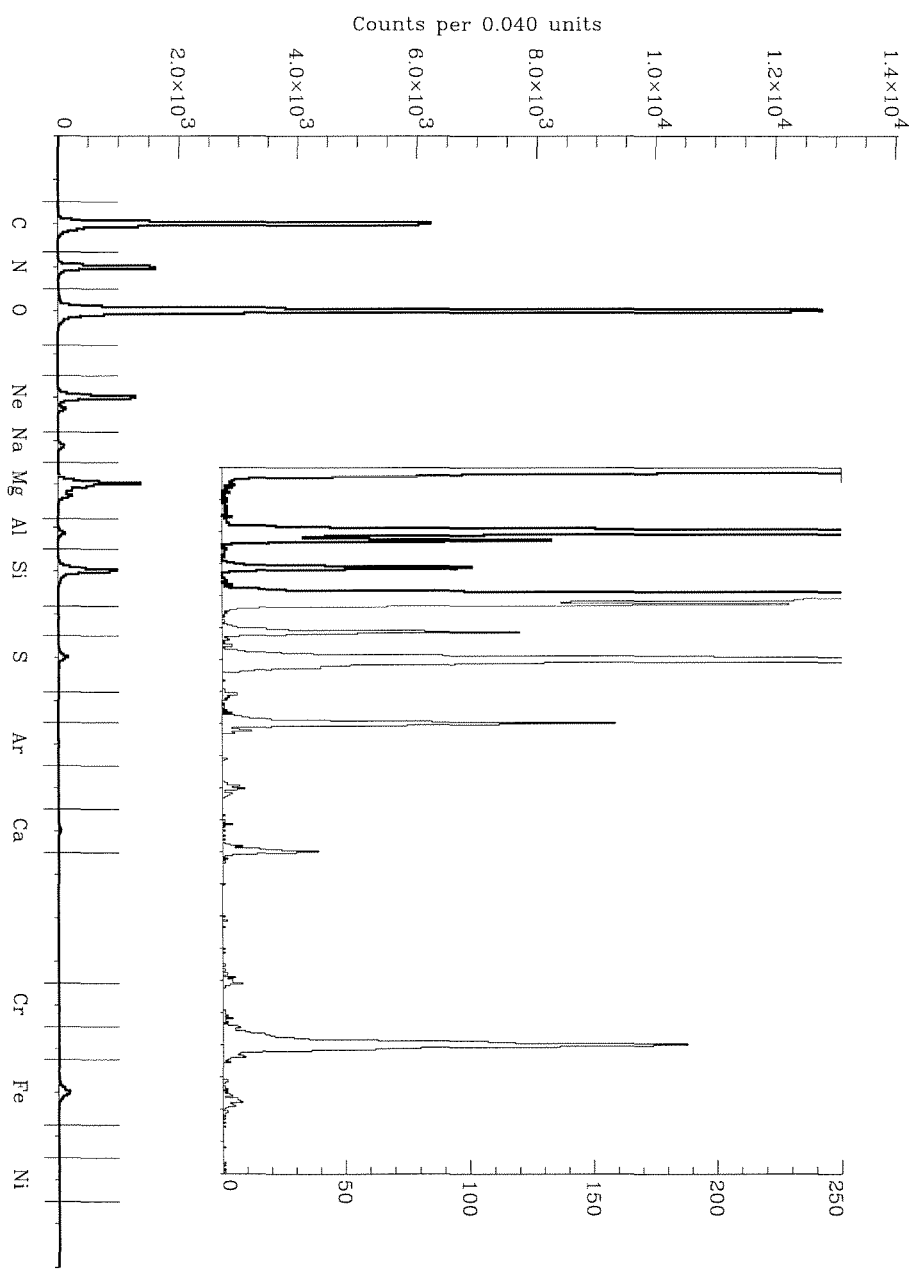

Figure 3.11: Charge histogram showing SEP element composition. All Ranges are shown. The data is combined from the two solar particle events observed in late 1992, using data from day 304 through day 335, 1992. The abundant elements are labeled with their chemical symbol, and the vertical lines show where the average charge is selected to identify particles of each element.

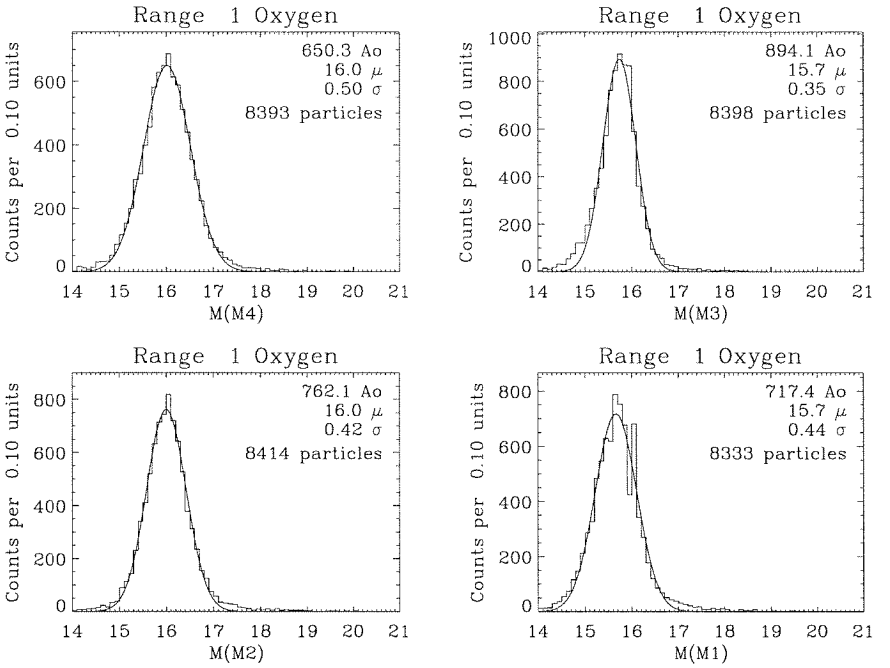

Figure 3.12: An example of the mass estimators for Range 1 oxygen data.

One might ask if the mass resolution can be improved. To investigate this question, note that the algebraic approximation for the mass is given by,

$$M = \left(\frac{k}{L \sec\theta Z^2} \left[(\Delta E + E')^{\alpha} - E'^{\alpha} \right] \right)^{\frac{1}{\alpha - 1}}$$

where ΔE and E' are the energies deposited, L is the thickness of the ΔE detector where the particle penetrates it, and θ is the particle's angle of incidence with respect to the instrument axis. A plot of mass versus each of these quantities has been made to search for any dependencies.

A plot of mass versus θ reveals that, at least for certain mass estimators in certain ranges, there is indeed a correlation between mass and incidence angle, as demonstrated in Figure 3.14. This shows the mass of Range 2 oxygen particles calculated using the M4 detector for the ΔE measurement, plotted as a function of angle. The mass is seen to decrease with increasing angle. The algebraic equation for mass shows that mass is approximately proportional to $(cos\theta)^{1.3}$. If no correction for

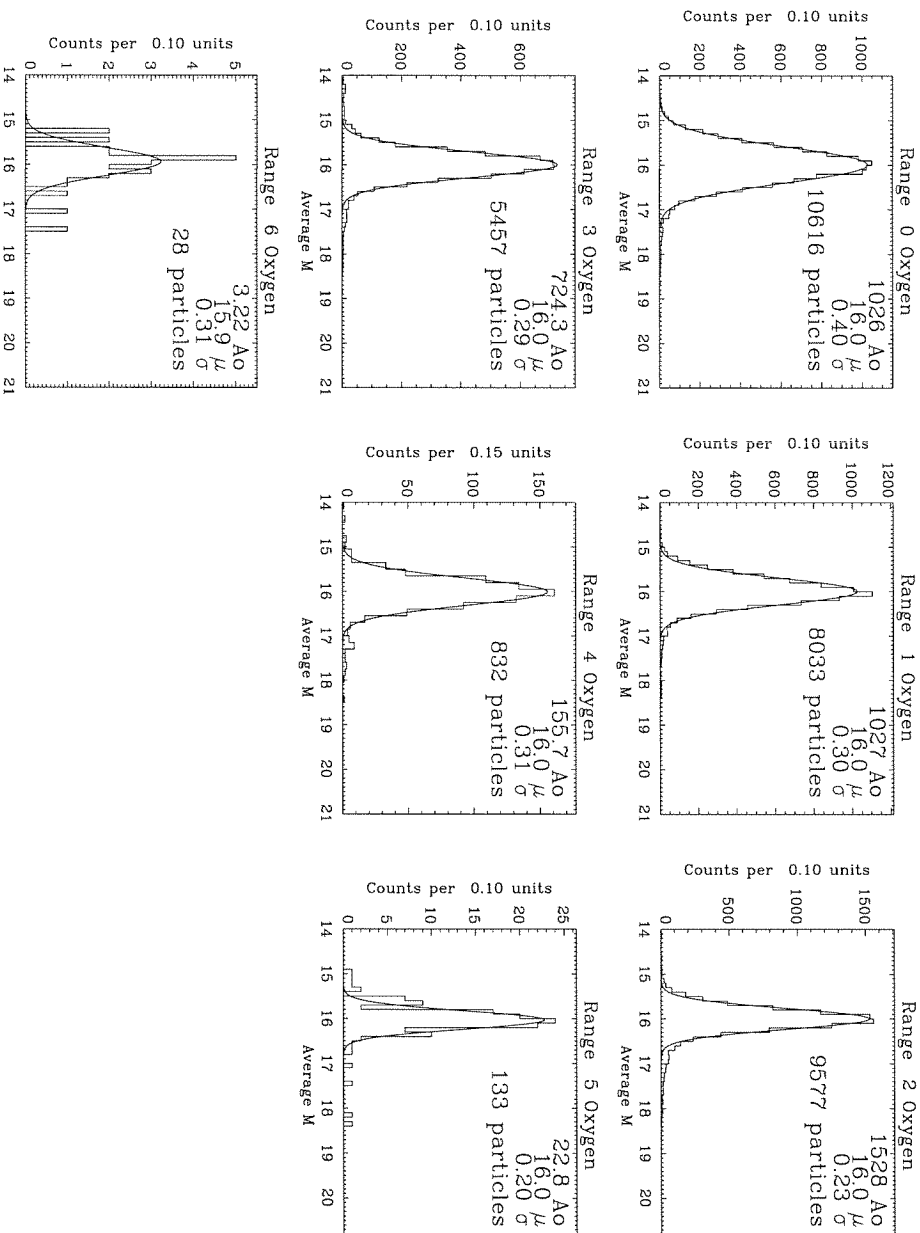

Figure 3.13: The weighted average mass of oxygen for each range. Each mass distribution is fit with a Gaussian shape.

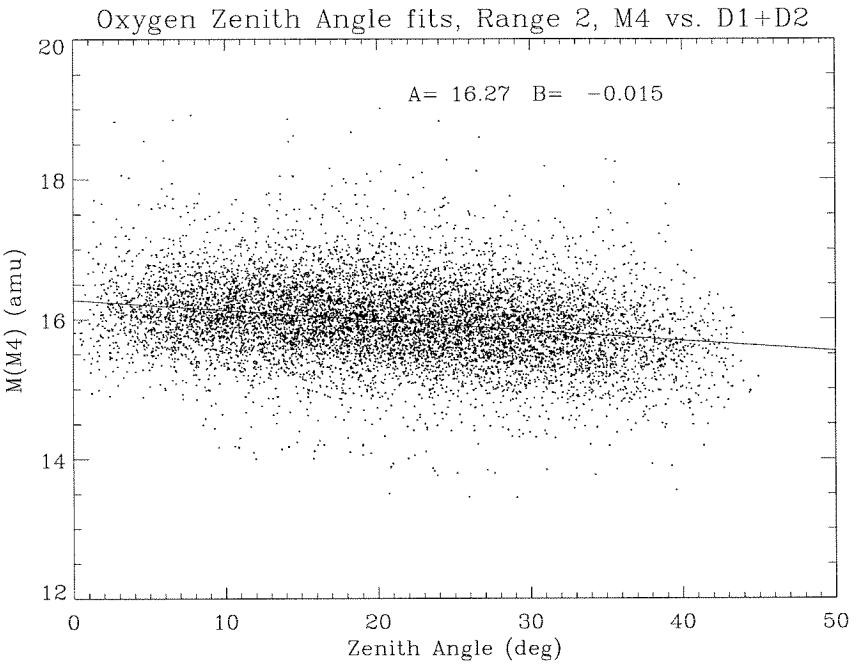

Figure 3.14: An example of the "Zenith Angle" correction to the data. This is Range 2 data, with mass calculated using the M4 detector as ΔE and D1+D2 detector as E'. The data are fit with a linear function of the form $M = A + B \times \theta$, and the coefficients are shown on the plot.

angle were made, the mass at large angles would appear to be greater than it actually is. This suggests that perhaps the angle used is larger than the actual angle, and that the factor $(cos\theta)^{1.3}$ is over-compensating for the angle.

How could the angle be too large? The angle is calculated using Equation 3.3. This indicates that perhaps ΔX or ΔY is too large, that $\Delta Z(x)$ or $\Delta Z(y)$ is too small, or some combination of these is occurring.

The strips on the matrix detectors have 0.5 mm pitch. Each detector has 93 strips, so that the total distance across the strips should be 4.65 cm. The full detectors are 5.08 cm in diameter. Prior to assembly of the instrument, the matrix detectors were placed under a microscope with a measuring translation stage, and the positions of the outer strips were measured. The distances between the outer edges of the outer strips were consistently between 2.27 and 2.32 cm, a variation of $\pm$ 1 percent.

An attempt was made to see whether using a different assumption of the hodoscope geometry could reduce or remove the dependence of mass on angle. First, the vertical separation of the upper matrix detectors, M1 and M2, from the lower matrix detectors, M3 and M4, was changed. Increasing the vertical separation decreased the angle used. This improved certain mass estimators in certain ranges. However, no single separation distance could remove the effect in all ranges. Furthermore, the separation distance required to straighten the mass estimators for ranges 0 and 1 was 3.5mm, far beyond the tolerances allowed in the instrument design and construction. Thus, it is difficult to understand how an error in the assumed vertical separation of the hodoscope could be the source of the angle dependence of the mass.

The distances across the matrix strips can also be altered to decrease the measured angle. It was found that in order to remove the dependence of mass on angle in Ranges 0 through 2, the distance across the strips had to be decreased by 8 percent. Given the measurements made beforehand, this is impossible. Also, no single value of the decrease in the strip separation works for all ranges.

Other possible design problems with the hodoscope configuration which could cause the angle to be wrong are that one of the detectors is off center, or that a detector is tilted, or even rotated. However, simulation of the data found that none of these effects could create the decrease in mass with angle as seen in the data.

There are two candidate phenomena which might explain the dependence on incidence angle. First, during calibration of the instrument, cross talk between the matrix detectors was observed. This could be occurring at the detectors themselves, due to image charges forming on pairs of neighboring matrix detectors, or it could be occurring between the wires bringing the signals from the detectors to the preamps.

Second, when the ions pass through the detectors, they can generate energetic "knock-on" electrons. These electrons will penetrate down to the next detector, adding to the signal on the following matrix detector. These low energy electrons are prone to scattering, and out near the edges of the detectors, a fraction of the knock-on electrons do not hit the next detector, but rather leave out of the detector sides. The result is that the distribution of energy loss is no longer centered on the particle track. Similar effects have been observed before in the calibration of higher-

energy instruments (Lau 1985). However, this phenomenon has not been explored for instruments such as MAST.

Since no cause for the dependence of mass on angle could be positively identified, it was decided that the best way to remove the dependence was to correct for it empirically. The mass is thus fit as linear function of angle and the dependence is taken out of the data using this linear fit. Figure 3.14 shows a linear fit to the mass plotted over the data. The correction is applied as follows:

$$M'' = M' \times \frac{M_I}{M_c(\theta)} \tag{3.6}$$

where $M_c = A + B\theta$ is the linear fit to the mass, M_I is the integer value of the dominant mass peak, and M' is the mass estimator which has been centered at M_I.

The angle correction has a weak dependence on mass, with the linear coefficients for iron being about 50% larger than those for oxygen. The size of this deviation is less than ~5% of the mass. Because of this dependence on mass, the data are divided into three sets. Each set uses the angle correction from an abundant element. Elements 6 through 11 use oxygen, 12 through 19 use silicon, and greater than 19 use iron to correct for this angle dependence.

The angle corrections improve the mass resolution for Ranges 0 through 4, as can be seen by comparing Figures 3.13 and 3.15. The deeper ranges have very little dependence on angle, and so are not greatly affected.

There are also trends in the mass as a function of ΔE, E', $\frac{E}{M}$, and other quantities related to the particle energy. The mass track could be straightened as a function of any of these quantities. However, this prevents a general correction to be made, since the energy deposited by each species in a given detector is different for each ΔE-E' combination. Therefore, we chose to correct the mass as a function of "residual range," R_r. This is the penetration depth of the particle in the stopping detector, measured in microns. An advantage of this quantity is that it ranges from zero to the detector thickness divided by the cosine of the particle angle, independent of particle species.

An example of such a correction is shown in Figure 3.16. To straighten this

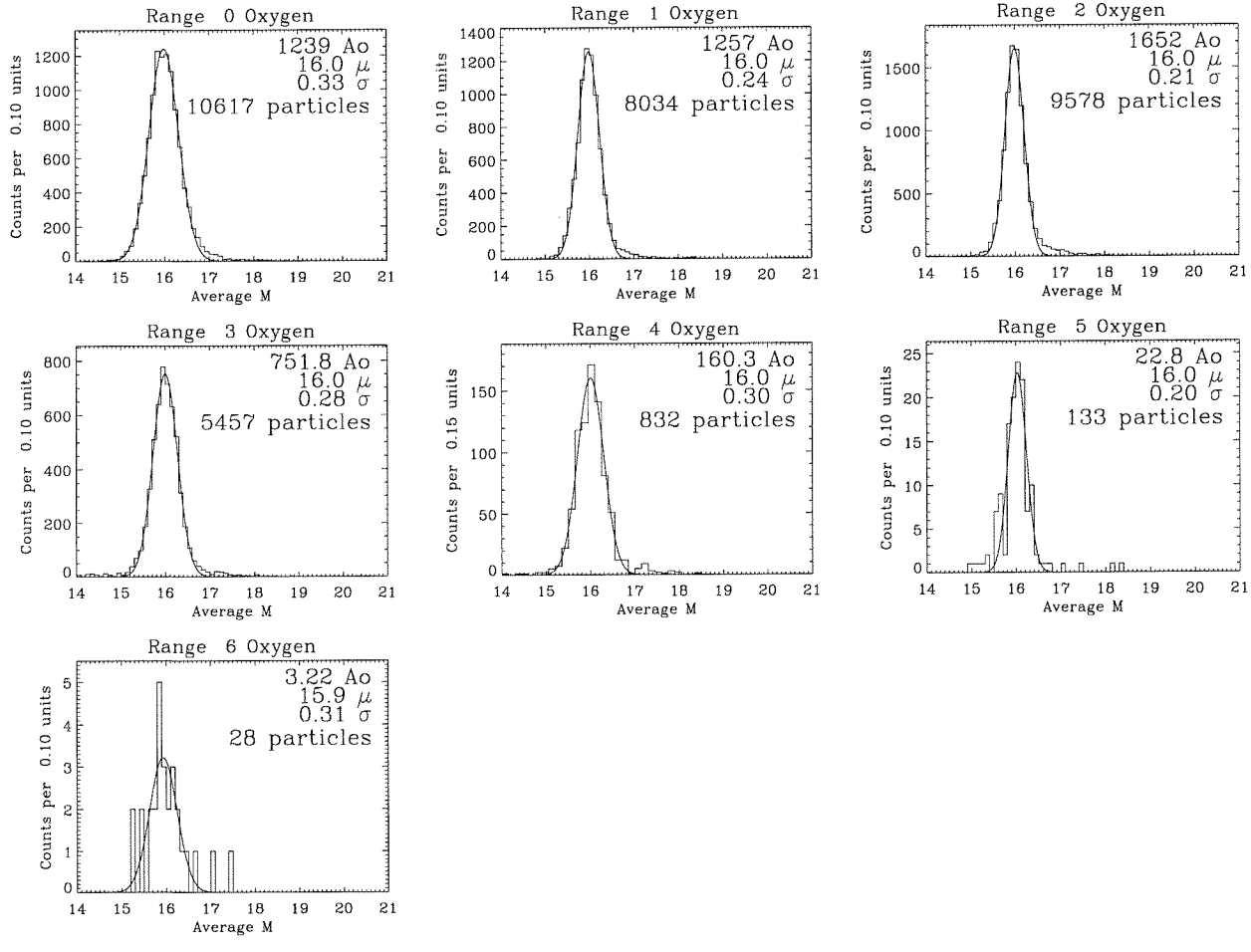

Figure 3.15: The weighted average mass of oxygen for all ranges, after they have been corrected for a residual dependence on the angle of incidence. The data were obtained from days 304 through 335, 1992. The particles in Range 5 and 6 are contaminated by galactic cosmic rays, which dominate the particle populations beyond ~70 MeV/nucleon.

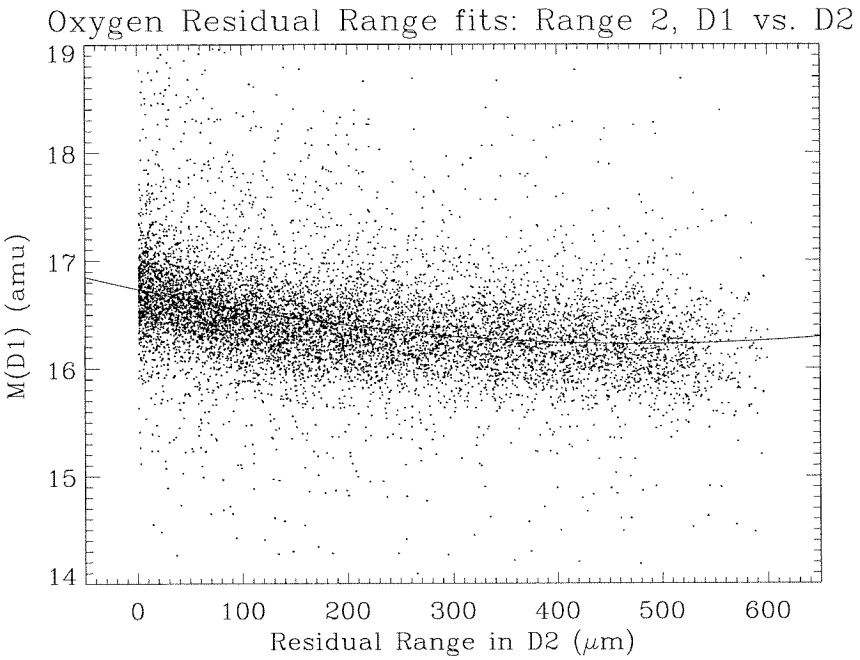

Figure 3.16: An example of the "Residual Range" correction to the data. This is range 2 data, with mass calculated using the D1 detector as ΔE and the D2 detector as E'. The data were obtained from days 304 through 335, 1992.

track the mass distribution is fit as a second-order polynomial in R_r. This form of the correction factor is the least complex one which will straighten the track.

For each ΔE-E' combination a 2nd order correction is calculated. Again this means there are Range+3 corrections per range. This correction factor is applied as follows:

$$M''' = M'' \times M_I / M_r(R_r) \tag{3.7}$$

where M'' is the mass of an individual particle which has been corrected for angle dependence, M_I is the dominant mass for the element which was fit, R_r is the residual range, and $M_r(R_r)$ is the fit of the mass to residual range. As with the angle dependence, the residual range correction depends weakly on mass. So the data are divided into three sets, as with the two previous corrections. Oxygen particles which have been corrected for residual range are shown in Figure 3.17.

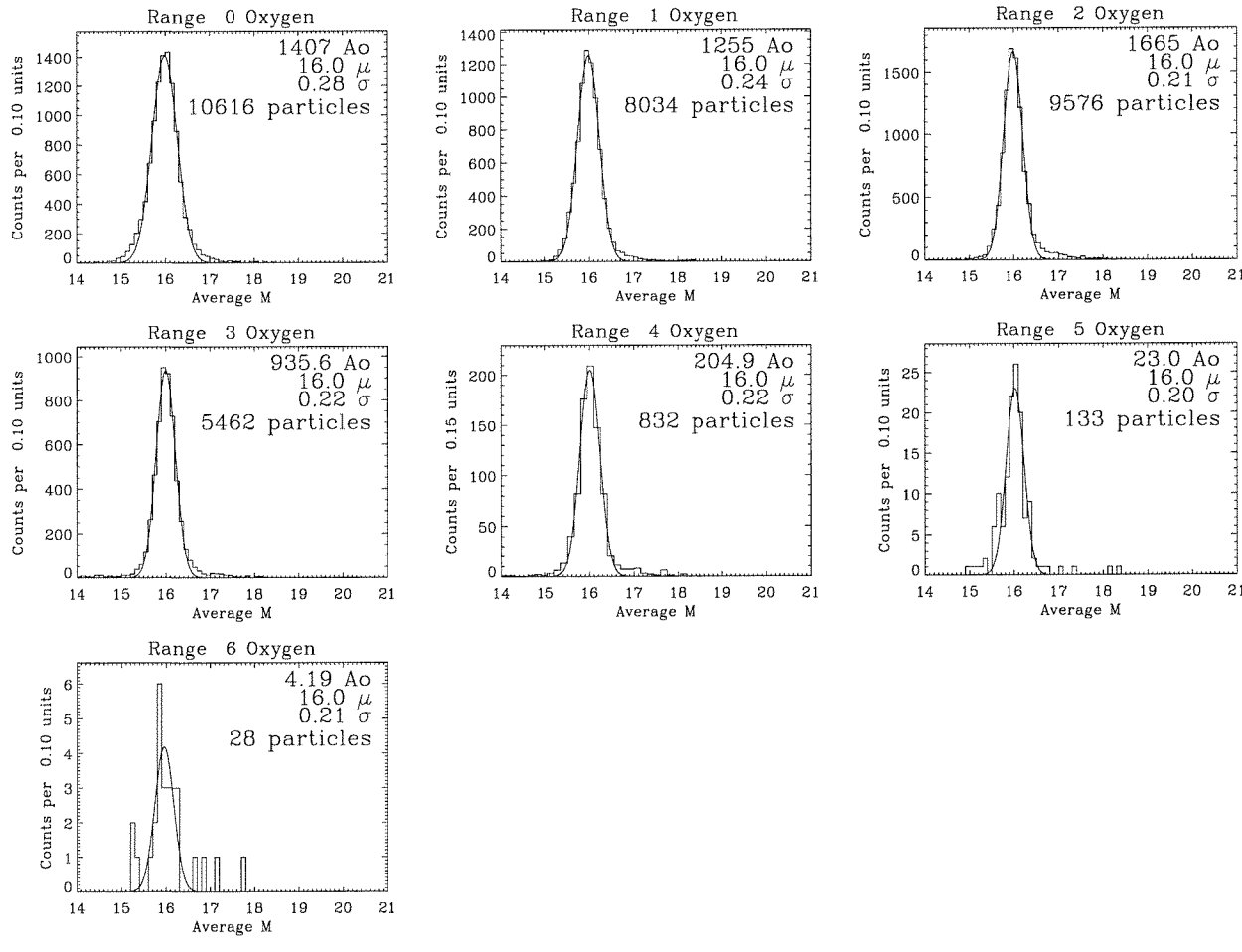

Figure 3.17: The weighted average mass of oxygen for all ranges, after they have been corrected for dependence on both the angle of incidence and the residual range. The data were obtained from days 304 through 335, 1992.

TABLE 3.5

The width of the oxygen distribution for each range, before and after systematic corrections to the mass are made. Note that while some ranges are strongly affected by the corrections, others, like Range 5, are hardly affected at all.

	Width (amu)			
Range	No Correction	Theta Fit	Range Fit	Theory
0	0.40	0.33	0.28	0.15
1	0.30	0.24	0.24	0.12
2	0.23	0.21	0.21	0.12
3	0.29	0.28	0.22	0.12
4	0.30	0.29	0.22	0.12
5	0.20	0.20	0.20	0.13
6	0.31	0.31	0.21	0.17

A diagnostic of how well the corrections work is the width of the resulting mass distribution. The width of the mass distribution of oxygen for each range is summarized in Table 3.5. The width before and after each of the corrections is shown, as is the theoretical calculation of the mass resolution. The mass resolution is not as good as theory predicts. This may be because the maps are not as accurate are expected, or for some other unknown reason.

3.2.5 Total Kinetic Energy

The total amount of energy deposited in the telescope is just the sum of the energy deposited in each detector, including corrections for the energy deposited in the detector dead layers. Knowing this and the charge and mass of each particle, the energy lost in the telescope windows can be calculated. This gives $\mathcal{E}_0$ the total kinetic energy of the particles outside of the instrument, and hence in interplanetary space. The distribution of $\mathcal{E}_0$ for oxygen particles in two solar energetic particle events is shown in Figure 3.18. These SEP events are discussed in more detail in Chapter 4.

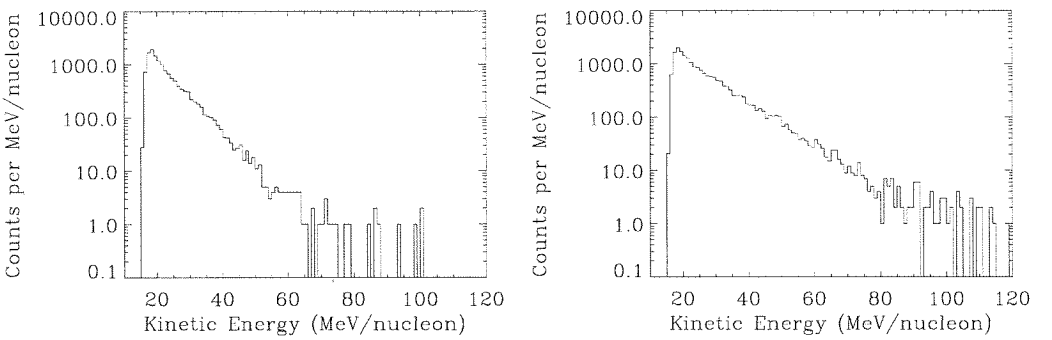

Figure 3.18: Total kinetic energy for oxygen particles in two SEP events which occurred in October and November 1992. These events are discussed in more detail in Chapter 4.

3.3 PHA Data Selection

In this section we discuss how the MAST PHA events are selected so that background is removed and isotopes may be cleanly resolved. The first selection fixes a problem in the data readout on board the spacecraft. The second involves the trajectory quality. The third selection deals with the consistency of the different mass estimators. The final selection criteria addresses the effect of high fluxes of low-energy particles on the MAST trajectory system.

3.3.1 Duplicate Events

For unknown reasons, a small fraction (2.2%) of the MAST PHA events are duplicates of previous events. This appears to be due to events which are "stuck" in the buffer, and not cleared out after being read by the DPU. These events can be identified and removed from the data. There is no evidence that duplication depends on element species, and thus should not bias the elemental or isotopic abundance measurements.

3.3.2 Trajectory Cuts

In order to make certain that particles pass through the detectors, the data is selected by trajectory. We require that the projected radius of a particle in M1, M4 and the stopping detector be within the physical radius of each of those detectors. Particles which do not have a complete trajectory measurement cannot be used for mass measurements, and are rejected from the data.

However, this selection by trajectory is not sufficient to obtain a "clean" set of data. The design of the MAST telescope is such that it will pulse-height analyze particles which do not stop within the detector stack for certain ranges. For example, a particle can hit M1-M4, and yet miss D1, passing out of the side of the stack. As far as the MAST electronics are concerned, this is still a valid Range 0 particle. However, since it does not stop in M4, the measurement of the particle's mass using the $\frac{dE}{dx}$ versus E' technique cannot be made. In a similar fashion, a particle can hit M1-D1, yet miss D2, going out the side, yet counting as a valid Range 1 particle; a particle can also hit M1-D2 yet miss D3, counting as valid a Range 2 particle. The geometry of these three possibilities are illustrated in Figure 3.19.

This problem was noticed while looking for trends in particle charge as a function of the projected radius in various detectors. Figure 3.20 shows the average charge for range 1 particles plotted versus the projected radius in the D2 detector. In this plot, it is clear that a significant fraction of events which could have missed the D2 detector (radius of 2.5 cm) have a poor charge measurement. Further analysis reveals that the only certain way to eliminate such particles from the data is to select only data which have a projected radius less than the radius of the D2 detector. Thus, a complete set of trajectory cuts selects data whose projected radii occur within the physical radii of M1, M4, the stopping detector, and the detector after the stopping detector. Note that such cuts have little effect on particles in ranges 3-6. There, the detectors are close together, and have guard rings. This prevents events from leaving the stack without triggering one of the guards.

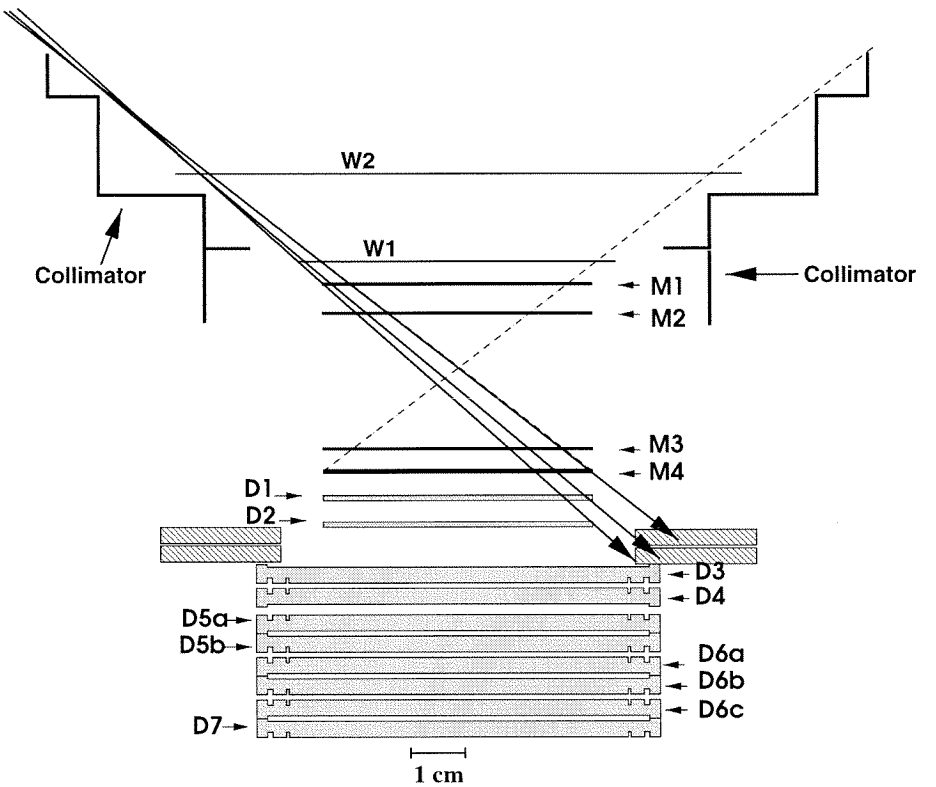

Figure 3.19: Demonstration of how particles can leave the detector stack, while the instrument registers them as stopping within the stack. The geometry of the detectors and the collimator allow this phenomenon to happen for particles stopping in Detectors M4 and D1 (Ranges 0 and 1). A lip of Delrin which separates the upper housing (M1-D2) from the lower housing (D3-D7) allows a small percentage of such particles to occur for Range 2 as well. The guards on the LiD detectors prevent this from happening for particles stopping in D3 through D6 (Ranges 3 through 6).

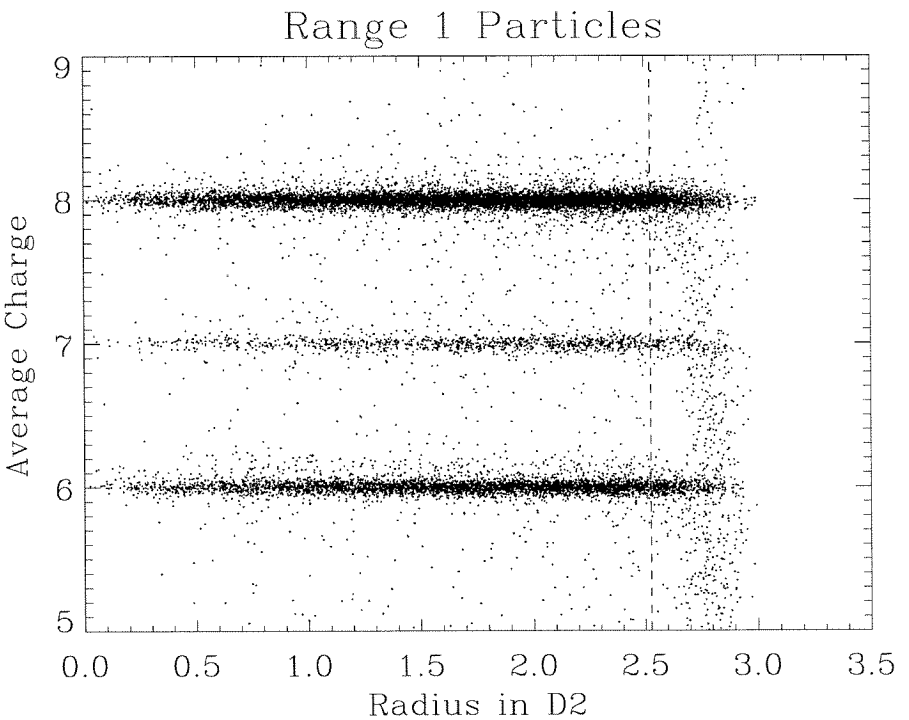

Figure 3.20: A plot of radius in D2 versus the average charge for range 1 particles. Particles which miss the D2 detector can still be accepted as range 1 particles. However, the charge measurement of such particles is incorrect.

3.3.3 Chi-Square Analysis

The trajectory cuts do not eliminate all non-physical events. There is a background at the 3% level of events which for unknown reasons are "scrambled." For these PHA events the detector pulse heights are shifted by a number of bytes, and the full set of pulse heights cannot be determined. Unfortunately, there is no sure way of eliminating these particles. Other data of poor quality may also be caused by inaccuracies in the detector thickness maps or a number of other phenomena. As a "catch-all" to remove such events, we analyze the statistical distribution of the events using the information obtained from each mass estimator. An underlying assumption is that the probability distribution of the measured mass for each ΔE-E' combination follows a Gaussian distribution,

$$p(m) = A \exp\left[-\frac{1}{2}\left(\frac{m-\mu}{\sigma}\right)^2\right] \tag{3.8}$$

where μ is the integer value of the mass, and σ is the width of the distribution. This form of the Gaussian distribution is quite amenable to fitting histograms. If we have a histogram of a Gaussian-distributed variable, A is simply the maximum height of the histogram, μ is its mean value, and σ is its standard deviation. The derivatives of this function with respect to each of these three variables are easily calculated. Thus, it is quite simple to formulate a first guess for the parameters of the distribution, and also easy to calculate the optimal parameters using a gradient-based search algorithm.

Given that the mass follows a Gaussian distribution, we may construct two chi-square quantities for evaluating the data. The first quantity, designated $\chi^2_{\nu,m}$, measures how well a particular set of $R+3$ mass estimators, M_i, agree with their weighted average, $\overline{M}$,

$$\chi^2_{\nu,m} = \frac{1}{R+2}\sum_{i=1}^{R+3}\left(\frac{\overline{M}-M_i}{\sigma_i}\right)^2 \tag{3.9}$$

This is a chi-square quantity with $R+2$ degrees of freedom. Note that while this quantity is quite sensitive to monotonic trends in the mass estimators, it can

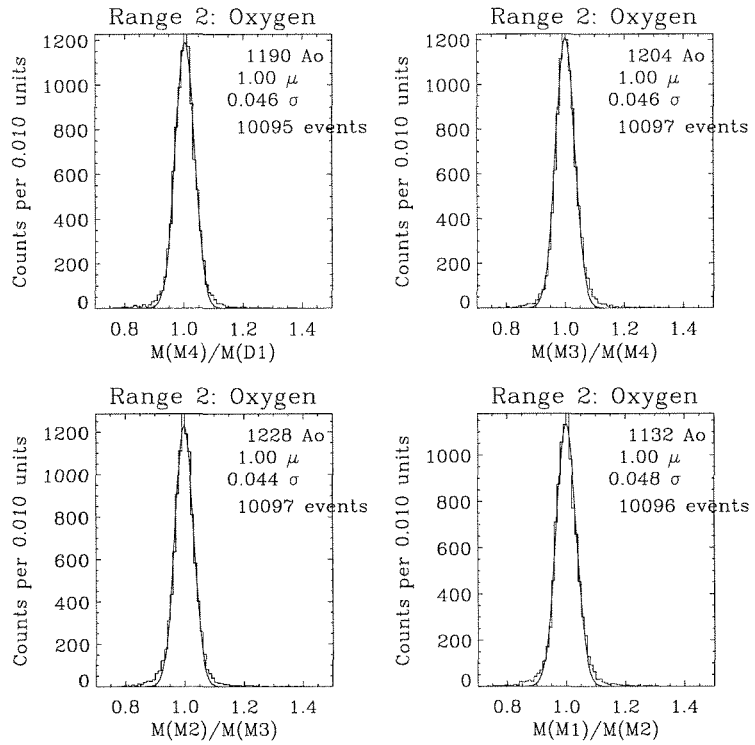

Figure 3.21: Mass ratios calculated for Range 2 oxygen data.

miss particles for which all but one of the mass estimators are in good agreement.

To identify cases in which there is one "bad" mass estimate, we construct a second quantity, designated $\chi^2_{\nu,r}$. This quantity is based on the ratio of one mass estimator with the next mass estimator. An example of the distribution of this quantity is given in Figure 3.21. This measures the consistency of the ratio of neighboring masses.

$$\chi^2_{\nu,r} = \frac{1}{R+1} \sum_{i=1}^{R+2} \left(\frac{\frac{M_i}{M_{i+1}} - r_0}{\sigma_{i,i+1}} \right)^2 \tag{3.10}$$

The widths and the offsets of $\frac{M_i}{M_{i+1}}$, designated $\sigma_{i,i+1}$ and r_0, are found by fitting the distributions with Gaussians for each pair of mass estimators. In general, $r_0 = 1$. This quantity is more sensitive to variations between individual mass estimators than the mass-average chi-square, as might appear if a particle suffered a nuclear

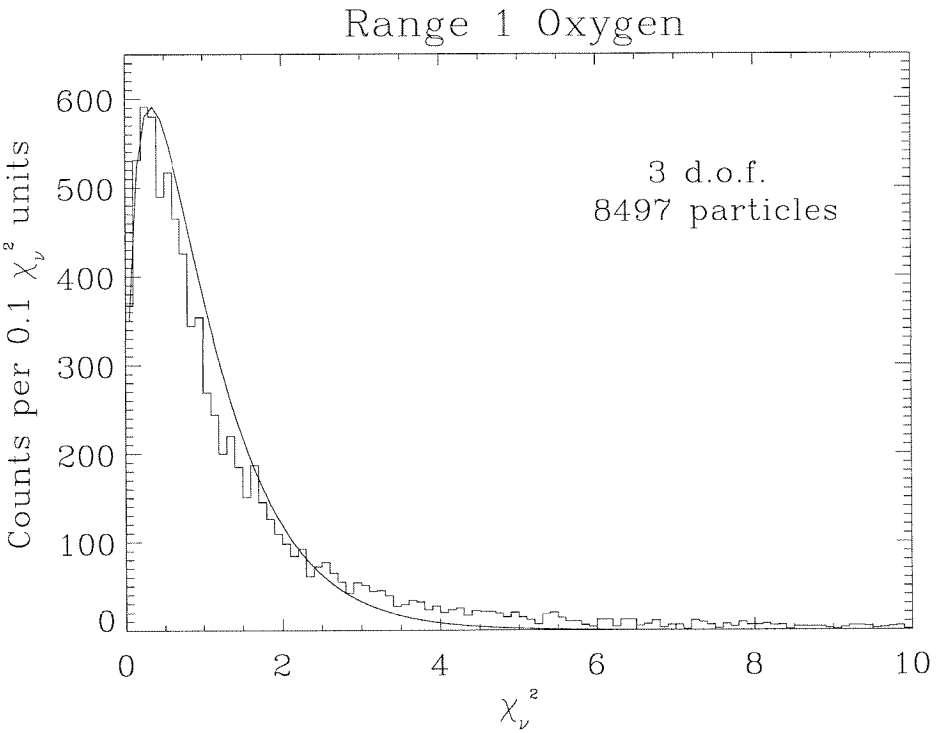

Figure 3.22: Distribution of $\chi^2_{\nu,m}$ for Range 1 oxygen particles. The solid line is a plot of the expected distribution of χ^2_ν for ν=3, which is the degree of freedom for range 1 particles, which have four mass estimators.

interaction within the detector stack.

The χ^2_ν is a standard "goodness of fit" measure in statistical analysis. We can explore the quality of the data by comparing the distribution of χ^2_ν from the data to a theoretical distribution, as is shown in Figure 3.22. When data is selected based on chi-square, we can compare the fraction of data removed with the expected fraction of data which would be removed if the data's true distribution were Gaussian. In general, we find that more data is removed than would be expected.

Note that particles with large chi-square are not intrinsically "bad" measurements. It is just that such particles should be rare. The overabundance of particles with large χ^2_ν indicates that the majority of those particles are contaminated for reasons which have not been identified, and that non-Gaussian processes exist in the mass measurements.

In Chapter 4, data are selected by limiting values of χ^2_ν. This quantity is simply the normalized quadratic sum of $\chi^2_{\nu,m}$ and $\chi^2_{\nu,r}$. The use of chi-square and the effect of the chi-square cuts on the isotopic ratios are discussed in the next chapter.

3.3.4 Low-Energy Particle Coincidences

When first examining the solar energetic particle data from MAST, it was noticed that the mass distributions had unexpected tails on the high side of the carbon and oxygen mass distributions. It was found that when the flux of particles was high, as measured by the ADCOR[1]rate, these tails appeared. When particles are selected so that the ADCOR is at low levels, these tails are not seen. Yet, unfortunately, the times of highest ADC counting rate are also times when the flux of heavy ions is the greatest, and so the majority of the data in an SEP event is collected during times of high flux.

In order to show how the tails correlate with counting rate, the data are divided into four parts according to ADCOR rate, each part having roughly the same number of particles. The first set of particles were measured when the ADCOR rate is between 0 and 6,000 counts per second, and the fourth set contains particles measured when the ADCOR is between 57,000 and 350,000 counts per second (The maximum ADCOR rate encountered in the two SEP events was 322,464 counts per second).

Figure 3.23 shows normalized histograms of average mass of carbon and neon particles which are measured during the highest 25% of the counting rates, and at the lowest 25%.

The high-side tail on the mass is sufficient to prevent the ratio $^{13}C/^{12}C$ or $^{21}Ne/^{20}Ne$ from being measured, and so the data must be selected so that only particles measured below a certain ADCOR rate are used. This effect is caused by low-energy protons and alpha particles hitting the instrument in coincidence with heavy ions. A similar problem occurred with the Phoenix-I instrument on the S81-1 mission (Simpson et al. 1984). An explanation of this effect, and evidence for this hypothesis, follows.

[1]The ADCOR rate, as discussed in Section 2.3.4, is the logical OR of all the MAST detectors.

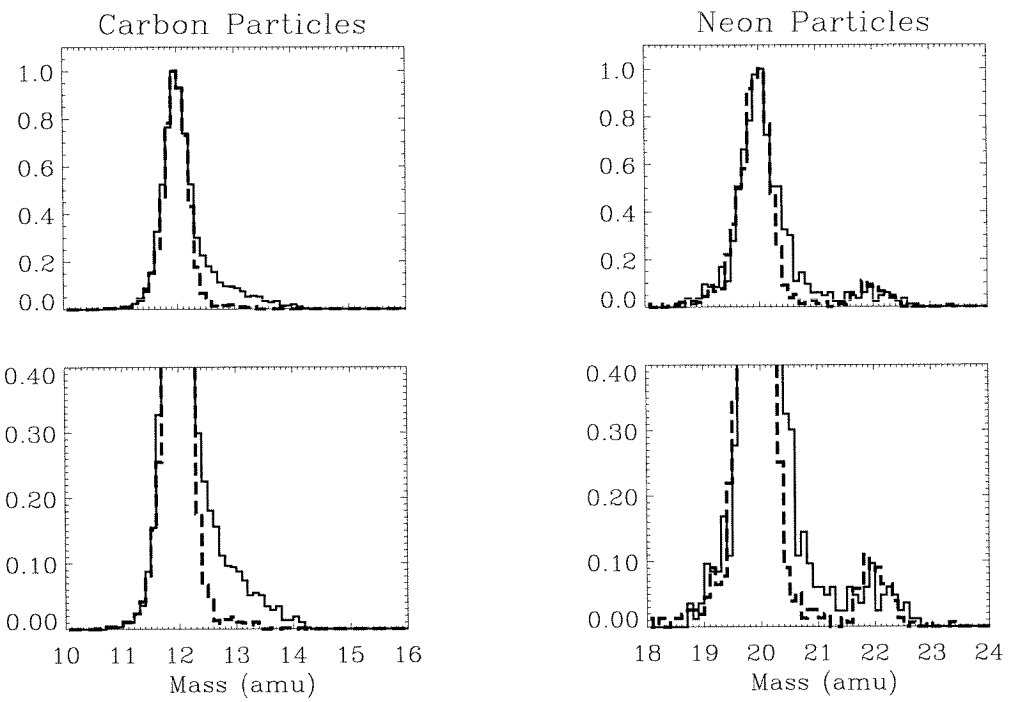

Figure 3.23: Normalized mass histograms of particles measured during the highest and lowest levels of particle activity. The solid line corresponds to particles at the highest ADCOR rates, from 57,000 to 350,000 counts per second. The dashed line corresponds to particles at the lowest ADCOR rates, from 0 to 6,000 counts per second. There are roughly 4,000 particles in each carbon histogram, and 1,000 particles in each neon histogram.

During solar particle events, the flux of low energy protons is high enough that the chance that the measurement of a heavy ion will be affected by a coincident proton is not negligible. Though the energies these particles deposit is small ($\sim$4 MeV), they can alter the apparent trajectory of light elements in the matrix detectors, making the mass estimate incorrect.

In Figure 3.23 the tails are predominantly on the high side of the mass distribution. At first thought it is not obvious that multiple coincidences should only cause a tail in the high side, but there are numerous effects at work. First, a coincident particle alters the energy deposited in the detector or detectors it hits. If this were the predominant effect, then it might be expected that cuts on the ratios of mass estimators could eliminate some fraction of these events. Second, the coincident particle will alter the apparent trajectory of the heavy ion. This could either increase or decrease the measured angle of incidence, leading to a mass which was either higher or lower than expected. There is no simple way to remove such events.

A further complication arises from the timing of the MAST matrix electronics. When an ion deposits energy in a detector, the shape of a signal coming out of the preamplifier is bipolar, with a negative amplitude about 33% the size of the positive, and lasting on the order of 15 μs. If another particle deposits charge either before or after the heavy ion, its voltage pulse will be added to that of the heavy ion. The resulting signal can be higher or lower than the original heavy ion signal, depending on how the two signals added.

To understand this effect better, a computer simulation of the instrument was built, which had the ability to mimic the electronic response of the detectors to multiple particles. This revealed several trends which were then verified in the observed data:

- Light elements ($Z < 9$) are more affected than heavy ones ($Z \geq 9$), due to the fact that the energy of the coincident protons is a much smaller fraction of the total energy deposited by the heavier particles. The flight data exhibit this behavior, as shown in Figure 3.23.

- Particles of the same species which penetrate deeper into the telescope are more

affected than ones which stop at shorter ranges, because the energy deposited in the matrix detectors is lower than for particles of the same species which stop at shorter ranges.

- The main cause of the altered mass measurement is the effect on the particle position in the matrix detectors, particularly the M1 detector. This means that all of the mass estimators are affected, in contrast to the case if the mass were off due to a bad signal in the M1 detector, which would only affect the M1 mass estimator. Thus, there is not an efficient way to select "good" particles.

- A hard spectrum of protons has a greater affect on the mass, causing the tails to appear at lower counting rates than would occur for a softer spectrum.

In the next chapter we will discuss how best to select data to avoid this problem of chance coincidences.

3.4 Rate Data Analysis: Particle Fluxes

The discussion so far has dealt with data from the EM sets. We now must look at the rate data, given in the RS sets, in order to measure the fluxes of particles. In the following section, I will describe how the MAST data is used to calculate the fluxes of particle species, and will give a few examples. The elemental and isotopic fluxes and abundances will be discussed in more detail in Chapter 4.

To measure fluxes we rely on the instrument low-resolution (RS) data sets (see Section 3.1.3). The RS sets contain counting rates of various discriminators, such as those listed in Table 2.8, and MAST event types, such as those listed in Table 2.9. It also contains the livetime counter, which is used to correct these rates for instrument livetime.

The flux of energetic particles in general is a function of energy, E, time, t, and direction, θ, ϕ. However, solar energetic particles are observed to have an approximately isotropic distribution except very early in the event, so that we can

treat J as though it is isotropic. It is also a function of the charge of the particle, Z, and so we can denote this flux as

$$J_Z = J_Z(E,t) \tag{3.11}$$

When a charged-particle detector is exposed to such a flux, the number of particles which it will measure within energy interval from E_0 to $E_0 + \Delta E$ and time interval Δt is given by

$$N_Z = \int_{t_0}^{t_0+\Delta t} dt \int_{E_0}^{E_0+\Delta E} dE \int_{\Omega} d\Omega \int_{A} d\vec{A} \cdot \vec{n}\, J_Z(E,t)\, \epsilon_Z(\Omega, d\vec{A}, E) \tag{3.12}$$

where the $\vec{n}$ is the unit vector normal to the detector surface and $d\vec{A}$ is an element of the detector surface. The only dependence on direction comes from $\epsilon_Z(E, d\Omega, d\vec{A})$, which is the efficiency of the instrument for measuring particles of charge Z in the solid angle $d\Omega$ over the element of surface area $d\vec{A}$.

The terms which are independent of the specific instrument can be separated from those which are not, and the response function can be written,

$$N_Z = \int_{t_0}^{t_0+\Delta t} dt \int_{E_0}^{E_0+\Delta E} dE\, J_Z(E,t) \left[\int_{\Omega} d\Omega \int_{A} d\vec{A} \cdot \vec{n}\, \epsilon_Z(\Omega, \vec{A}, E) \right] \tag{3.13}$$

The factor consisting of the double integral over the detector surface and solid angle is called the *geometry factor* of the instrument.

$$G_Z(E) = \int_{\Omega} d\Omega A(\Omega) \int_{A} d\vec{A} \cdot \vec{n}\, \epsilon_Z(\Omega, \vec{A}, E) \tag{3.14}$$

3.4.1 Calculation of Geometry Factors

The geometry factor of a telescope is a measure of the detection efficiency of an instrument in units of area times solid angle (cm^2 steradians). A Monte Carlo

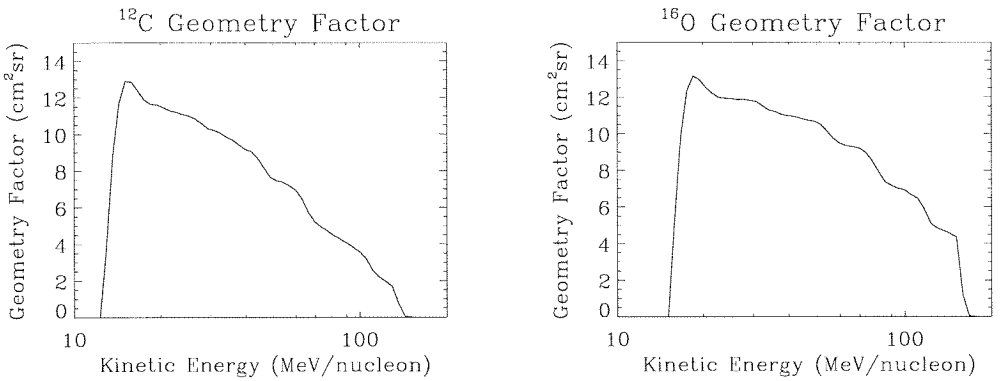

Figure 3.24: Geometry factors for ^{12}C and ^{16}O calculated by a Monte Carlo simulation of MAST. Note how the carbon geometry factor falls off more steeply at higher energies than that of oxygen. This is because at deep ranges, carbon no longer deposits sufficient energy in the matrix detectors to trigger them.

computer simulation was written to calculate the geometry factor of MAST as a function of energy. In this program, particles are generated from an isotropic distribution at the MAST collimator, and are required to pass through the M1 detector. These "initial events" have a geometry factor, obtained by the two-detector formula (Sullivan 1971), which is $G_0 = 53.6 cm^2 sr$. From those initial particles we find the geometry factor of a given event type and element by taking the ratio of the number of events which satisfy that event's logic equation to the total number of initial events, as in the formula:

$$G_Z(E) = \frac{N_{\text{Good}}}{N_{\text{Total}}} G_0$$

where N_{Good} is the number of events of charge Z, generated with energy E, which are registered as valid MAST events, and N_{Total} is the total number of events generated in the simulation.

The geometry factors for MAST have been calculated over a range of energies for all the nuclear species investigated in this thesis. Examples of the geometry factors of carbon and oxygen as a function of energy are given in Figure 3.24.

Since this calculation performs the integration over $d\Omega$ and dA, Equation 3.12 becomes

$$N_Z = \int_{t_0}^{t_0+\Delta t} dt \int_{E_0}^{E_0+\Delta E} dE\ J_Z(E,t) G_Z(E) \tag{3.15}$$

3.4.2 Timing Intervals

The smallest time interval which MAST can measure is given by the time resolution of the RS sets, which is Δt =6 seconds. The instrument is not necessarily live during this whole time interval. Rather, the instrument livetime, τ, is given by Equation 2.1. This means that MAST cannot resolve changes in particle flux over time scales shorter than 6 seconds, and so for the i^{th} RS set, the integral of the flux over that time interval is given by

$$\int_{t_0}^{t_0+\Delta t} J(E,t)dt = \tau_i J_{Z,i}(E)$$

where $J_i(E)$ is the average value of $J(E,t)$ over the time interval i. Equation 3.12 then becomes

$$N_{Z,i} = \tau_i \int_{E_0}^{E_0+\Delta E} J_{Z,i}(E) G_Z(E) dE \tag{3.16}$$

3.4.3 Energy Intervals

The integral in the previous equation still cannot be solved without knowing $J_i(E)$. In our approach we select an energy interval, ΔE_j, over which we take an average of $J_i(E)$. The energy interval is selected so that the geometric response of the instrument does not change significantly over the energy interval E_j to $E + \Delta E$. This is then designated as

$$G_{Z,j} = \frac{1}{\Delta E_j} \int_{E_j}^{E_j+\Delta E_j} G_Z(E) dE \tag{3.17}$$

The equation for particles counted by the instrument then falls into a very useful form

$$N_{Z,i,j} = \tau_i J_{Z,i,j} \Delta E_j G_{Z,j} \tag{3.18}$$

Equation 3.12 can now be inverted to solve for the particle flux,

$$J_{Z,i,j} = \frac{N_{Z,i,j}}{\tau_i \Delta E_j G_{Z,j}} \tag{3.19}$$

3.4.4 Event Readout Efficiency

The quantity $N_{Z,i,j}$ is the number of particles of charge Z the instrument would ideally count in a particular time interval, in a particular energy interval. However, this does not take into account two instrumental considerations. First, if a particle follows too closely another event trigger, it is tagged as a hazard event. This is incremented in the rates, but not written out as an event. Thus, the number of PHA events must be corrected by the number of PHA events which were thrown out due to the hazard flag.

A second instrumental consideration is that the MAST events are placed in one of nine buffers, and each buffer has a different readout priority, as shown in Table 2.14. The SAMPEX DPU takes events in order from these buffers. If the DPU quota is filled, it stops taking events. Thus, events in the top buffer are preferred over others when instrument event rates are high.

These two phenomena contribute to the *event readout efficiency.* The readout efficiency for particles in range r is the number of events in that range divided by the total number of rate counts for that range, r. For a given time interval, the number of HiZ events in Range R is denoted as $HIZE_R$. Likewise the number of rate counts in that time interval for Range R is denoted $HIZR_R$. The readout efficiency for range R events is then

$$\epsilon_R = \frac{HIZE_R}{HIZR_R}$$

Now taking into account the readout efficiency, the number of events actually recorded by the instrument is

$$n_{R,Z,i,j} = \epsilon_R N_{R,Z,i,j} \tag{3.20}$$

where $N_{R,Z,i,j}$ is the actual number of particles which hit the instrument. The flux measurement is then

$$J_{Z,i,j} = \frac{1}{\tau_i \Delta E_j G_{Z,j}} \sum_{R=0}^{6} \frac{n_{R,Z,i,j}}{\epsilon_R} \tag{3.21}$$

This is the flux of particles of element Z, in the time interval τ_i, in the energy interval ΔE_j, corrected for instrument readout bias and for instrument response. In this thesis, the flux is measured in units of particles per second per square centimeter per steradian per MeV/nucleon.

The quantities $N_{R,Z,i,j}$ and ϵ_R are measured by MAST while $G_{Z,j}$ is obtained through the Monte Carlo program for geometry factors. The time interval τ_i and the energy interval ΔE_j must be chosen carefully, depending on the time and energy properties of the particle flux being measured. Selection of time and energy intervals and the use of the flux is discussed in the next chapter.

3.5 Chapter Summary: Interplanetary Fluxes

The data analysis techniques discussed in this chapter are all brought together to calculate particle fluxes. The fluxes form part of the SAMPEX *Yellowbook Plots* which are published in the *Solar Geophysical Data Bulletin* (NOAA 1993). Each of the SAMPEX instrument teams contributes their data to produce a set of these plots for each month. These fluxes are taken only over the geomagnetic poles, where particles have equal access from interplanetary space. Examples of these plots for the month of October, 1992, are shown in Figures 3.25 and 3.26. These plots are made available to the public via the SAMPEX home page

(`http://lepsam.gsfc.nasa.gov/www/sampex.html`) and at the National Space Science Data Center (`http://nssdc.gsfc.nasa.gov/`).

The figures show a fairly steady background of particles, due to galactic and anomalous cosmic rays, as discussed in the Introduction. The feature on day 279 is associated with the passing of solar active region number 7321. A solar active region is an area of magnetic activity on the Sun, where energetic phenomena such as sunspots, small flares and prominences often occur. Such regions can persist for months at a time. When the solar magnetic field lines from such a region rotate past the Earth, an increase in particle activity is often seen. Since the Sun rotates approximately every 27 days, the active regions appear every 27 days in the energetic particle data.

Note that on day 304, approximately 27 days after the active region from day 279 was observed, the flux of all particles suddenly increased by five orders of magnitude. The field lines from the active region 7321 were once again connected to the Earth, yet something more was occurring — a large solar energetic particle event associated with that active region was taking place. Such events are one of the primary phenomena that MAST was designed to investigate. The analysis of this SEP event, and another large event following this one, are discussed in the next chapter.

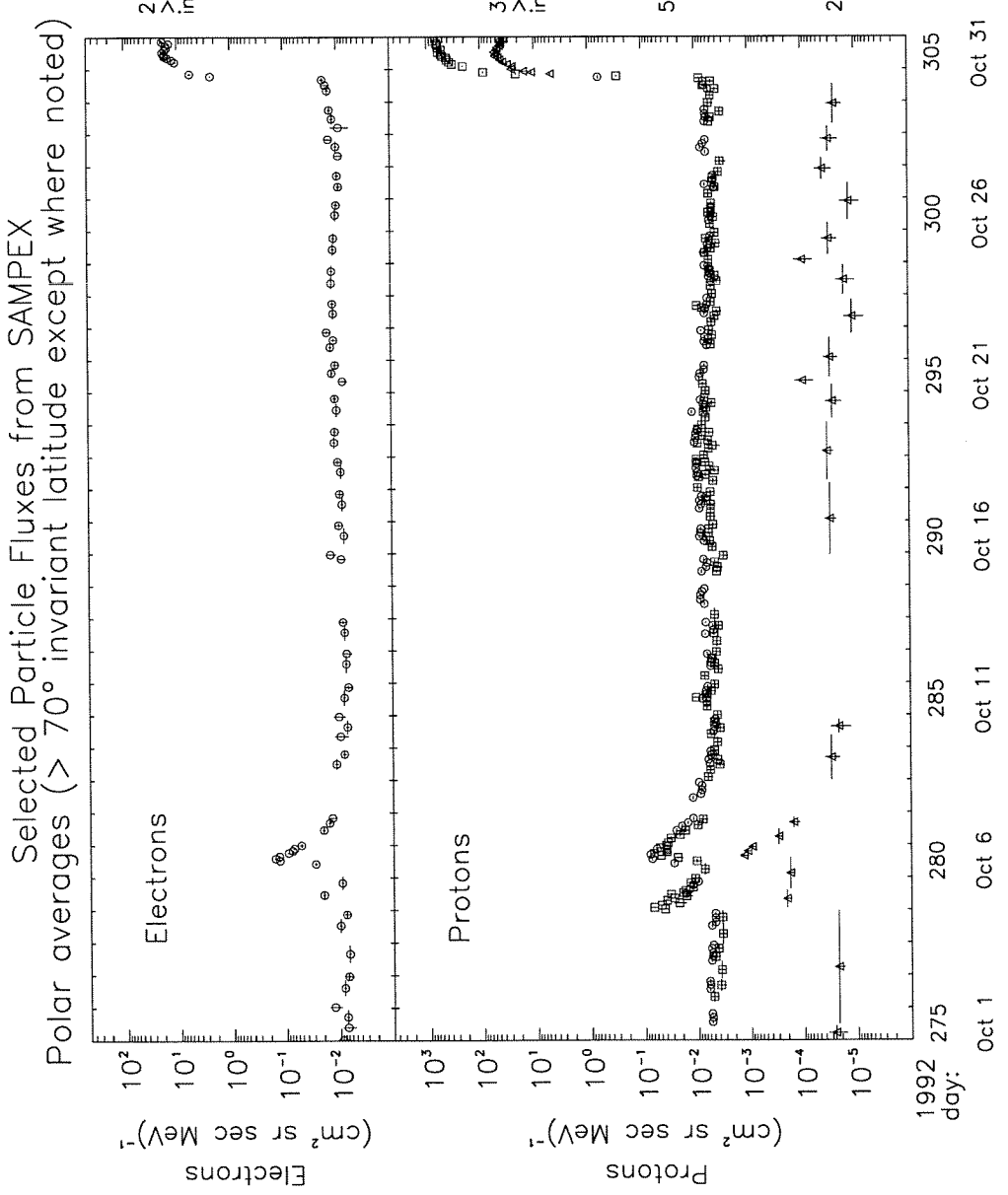

Figure 3.25: Plot of the interplanetary flux of electrons and protons as released to the NSSDC by the SAMPEX instrument team. The 2-6 MeV electron flux and the 20-29 proton flux are from the PET instrument; the 3.2-11 MeV proton flux is from HILT, and the 5-10 MeV proton flux is from MAST.

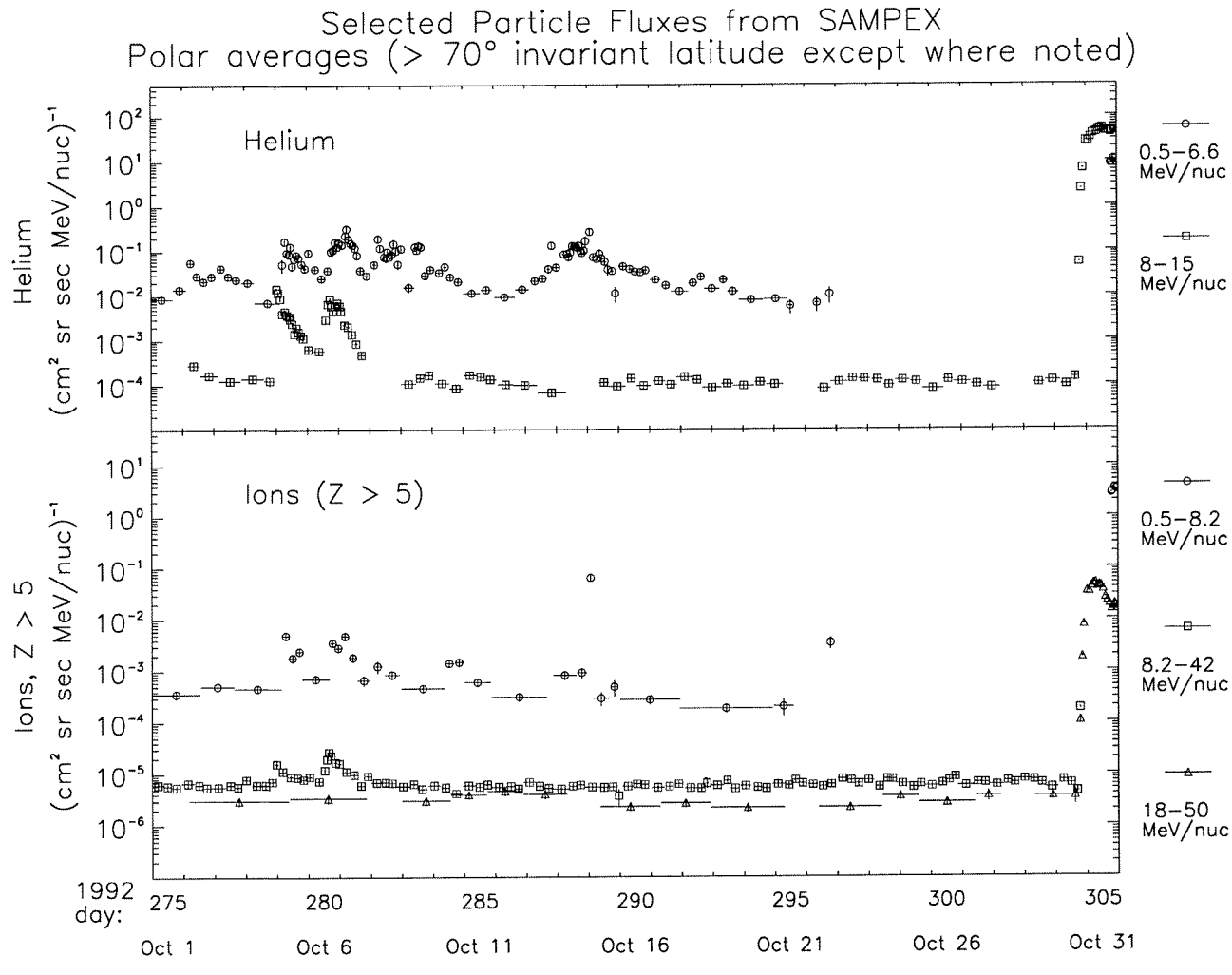

Figure 3.26: Plot of the interplanetary flux of helium and heavy ions (Z>5), as released to the NSSDC by the SAMPEX instrument team. The 0.5-6.6 MeV/nuc helium and 0.5-8.2 MeV/nuc heavy ion flux are from the LICA instrument; the 8.2-4.2 MeV/nuc heavy ion flux is from HILT, and the 8-15 MeV/nuc helium flux and the 18-50 MeV/nuc heavy ion flux are from MAST.

Chapter 4

Observations

4.1 Overview

This chapter presents the observations of solar energetic particles (SEP) made by MAST. We begin by describing the particle environment in low-Earth orbit which SAMPEX experiences. We briefly discuss the effect of the Earth's magnetic field on charged particles, and explain the relationship between the rigidity of a particle and its geomagnetic cutoff. The primary focus of this chapter, however, is the observation of two solar energetic particle events which occurred in late 1992. The first event began on 30 October, and is often referred to as "Event #1" in a few of the plots, while the second event began on 2 November, and is often referred to as "Event #2." We discuss how the particles from these events are distinguished from anomalous and galactic cosmic-rays, and the effect that the magnetosphere has on the measurements. We discuss the selection criteria which are used to determine the elemental abundances, and discuss the variation of the abundances with time. Then we look at the energy spectra of the elements and measure their relative abundances. The abundances are examined in the context of the current understanding of SEP abundances and their variation from one SEP event to another.

4.2 Operating in Low-Earth Orbit

4.2.1 Magnetospheric Coordinates

We now introduce magnetospheric coordinates and particle dynamics in the magnetosphere, with the aim that the reader understand the concept of the geomagnetic cutoff of solar energetic particles. Only the basic ideas needed for this thesis are discussed. For a comprehensive discussion the reader is referred to *Introduction to The Physics of Space* (Rossi and Olbert 1970), which provides a detailed mathematical treatment of the subject (see also Tascione 1988; Rossi 1964; Longair 1992).

Below the altitude of about 6 Earth radii, the Earth's magnetic field to a fair approximation resembles a dipole, as sketched in Figure 4.1. The dipole has a moment of 7.8×10^{25} gauss-cm^3. It is offset from the Earth's rotation axis by ~426 km, toward the Western Pacific Ocean, and is tilted by 11.3°. At the Earth's surface, the field strength ranges from ~0.67 gauss at the poles to ~0.25 gauss near the equator.

The magnetic field lines of the dipole can be parameterized by the B-L coordinate system, in which B is the magnetic field strength at a point on the field line, and L, called the magnetic L-shell parameter, is the distance from the center of the dipole to the point where a field line crosses the magnetic equator. L, measured in Earth radii, identifies a field line, and B gives the location along the field line. This coordinate system is very useful for describing the motion of charged particles in the magnetosphere.

At distances greater then 6 Earth radii, the solar wind greatly affects the shape of the Earth's magnetic field lines, compressing them on the upwind side to form the Earth's bow shock, and stretching out the field lines on the downwind side to form the magnetotail. The dipole approximation no longer accurately describes the magnetic fields at these distances.

In practice, the B-L coordinate system is calculated from a magnetic field model which approximates the Earth's magnetosphere much more accurately than the dipole model. The model used for SAMPEX data processing is the *1990 International Geomagnetic Reference Field.* The B-L coordinates are calculated by the subroutine

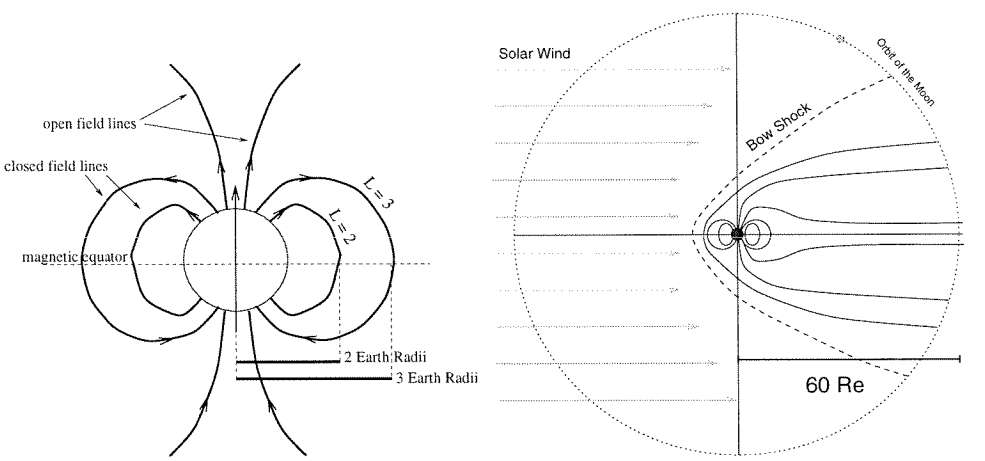

Figure 4.1: *Right:* A magnetic field line in a dipole can be characterized by the point at which it crosses the magnetic equator. The L-shell parameter is defined as the distance from the equatorial crossing point to the center of the dipole, measured in Earth radii. For example, the field line which crosses the magnetic equator at two Earth radii from the dipole axis is parameterized by L=2. *Left:* At distances beyond ~6 Earth radii, the geomagnetic field lines are altered by the solar wind, and the dipole approximation is no longer valid. However, the B-L coordinate system remains useful for describing the behavior of charged particles.

BL_IGRF written by M. McNab of Aerospace Corporation (Mazur, Walpole, and Mason 1998).

A quantity based on the magnetic L-shell which is used in this study is the magnetic *invariant latitude*, λ. If the Earth had a perfect dipole field aligned with its spin axis, then this would be equivalent to the geographic latitude at the point where the field line intersects the Earth's surface. Instead, the invariant latitude is defined as

$$\lambda = \cos^{-1}\sqrt{\frac{1}{L}} \tag{4.1}$$

Near the Earth's surface, and in the low-Earth orbit of SAMPEX, λ is analogous to geographic latitude, with the addition of the dipole tilt. However, since contours of λ are contours of L, at large distances from the surface there is little correspondence between the invariant and geographic latitudes (see Figure 4.1).

4.2.2 Motion of a Charged Particle in a Magnetic Field

A charged particle traveling through a uniform magnetic field $\vec{B}$ experiences a force perpendicular to both the magnetic field and to the component of its velocity perpendicular to the field direction, as expressed in the Lorentz law of force,

$$F = \frac{d\vec{p}}{dt} = qe\frac{\vec{v}}{c} \times \vec{B} \tag{4.2}$$

where q is the charge number of the particle, e is the electron charge, c is the speed of light, and $\vec{v}$ is its velocity vector. The component of velocity perpendicular to $\vec{B}$ causes a force which bends the path of the particle into a circle in the plane perpendicular to $\vec{B}$. The radius of this circle, called the *gyroradius*, can be written as

$$r_g = \frac{pc}{qe}\frac{sin\alpha}{B} \tag{4.3}$$

where p is the relativistic momentum of the particle, and α is the angle of particle's velocity with respect to the magnetic field. Thus, a particle with $\alpha = 0°$ experiences

no force, and moves in a straight line, while a particle with $\alpha = 90°$ experiences a purely tangential force and moves in a circle. A particle with another value of α would execute a helical motion.

Notice that if particles with the same ratio of momentum to charge are injected into a magnetic field at the same angle α, they will have the same gyroradius, and thus the motion they follow will be identical. This ratio of momentum to charge is called the *magnetic rigidity*, designated $\mathbb{R}$. Even in magnetic fields which are not uniform, particles with the same rigidity will follow the same paths through the field. Thus, rigidity is very useful for organizing the behavior of particles in the Earth's magnetosphere.

$$\mathbb{R} = \frac{pc}{qe} \tag{4.4}$$

The momentum is measured in eV/c, so the dimension of rigidity is volts. Note that two particles with the same rigidity can travel at very different velocities, if they have different charge and/or mass. This behavior is relevant in the acceleration of particles by shocks, where the acceleration can depend on particle velocity.

The rigidity of an individual particle cannot be directly measured by MAST. The instrument measures the total kinetic energy, E_T, nuclear charge, Z, and atomic mass number, M, of each individual particle, but it cannot directly measure the charge of a particle. However, by studying SEP cutoff latitudes, Leske et al. (1995) has calculated the mean ionic charge state, Q, of a number of elements in each of the two solar energetic particle events. We use these measurements of charge states to calculate the rigidity of a given particle in unit of MV (10^6 volts),

$$\mathbb{R} = \frac{E_{\text{Rest}}}{Qe}\sqrt{\gamma^2 - 1} \tag{4.5}$$

where the rest mass energy of the nucleon is approximated by $E_{\text{Rest}} = m_u c^2 M$, with m_u=931.5 MeV/c^2, the unified mass unit. The Lorentz factor of the nucleon is then given by

$$\gamma = 1 + \frac{E_T}{E_{\text{Rest}}} \tag{4.6}$$

The rigidity has many uses. In particular it can be used to calculate how deep a solar energetic particle can penetrate into the magnetosphere, and thus, whether that particle has access to SAMPEX.

4.2.3 Charged-Particle Cutoffs

In the 1950's the Norwegian geophysicist Carl Størmer studied the paths of particles in a dipole magnetic field, in hopes of explaining aurorae. Though he did not succeed in solving the aurora puzzle, the mathematical framework he established was quite successful in describing the paths of energetic particles in the Earth's magnetosphere.

In particular, Størmer established a relation between the rigidity of a particle and the lowest invariant latitude that the particle can reach at a given altitude. This lowest latitude is called the *geomagnetic cutoff latitude*, λ_c. Note that this is measured in magnetic invariant latitude, not geographic latitude.

According to Størmer's calculations, the cutoff latitude, for a particle of rigidity $\mathbb{R}$ at an altitude r, is given by (see Zombeck 1992)

$$\mathbb{R} = \frac{300 M_\oplus}{r^2} \frac{\cos^4 \lambda_c}{[(1 + \cos\theta \cos^3 \lambda_c)^{\frac{1}{2}} + 1]^2} \tag{4.7}$$

where $M_\oplus$ is the Earth's magnetic dipole moment, which is 7.8×10^{25} gauss-cm^3, and the factor of 300 converts the cgs units of gauss-cm into the MKS unit of volts. The angle θ is the angle between the arrival direction of the particle and the tangent to the circle of latitude. For positively charged particles, $\theta = 0$ corresponds to arrival from the west. For a typical SAMPEX altitude of 600 km, r=6970 km. Since SAMPEX was pointing upward over the polar passes during this phase of its mission, the cutoff rigidity in units of 10^9 volts (GV) for particles at SAMPEX's altitude is

$$\mathbb{R} = 12 \cos^4 \lambda_c \tag{4.8}$$

Particles cannot be observed if their rigidity is less than this cutoff rigidity for a given value of λ. Higher rigidity particles can penetrate to lower invariant latitudes, and cosmic rays with energy above ~8 GeV/nucleon can penetrate directly to the orbit of SAMPEX at the equator.

The Størmer relation is only an approximation. Fortunately, the cutoff latitude for heavy ions was measured by MAST (Leske et al. 1995), and an empirical relation was found relating the rigidity and the cutoff latitude:

$$\mathbb{R} = 13.452 \cos^4 \lambda_c - 0.3873 \tag{4.9}$$

This empirical relation resembles the Størmer cutoff formula with an offset. Over the rigidity range of the MAST SEP measurements (300 to ~1000 MV), the empirical cutoff found by Leske differs from the Størmer cutoff by a few degrees. Leske also found that the cutoff varies with time by up to 4 degrees during a major solar disturbance. The time variations are correlated with the D_{st} index, a measure of magnetic activity taken by magnetometers on the ground.

Typical values of the cutoff invariant latitudes for the particles measured by MAST are shown in Table 4.1, along with their minimum rigidities.

4.2.4 Magnetospheric Structures Relevant to MAST

As SAMPEX orbits the Earth, it passes through many regions of the Earth's magnetosphere. Each region has a distinct population of particles, which affect the instrument in different ways. Figure 4.2 shows the response of the ADCOR rate over slightly more than one orbit. Over the north and south magnetic poles, galactic cosmic rays trigger the instrument at all energies, and the flux is quite constant once the spacecraft is fully into the polar regions. As SAMPEX passes out of the polar regions, the low-energy GCRs are filtered out by the geomagnetic field, and so the

TABLE 4.1

Geomagnetic cutoff latitude for four elements at the lowest energies they are measured with MAST. The mean charge state is from Leske et al. (1995) (note that the charge state of carbon in that work is assumed to be between 5.7 and 6.0). The mass of each element used in that study is the average mass as reported in Cameron (1982). Carbon has the lowest rigidity of the heavy ions studied (Z≥6), and thus the highest cutoff latitude.

Element	Mean Charge State	Minimum Energy/nuc.	Minimum Rigidity	Cutoff Latitude
C	5.85	13.80	328.91	61.29
O	6.95	16.08	398.46	60.55
Si	10.54	21.29	529.07	59.28
Fe	15.18	26.84	824.92	56.78

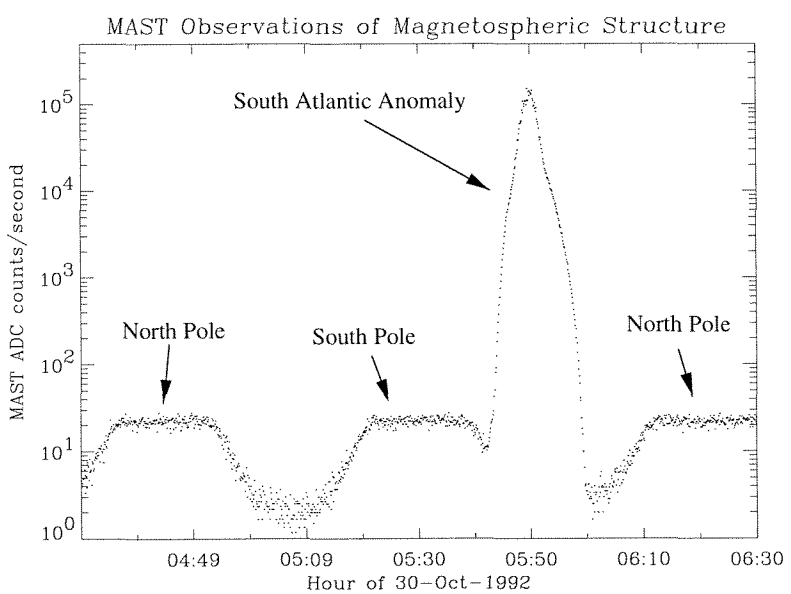

Figure 4.2: MAST ADCOR rates during quiet times. The plateau observed over the polar regions is due to galactic cosmic ray nuclei. The South Atlantic Anomaly is also seen.

counting rates decrease. The flux of GCRs is steady over periods of months, and so they present a fairly constant background of events when compared to SEPs, which typically persist for no more than one week. Over part of the South Atlantic ocean is a region of trapped protons, the South Atlantic Anomaly (SAA), where the inner Van Allen radiation belt, composed primarily of protons, dips close to the Earth's upper atmosphere. These protons mainly trigger the detectors near the front of the instrument, such as M1 and M2. As the Earth rotates with respect to the orbital plane of SAMPEX, the spacecraft passes through to the SAA on about 10 of its 15 orbits per day.

Like the low-energy galactic cosmic rays, SEPs are observed only over the polar regions. Thus, MAST can only measure such particles during the one-third of each orbit which is spent over these regions. This limits the instrument's ability to precisely measure the start of an SEP event.

4.3 Solar Energetic Particle Observations

A class X1.7/2B solar flare began at 17:02 UT on October 30, 1992. It achieved maximum brightness at 17:30, and ended at 22:03. The flare was associated with calcium plage region 7321, located at 22° south solar latitude, 61° west of the solar central meridian. Protons from this event were seen by the GOES spacecraft soon after 18:00UT. The proton fluxes for the event were over 1,100 *pfu* (proton flux units[1]) for protons of energy greater than >10 MeV, 97 *pfu* for >50 MeV, and 9 *pfu* for >100 MeV. The flare was associated with a coronal mass ejection off the southwest limb of the Sun (NOAA 1993).

Beginning around 19:00 UT MAST observed an increase in the ADCOR counting rate above the polar regions by 5 orders of magnitude, as shown in the top two plots of Figure 4.3. The increase in flux above the cosmic-ray background due to this event continued until 2 November, when that flux was overshadowed by the arrival of particles from a second SEP event.

[1]One proton flux unit, or *pfu*, is equal to one particle per cm^2 steradian second.

The second flare was class X9.0. It began at 02:30 UT on 2 November 1992. This event was also associated with region 7321, yet since that region had rotated beyond the solar limb at that time, no optical classification could be assigned to it. The maximum X-ray flux occurred at 03:08, and ended at 10:48. Protons from this event were observed by the GOES spacecraft just after 03:00UT. The proton fluxes were 120 *pfu* for >100 MeV, 300 *pfu* for >50 MeV, and 790 *pfu* for >10 MeV, making this event one of the hardest proton spectra observed for events during Solar Cycle 22. An associated coronal mass ejection was observed rising over the solar limb beyond the point where active region 7321 had rotated out of view (NOAA 1993).

After 04:30UT particles from the 2 November event were observed at MAST as an increase in the ADCOR counting rate by a factor of about six, as shown in the bottom two plots of Figure 4.3. The heavy ion flux continued to be above background levels until day 313 (November 8).

MAST only observes SEPs over roughly one-third of its orbit when it is over the polar regions, so its effective livetime is one-third that of a spacecraft in interplanetary space. The time sampling of the particles means that a precise time for the beginning of each SEP event cannot be set using the MAST data. Instead, the beginning of each SEP event is defined by the arrival time of protons at the GOES spacecraft. Such times are indicated by dotted lines in Figure 4.3.

4.3.1 Invariant Latitude Restrictions

In order to measure unbiased solar particle fluxes, it is necessary to use time periods when all SEPs have geomagnetic access to SAMPEX. Since the lowest-rigidity element of interest is carbon, the low-energy carbon particles will be most restricted in their access to low invariant latitudes. If low-energy carbon can penetrate down to a certain invariant latitude, then all the heavier elements also have access to that invariant latitude. The distribution of low-energy carbon with respect to invariant latitude and time, Figure 4.4, shows where carbon nuclei begin to be filtered by the magnetosphere. Leske et al. (1995) found that the cutoff latitude of particles could vary from -2 to +4 degrees in these two SEP events. Since the cutoff latitude of

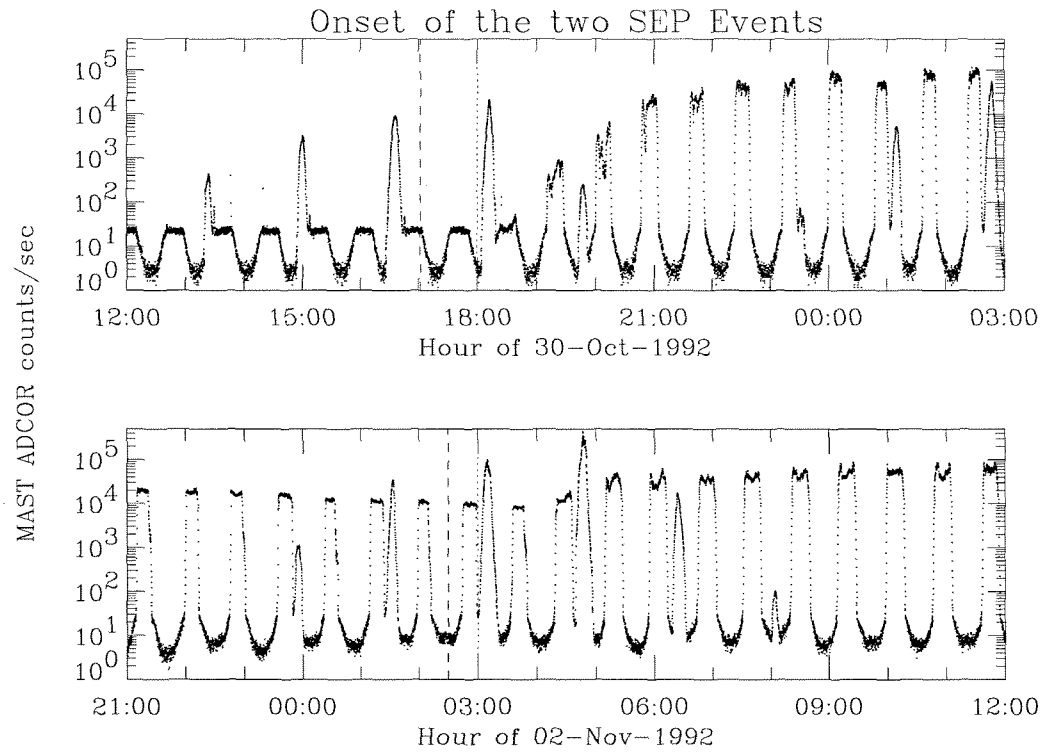

Figure 4.3: *Top:* Onset of the 30 October SEP Event. The nominal structure seen in Figure 4.2, with the north and south poles and the SAA, is overwhelmed by increased particle activity over both poles. The beginning of the X-ray flare at 17:02UT is marked by the vertical dashed line and the arrival of protons at the GOES spacecraft is indicated by the vertical dotted line. *Bottom:* Onset of the 2 November SEP Event. Counting rates were still elevated due to the previous event on 30 October. The beginning of the X-ray flare at 02:30UT is marked by the vertical dashed line, and the arrival of protons is marked by the vertical dotted line.

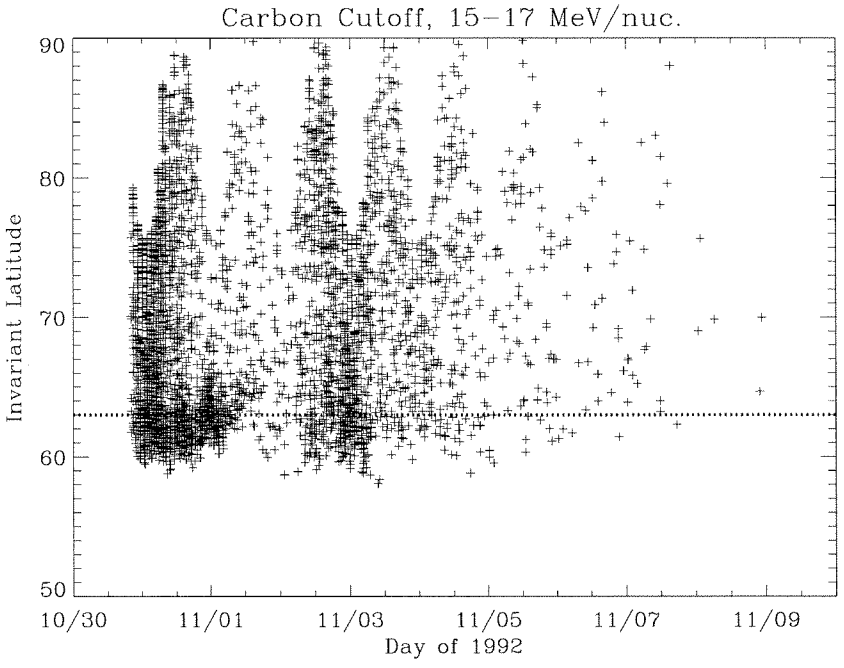

Figure 4.4: Invariant latitude of the lowest-energy carbon ions for the two SEP events. Carbon has the lowest rigidity of all the heavy (Z≥6) ions observed by MAST, and always penetrates as low as 65°.

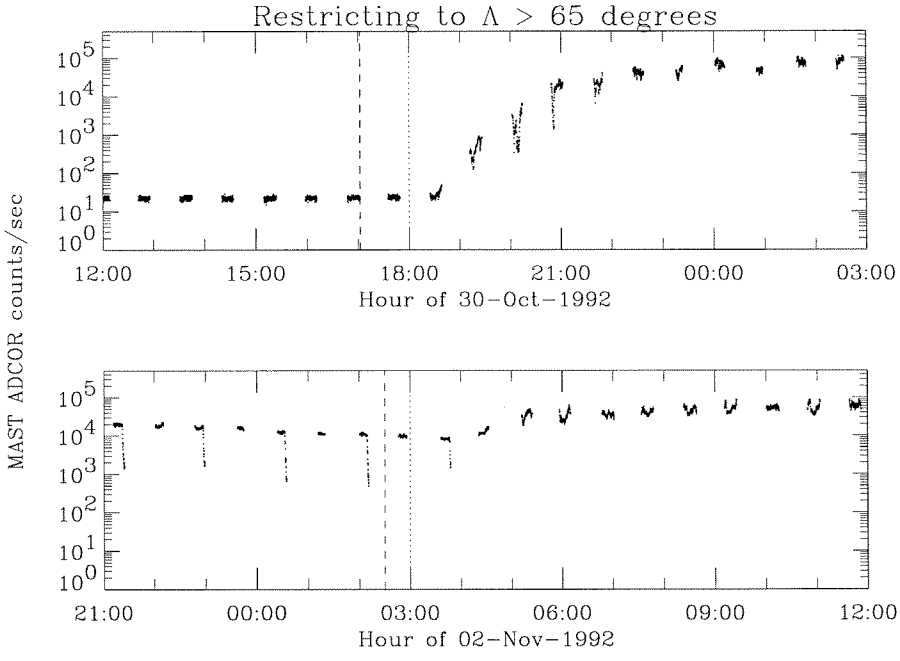

Figure 4.5: The same plot as in 4.3, but including only data taken at invariant latitudes above 65°.

low-energy carbon is 61°, we thus define polar passes to be when the spacecraft is at invariant latitudes greater than 65°so that our observations are not affected by geomagnetic access.

In order to study elemental composition, it is necessary to ensure that the composition is not affected by the geomagnetic field. Thus, in the following discussion we will be discussing only data taken at invariant latitudes greater than 65°. A plot showing the onsets of the two SEP events, using only data above 65°, shows more clearly when the rise in flux from each SEP begins (Figure 4.5).

4.3.2 Polar Averages

A natural unit of time in which to measure fluxes is the polar pass, which lasts about 15 minutes. For rare elements, averages must be taken over a number of passes in order to build up sufficient statistics. Three quantities relevant to flux calculations are shown in Figure 4.6, all taken as averages per polar pass. The upper trace is the ADCOR rate, which shows the general activity of the instrument. This is related to the livetime of MAST, which is shown as a fraction in the lower trace. The rate of heavy-ion triggers for Range 0 through 6 HIZ particles is the middle trace. Though this rate goes as high as 100 counts per second, the actual number of events which are pulse-height analyzed and stored is much less due primarily to the HAZ flag, and secondarily to the event readout priority system, which limits the number of events read out in each buffer to 12 per second. Since there are five HIZ buffers (see Table 2.14), the maximum number of HIZ particles that can be stored is 60 per second.

4.3.3 Element Identification

For element identification, trajectory cuts are first applied to the data, as discussed in Section 3.3.2. The residual range of particles is also restricted to be between zero and the maximum possible range for particles in the designated stopping detector. The weighted average charge determines the elemental species of a particle. The reduced chi-square of the charge measurements, χ^2_ν, is used to determine the

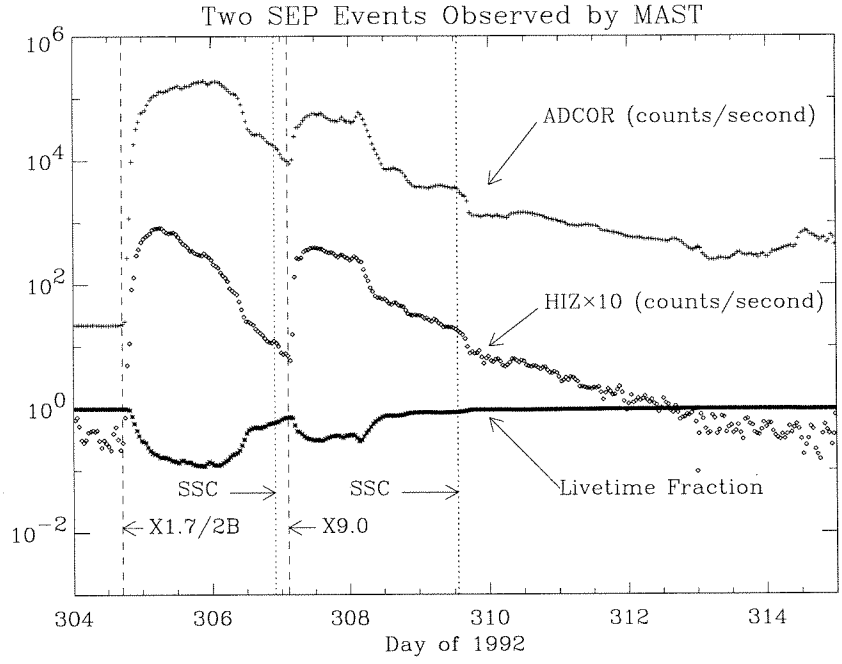

Figure 4.6: Time profile of the two SEP events, with the start of the X-ray flares marked by dashed lines, and the onset of the geomagnetic storms (SSC) associated with the events marked by dotted lines. The ADCOR rate is the logical OR of all the instrument triggers, and HIZ is the rate of heavy ion events. The livetime fraction ranges from 100% before and after the events, and bottoms out around 13% during the most intense periods. Each of these three quantities is averaged over each polar pass ($\Lambda > 65°$).

quality of the particle identification. A plot of charge versus χ^2_ν is shown in Figure 4.7, which combines the data from both solar particle events. Since the elements are fairly well separated, and since we do not wish to remove more data than necessary, the data used for studying elemental composition is chosen to have $\chi^2_\nu < 10$, as shown by the upper dotted line in the figure. The dashed line at $\chi^2_\nu = 4$ shows the boundary used for selecting particles for isotopic analysis, and the dashed line at $\chi^2_\nu = 2$ shows the chi-square cut used to verify that the resulting isotopic ratios are not significantly affected by the choice of chi-square. Shown by vertical lines are the boundaries used to determine the elemental species of the particles.

Figure 4.8 shows a histogram of the elements, selected with $\chi^2_\nu < 10$. Elements which have measurable quantities of particles are marked with their chemical symbols in this figure. The solid lines between elements show the limits used to identify each element. The effect of this chi-square selection, and the further restrictions of $\chi^2_\nu < 4$ and $\chi^2_\nu < 2$, are shown in Table 4.2. Abundant elements such as carbon and oxygen are not greatly affected when the data is chosen such that $\chi^2_\nu < 2$. However, particles which are assigned to rare elements such as fluorine and scandium are almost entirely removed from the dataset by this selection, indicating that such particles are mainly due to background.

Note that iron particles are not well separated from the manganese and cobalt. However, the relative abundances of manganese and cobalt to iron are expected to be on the order of 1.4% and 0.3%, respectively. Since the manganese and cobalt are not used in the element analysis, the charge selection criteria for iron is set so that it contains the majority of the data in the iron charge peak. As can be seen in the inset in Figure 4.8, this data may contain a small amount of overlapping manganese and cobalt as well.

4.3.4 Kinetic Energy

The kinetic energy of the particles is obtained by adding together all of the energy deposited in the telescope, and accounting for the energy lost in detector dead layers and in the instrument windows. The kinetic energy per nucleon is the

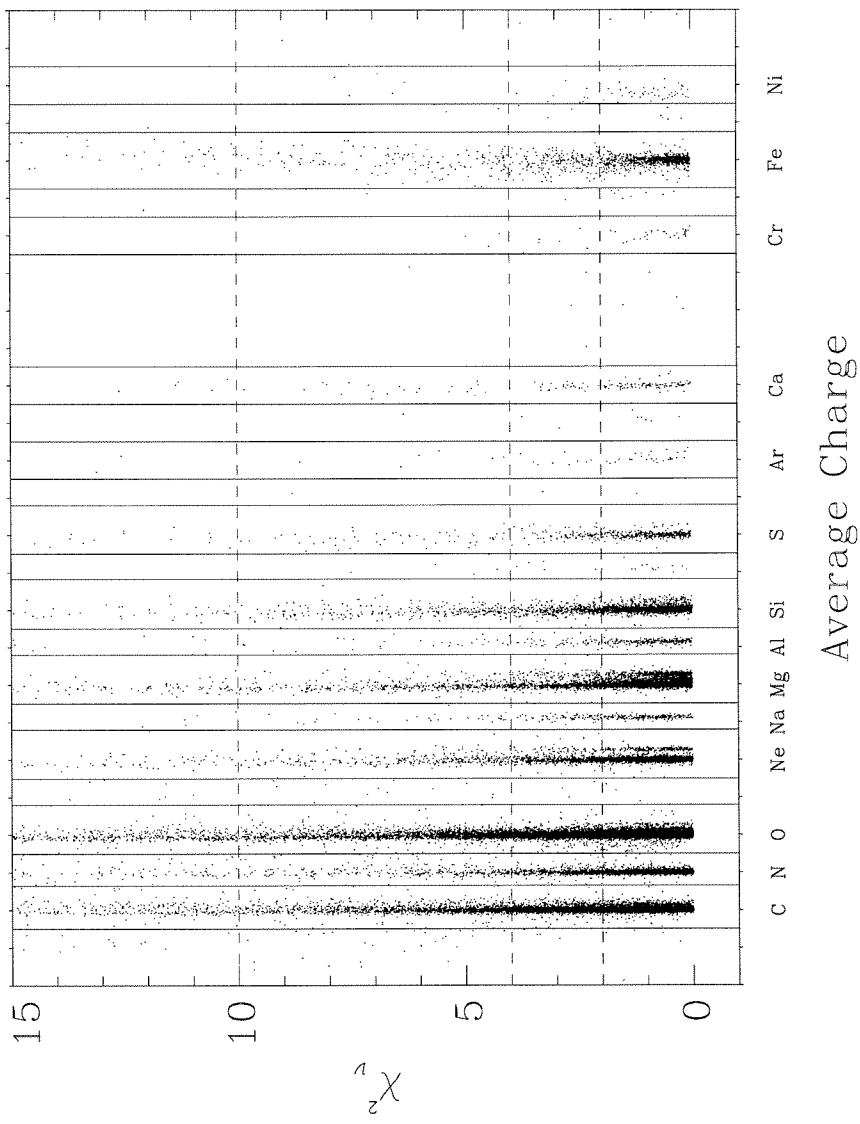

Figure 4.7: Plot of average charge versus the reduced chi-square. For identification of elements, the reduced chi-square, χ^2_ν, is required to be less than 10. For isotope identification, χ^2_ν must be less than 4. Analysis of the data with χ^2_ν less than 2 was found to yield equivalent results. The data include no latitude cuts, and contain particles from day 304 through day 335 of 1992.

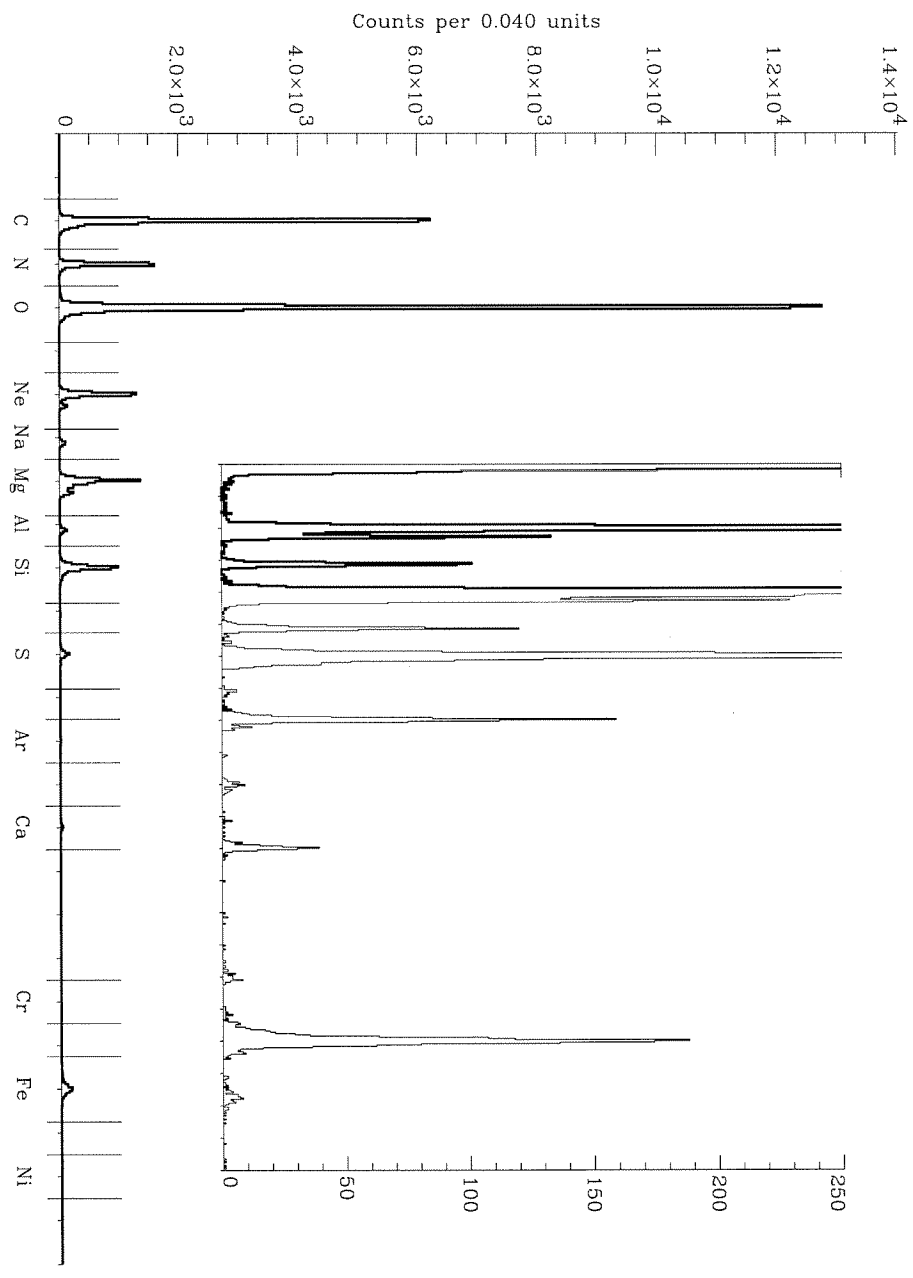

Figure 4.8: Histogram of the average charge for all MAST SEP particles. Only elements which are used in the data analysis are labeled. The solid vertical lines between element peaks show the boundaries used to identify charge. This data is the same as that of Figure 4.7.

TABLE 4.2

The number of each element observed from days 304.75 through day 312, with no cuts on invariant latitude. The number of events below three values of χ^2_ν is also shown. Elements in boldface and normal type are used in the analysis of elements, while those in italics do not have a sufficient number of particles for element analysis. Elements in boldface are used in the isotopis measurements.

			χ^2_ν<10		χ^2_ν<4		χ^2_ν<2	
Element	Z	Total	Number	%	Number	%	Number	%
C	**6**	**17445**	**16587**	**95.1**	**15011**	**86.0**	**11982**	**68.7**
N	**7**	**4550**	**4253**	**93.5**	**3938**	**86.5**	**3328**	**73.1**
O	**8**	**35958**	**34603**	**96.2**	**32449**	**90.2**	**27993**	**77.8**
F	*9*	*53*	*18*	*34.0*	*6*	*11.3*	*3*	*5.7*
Ne	**10**	**4336**	**4124**	**95.1**	**3786**	**87.3**	**3113**	**71.8**
Na	11	352	323	91.8	292	83.0	209	59.4
Mg	**12**	**5020**	**4759**	**94.8**	**4334**	**86.3**	**3507**	**69.9**
Al	13	382	355	92.9	324	84.8	273	71.5
Si	**14**	**3541**	**3423**	**96.7**	**3148**	**88.9**	**2696**	**76.1**
P	*15*	*30*	*26*	*86.7*	*21*	*70.0*	*15*	*50.0*
S	16	615	577	93.8	519	84.4	420	68.3
Cl	*17*	*5*	*3*	*60.0*	*2*	*40.0*	*1*	*20.0*
Ar	18	49	43	87.8	37	75.5	28	57.1
K	*19*	*10*	*9*	*90.0*	*8*	*80.0*	*6*	*60.0*
Ca	20	164	150	91.5	128	78.0	103	62.8
Sc	*21*	*4*	*1*	*25.0*	*1*	*25.0*	*0*	*0.0*
Ti	*22*	*4*	*4*	*100.0*	*4*	*100.0*	*3*	*75.0*
V	*23*	*3*	*2*	*66.7*	*1*	*33.3*	*0*	*0.0*
Cr	24	41	40	97.6	36	87.8	30	73.2
Mn	*25*	*22*	*12*	*54.5*	*10*	*45.5*	*8*	*36.4*
Fe	26	1310	1188	90.7	1036	79.1	839	64.0
Co	*27*	*26*	*12*	*46.2*	*9*	*34.6*	*5*	*19.2*
Ni	28	63	58	92.1	53	84.1	44	69.8

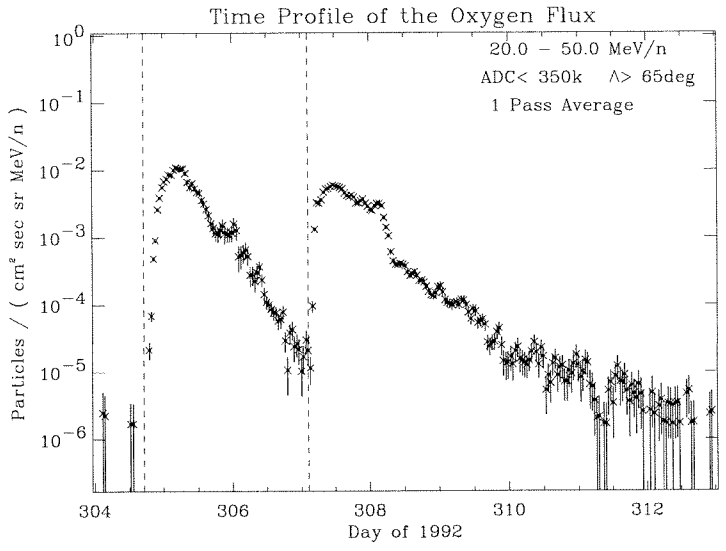

Figure 4.9: Flux of oxygen in the energy interval 20-50 MeV/n, averaged over each polar pass, with invariant latitude greater than 65°. The start of each associated X-ray flare is marked with vertical dashed lines.

total kinetic energy of a particle divided by its weighted average mass. The kinetic energy is used to derive such quantities as the Lorentz factor, the velocity, and the momentum of each particle.

4.3.5 Particle Fluxes

Now that the criteria are set for calculating the flux of each species, the flux of nuclei versus time can be examined. Recall that polar passes are defined by invariant latitude greater than 65°, and the averaging interval is set to be an integral multiple of polar passes. Oxygen is the most abundant element in the SEP data, and, as shown in the geometry plots of Figure 3.24, MAST is sensitive to oxygen nuclei from ~17 to ~150 MeV/nucleon. The flux of oxygen from 20-50 MeV/nucleon as a function of time is shown in Figure 4.9.

The background flux of galactic cosmic ray oxygen nuclei in this energy interval is $\sim 10^{-6}$particles$(\mathrm{cm}^2 \mathrm{sr\,sec\,MeV/nuc.})^{-1}$. This flux is observed before the first event begins. The solar energetic particles dominate the observed energetic

particle population until after 11/07/92, after which time the oxygen flux decreases to background GCR levels. During quiet time it is necessary to integrate the polar averages over longer periods to obtain statistically meaningful fluxes.

4.3.6 Energy Spectra

The energy spectrum of oxygen for both events is shown in Figure 4.10. The flux of each event can be fit with an exponential in energy,

$$\frac{dJ}{dE} = J_0 \exp\left(-E/E_0\right) \tag{4.10}$$

The fluxes are fit in the energy interval 30-60 MeV/nucleon. The e-folding energies for the events are 6.06± 0.25 for the first event and 10.89± 0.33 for the second event. The second event has a much harder spectrum for heavy nuclei than the first one; this was also seen in the proton spectra observed by the GOES satellites (Courtesy of the Solar Terrestrial Dispatch, at http://solar.uleth.ca/solar).

Figure 4.11 shows the fluxes of many elements with respect to kinetic energy. The spectra shown are consistent with a single spectrum. To find the e-folding energy for each SEP event, the abundant elements C, N, O, Ne, Mg, Si, and Fe were simultaneously fit to an exponential function over a common energy interval from 30 to 60 MeV/nucleon. This fit is shown in Figure 4.11. The e-folding energies are 7.26±1.21 and 10.54±1.09 MeV per nucleon. Since these fits are made to many elements, the uncertainties are larger than they would be if each element were fit individually. Yet the multi-element indices are in reasonably good agreement with the spectra made from fitting oxygen alone. If we assume that these indices truly represent the spectra, then they can be used to determine the relative abundances of the elements with respect to oxygen. These abundances are listed in Table 4.3.

Some features are notable in the relative abundances. The relative abundance of certain elements, such as silicon, are higher in the second event than in the first. Other elements, such as carbon, are relatively less abundant in the second events as compared to the first events. So the composition clearly differs between these two events. The abundances are discussed in more detail in Section 4.4.

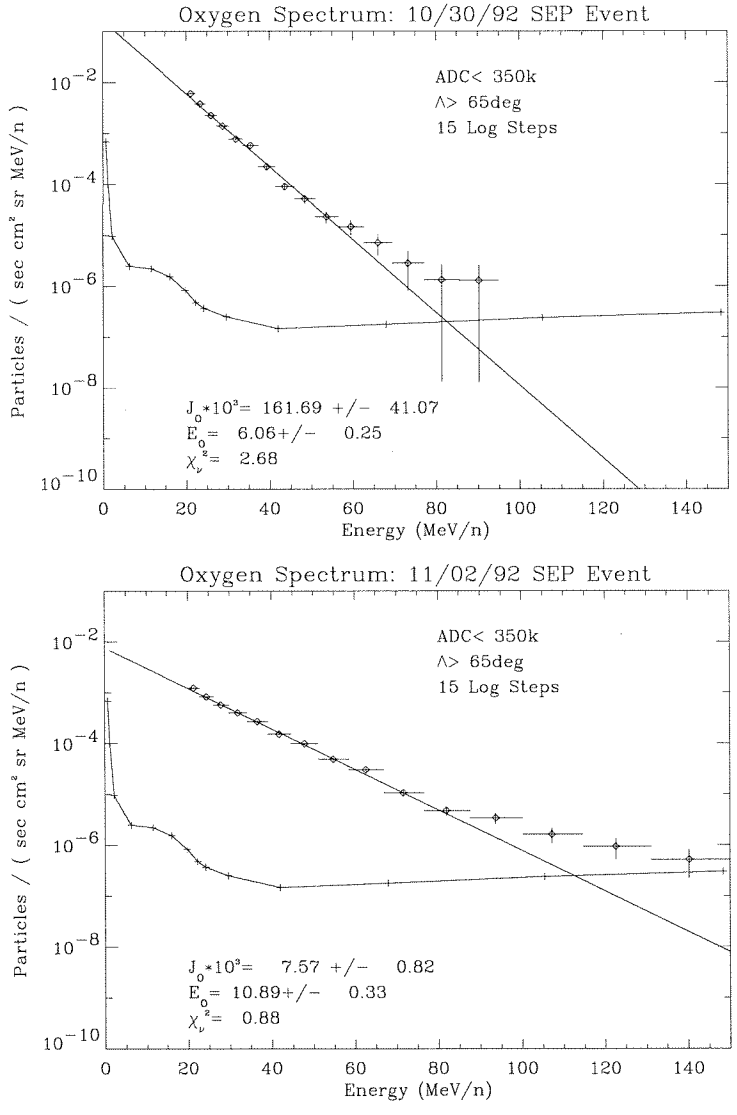

Figure 4.10: The energy spectrum of SEP oxygen for the two events is shown in these plots. Over plotted with the connected diamonds are the quiet time spectra of oxygen as measured by the instruments on SAMPEX from November 1992 through April 1993 (Mewaldt et al., 1993).

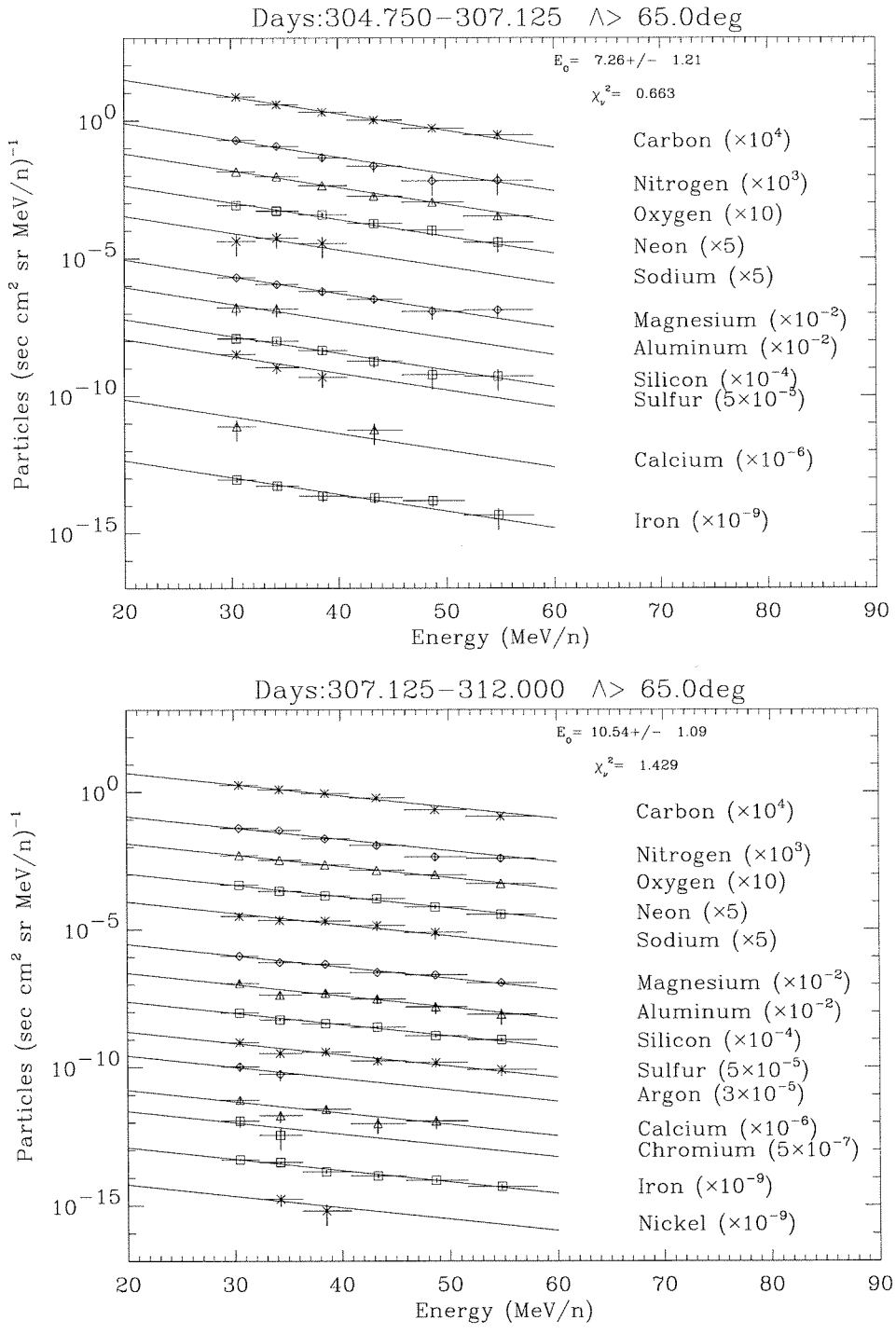

Figure 4.11: Spectra of the elements for each SEP event. The fluxes of all the elements are simultaneously fit to a function of the form $J(E) = J_0 exp(-E/E_o)$.

TABLE 4.3

Measured abundances of heavy ions normalized to Oxygen=100, for particles at energies of 30-60 MeV/nucleon. Also shown are spectroscopic photospheric abundances and SEP-based coronal abundances from Garrard and Stone (1993).

	Relative Abundance		Coronal	Photospheric
Element	30 October Event	1 November Event	Abundance	Abundance
C	47.65± 3.27	36.48± 1.38	42.76± 4.33	46.77± 5.39
N	12.62± 1.43	9.62± 0.61	12.33± 0.91	11.75± 1.35
O	100.00± 5.18	100.00± 2.56	100.00± 5.99	100.00± 9.21
Ne	13.71± 1.41	15.89± 0.74	14.16± 1.43	13.80± 5.72
Na	1.08± 0.41	1.52± 0.22	1.18± 0.11	0.25± 0.02
Mg	14.14± 1.41	21.85± 0.88	19.32± 1.11	4.47± 0.51
Al	1.41± 0.50	1.96± 0.24	1.43± 0.07	0.35± 0.06
Si	9.66± 1.13	17.81± 0.78	16.44± 0.00	4.17± 0.19
S	3.63± 0.74	2.88± 0.29	3.77± 0.16	1.91± 0.26
Ar	n/a	0.66± 0.18	0.37± 0.06	0.45± 0.19
Ca	1.16± 0.58	1.12± 0.18	1.19± 0.20	0.27± 0.02
Cr	n/a	0.38± 0.14	0.26± 0.05	0.05± 0.01
Fe	7.02± 0.96	9.32± 0.54	17.18± 2.25	3.55± 0.41
Ni	n/a	0.43± 0.16	0.61± 0.11	0.21± 0.02

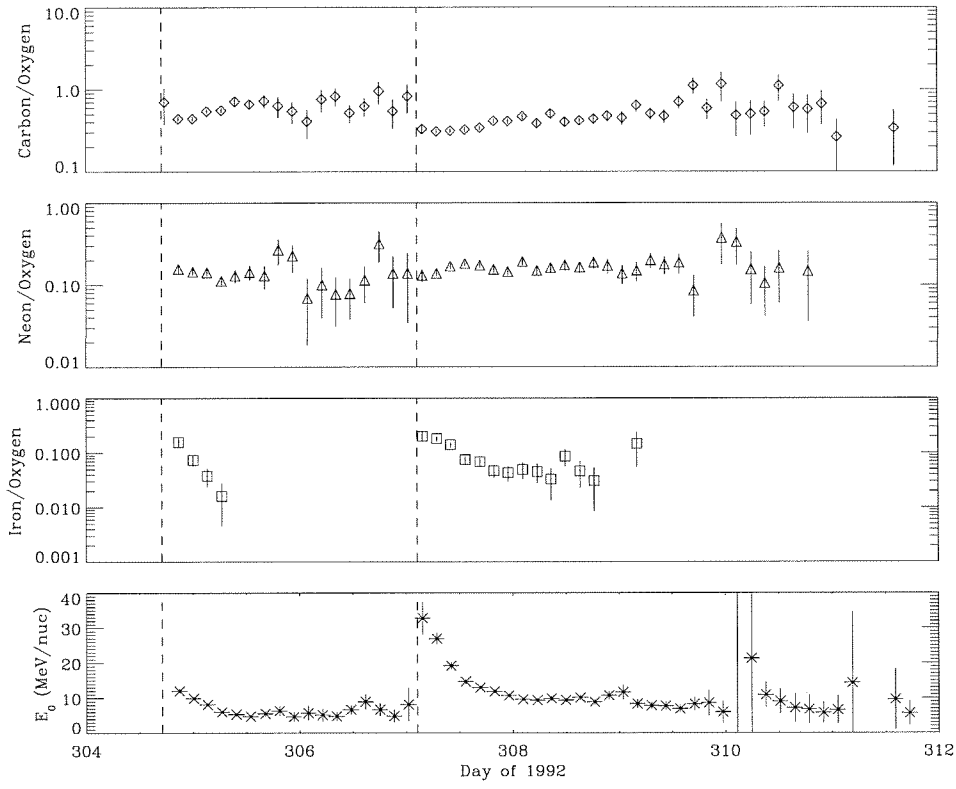

Figure 4.12: Dispersion in the arrival of certain elements is demonstrated by plots of the abundance of an element with respect to oxygen as a function of time. The energy interval is 20-60 MeV/nucleon for carbon and neon, and from 30-60 MeV/nucleon for iron. Data is chosen with $\Lambda > 65°$ and $\chi^2_\nu < 10$. The e-folding energy of the oxygen spectrum, shown on the bottom plot, is calculated using five energy intervals from 30-60 MeV/nucleon. For reference, the start of each X-ray flare is marked by a dashed line.

The abundances of abundant elements relative to oxygen as a function of time can be studied. In order to have sufficient statistics for such analysis, averages are taken over four polar passes (two orbits) to ensure that there are enough particles. Figure 4.12 shows the relative abundances as a function of time. Also shown is the e-folding energy of the spectrum, calculated for oxygen at each time step. Note that the C/O ratio rises with time, Ne/O remains fairly constant, and Fe/O drops with time. In both SEP events, the oxygen spectrum begins hard, but softens after a few hours.

The element ratios are consistent with the observation that the acceleration of these particles and the transport through interplanetary space is a function of particle rigidity. For particles with the same velocity, or energy per nucleon, the time of arrival should be organized by Q/M, the particle charge-to-mass ratio. Particles with higher rigidities should arrive first, followed by particles at lower rigidities. Since iron particles have lower Q/M than oxygen particles at the same energy, they have correspondingly higher rigidities, and travel to Earth more easily, thus arriving earlier. Carbon particles with a slightly higher Q/M and hence lower rigidities, arrive after the oxygen. Neon particles, with Q/M about the same as oxygen, arrive simultaneously, and so the Ne/O ratio does not appear to change significantly over the course of either SEP event.

The e-folding energy of the oxygen spectrum is also shown as a function of time. This is calculated in 5 bins of energy, from 20-80 MeV/nucleon. The oxygen spectrum is hardest at the start of each event, and softens over time.

Time-variations in the particle spectra and arrival times are related to the rigidity-dependent transport of the particles to Earth. The effect of these phenomena on the observed elemental abundances can be compensated for, as discussed the next section. Because of this, the time periods between the arrival of protons at GOES and the maximum flux of particles are included in the analysis.

4.4 Relating SEP to Solar Abundances

As mentioned in the Introduction, the composition of SEPs is related to the composition of the solar corona and photosphere, and the precise relationship was worked out by Breneman and Stone (1985). The formal mathematical treatment of these relationships are clearly described in Garrard and Stone (1994), and we follow their example in this section.

There are three main fractionation processes which act on the SEP material. First, the coronal material which serves as the source of SEPs is depleted in low-FIP elements with respect to the solar photosphere; second, the coronal material can be fractionated during acceleration to SEP energies; and third, the accelerated SEPs can

be fractionated as they propagate through the interplanetary medium to SAMPEX.

The second and third fractionation processes both depend on the rigidity (momentum per unit charge) of the particles. Since our abundance measurements are made in a common energy/nucleon interval, rigidity is proportional to the charge to mass ratio, Q/M. The difference between a rigidity-dependent bias in acceleration versus a rigidity-dependent bias in transport of the SEPs is difficult to separate, since we are observing the end-product of both processes. However, Brenneman and Stone found that the overall fractionation due to both processes can be fit with a power law in Q/M. In order not to be misled by differences in the coronal and photospheric composition, the "Q/M effect" is explored only for those elements which are not fractionated between the photosphere and the corona. These are the elements which have a first ionization potential (FIP) less than 10 eV.

The photospheric abundances to compare these abundances to come from a compilation by Garrard and Stone (1993). The abundances are listed in Table 4.3.

Study of the Q/M fractionation uses the mean charge state measurements of Leske et al. (1995). Figure 4.13 shows the relative abundances of low-FIP SEPs with respect to the spectroscopic abundances measured in the solar photosphere. Both SEP events exhibit a depletion of elements which have a low charge-to-mass ratio relative to silicon. The depletion can be fit with a power law, and the indices found for each SEP event are A_1=0.92± 0.56 for the first events, and A_2=1.15± 0.29 for the second event. In their survey of SEP events, Garrard and Stone (1994) looked at the distribution of these indices in 33 gradual SEP events. They found that the distribution of the indices had a mean value of -0.007 and a standard deviation of 1.97. So the indices found in our two events are typical.

If we assume that the Q/M correction adequately describes the acceleration and propagation fractionation of the SEPs, then by correcting for this fractionation, we should be able to obtain the relative abundances of the source material of the SEPs. These abundances are referred to as the "SEP-based" coronal abundances. This composition can the be compared to the photospheric composition to examine the photospheric-coronal depletion as a function of FIP and FIT. Such comparisons are shown in Figure 4.14. The results are quite interesting. While the FIP depletion

TABLE 4.4

The first ionization potential (FIP) (Brenneman, 1985), first ionization time (FIT) (Marsch et al., 1995), and charge to mass ratio (Q/M) (Leske et al., 1995) of the elements used in this analysis.

Element	FIP (eV)	FIT (s)	Q/M
6	11.26	27	0.487
7	14.53	68	0.462
8	13.62	62	0.434
10	21.56	81	0.424
11	5.14	n/a	0.396
12	7.65	0.78	0.424
13	5.99	0.30*	0.411
14	8.15	1.1	0.375
16	10.36	11.6	0.338
18	15.76	50	0.278
20	6.11	0.70	0.286
24	6.77	n/a	0.254
26	7.87	3.2*	0.272
28	7.635	n/a	0.215

*- FIT data from von Steiger et al. (1997).

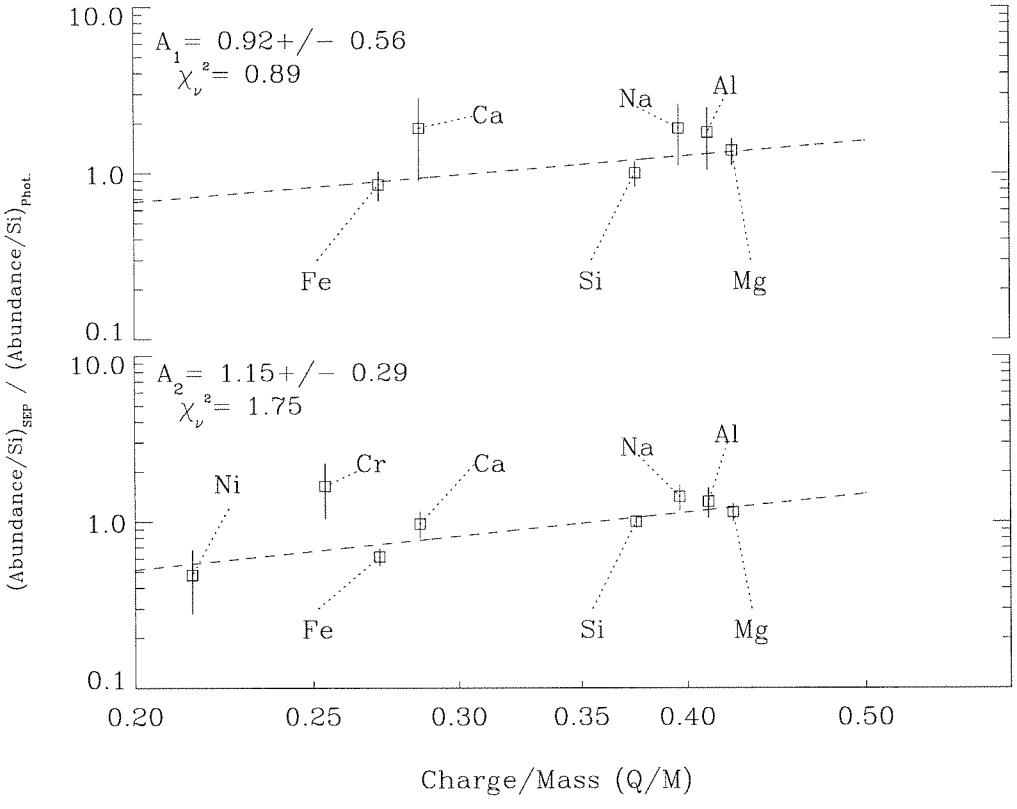

Figure 4.13: Comparison of element abundances in SEPs compared to that of the photosphere for low-FIP elements. The data is fit as a power law with respect to the element charge-to-mass ratio. A_1 and A_2 are the power-law indices of the fit.

factor is 3.00± 0.20 for the first SEP event, it is 5.82± 0.16, approximately a factor of two larger, for the second event. Yet both values are within the observed range reported by Garrard and Stone (1993), who found that the mean value of the depletion factor from their survey of 33 SEP events was 4.3, with a standard deviation equal to 2.1. Unfortunately, no one has looked to see whether there is a correlation between the Q/M fractionation index and the FIP depletion factor. Perhaps such work can be accomplished during the upcoming solar maximum.

The exact reason for the FIP depletion is not known. A model has been proposed (Geiss 1982; Geiss and Bochsler 1985; Marsch et al. 1995) in which initially neutral material from the photosphere is lifted into the upper chromosphere by magnetic buoyancy. The material is driven through the magnetic field by both a density gradient and by gravity. While this happens, the material is ionized by UV radiation. Since the thermal diffusion coefficients are greatly different for ions and neutrals, this ionization affects the transport of the material. Non-ionized material can leak out of the magnetic field structures, and thus the remaining material contains an overabundance of high-FIP material.

Early applications of this model found that the fractionation of elements divided into roughly three groups: those with low-FIP ($\lesssim$10 eV), those with high-FIP ($\gtrsim$10 eV), and those which are at intermediate values, such as C and S. The abundances of elements relative to photospheric abundances can be plotted as a function of FIP, and the data appears to be a step-function, with the low-FIP elements at the upper level, and the high-FIP elements at a common depletion of $\sim$0.25. However, the usefulness of FIP as an organizing parameter came into question when observations of Kr and Xe in lunar soils indicated that the abundances of these elements are higher than this simple two-plateau model predicts. Thus, it has been suggested that the first ionization time (FIT) of elements be used to organize the data (Geiss et al. 1984). When plotted as a function of FIT, low-FIP elements are located on a plateau, while elements with a FIT greater than 5 seconds are depleted as a power-law in FIT, with the power law index at about -0.5. Such a plot is shown in Figure 4.15. Note that in both the FIP and FIT plots carbon appears to be underabundant in the second SEP event.

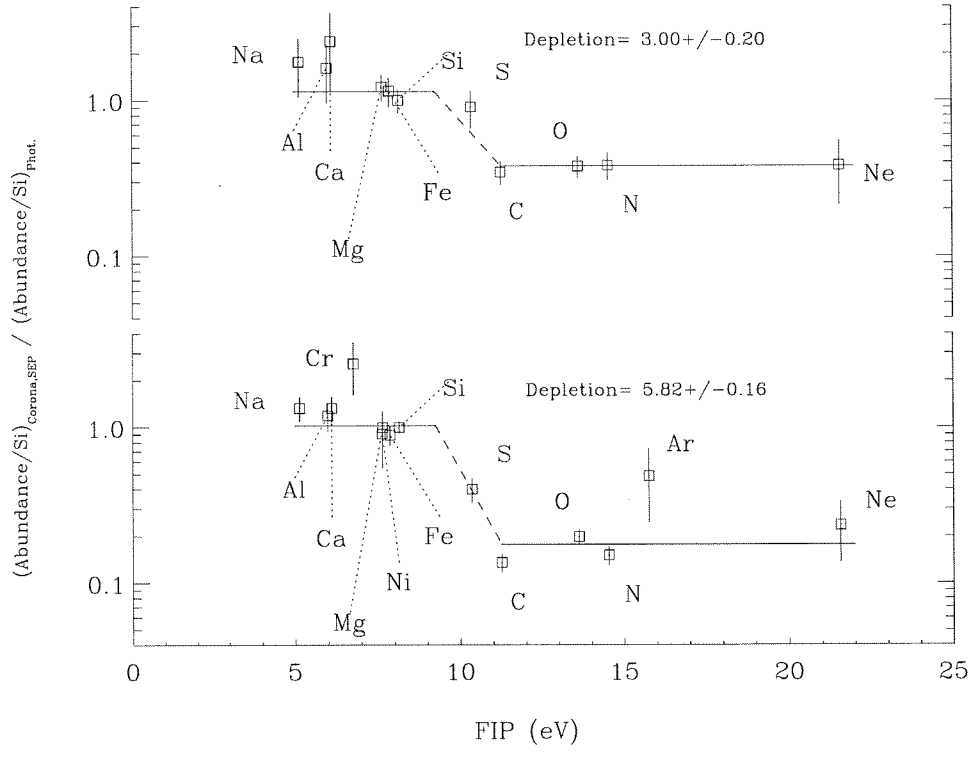

Figure 4.14: SEP-derived coronal composition for each of the SEP events is compared to the spectroscopic photospheric composition. This shows the depletion of elements with high first ionization potential (FIP).

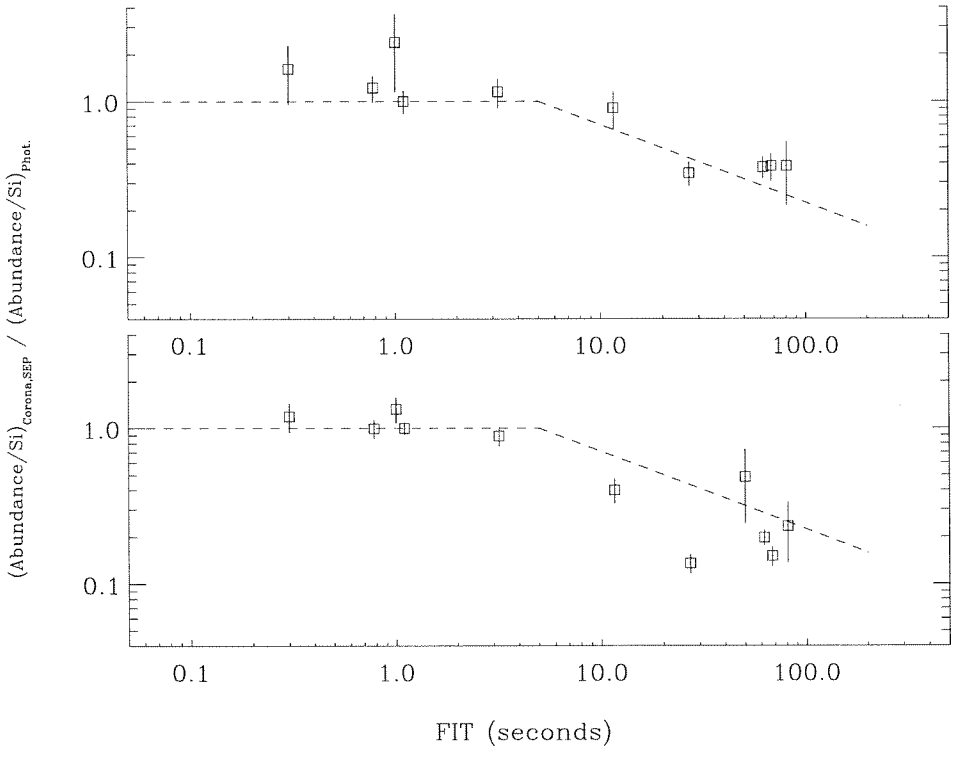

Figure 4.15: SEP-derived coronal composition for each of the SEP events, compared to the average SEP-based photospheric composition, as a function of the first ionization time (FIT). The dashed line is flat up to a FIT of 5 seconds, then decreases as a power law with index -0.5, as in von Steiger et al. (1987).

4.5 Chapter Summary

It appears that the elemental abundance variations proposed by Breneman and Stone (1985) apply to the two SEP events which MAST has observed. The parameters describing these variations, namely the Q/M power-law index, and the FIP depletion factor, all appear to fall within the values measured in other SEP events. Thus, the October and November 1992 events are rather typical gradual SEP events. Are the isotopic abundances in these events also "typical" abundances? We address this question in the next chapter.

Chapter 5

Isotope Analysis

In this chapter we discuss the steps needed to obtain isotopic abundance ratios and the final results of these measurements. First we discuss the techniques used to measure the ratios. Second we discuss how to obtain a set of the data which is of sufficient quality to make the isotopic measurements. We also discuss how this selection may bias the isotopic abundance ratios. Third, we discuss the biases in the isotopic abundance ratios which are due to the instrument design. Finally, we show how the measured isotopic abundance ratios can be used to deduce the isotopic composition of the coronal source material.

The elements for which isotopic composition can be measured in each of the two SEP events are carbon, nitrogen, oxygen, neon, magnesium, and silicon. Other elements do not have a sufficient number of particles for isotopic measurements to be made. These elements each contain one dominant isotope, with one or two less abundant isotopes at higher mass number. Based on the solar system abundances of Anders and Grevesse (1989), the most abundant non-dominant isotope in this group should be ^{26}Mg, which occurs as 11% of all magnesium. The rarest isotopic ratio which can be measured depends on the number of particles available and the mass resolution of MAST. This works out to be $^{18}O/^{16}O$, at an expected value of 0.2%.

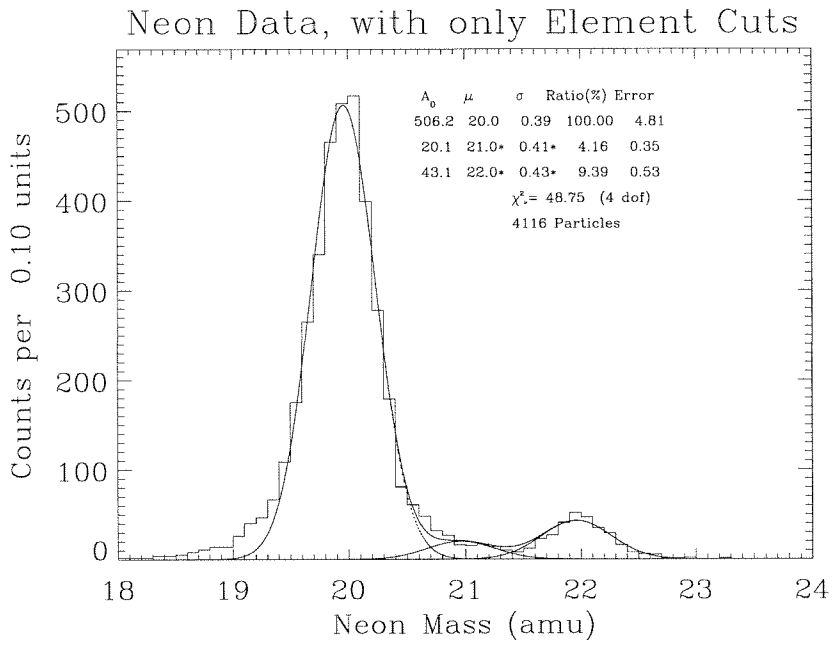

Figure 5.1: Neon data from both SEP events. The data is selected by trajectory, residual range, and $\chi^2_\nu < 10$, which are the criteria needed to resolve elements. The histogram is fit with Gaussian shapes, as described in the text.

5.1 Measuring Abundances

Two techniques for calculating isotopic ratios are discussed. The first one, multiple-Gaussian fits to a histogram, is easy to implement and easy to display. However, it is also subject to systematic errors caused by non-Gaussian tails on the distributions, and so tends to overestimate certain isotopic ratios. The second one, the maximum likelihood technique, is more computationally intensive, and it is less easy to display its results. However, it is mathematically correct, makes better use of the available data, and is less affected by non-Gaussian tails on the data.

5.1.1 Multiple Gaussian Fitting

To illustrate the multiple-Gaussian fitting technique, let us consider the distribution of the weighted average mass for neon particles, as shown in Figure 5.1. This

data has been selected using only the criteria necessary for identifying the element neon. As mentioned in Chapter 1, the isotopic abundance ratios for neon in the solar wind are 0.24± 0.03% for $^{21}Ne/^{20}Ne$, and 7.30± 0.16% for $^{22}Ne/^{20}Ne$. A look at the histogram finds that indeed the number of ^{22}Ne relative to ^{20}Ne is somewhere around 10%. However, any ^{21}Ne is buried beneath a tail from the ^{20}Ne. In a later section we discuss how to deal with these tails.

In this approach, the weighted average mass is binned into a histogram, as shown in Figure 5.1. It is assumed that the shape of the distribution of each isotope mass is described by a Gaussian of the form

$$P_G(m;\mu,\sigma) = A\exp\left[-\frac{1}{2}\left(\frac{m-\mu}{\sigma}\right)^2\right] \tag{5.1}$$

μ is the mean of the distribution, and σ is its standard deviation. For a properly normalized distribution, $A = \frac{1}{\sqrt{2\pi}\sigma}$.

Each isotope is described by such a distribution. If element Z has N_I isotopes and if the abundance of the i^{th} isotope is A_i, then the distribution of masses for that element is given by superposition of Gaussian functions.

$$P_{G,Z}(m;A_i,\mu_i,\sigma_i) = \sum_{i=1}^{N_I} A_i \exp\left[-\frac{1}{2}\left(\frac{m-\mu_i}{\sigma_i}\right)^2\right] \Big/ \sum_{i=1}^{N_I} A_i \tag{5.2}$$

where μ_i and σ_i are as described above. Not all of the parameters, A_i, σ_i, and μ_i, are free. The center of the dominant isotope (^{20}Ne for neon) is allowed to vary, yet the locations of the secondary isotopes are set to integer additions to this center value (for neon, $\mu_2 = \mu_1 + 1$, and $\mu_3 = \mu_1 + 2$). The width for the dominant isotope is allowed to vary, yet the widths for the secondary isotopes are scaled from that width. Since the mass resolution scales approximately with mass, the scale factor is simply the mass of the secondary peak divided by the mass of the dominant peak. The total area of the distribution is held fixed, yet the relative abundance of each isotope is allowed to vary. The abundances are calculated relative to the dominant isotope. In the case of neon, the ratios measured are then $^{21}Ne/^{20}Ne$ and $^{22}Ne/^{20}Ne$.

The histograms are then fit to a set of Gaussian functions using the Levenberg-Marquardt method (Press et al. 1995, chapter 15). This performs a gradient search of the parameter space, finding the parameters which yield the best chi-square. The uncertainties on the returned parameters are based on the covariance matrix from the fit.

Figure 5.1 shows the average neon masses fit with three Gaussians, one for each expected isotope. Though a peak is fit to ^{21}Ne, the data around mass 21 are mainly due to a tail on the ^{20}Ne and ^{22}Ne distributions. Since a large tail also exists at masses lower than 20, this suggests that the data is not clean enough to measure a true ^{21}Ne peak. Thus, although this fitting technique is easy to understand and to check visually, it can be fooled by non-Gaussian tails on the data.

5.1.2 Maximum Likelihood Fitting

Fitting the weighted average mass with a set of Gaussian functions does not make optimal use of the data. The shape of the distribution of each mass estimator is more complex than a Gaussian. Many processes which contribute to the mass resolution tend to lower the mass, and so even under conditions without multiple coincidences, the mass distribution will have a low-mass tail. And as discussed in Section 3.3.4, during a SEP event chance coincidences add a high-mass tail. Such tails can cause the fitting procedure to assign a higher abundance to an isotope which is separated by only one mass unit from the dominant peak, such as ^{21}Ne, in an attempt to fit that tail. The fitting routine we would like to use would contain more information about the true shape of the mass distribution. Such a distribution can be found in the data itself.

To construct this template distribution, we make use of the oxygen data. Of all the elements, oxygen is the one most dominated by a single isotope, ^{16}O. The abundance of ^{17}O is expected to be less than 0.04%. This means that out of the $\sim$35,000 oxygen particles, only 14 are expected to be ^{17}O. Analysis of the oxygen data shows that such a signal is buried by the tail from ^{16}O. This is actually a benefit, as it allows us to use the ^{16}O distribution to approximate the shape of a

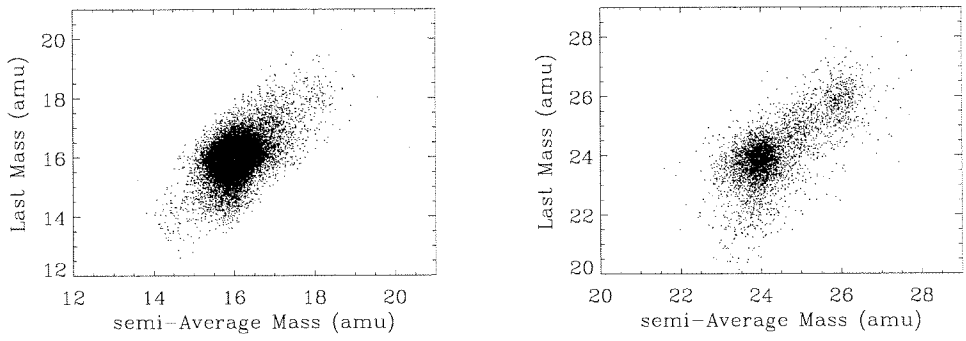

Figure 5.2: Two-dimensional distribution of mass measurements. The left plot is oxygen particles, and the right plot is magnesium particles. The x-variable is the weighted average of all the mass estimators except for the last ΔE-E' combination. The y-variable is the mass estimator from the last ΔE-E' combination. The data is selected to have $\chi^2_\nu < 2$.

single isotope. The ^{18}O is removed from this distribution by only using particles which have an average mass less than 17.5 amu.

Using only the weighted average mass has a further disadvantage in that it loses the information found in each of the individual mass estimators, and also does not allow for correlated effects between estimators. The shape of each mass estimator is unique, and it would be ideal to use the information contained in each one for fitting. However, the distributions must be made from the data itself, which limits our ability to characterize these distributions and joint distributions. Therefore, we make a probability distribution using two quantities. One is the mass estimator which uses the stopping detector as the E' measurement, and the last fully penetrated detector as the ΔE measurement. This is called the "last mass." This mass estimator is least affected by energy loss straggling, which is a major source of uncertainty in the mass measurements. Thus, the distribution of this mass estimator should have the smallest standard deviation. The other quantity is the weighted average of the remaining mass estimators, called the "semi-average mass." As an example, these two quantities are plotted for oxygen and magnesium in Figure 5.2.

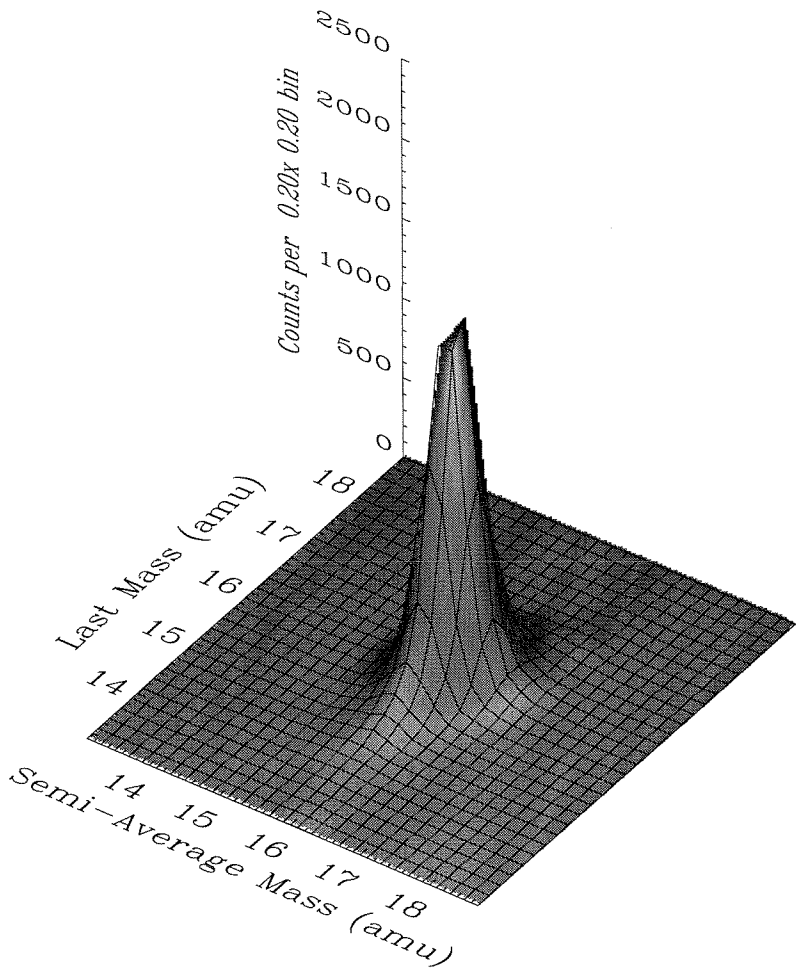

Figure 5.3: Map of oxygen events for the selection criteria $\chi^2_\nu < 2$, and ADCOR $< 50 \times 10^3$ counts/sec. The ^{18}O has been removed from the distribution by selecting the average mass to be less than 17.5 amu.

The Empirical Mass Distribution

A two-dimensional map of this mass distribution is shown in Figure 5.3. The x component of the map is the last mass, and the y component is the semi-average mass. The data is binned into 0.2 by 0.2 amu^2 cells, from 13 to 19 amu, making a map containing 30 rows and 30 columns, for a total of 900 cells. In order to remove ^{18}O from this reference distribution, the oxygen data is selected so that the

weighted average mass is less than 17.5 amu. In doing this, the ability to accurately measure the ^{17}O peak is lost, and so measurements of $^{17}O/^{16}O$ are only quoted as upper limits.

The map thus made is a template for the probability density function for the masses, where the probability density for an event to occur in cell (x, y) is the number of events in that bin, $n(x, y)$, divided by the total number of events which went into making the map, N_T. The distribution is smoothed using bilinear interpolation so that the probability is continuous across the map. For cells which have zero data in them, the probability is set to $\frac{1}{N_T}$.

This reference distribution is much like the Gaussian distribution discussed earlier, in that it describes the probability density for any given measurement of x and y for a single isotope peak. The distribution described above is centered at the coordinates $(x, y) = (16, 16)$. However, to use this distribution it is necessary to center it at the origin, $(x, y) = (0, 0)$. This distribution is the reference distribution needed, and can be designated P_R. Just as the Gaussian distribution can be translated into another one by adding an offset and a width, so too can this distribution be translated to another location by the coordinate transformation,

$$x' = \frac{x-\mu_x}{S_x}; \quad y' = \frac{y-\mu_y}{S_y}$$

The resulting distribution can then be re-normalized, which yields,

$$P_0(x, y; \mu_x, \mu_y, S_x, S_y) = \frac{1}{S_x S_y} P_R(\frac{x-\mu_x}{S_x}, \frac{y-\mu_y}{S_y}) \tag{5.3}$$

This normalized probability can be used to construct a new distribution which describes an element with a number of isotopes. Let us designate such a distribution as $P_{R,Z}$, where Z is the charge of the element. For example, if the isotopes ^{12}C and ^{13}C occurred with equal probability in carbon, and if the mass resolution of each isotope were half that of ^{16}O, then probability distribution for the measured mass of carbon would be given by

$$P_{R,6}(x, y) = \frac{1}{2}\left[P_0(x, y; 12, 12, 0.5, 0.5) + P_0(x, y; 13, 13, 0.5, 0.5)\right] \tag{5.4}$$

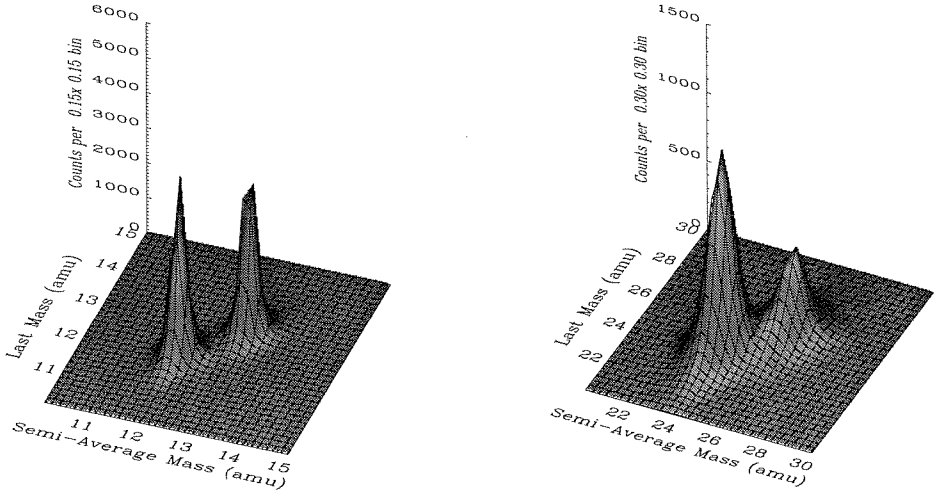

Figure 5.4: Synthetic probability distributions for carbon and magnesium, based on oxygen reference distribution. The distributions are actually smoother than they appear. The jagged appearance is due to the plotting routine used. Such distributions, when properly normalized, are used in the maximum likelihood technique.

As another example, if the mass resolution of magnesium were twice that of oxygen, and if ^{24}Mg and ^{26}Mg occurred at a ratio of 10:1, then the distribution of magnesium would be given by

$$P_{R,12}(x,y) = \frac{1}{10}\left[9 \times P_0(x,y;24,24,2,2) + P_0(x,y;26,26,2,2)\right] \tag{5.5}$$

The expected distributions of both the carbon and magnesium particles just described is shown in Figure 5.4.

Let us now simplify the notation a bit. Let ρ represent the measured value of x and y for a single particle. Let the vector $\vec{\alpha}$ designate both the translation parameters and the abundances for all isotopes of an element, and let A_j be the abundance of the j^{th} isotope. For an element with N_I isotopes, $\vec{\alpha}$ is given by

$$\vec{\alpha} = (A_1, \mu_{x1}, \mu_{y1}, S_{x1}, S_{y1}, ..., A_{N_I}, \mu_{xN_I}, \mu_{yN_I}, S_{xN_I}, S_{yN_I}) \tag{5.6}$$

The full probability distribution for such an element can then be given by

$$P_{R,Z}(\rho;\vec{\alpha}) = \frac{\sum_{j=1}^{N} A_j \times P_R(\rho, \mu_{xj}, \mu_{yj}, S_{xj}, S_{yj})}{\sum A_j} \tag{5.7}$$

This is the probability density for the mass measurements x and y. The proper formulation of this quantity is essential for the maximum likelihood technique.

Maximum Likelihood Technique

We have now constructed a quantity which gives the probability density for any measurement $\rho = (x, y)$. If the measurement is made in a small bin $\Delta x \Delta y$, the probability that any particular value of ρ will be measured in an experiment is given by

$$\text{Probability to measure } \rho = P_{R,Z}(\rho;\vec{\alpha})\Delta x \Delta y \tag{5.8}$$

Given a set of N measurements, ρ_1, ρ_2,...ρ_N, we can ask what is the joint probability of observing that set of measurements. This joint probability is the *likelihood* of observing the set of measurements $\vec{\rho} = (\rho_1, ...\rho_N)$, given the probability distribution $P_{R,Z}(\rho;\vec{\alpha})$. It is given by

$$\mathcal{L}(\vec{\rho}|P_{R,Z}(\vec{\rho};\vec{\alpha})) = P_{R,Z}(\rho_1;\vec{\alpha})\Delta x \Delta y \times \cdots \times P_{R,Z}(\rho_N;\vec{\alpha})\Delta x \Delta y \tag{5.9}$$

$$= (\Delta x \Delta y)^N \prod_i^N P_{R,Z}(\rho_i;\vec{\alpha}) \tag{5.10}$$

The essence of the maximum likelihood technique is that we want to find the set of parameters, $\vec{\alpha}$, which yield the maximum value of $\mathcal{L}$, given the set of measurements, $\vec{\rho}$. Note that this technique requires that we assume a form of the probability distribution. For example, we could use a Gaussian distribution, or the empirical probability derived above, or even a uniform distribution. The proper form of the distribution must be chosen using the best knowledge available, since the maximum

likelihood technique will simply find the best parameters for that assumed distribution. Since we believe that the empirical distribution describes the distribution of mass measurements for an isotope, we use it. The parameters of the distribution are free variables, and we thus seek to find the set of $\vec{\alpha}$ which maximize the likelihood.

The probability of observing any single particle in a given (x, y) is quite small; typical values are less than 10%[1]. The likelihood is an even smaller number, on the order of 10^{-N}, where N is the number of particles in the likelihood calculation. The number of particles of a particular element ranges from several hundred to several thousand, and so the likelihood is an extremely small number. Since such numbers are impractical to compute, we instead take the log of the likelihood, since this quantity involves addition of numbers of order ten, rather then multiplication of numbers less than one. In practice, we actually multiply the log of the likelihood by a factor of -2, and minimize this with respect to $\vec{\alpha}$.

$$\chi^2 = -2\ln(\mathcal{L}) \tag{5.11}$$

The reason we use this particular expression is that this quantity is equal to the chi-square under certain conditions (Cash 1979; Baker and Cousins 1984; Hoel 1965). The chi-square is then minimized with respect to the parameters $\vec{\alpha}$, as described below. This χ^2 can be thought of as a function of $\vec{\alpha}$, given a fixed reference distribution, $P_{R,Z}$, and a set of measurements $\vec{\rho}$.

Note that if all of the measurements are considered of equal weight, then each of the $\Delta x \Delta y$ are then equal. This term is thus constant, and does not affect the minimization of χ^2.

Parameter Search

The reference distribution is derived from a smoothed distribution of the data, and so unlike the Gaussian distribution, it is not analytic. The gradient-based

[1] In a typical empirical map, there are approximately 10,000 oxygen particles. The highest number of particles in a cell is approximately 1000 particles. Thus, the maximum probability in a cell is 10%.

methods used in fitting multiple Gaussians thus do not apply. Instead the parameters are found through an "amoeba" search which uses the downhill simplex method with simulated annealing, as discussed in chapter 10 of *Numerical Recipes* (Press et al. 1995).

As in the Gaussian fits, there are constraints on certain parameters. The centers of the dominant isotope peak, μ_{x1} and μ_{y1}, are free to vary, but the centers of each non-dominant isotope are integral additions to the centers of the dominant isotope. This is necessary since the fitting routine is otherwise likely to place all of the non-dominant peaks on top of the dominant peak. The scale factors of the dominant isotope, S_{x1} and S_{y1}, are free to vary, and the scale factors of the non-dominant isotopes are scaled according to the formula $S_{xi} = \frac{\mu_{xi}}{\mu_{x1}} S_{x1}$, and likewise for the y scale factor. Since the scale factors are proportional to the standard deviations from a Gaussian distribution, this simply means that we assume the mass resolution scales with mass, just as in the Gaussian fits. The isotope abundances are free to vary, except for the abundance of the dominant isotope, A_1, which is set equal to one. Thus, for an element with N_I isotopes, the number of free parameters is $N_I - 1$ from the abundances, plus 2 for the centers, and 2 for the scale factors, for a total of $N_I + 3$ free parameters, and hence $N_I + 3$ degrees of freedom.

The downhill simplex technique seeks to minimize a quantity, in this case, χ^2, with respect to a set of M parameters, $\vec{\alpha} = (\alpha_1, ..., \alpha_M)$, where the components of $\vec{\alpha}$ are the same as described above, and so $M = N_I + 3$. If the number of parameters in $\vec{\alpha}$ is M, then the search is in M+1 dimensions. An initial guess for $\vec{\alpha}$ is found by making Gaussian fits to x and to y separately, which yields a good guess for the values of $\vec{\alpha}$. From this initial $\vec{\alpha}$, a set of M+1 other $\vec{\alpha}$ are created. Each of these $\vec{\alpha}$ has one if its parameters, α, varied by a small amount.

This set of M+1 new $\vec{\alpha}$ can be thought of as a geometric shape in M+2 dimensions, where the last dimension is χ^2, which can be thought of as the "height." χ^2 is calculated for each of the $\vec{\alpha}$ thus made. The corner of the simplex which has the highest value of χ^2 is identified, and the simplex is made to wander away from that point through a set of geometric transformations. These transformations allow the simplex to grow larger when it is far from a minimum, and to shrink when it is near

a minimum. In this manner, the simplex is made to wander in a "downhill" direction toward the minimum value of χ^2, and "fall into" the minimum it finds. The search is terminated when fractional differences between the χ^2 for each vertex is less than 10^{-7}. In practice, this technique completes in about 150 iterations.

With the addition of simulated annealing, a random number, $T \log u$, is added to χ^2 with each evaluation of the simplex. u is a uniform random number on the interval $(0, 1)$, and T is the "temperature." When T is on the order of χ^2, the simplex undergoes a random walk, and as the temperature is slowly lowered, the simplex is allowed to settle down to find the minimum. This approach enables the search to avoid local minima which might otherwise trap the amoeba. Let the set of parameters found by the amoeba search be designated by $\vec{\alpha}_0$. This set of parameters maximizes the likelihood, and the values of A_i thus obtained are the isotopic abundances relative to the dominant isotope.

The amoeba-based solution finds the best set of parameters, but since it does not use analytic expressions for the gradients of the likelihood, it does not yield a measure of the uncertainties in those parameters. To find the uncertainties the likelihood ratio test (Hoel 1965) is used.

In this approach, one of the parameters (α_i) is varied by an amount ϵ_i and the ratio of that likelihood to the optimal likelihood, $\mathcal{L}(\vec{\alpha}_0)$, is studied as a function of ϵ_i. The likelihood ratio obtained by varying the i^{th} parameter by an amount ϵ_i is thus

$$\lambda_i(\epsilon_i) = \frac{\mathcal{L}(\alpha_1, ...\alpha_i + \epsilon_i, ...\alpha_M)}{\mathcal{L}(\vec{\alpha}_0)} \tag{5.12}$$

Examples of the likelihood ratios are shown in Figure 5.5. These are fits to the isotopic abundances for carbon and neon in each of the SEP events. Note that the fitting is done four times for these plots, once for each element, and once for each SEP event. The optimal, or most likely, values for the isotope ratios occur at the peak of the distribution, where the likelihood ratio is equal to one. This is marked by the vertical solid line in each plot. The 1-sigma confidence intervals are shown by the vertical dashed lines on either side of the most likely value. There is a 68.3% chance

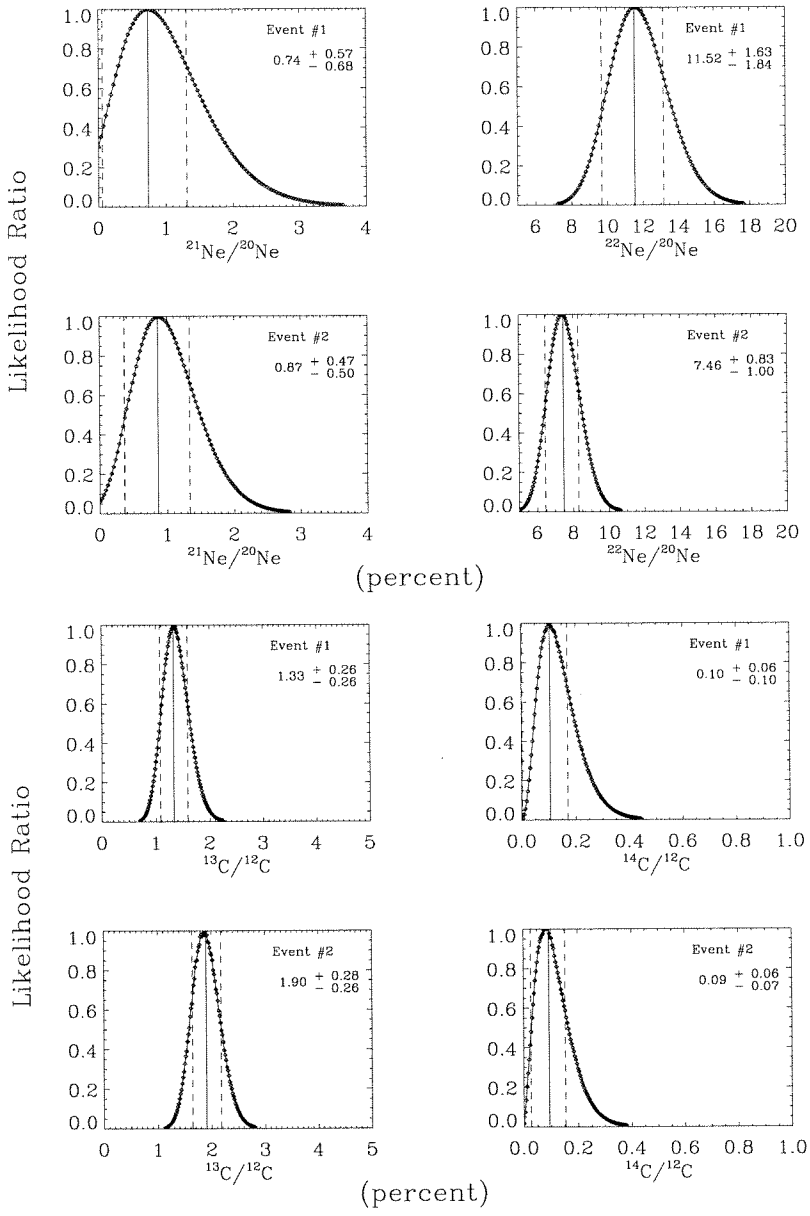

Figure 5.5: The confidence limits on the isotopic abundance ratios are found by examining the likelihood ratio as a function of isotopic abundance ratio. The upper four plots show this for the isotopes of neon, and the lower four plots show this for the isotopes of carbon. Both are from data selected with ADCOR$< 20 \times 10^3$ counts per second, as discussed later in the text. The vertical solid line is the optimal value of the ratio. The vertical dashed lines mark the intervals containing 68.3% of the area under each curve.

that the true values of the ratio lies within these confidence intervals. The confidence intervals are calculated such that half of the 68.3% lies between the lower limit and the optimal value, and the other half lies between the optimal value and the upper limit. This makes for asymmetric uncertainties for isotopes which are not clearly resolved. Similar asymmetric uncertainties are observed when applying Poisson statistics to the measurement of small numbers (Selesnick 1996; Gehrels 1986). Sometimes the lower limit is consistent with zero, as for the $^{14}C/^{12}C$ ratio for the first SEP event, as shown in the figure. In such cases, 84% of the area lies below the upper limit.

A full set of oxygen isotopic ratio measurements was also made using a two-dimensional Gaussian distribution as the template. The results were consistent with the measurements using the empirical probability distribution.

Now that the two methods for measuring isotopic ratios have been explained, let us now explore how to select a data set for measuring these ratios.

5.2 Invariant Latitude Selection

In Section 4.3.1 it was explained why only particles found above 65° invariant latitude were used to calculate elemental abundances and spectra. This selection was made to ensure that the elemental abundances and spectra were not affected by magnetospheric filtering. This approach works well for elements, since there is a large number of particles available. Isotopic analysis, however, is primarily limited by statistics, so requires use of as much data as possible. The lowest isotope ratio to be measured is $^{18}O/^{16}O$, which has a terrestrial value of 0.2%. In order to expect to see a single ^{18}O, we need approximately 500 ^{16}O. A look at the distribution of oxygen nuclei as a function of invariant latitude, shown in Figure 5.6, shows that a significant fraction of these particles occur below 65°. In fact, there is a second population of oxygen nuclei, the *trapped anomalous cosmic rays* (TACR), which are trapped in the magnetosphere, and occur at latitudes lower than 52° (Cummings et al. 1993). Thus, in order to maximize the amount of data for isotope analysis and to protect against contamination from TACR, we need to select particles above 52° invariant latitude. The number of particles of each species for three regions of

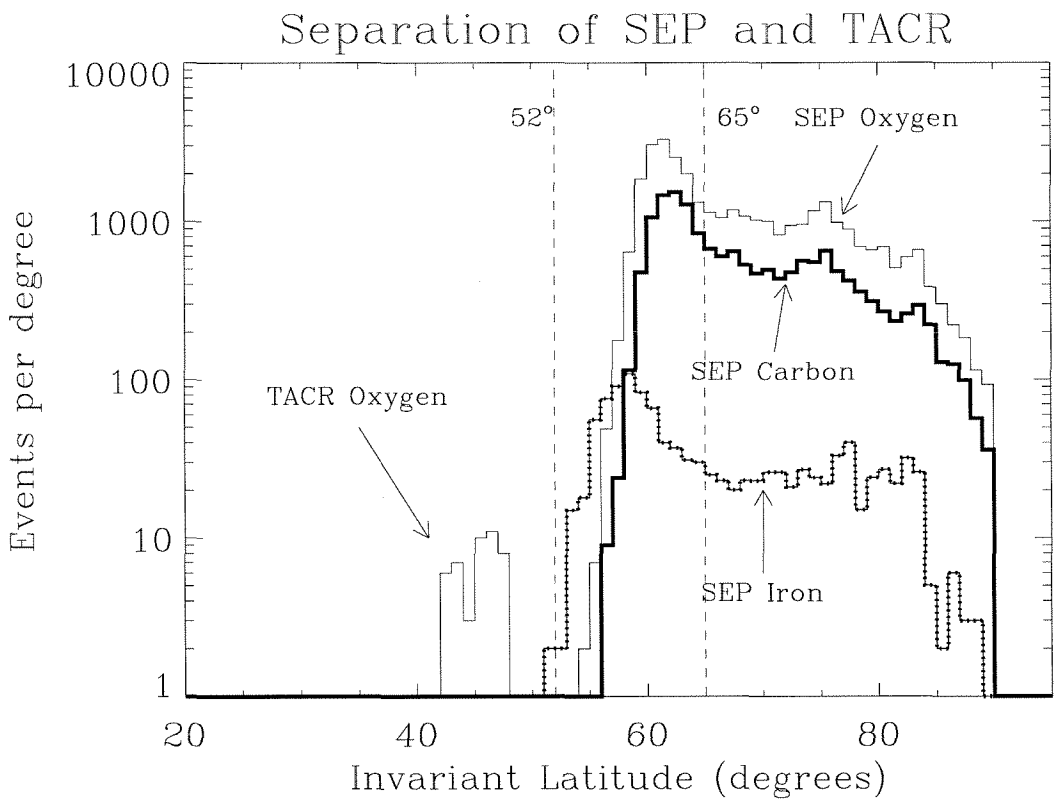

Figure 5.6: Separation of trapped anomalous cosmic rays (TACR) and solar energetic particles (SEP) is made by only accepting particles above 52°. Note that the y-axis is logarithmic, and that approximately half of the SEP oxygen particles are found between 52 and 65°.

TABLE 5.1

This table lists the number of particles of each element which occur in each of the three regions defined by invariant latitude, Λ. Limiting the data to particles which occur above 65° invariant latitude reduces the data set by ~45%. These particles are observed between day 304.75 and day 312 of 1992.

	Total	$\Lambda \geq 65°$		$52° < \Lambda < 65°$		$\Lambda \leq 52°$	
Elem.	$\chi^2_\nu < 10$	Number	Percent	Number	Percent	Number	Percent
C	16587	9669	58.3	6917	41.7	1	0.0
N	4253	2387	56.1	1852	43.6	14	0.3
O	34603	19288	55.7	15259	44.1	56	0.2
Ne	4124	2313	56.1	1811	43.9	0	0.0
Na	323	164	50.8	159	49.2	0	0.0
Mg	4759	2633	55.3	2126	44.7	0	0.0
Al	355	187	52.7	168	47.3	0	0.0
Si	3423	1788	52.2	1635	47.8	0	0.0
P	26	14	53.9	12	46.2	0	0.0
S	577	264	45.8	313	54.3	0	0.0
Ar	43	24	55.8	19	44.2	0	0.0
Ca	150	63	42.0	87	58.0	0	0.0
Cr	40	23	57.5	17	42.5	0	0.0
Fe	1188	522	43.9	662	55.7	4	0.3
Ni	58	20	34.5	38	65.5	0	0.0

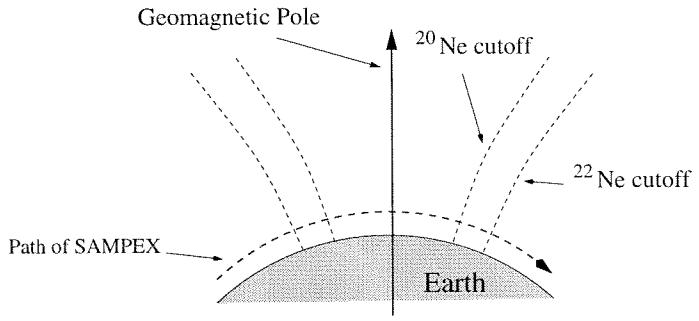

Figure 5.7: Given two particles which have the same energy per nucleon, the heavier particle will have a lower cutoff latitude. SAMPEX will be able to observe that particle for longer periods than it can the lighter particle. This leads to the geomagnetic bias of elements and isotopes (Not to scale).

invariant latitude is shown in Table 5.1. This reveals that roughly half of all particles are found at latitudes between 52° and 65°.

It is assumed that two isotopes of the same element have the same mean charge state at the same energy per nucleon. Their mean rigidities then differ by the ratio of their masses. This means that at the same velocity, heavier isotopes will have a lower cutoff latitude, λ_H, than the lighter isotope with cutoff λ_L, and will thus penetrate to lower L-shells. The spacecraft will spend more time in regions accessible to the heavier ion than the lighter one, as is illustrated in Figure 5.7. This introduces a bias to the measured isotopic ratio. The result is that the measured ratio of heavy to light isotopes will be higher than if the spacecraft were outside of the magnetosphere. This effect is called the *geomagnetic bias.*

A rough calculation reveals the size of the geomagnetic bias. An approximate difference between the cutoff latitude of two isotopes such as ^{12}C and ^{13}C is about 0.7 degrees, according to Equation 4.9. If the orbit were polar and circular, and if the cutoff latitude for ^{12}C were 60 degrees, then the heavy isotope would be favored by 0.7 out of 30 degrees, or 2.3% of the time. This is a lower limit to the effect, since the spacecraft rarely reaches 90° invariant latitude. However, these calculations assume that the livetime of the instrument is equal over all parts of its orbit. This is not the case, as discussed in Section 5.4.2.

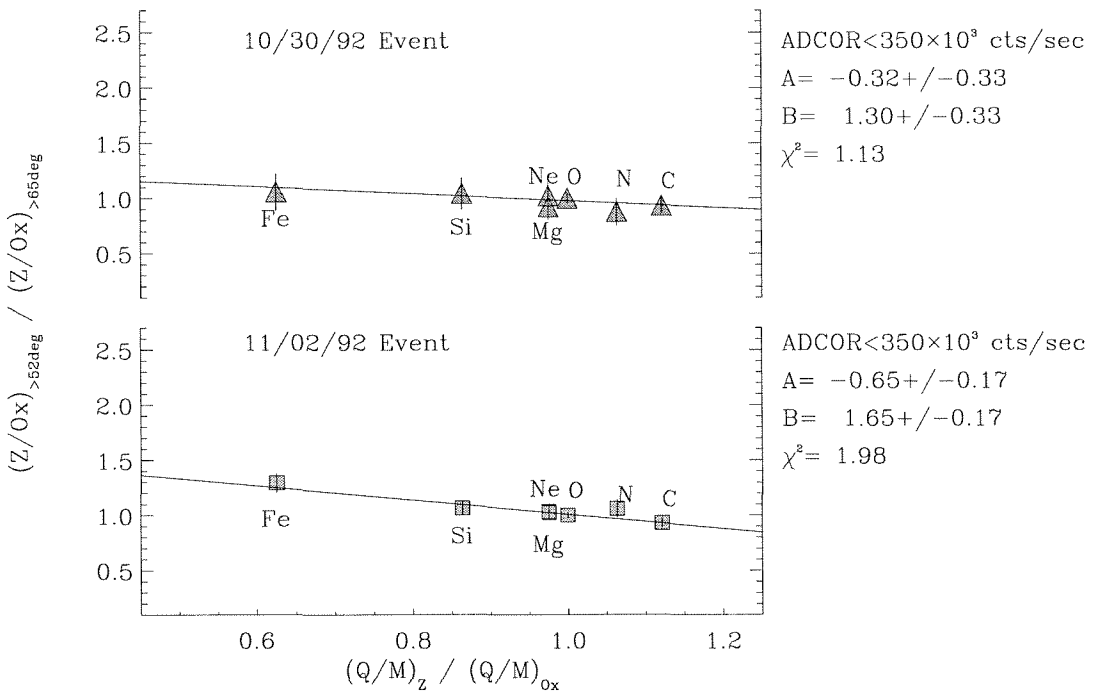

Figure 5.8: Geomagnetic bias of the elements in the energy interval from 30 to 60 MeV/nucleon. The charge state of each element, Q, was measured by Leske et al. (1995). The mass used is the average mass from Cameron (1982). The data are fit with a linear function, so that the fractionation, f, can be written as $f = A \times r + B$, where r is the Q/M value of the element over the Q/M value of oxygen.

TABLE 5.2

Geomagnetic bias observed in $^{22}Ne/^{20}Ne$ ratio. The bias factor is ratio of the isotopic ratio calculated using particles above 52° divided by the isotopic ratio calculated using particles above 65°. This should be the same as the bias found comparing elemental abundances greater than 52° to those above 65°. The biases are consistent, though the bias factors found using isotopic ratios have much larger uncertainties.

	$^{22}Ne/^{20}Ne$ Ratio (percent)			Measured
	$52° < \lambda \leq 65°$	$\lambda > 65°$	Ratio	Bias Factor
Event #1	10.69 ± 1.43	8.92 ± 1.47	1.20 ± 0.25	1.11 ± 0.24
Event #2	9.42 ± 1.08	7.79 ± 0.78	1.21 ± 0.10	1.08 ± 0.16

The geomagnetic bias can be measured more precisely by using the elemental abundances. Particles which are found above 65 degrees are not affected by magnetospheric effects. The relative composition of these particles in a common energy interval can be used as a baseline to observe how the composition is altered by the geomagnetic field at lower invariant latitudes. As when calculating the elemental abundances, we observe the composition in the 30-60 MeV/nucleon energy interval. The abundance of each element with respect to oxygen as measured above 65° is compared to the same abundance ratio for particles measured above 52°. The two relative abundances then form a double ratio. Since the magnetosphere acts on the rigidity of the particles, its effects are expected to be observed as a function of the elemental charge-to-mass ratio.

The double ratios are plotted as a function of Q/M in Figure 5.8. As expected, elements with lower charge-to-mass ratio than oxygen are enhanced at lower latitudes, while elements with higher charge-to-mass ratios are relatively depleted. This bias can be fit by a line. The resulting linear fit can be used to calculate the expected bias between any other two nuclei with different charge-to-mass ratios. For example, the geomagnetic bias expected for the ratio $^{22}Ne/^{20}Ne$ is 1.04 ± 0.02 for the first event, and 1.06 ± 0.02% for the second event.

We can also use the observed isotopic ratios to find the geomagnetic bias of $^{22}Ne/^{20}Ne$ empirically. In Table 5.2 we show the neon isotopic ratios in each SEP event. The first measurement is of particles which are observed between 52° and 65° invariant latitude, and the second is of particles observed above 65° invariant latitude. The first ratio is larger than the second for both SEP events, in agreement with the expectation that the heavier isotopes have more access to lower invariant latitudes. The bias factors are 1.11± 0.24 for the first SEP events, and 1.08± 0.16 for the second. These numbers are consistent with the biases calculated in the previous paragraph, but their uncertainties are extremely large. Thus, the elemental biases are the most reliable way to calculate the biases to the isotopes.

5.3 Instrument Biases

The isotopic abundance ratios measured using the maximum likelihood technique are the best fits to the particle data, which have been corrected for biases introduced by the selection of the data. However, the instrument itself can bias the measurements in two ways. First, the SEP particles may interact with the instrument windows or detector material and fragment into secondary nuclei. The instrument may not be able to discriminate between these secondaries and unfragmented particles. Second, the range of energies which the instrument measures is slightly different for isotopes of the same element. Since the flux of particles changes with energy, this introduces a bias also. In this section we discuss these biases and how we correct for them.

5.3.1 Nuclear Interaction Contamination

The energetic nuclei which MAST can measure have ~15-250 MeV/nucleon of kinetic energy. At these energies, solar energetic nuclei can overcome the coulomb barrier and interact with other nuclei in the telescope material. These interactions can break up the nuclei and produce secondary particles. For example, a ^{18}O nucleus colliding with hydrogen can undergo a (p, α) reaction to form a ^{15}N nucleus. Since

the SEP isotopes being measured are rather rare, it is important to investigate the production of such secondary nuclei. If secondary nuclei are produced in sufficient quantities, the isotope abundances measurements cannot be attributed solely to SEPs. In order to estimate the contribution from these secondaries, the cross sections for the production of secondary nuclei by collisions of solar energetic particles with possible "target" material are used. In the following discussion, we make a conservative estimate for the contribution by secondaries.

Because of the great interest in the propagation of galactic cosmic rays through the interstellar medium, the cross sections for production of secondary nuclei in nucleus-proton collisions have been studied for many years. The total cross sections have been fairly well measured above ~50 MeV/nucleon (Kox et al. 1987), while the partial cross sections for the production of specific secondary nuclei have in general only been well measured above ~300 MeV/nucleon (Webber et al. 1990, and references therein). Tsao and Silberberg and their collaborators (Silberberg and Tsao, 1973a,b; Sihver et al. 1993) have developed algorithms for calculating these cross sections and have implemented them into a computer program which has been released for public use. The code is improved as experiments add new data. The latest version, called `YIELDX_071397.FOR`, was released in July, 1997. It can be obtained from the LSU Cross Section Database, at `http://spdsch.phys.lsu.edu/SPDSCH_Pages/`. Sample results from this program are given in Figure 5.9.

These cross sections are used in the following analysis. Although the cross sections depend on energy, they will be treated as constant in order to simplify the calculation. The cross sections which are used are equal to the maximum value of each cross section in the 15-250 MeV/nucleon energy range.

The `YIELDX` program provides nucleus-proton cross sections. However, nucleus-nucleus cross sections are needed for the calculations. The nucleus-nucleus cross sections are obtained by scaling the nucleus-proton cross sections. The scale factor is based on an expression for the total cross section of two nuclei, n and n', given by Sihver et al. (1993),

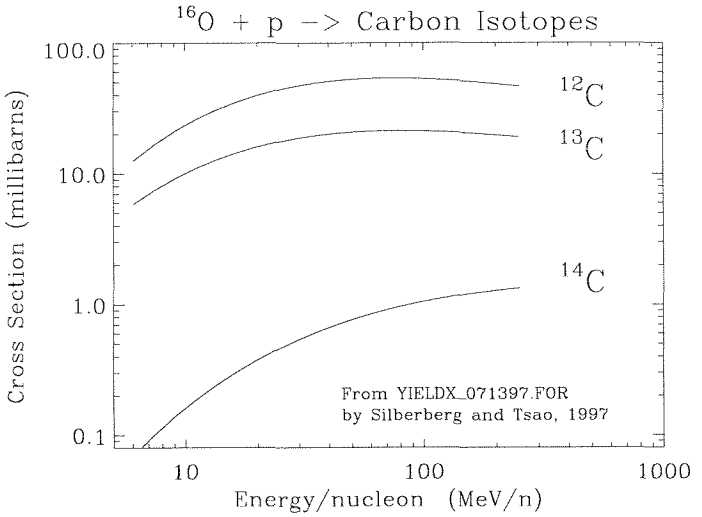

Figure 5.9: Partial cross sections for production of carbon isotopes by the collision of ^{16}O on target protons. Calculated by program YIELDX_071397.FOR, as described in the text.

$$\sigma_{nn'} = \pi r_0^2 (A_n^{1/3} + A_{n'}^{1/3} - b_0)^2 \tag{5.13}$$

where the radius of a nucleus of mass A is given by $r_A = r_0 A^{1/3}$. The overlap parameter, b_0, is given by

$$b_0 = 1.581 - 0.876[A_n^{-1/3} + A_{n'}^{-1/3}]$$

This expression is simply the total area of the two nuclei minus an overlap parameter. The nucleus-proton cross section can be expressed in a similar fashion, with $A_{n'} = 1$, and

$$b_p = 2.247 - 0.915[A_n^{-1/3} + 1] \tag{5.14}$$

These expressions can be used to calculate the relative scaling between the nucleus-proton cross section, σ_{np}, and the nucleus-nucleus cross section, $\sigma_{nn'}$, as follows:

$$\sigma_{nn'} = \frac{(A_n^{1/3} + A_{n'}^{1/3} - b_0)^2}{(A_n^{1/3} + 1 - b_p)^2}\sigma_{np} = S(A_n, A_{n'})\sigma_{np} \tag{5.15}$$

The cross section for the production of a particular secondary nucleus is used to calculate the number of primary nuclei which could have fragmented into it. The probability that a particle has interacted after traveling a distance x centimeters through a material with cross section σ is

$$p = 1 - \exp\left(-x\frac{\rho N_A}{M_T}\sigma\right) \tag{5.16}$$

where ρ is the target density in grams per cubic centimeter, N_A is Avogadro's number in atoms per mole, and M_T is the atomic weight of the target in grams per mole. The cross section is measured in square centimeters per atom, and x is in centimeters. This probability is calculated for each primary nucleus. The number of these secondary nuclei produced by these primary nuclei is then the number of primary nuclei times this probability. The "secondary fraction" is the number of secondary nuclei produced relative to the number of dominant isotopes that are present.

There are three kinds of material which are possible targets for the production of secondary nuclei: 1) coronal and interplanetary material, 2) the instrument windows, and 3) the detector material itself.

The amount of coronal and interplanetary material which the SEPs have passed through is constrained by measurements of the SEP charge states (Leske et al. 1995). These measurements reveal that the observed Fe nuclei could not have passed through more than 600 μg cm^{-2} of material, or else more electrons would have been stripped from the ions. Secondary particles produced in this manner cannot be distinguished from primary SEPs.

A second source of nuclear contamination is the inner and outer windows which shield MAST from sunlight. They are composed of Kapton® ($C_5H_4O_2$), which has a density of 1.42 grams per cubic centimeter. The outer window is 1 mil thick, and the inner window is 3 mil thick, for a total thickness of 101.6 μm or a mass

thickness of 1.44×10^{-2} g cm^{-2}. Particles which interact in the window may or may not be identified as valid particles. If the secondary is accompanied by another nuclear fragment it will likely be rejected from the data, since the pattern of energy deposits will be inconsistent with a single particle.

Nuclei can also interact in the detector material itself. The detector material is primarily silicon, at a density of 2.33 gcm^{-3}. As with production in the windows, secondaries produced in the detector material can be rejected if they are accompanied by another secondary particle, or if they are scattered out of the telescope. Furthermore, if the charge of the projectile changes in one detector, the energy deposited in the further detectors will be characteristic of the new charge. In such an interaction there is also likely to be additional energy loss due to the recoiling target ion. Such events will have a poor chi-square and will likely be removed from the analysis. (For an illustration of this, Looper et al. (1996) demonstrate how isotopes produced in the PET telescope can be identified by the inconsistent energy deposits).

The estimated contamination levels are found as follows. Secondary nuclei which are relatively rare in the SEPs, and which could be contaminated, are identified. For example, the abundances of ^{13}C, ^{15}N, and ^{18}O with respect to their dominant isotopes are expected to be few percent or less, and there are large numbers of heavier nuclei which could fragment into those isotopes. Nuclei which could serve as primaries, and which have a non-negligible cross section for producing these secondaries are identified. For example, both ^{16}O and ^{18}O can fragment into ^{13}C, with maximum cross sections equal to 21.3 and 24.1 millibarns, respectively. However, the abundance of ^{18}O is much less than that of ^{16}O. Since both reactions produce ^{13}C, the oxygen may as well be treated as pure ^{16}O in the calculations.

The number of primary nuclei is based on the number of particles which are used in isotope analysis, as given in Table 4.2. For example, there are ~17,000 carbon nuclei, and ~36,000 oxygen nuclei. The number of ^{13}C which could be produced by the oxygen is calculated, assuming it is all ^{16}O. The production of ^{13}C due to Ne, Mg, Si, and Fe is also calculated, assuming that the elements are all composed of their dominant isotopes (the cross sections for the neutron-rich isotopes of these nuclei are not significantly higher than those of the dominant isotopes). The "secondary

TABLE 5.3

Upper limits to the number of secondary heavy isotopes relative to the number of primary particles, for three possible target materials which could produce secondary particles. The fraction is cumulative over each target.

Target material from SEP source through...	Secondary Fraction $^{13}C/^{12}C$	$^{15}N/^{14}N$	$^{18}O/^{16}O$
...corona/IP material only	1.9×10^{-5}	1.5×10^{-4}	3.5×10^{-7}
...MAST Window	2.5×10^{-5}	2.6×10^{-4}	6.0×10^{-7}
...M4 detector	4.5×10^{-4}	3.5×10^{-3}	8.4×10^{-6}

fraction" is then the number of secondary nuclei produced relative to the total number of primary nuclei.

In Table 5.3 the estimated amount of secondary contamination is listed for the ratios $^{13}C/^{12}C$, $^{15}N/^{14}N$, and $^{18}O/^{16}O$. In the first row the ratio of contamination is calculated for particles which have passed through the coronal and interplanetary material. If there were no secondary production in the instrument, and if the SEPs did pass through all of the 600μg cm^{-1} upper limit imposed by the Fe charge states, then this would be the contamination level. Next the level of contamination is shown for particles which have passed through the coronal/interplanetary material and then through the Kapton® windows of the instrument. Finally the level of contamination is shown for particles which have also passed through the M1 through M4 detectors. Note that this last number is an upper limit which assumes that all of the secondary particles will be measured by the instrument. In reality, most of these events will be rejected as discussed above.

As Table 5.3 shows, even with conservative estimates for the nuclear cross sections, the level of contamination of SEP ratios due to nuclear interactions is well below the isotopic abundance ratios being measured for $^{13}C/^{12}C$ and $^{18}O/^{16}O$. The upper limit to the level of contamination for ^{15}N, however, is comparable to the ratio being measured. This is one reason why the measured $^{15}N/^{14}N$ ratio will only be

considered as an upper limit.

The relative abundances of ^{21}Ne, ^{22}Ne, ^{25}Mg, ^{26}Mg, ^{29}Si, and ^{30}Si are expected to be from 3 to 15%, and so these isotopic abundances will be affected by secondaries even less than the ones in Table 5.3. There are also relatively fewer primary nuclei present which can produce these isotopes, as compared to ^{13}C and ^{15}N, which have oxygen as primaries. Thus, nuclear interaction contribution to any of the measured isotopic ratios is not significant.

5.3.2 Range Bias

The range of energies to which a detector is sensitive depends on the isotopic species under consideration. A particle must penetrate an amount of material before reaching a given detector, and since the range of a particle for a given energy per nucleon, $\mathcal{E}$, scales with mass, heavier particles can reach a given detector with a lower value of $\mathcal{E}$ than lighter ones. Likewise, heavier particles penetrate to the next detector with lower values of $\mathcal{E}$, and so the total energy per nucleon interval which a detector samples is lower for a heavier isotope than for a lighter one. If the spectrum of particles is falling with increasing $\mathcal{E}$, then the observed ratio of heavy to light isotopes will be higher than would be expected if we sampled across an equal interval of $\mathcal{E}$. This is illustrated in Figure 5.10.

The number of particles which the instrument measures over a given time, Δt, is a convolution of the differential energy spectrum of the particles and the instrument geometry factor over the energy interval and response angles of the telescope. This can be written:

$$N = \Delta t \int_{\mathcal{E}_i}^{\mathcal{E}_f} G_Z(\mathcal{E})\, J_Z d\mathcal{E} \tag{5.17}$$

When considering the range bias of isotopes, the geometry factor is taken to be constant over the energy interval concerned. This reduces the response function to:

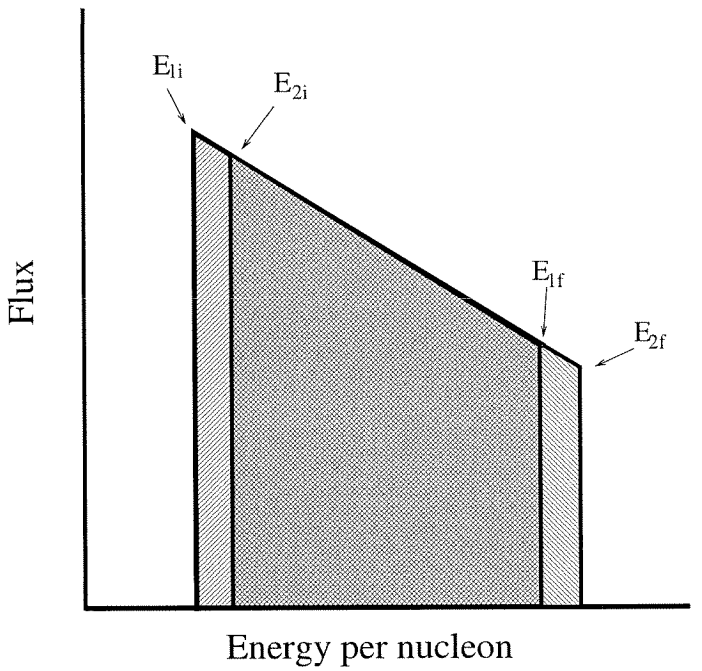

Figure 5.10: Range bias of two isotopes. The heavier isotope is measured in the energy interval $\mathcal{E}_{1i}$ through $\mathcal{E}_{1f}$, and the lighter isotope is measured from $\mathcal{E}_{2i}$ through $\mathcal{E}_{2f}$. In this illustration both isotopes are equally abundant. The area under the curve for the heavy isotope is greater than that for the light isotope, and so the abundance ratio of the heavy to the light isotope in this case will be artificially high.

$$N = \Delta t \overline{G}_Z \int_{\mathcal{E}_i}^{\mathcal{E}_f} J_Z(\mathcal{E}) d\mathcal{E} \tag{5.18}$$

In order to make sense of the measured abundance ratio for two species, we must make some assumption about the form of the flux, J. Mewaldt, Spalding, and Stone (1985) found that the energy per nucleon, $\mathcal{E}$, provided the best organizational parameter for the SEP event which they observed, since the elemental abundances were constant as functions of E. As discussed in Chapter 4, this assumption is also valid for the two events observed by MAST. If we assume that all isotopes of a given element follow the same spectrum in $\mathcal{E}$, then we can write the flux as

$$J_{Z,M} = K_M f_Z(\mathcal{E}) \tag{5.19}$$

Here K_M is the abundance of isotope M, while f_Z describes the shape of the particle distribution.

Following Mewaldt, Spalding, and Stone (1985), the measured ratio of two isotopes of the same element, labeled 1 and 2, is then

$$\frac{N_1}{N_2} = \frac{K_1 \int_{\mathcal{E}_{i1}}^{\mathcal{E}_{f1}} f_Z(\mathcal{E}) d\mathcal{E}}{K_2 \int_{\mathcal{E}_{i2}}^{\mathcal{E}_{f2}} f_Z(\mathcal{E}) d\mathcal{E}} = \frac{K_1 C_1}{K_2 C_2} \tag{5.20}$$

In Section 4.3.3 it was found that the particle spectra were well fit by exponentials in energy per nucleon,

$$f_Z(\mathcal{E}) = e^{-\frac{\mathcal{E}}{\mathcal{E}_0}}$$

which yields,

$$C_j = -\mathcal{E}_0 \left(e^{-\frac{\mathcal{E}_{fj}}{\mathcal{E}_0}} - e^{-\frac{\mathcal{E}_{ij}}{\mathcal{E}_0}} \right) \tag{5.21}$$

The overall correction factor is then

$$C_{21} = \frac{C_2}{C_1} = \frac{e^{-\frac{\mathcal{E}_{i2}}{\mathcal{E}_0}} - e^{-\frac{\mathcal{E}_{f2}}{\mathcal{E}_0}}}{e^{-\frac{\mathcal{E}_{i1}}{\mathcal{E}_0}} - e^{-\frac{\mathcal{E}_{f1}}{\mathcal{E}_0}}} \tag{5.22}$$

and the true isotope ratio inferred from the measured ratio is thus

$$\frac{K_1}{K_2} = C_{21}\frac{N_1}{N_2} \tag{5.23}$$

The initial energy of the most dominant isotope of the pair, $\mathcal{E}_{i2}$, is calculated using the geometry factor for that isotope. (Note that the most dominant isotope is always lighter in our isotopic ratio measurements). The lower energy at which that geometry factor falls to half of its maximum value is used as the initial energy. The initial energy of the other, less dominant, isotope is obtained by scaling $\mathcal{E}_{i2}$ using the empirical range-energy relationship:

$$\mathcal{E}_{i1} = \left(\frac{M_2}{M_1}\right)^{\frac{1}{\alpha}} \mathcal{E}_{i2} \tag{5.24}$$

where $\alpha = 1.77$. The maximum value of $\mathcal{E}$ for every particle is restricted to be less than 70 MeV/nucleon, and so $\mathcal{E}_{f1} = \mathcal{E}_{f2}$. This is done in order to ensure that the results are not contaminated by galactic cosmic rays (see Figure 4.10). The correction factors for the two observed SEP events are given in Table 5.4. The correction factors are larger for the first event because that event had a steeper energy spectrum. The correction factor with the greatest effect on the ratios is 0.854, for $^{14}C/^{12}C$.

As with the geomagnetic biases, we can use the ratio $^{22}Ne/^{20}Ne$ to calculate an empirical value of the correction factor by selecting only data in a fixed energy interval, say, 22 to 70 MeV/nucleon, and comparing the ratio to that found with no energy selection. The results of such a test are shown in Table 5.5. We find that the resulting correction factors are consistent with those above, though the uncertainties on the empirical factors are much larger than those found using the method just discussed.

TABLE 5.4

Correction factors due to the different energy/nucleon intervals measured for isotopes. The e-fold energies for the first and second events are 7.28± 1.10 and 10.49± 1.03 MeV/nucleon, respectively.

Mass	Correction Factor (percent)	
Ratio	30 Oct. Event	2 Nov. Event
$^{13}C/^{12}C$	92.29 ± 1.11	94.57 ± 0.51
$^{14}C/^{12}C^{*}$	85.96 ± 1.96	90.00 ± 0.91
$^{15}N/^{14}N^{*}$	92.38 ± 1.10	94.62 ± 0.50
$^{17}O/^{16}O^{*}$	92.83 ± 1.04	94.94 ± 0.47
$^{18}O/^{16}O$	86.74 ± 1.86	90.55 ± 0.86
$^{21}Ne/^{20}Ne^{*}$	93.48 ± 0.95	95.40 ± 0.43
$^{22}Ne/^{20}Ne$	87.81 ± 1.72	91.32 ± 0.79
$^{25}Mg/^{24}Mg$	94.02 ± 0.87	95.78 ± 0.39
$^{26}Mg/^{24}Mg$	88.72 ± 1.59	91.98 ± 0.73
$^{29}Si/^{28}Si$	94.41 ± 0.81	96.06 ± 0.36
$^{30}Si/^{28}Si$	89.41 ± 1.50	92.47 ± 0.68

*- Only upper limits to these ratios are measured.

TABLE 5.5

Range bias, as deduced from the $^{22}Ne/^{20}Ne$ ratios. This empirical bias is in good agreement for both SEP events, within statistical accuracy.

	$^{22}Ne/^{20}Ne$ Ratio (percent)	
	Event #1	Event #2
No cuts	10.67± 1.17	8.52± 0.69
$22< \mathcal{E} <70$ MeV/nuc.	8.30± 1.10	7.93± 0.70
Cut/Uncut Percentage	78± 13	93± 11

5.4 Obtaining High-Resolution Data

Based on the number of particles for each element listed in Table 5.1, there is quite a large number of particles available for measuring isotopic abundances. Unfortunately, however, not all of those particles can be used. The primary problem is the high-mass tails on the mass distributions caused by multiple particle coincidences. In Section 3.3.4 the effect of chance coincidences on the carbon data was shown. We found there that that if we select the one quarter of all the particles which occur at the lowest counting rates, then the high-mass tail is negligible. However, this one-quarter figure was made for convenience, and it is possible to use a larger fraction of the data.

Further restrictions on the data are required in order to obtain a set which is clean enough for mass measurements to be made. While the data selection based on trajectory, residual range, and χ^2_ν provide good criteria for identifying elements, the resulting data set is not adequate for resolving isotopes. Two further selection criteria must therefore be applied to the data in order to sufficiently resolve isotopes: a tighter χ^2_ν selection, and a restriction on the ADCOR rate.

5.4.1 Chi-square Cuts

The tails on the mass distributions can be removed to some extent by requiring that the chi-square be below a certain level. For identifying elements, we chose $\chi^2_\nu<10$. A glance at Figure 4.7 and Table 4.2 from Chapter 4 reveals that the number of particles is not strongly affected by the choice of χ^2_ν until χ^2_ν is less than 2. Thus, one might expect that the measured isotopic ratios should not be strongly affected by the choice of χ^2_ν either.

The effect of the choice of χ^2_ν on the isotopic abundance ratios is best illustrated using the neon data, as in Table 5.6. In order to make sure that the data is not overly affected by chance coincidences, which is an issue to be discussed later, we use only data which is taken when the ADCOR rate is less than 50,000 counts per second. Note that the cut at $\chi^2_\nu<1$ removes a little more than 50% of the data, which

TABLE 5.6

Neon isotope abundances as a function of maximum χ^2_ν. The data are chosen with the ADCOR rate to be less than 50,000 counts per second, Λ >52°, and $\mathcal{E}$<70 MeV/nucleon. In order to simplify the table, the average of the upper and lower asymmetric errors on the likelihood fits are shown.

χ^2_ν less	Number	Percent	Gaussian Fit		Maximum Likelihood	
than	Left	Left	$^{21}Ne/^{20}Ne$	$^{22}Ne/^{20}Ne$	$^{21}Ne/^{20}Ne$	$^{22}Ne/^{20}Ne$
First SEP Event						
10	793	99	0.6± 0.3	12.0± 1.4	0.0± 0.6	10.2± 1.3
4	723	90	0.6± 0.3	12.0± 1.4	0.2± 0.6	10.3± 1.4
2	581	72	1.0± 0.4	12.0± 1.6	0.5± 0.5	10.2± 1.5
1	365	45	1.7± 0.7	13.7± 2.2	1.0± 0.8	11.9± 2.1
Second SEP Event						
10	2217	98	3.6± 0.4	8.3± 0.7	1.3± 0.5	7.6± 0.7
4	2005	89	2.7± 0.4	8.1± 0.7	1.2± 0.4	7.5± 0.7
2	1585	70	1.7± 0.3	8.3± 0.8	0.5± 0.3	7.6± 0.8
1	979	43	2.3± 0.5	8.1± 1.0	1.2± 0.5	7.3± 1.0

would be expected for data which perfectly followed the chi-square distribution.

The abundances calculated using both multiple Gaussians and maximum likelihood fits are shown for comparison. In general, neither set of fits is strongly affected by the choice of χ^2_ν. However, the abundance of $^{21}Ne/^{20}Ne$ is higher from the Gaussian fit as compared to the maximum likelihood fit, due to the fact that the Gaussian fit tends to underestimate the contribution from the tails.

Fits using the maximum likelihood technique were made to the full data set, first using $\chi^2_\nu<2$, which retains 70% of the data, then using $\chi^2_\nu<4$, which retains approximately 90% of the data. All the analysis discussed in the following sections was made on both sets of data. No statistically meaningful difference was found in the resulting isotopic ratios, so the final measurements use data with $\chi^2_\nu<4$ in order to maximize the accepted number of particles, and minimize possible selection bias.

5.4.2 High Count-Rate Restrictions

As discussed in Section 3.3.4, mass measurements made during high flux periods have high-mass tails on the mass distributions due to chance coincidences of low-energy protons with the heavy ions. This high-mass tail can interfere with measurements of heavy isotopes. The only way to eliminate the tails from the data is to remove the particles which are measured during high counting rate periods, so that the fraction of such contaminated particles is negligible. There is of course a trade off in this, since much of the heavy-ion data is taken during periods of high counting rate. The number of heavy ions below various maximum ADCOR levels is listed in Table 5.7. There is a further complication in that restricting the ADCOR rate alters how the instrument samples the different regions of the magnetosphere, which will now be addressed.

The restriction on ADCOR rate complicates the geomagnetic bias, as illustrated in Figure 5.11. The particles which dominate the ADCOR are ~4 MeV protons, which must, at minimum, pass through the two instrument windows and also trigger the 1.78 MeV threshold of M1XS. The cutoff latitudes for these particles are typically 5 to 6 degrees higher than the cutoff for the lowest-rigidity heavy ions

TABLE 5.7

The number of particles for various levels of the maximum ADCOR rate. For this data, χ^2_ν is less than 4, and $\mathcal{E}$ is less than 70 MeV/nucleon, as discussed later in the text. Note that all particles are measured while the ADCOR rate is less than 350,000 counts per second, and all particles in the second SEP event are measured while the ADCOR rate is less than 100,000 counts per second.

Element	SEP	ADCOR Maximum counts/second $\div 10^3$				
		350	100	50	20	10
Carbon	1	7255	5520	4245	2826	2039
	2	7190	7190	6096	3467	2701
Nitrogen	1	1686	1332	1036	730	569
	2	1948	1948	1614	900	682
Oxygen	1	11981	9733	7664	5590	4460
	2	17704	17704	14753	7988	6224
Neon	1	1116	918	723	541	431
	2	2421	2421	2005	1073	847
Magnesium	1	1133	941	734	545	445
	2	3087	3087	2590	1407	1407
Silicon	1	630	549	460	351	301
	2	2200	2200	1869	1009	806

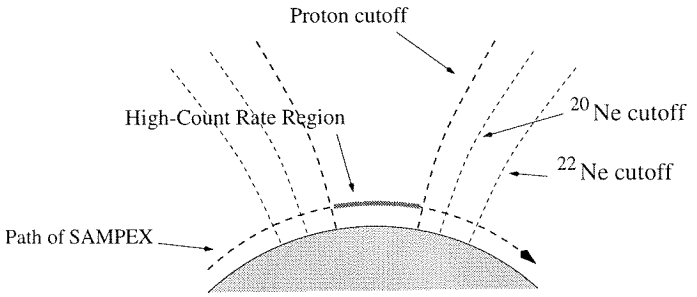

Figure 5.11: The restrictions on high ADCOR rate tends to remove the middle of the polar passes. This alters how SAMPEX samples the different regions of the magnetosphere, which changes the geomagnetic bias (Not to scale).

measured by MAST. This means that even during the most intense parts of the event, the ADCOR rate drops to low levels below the proton cutoff latitude. In this 5 to 6 degrees wide interval of invariant latitude, the particle measurements appear to be dominated by heavy ions during the SEP events. The instrument livetime is greater during these times, since the low-energy protons no longer dominate the instrument counting rates, and thus a large fraction of all the heavy particles collected during the SEP events are collected in this band of invariant latitude, as shown in Figure 5.12.

This complex sampling of invariant latitudes complicates the geomagnetic bias in the isotopic species. As an example let us consider an isotope pair ^{22}Ne and ^{20}Ne. Their rigidity differs by 10% at the same energy per nucleon. If the cutoff latitude of ^{20}Ne is 60°, the cutoff latitude of ^{22}Ne is 59.2°. If all the neon data is taken between 65°and the cutoff latitudes, then the time that ^{22}Ne is acquired is 16% greater than the time that ^{20}Ne is acquired, so the bias can be as large as 16%. In practice, we find that the bias is not this large, though it is larger than the bias due to the shape of the orbit alone.

Fortunately, the effect of the ADCOR cuts is qualitatively equivalent to the geomagnetic bias, in that it only affects particles according to their rigidity. Thus, we can look at the fractionation of the relative abundances due to the different ADCOR rates using the same approach as we used for finding the geomagnetic bias. Rather than comparing the relative abundances above 52° to those above 65°, we now compare the relative abundances for data which has been restricted in ADCOR rate

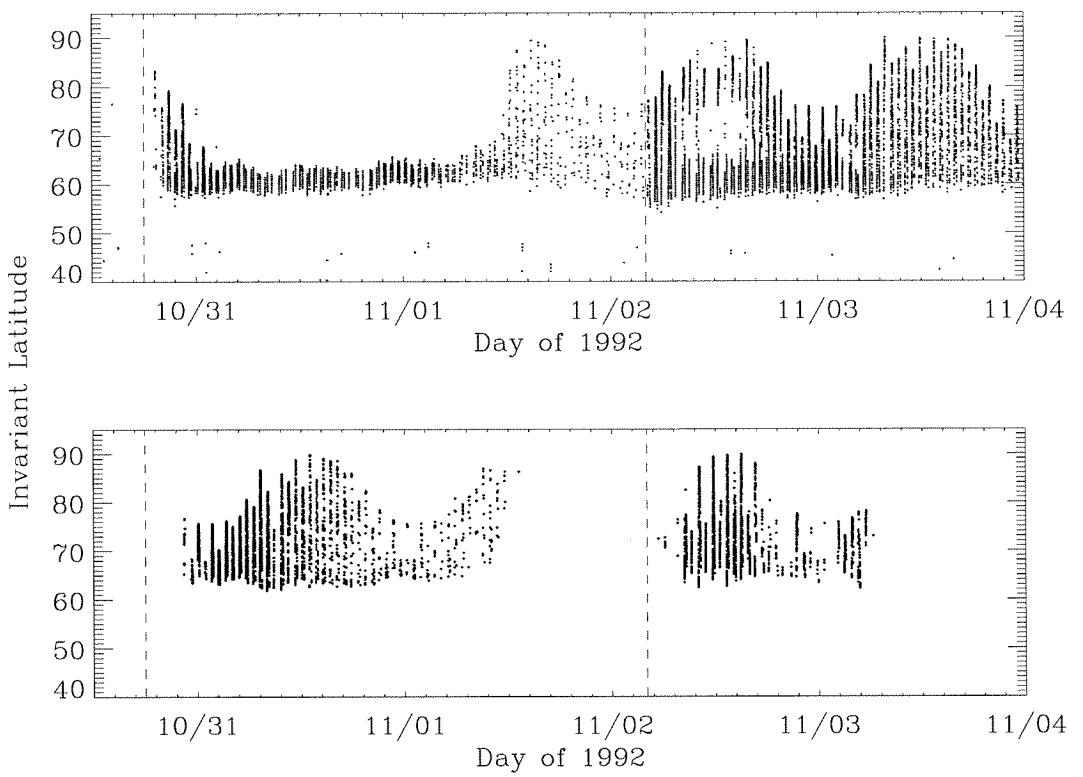

Figure 5.12: *Upper panel*: The invariant latitude of oxygen particles as a function of time for oxygen particles which are collected when the ADCOR rate is less then 50×10^3 counts per second. Note that even when the majority of the polar pass is excluded from this cut, there is a clear band of particles collected between ~56-64°. *Lower panel*: This shows the remaining oxygen particles, which are collected when the ADCOR rate is greater than 50×10^3 counts per second. In both plots, the start of each SEP event is marked by a vertical dashed line.

TABLE 5.8

Correction factors for the geomagnetic bias introduced by the orbit of SAMPEX and the limits on ADCOR rate of 50,000 counts per second, calculated as described in the text.

	Correction Factor (percent)	
Ratio	First Event	Second Event
$^{13}C/^{12}C$	93.0 ± 7.0	93.0 ± 7.0
$^{14}C/^{12}C^*$	87.7 ± 12.3	87.7 ± 12.3
$^{15}N/^{14}N^*$	94.4 ± 5.6	94.4 ± 5.6
$^{17}O/^{16}O^*$	95.6 ± 4.4	95.6 ± 4.4
$^{18}O/^{16}O$	92.0 ± 8.0	91.9 ± 8.1
$^{21}Ne/^{20}Ne^*$	96.5 ± 3.5	96.5 ± 3.5
$^{22}Ne/^{20}Ne$	93.5 ± 6.5	93.5 ± 6.5
$^{25}Mg/^{24}Mg$	97.0 ± 3.0	97.0 ± 3.0
$^{26}Mg/^{24}Mg$	94.4 ± 5.6	94.4 ± 5.6
$^{29}Si/^{28}Si$	97.9 ± 2.1	97.9 ± 2.1
$^{30}Si/^{28}Si$	96.0 ± 4.0	96.0 ± 4.0

*- Only upper limits to these ratios are measured.

above 52°, to those above 65°. The results for two levels of ADCOR are shown for illustration purposes in Figure 5.13. The correction factors for isotope measurements given a maximum ADCOR rate of 50,000 counts per second are listed in Table 5.8. These biases always act to reduce the observed ratios of heavier to lighter isotopes. The maximum bias to any of the ratios reduces the $^{13}C/^{12}C$ measurement by ~88%. This is the correction to that ratio when the ADCOR rate is less than 10 thousand counts per second (the $^{14}C/^{12}C$ measurement is only an upper limit).

To explore how the isotopic ratio measurements are affected by different ADCOR restrictions, a complete set of maximum likelihood fits were made to the data using five values of the maximum ADCOR rate: 10, 20, 50, 100, and 350 thousand

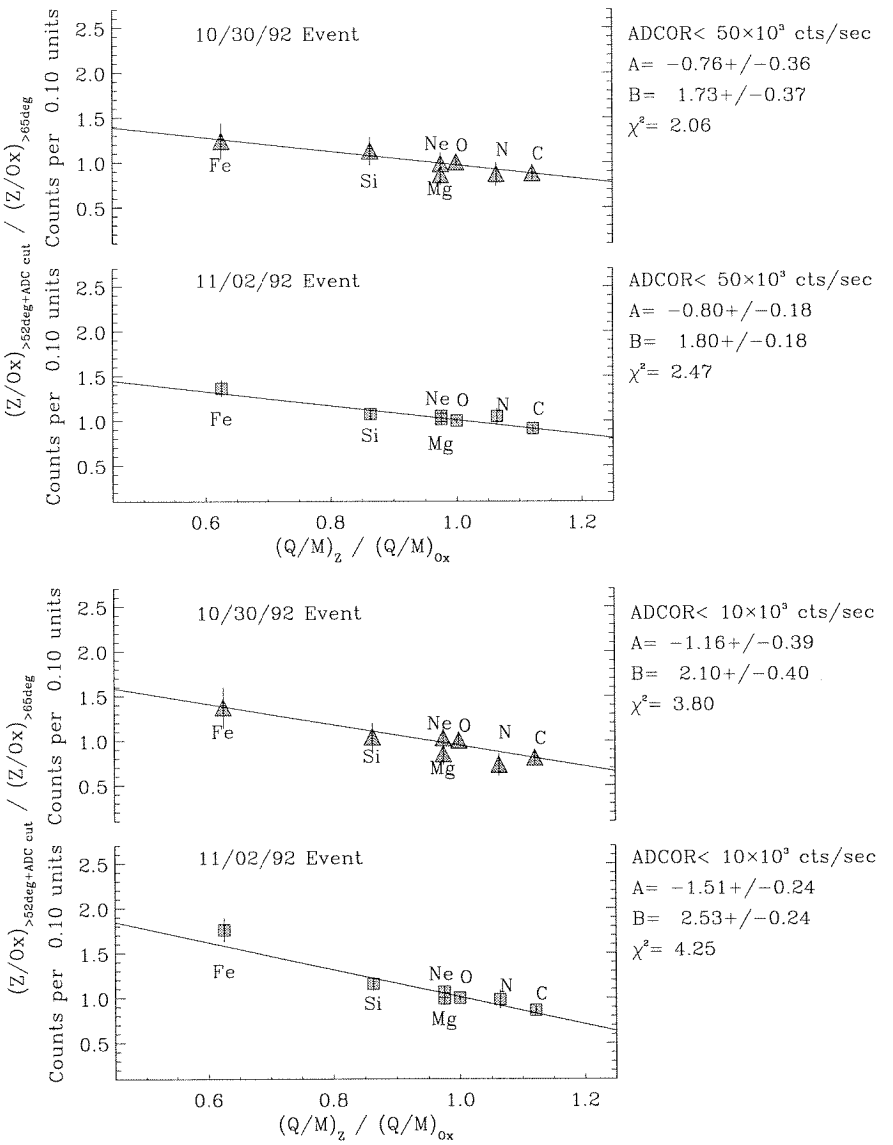

Figure 5.13: Bias in the element composition due to geomagnetic sampling and ADCOR selection. In the upper plots, the ADCOR level is less than 50,000 counts per second, and in the lower plot the maximum ADCOR rate is 10,000 counts per second. The geomagnetic fractionation becomes more pronounced as the maximum ADCOR level is lowered. The data are fit with a linear function $f = A \times r + B$, where r is the charge-to-mass value of each element divided by the charge-to-mass ratio of oxygen, and f is the bias.

counts per second. This creates a large set of data to look at. The results of the fits are summarized in three plots. In each plot, the asterisks and the heavy dashed lines represent data from the first SEP event, and the boxes with the light solid lines represent data from the second SEP event. The first plot, Figure 5.14, shows the offsets from the maximum likelihood fits. This is the center of the mass distribution of the dominant peak. The X-offset is the offset of the semi-average mass, while the Y-offset is for the last mass estimator, as described in an earlier section. The value found for each of these offsets is close the the expected integer value of the dominant mass number, and the offsets used vary by less than 0.2% for each element. Thus, no unusual behavior is occurring in the fitting of this variable. The second plot, Figure 5.15, shows the width of the mass distributions from the maximum likelihood fit. The σ_X is the width of the semi-average mass estimator, while the σ_Y is the width of the last mass estimator. These numbers do not vary greatly between the two SEP events, except for for the $^{25}Mg/^{24}Mg$ and $^{30}Si/^{28}Si$ ratios. However, the measured isotopic abundance ratios are not strongly sensitive to the value of the σ parameter, and so the abundance estimates should not be affected by this.

The third plot, Figure 5.16, shows the isotopic abundance ratios for the isotopes of each element, at the various ADCOR levels. In these plots, the upper and lower 84% confidence limits are also shown for the first and second SEP events by the heavy dashed lines, and the light solid lines, respectively. The dashed horizontal line appearing in most plots shows the isotopic abundance from AG89, for comparison. The ratios $^{14}C/^{12}C$ and $^{16}N/^{14}N$ are expected to be zero, but are present in order to show how the fitting technique responds to a null abundance.

Carbon: The element that should be most affected by coincidences at high ADCOR rates is carbon, according the the Monte Carlo results of Section 3.3.4. The ^{13}C ratio is consistently above zero for all values of ADCOR, while the ^{14}C ratio is consistent with zero. Thus, the $^{14}C/^{12}C$ measurement is considered an upper limit. For the second SEP event, the $^{14}C/^{12}C$ ratio is consistent for all values of ADCOR. However, for the first event, the $^{13}C/^{12}C$ ratio increases with ADCOR rate, changing significantly for 100 and 350 thousand counts per second. This suggests that the fits are somehow affected by the counting rates. The $^{17}O/^{16}O$ ratio also shows this trend,

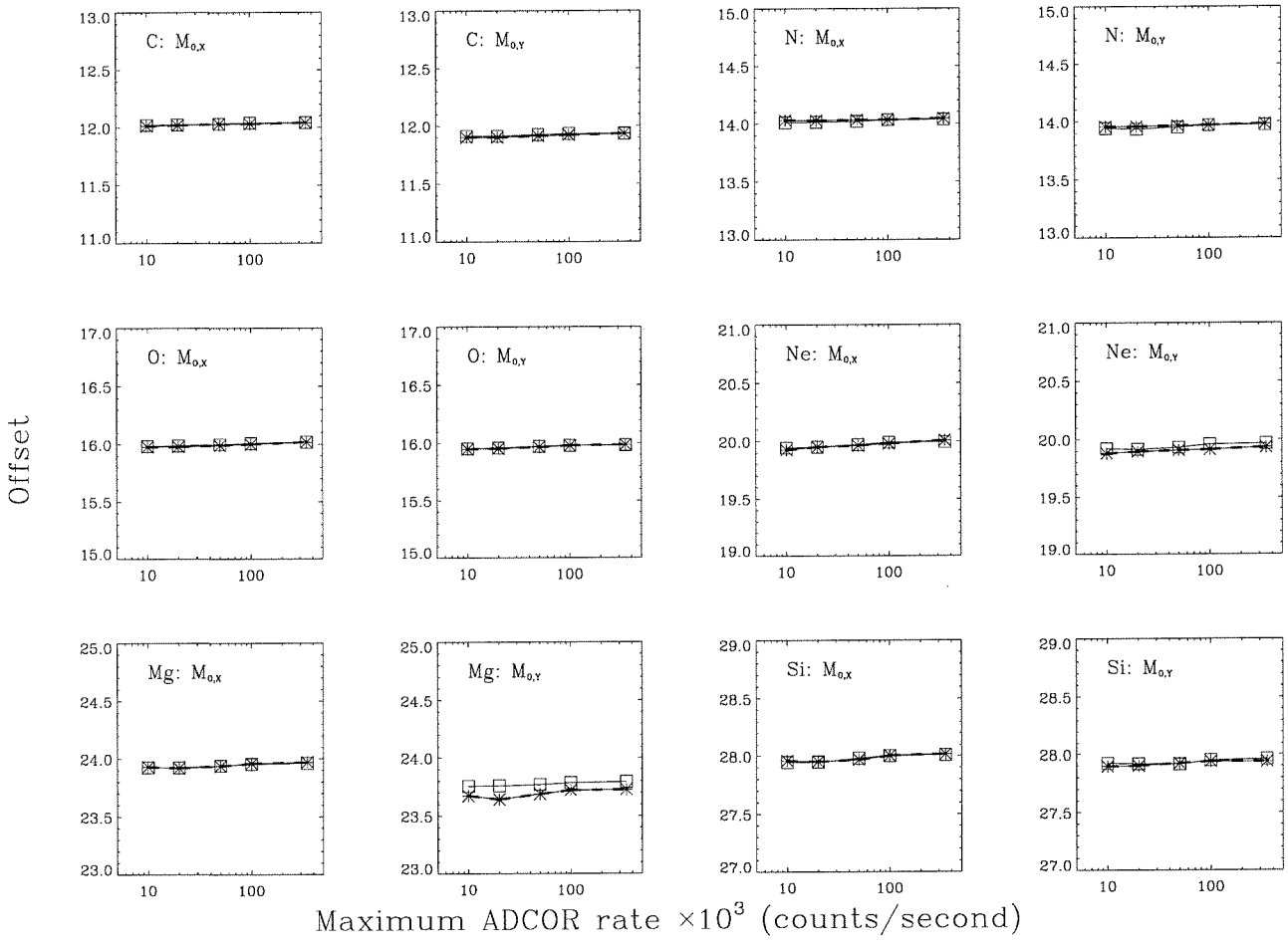

Figure 5.14: Offset parameter from the maximum likelihood fits. This parameter tells where the fit placed the center of the dominant mass peak for each element. The $M_{0,X}$ parameter represents the width of the semi-average mass, and the $M_{0,Y}$ parameter represents the width of the last mass estimator.

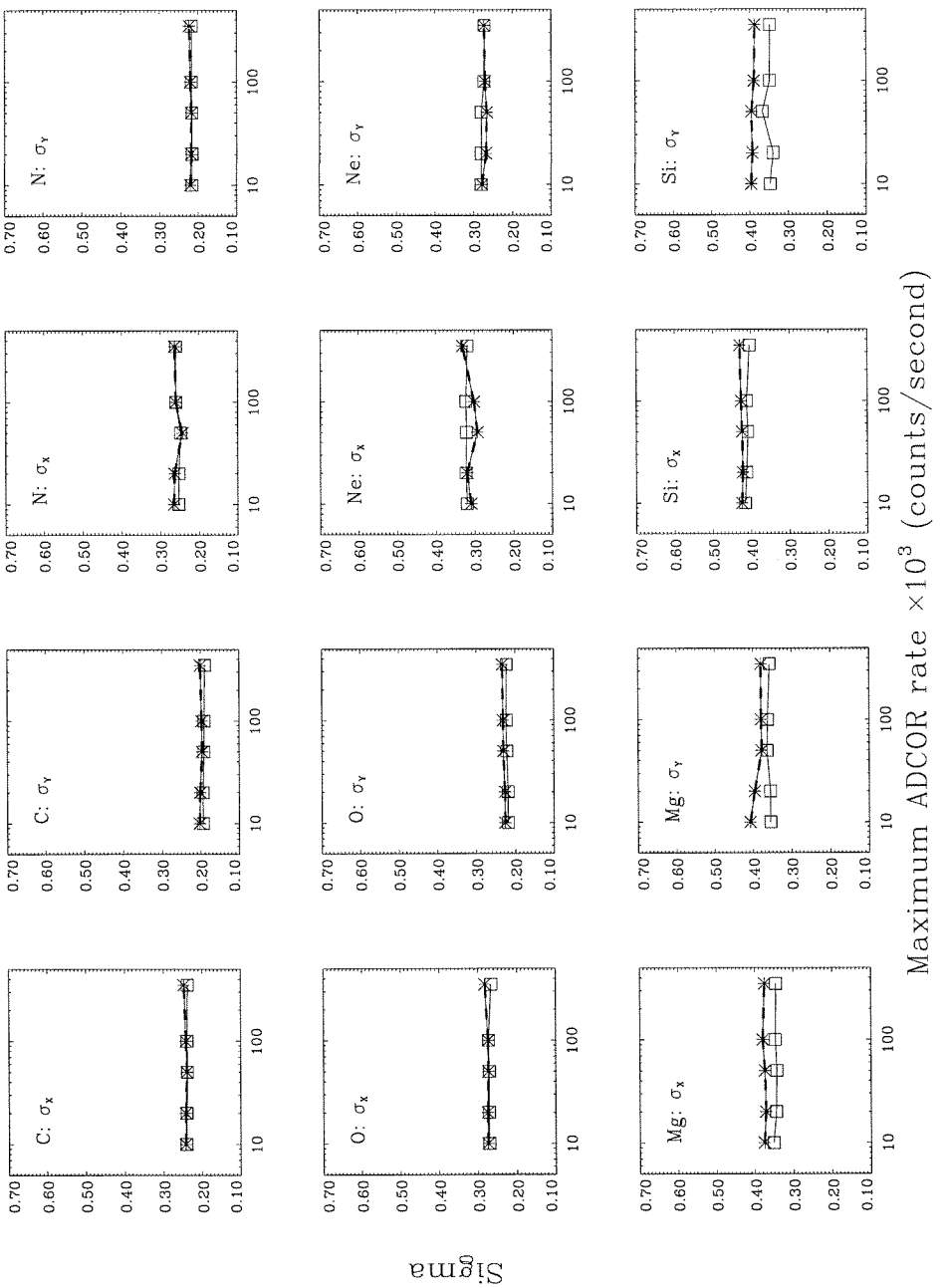

Figure 5.15: Sigma parameter from the maximum likelihood fits. This parameter is equivalent to the Gaussian width of the dominant mass peak for each element. The σx parameter represents the width of the semi-average mass, and the σy parameter represents the width of the last mass estimator.

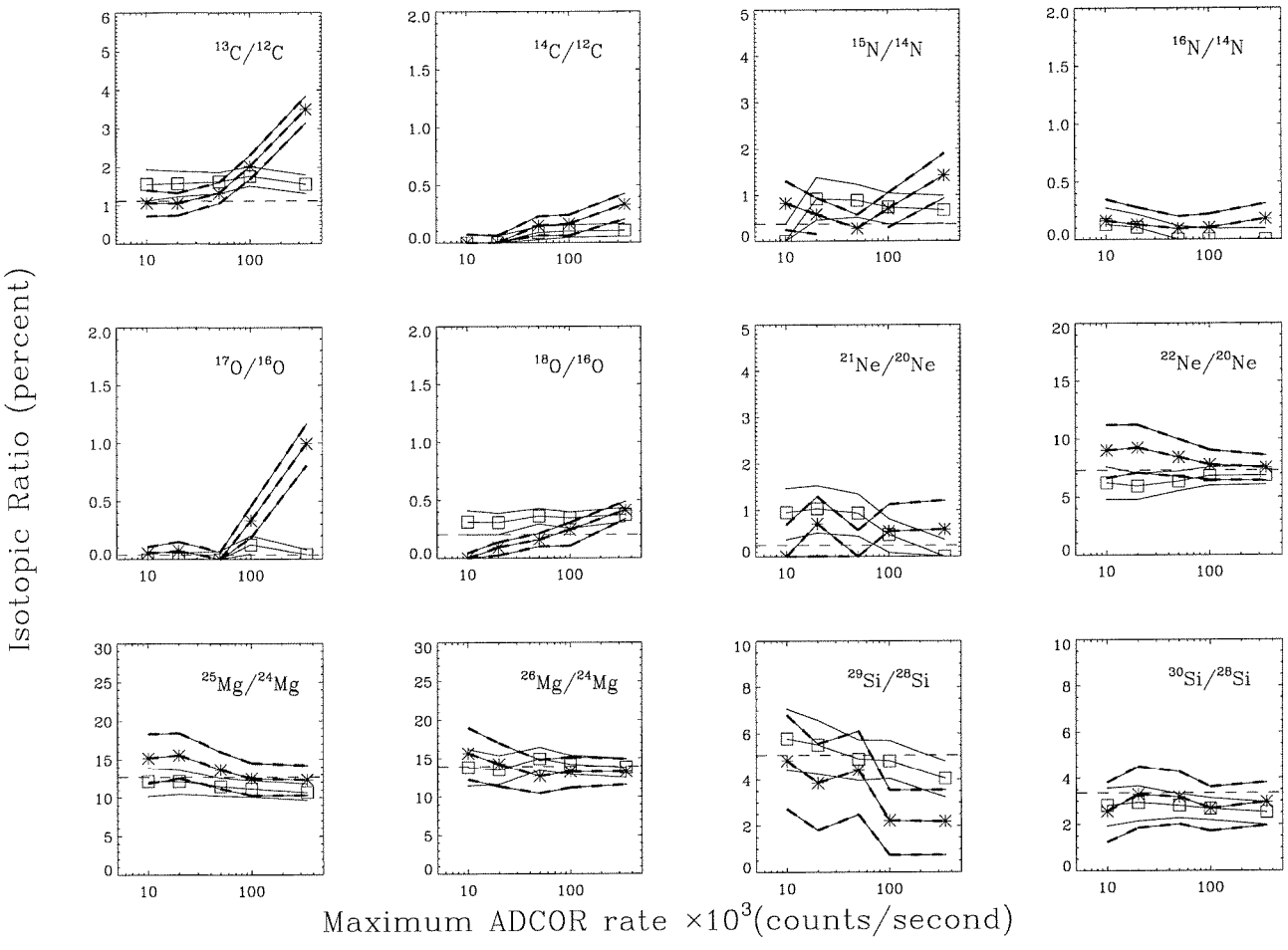

Figure 5.16: Isotopic ratios measured with different values of the maximum ADCOR rate. Data are selected with $\mathcal{E}$<70 MeV/nucleon, χ^2_ν<4 and Λ >52°. The heavy dashed lines are for the first SEP event, while the light solid lines are for the second event. These ratios have been corrected for geomagnetic bias, but not yet for instrumental bias. The horizontal dashed lines are the solar system ratios from Anders and Grevesse (1989).

although the ratio of $^{17}O/^{16}O$ is about a factor of four smaller than that of $^{13}C/^{12}C$. This suggests that the effect of multiple coincidences cannot be completely avoided, even using the maximum likelihood technique. Note, however, that the multiple Gaussian technique gives ratios about a factor of two higher for the ratios of both isotopes at the highest counting rates. The overall impression is that the carbon isotope ratios should be only used for ADCOR levels of 10, 20 or 50 thousand counts per second.

Nitrogen: Except for perhaps the highest ADCOR level for the first SEP event, all of the $^{15}N/^{14}N$ measurements are consistent with both the Anders and Grevesse (1989) value and zero. Thus, this ratio is considered only as an upper limit. The $^{16}N/^{14}N$ ratio is also consistent with zero, as it should be since ^{16}N is radioactive with a 7.13 second half-life.

Oxygen: As with the $^{13}C/^{12}C$ ratios in the first event, the ratios of $^{17}O/^{16}O$ and $^{18}O/^{16}O$ are high for the fits made at 100 and 350 thousand counts per second levels for the first SEP event. The ratios for the second event, however, are fairly constant for all ADCOR levels.

Neon: The $^{21}Ne/^{20}Ne$ measurements are only an upper limit in both of the SEP events. There is not an upwards trend in the $^{21}Ne/^{20}Ne$ ratio for the first event, suggesting that the chance coincidences do not strongly affect the measurements. This seems reasonable, since the effects of chance coincidences depends on the amount of energy deposited by the coincident particles relative to the energy deposited by the heavy ion. Since the energy deposited by an ion increases quadratically with charge, heavier nuclei should be less affected than the lighter ones.

For both SEP events, the $^{22}Ne/^{20}Ne$ ratio does not change significantly with the ADCOR level.

Magnesium: As with ^{22}Ne, the magnesium isotopes show no significant variation with ADCOR level. Furthermore, the values of the ratios are consistent between the first and second SEP events.

Silicon: Of the three heavy elements, with the six isotope measurements, the only oddly-behaved ratio is $^{29}Si/^{28}Si$. The $^{30}Si/^{28}Si$ ratio is consistent for all ADCOR values, but the ^{29}Si measurement decreases with increasing ADCOR level

TABLE 5.9

Criteria used to select particle data for isotope analysis.

Quantity	Requirement
Invariant Latitude	$\Lambda > 52°$
Kinetic Energy	$\mathcal{E} < 70$ MeV/nucleon
Chi-Square	$\chi^2_\nu < 4$
ADCOR Rate	ADCOR<50,000 counts per second
Time	SEP #1: Day 304.75 through 307.125
	SEP #2: Day 307.125 through 312

for both SEP events. From the constancy of the $^{25}Mg/^{24}Mg$ ratio, and the low level of the $^{21}Ne/^{20}Ne$ ratio, it appears that there is no systematic reason for this ratio to behave that way. It is possible that this behavior is simply a chance occurrence. The errors on the ratio are quite large, and except when comparing the ratio for <10 thousand counts per second with those for <350 thousand counts per second, the $^{29}Si/^{28}Si$ ratios are compatible with one another.

Based on this analysis of the isotopic abundances calculated at various ADCOR levels, it was decided that the data to quote as the final results should be based on the measurements made at less than 50 thousand counts per second. This allows the use of a maximum amount of particles, while limiting contamination due to the high counting rates.

5.5 Analysis of Isotopic Ratios

With the maximum ADCOR counting rate established, we have the final criteria for selecting the high-quality data set for isotope analysis. These criteria are listed in Table 5.9.

The number of particles used in the isotopic ratio fits for each element and each range is listed in Table 5.10. A notable feature in the table is that the second

TABLE 5.10

The number of particles used in the final isotopic ratio analysis. The ADCOR rate is less than 50,000 counts per second, the χ^2_ν is less than 4, and $\mathcal{E}$ is less than 70 MeV/nucleon.

Element	SEP Event	Total	Range						
			0	1	2	3	4	5	6
Carbon	1	4245	1270	1044	1250	619	58	4	0
	2	6096	1457	1242	1756	1381	229	31	0
Nitrogen	1	1036	338	296	265	132	5	0	0
	2	1614	388	330	493	343	57	3	0
Oxygen	1	7664	2552	1958	2145	945	64	0	0
	2	14752	3769	3114	4269	3066	507	0	0
Neon	1	723	252	183	202	81	5	0	0
	2	2005	536	469	612	347	64	0	0
Magnesium	1	734	281	212	169	66	6	0	0
	2	2590	760	575	788	432	35	0	0
Silicon	1	460	192	138	101	29	0	0	0
	2	1869	593	461	512	289	14	0	0

event has much more particles at higher energies than the first event, due to its harder spectrum.

A plot of these isotopic ratio measurements is shown in Figure 5.18 and listed in Table 5.11. We now address the question of how sensitive the results are to the ADCOR level chosen. The difference between the mean of the measurement at 50 and 20 thousand counts per second is taken, then divided by the uncertainty in the 50 thousand counts per second measurement. This quantity is calculated only for the measured ratios, not the upper limits. A histogram of these values is shown in Figure 5.17. All of the measurements are within 2 sigma, and less than 30% are within 1 sigma, which is reasonable.

Figure 5.17: Change in the isotopic ratios if 20 thousand counts per second were used rather than 50 thousand counts per second. Data from the first SEP event are filled with horizontal lines; data from the second SEP event are marked with diagonal lines.

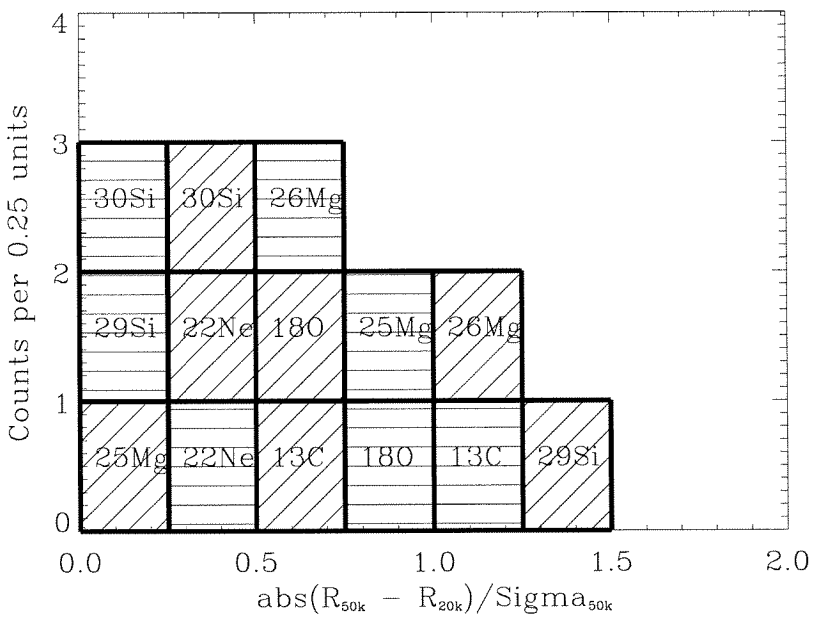

In Table 5.11 are listed the isotopic abundance ratios obtained from maximum likelihood fits, with corrections for geomagnetic bias and for range bias applied. The results are the isotopic abundance ratios in the SEP material as observed at Earth. There may also be biases introduced between the SEP composition and solar coronal composition, as is discussed in the next section.

Also listed in Table 5.11 are the Anders and Grevesse (1989) values for the solar system composition. In the last two columns is shown the difference between the SEP isotopic ratios and the AG89 values divided by the uncertainties in the SEP measurements. This figure indicates the level of agreement between the SEP ratios and the AG89 ratios. Most of the isotopic ratios appear to be consistent with the solar system values. The largest disagreement is in the $^{18}O/^{16}O$ ratio in the second SEP event.

For reference, histograms of the weighted average mass of each element are shown in Figures 5.20 and 5.19. Note that ^{13}C does not appear to be clearly separated from ^{12}C in these plots, and a multiple-Gaussian fit to that isotope greatly overestimates its abundance. In Figure 5.21 we show histograms of the weighted average mass for data which has been greatly restricted in χ^2_ν and in ADCOR rate. This is to illustrate the fact that if the data is severely restricted, then the multiple-Gaussian approach is able to resolve the ^{13}C and ^{18}O isotopes.

5.6 Time and Energy Dependence

The isotopic ratios calculated in the previous section are for the full time period of each SEP event, and up to 70 MeV/nucleon. Let us look at the $^{22}Ne/^{20}Ne$ ratio in detail now, to see what can be said about the neon isotopic composition as a function of time and energy.

First we examine the ratio as a function of time. The first SEP event lasts from day 304.75 through day 307.125. To avoid the range bias, we only use data in the energy interval 19-70 MeV/nucleon. The invariant latitude is greater than 52°. The ratio as a function of time is shown in Figure 5.22. In both SEP events there is some evidence that the isotopic abundance ratio decreases with time. This

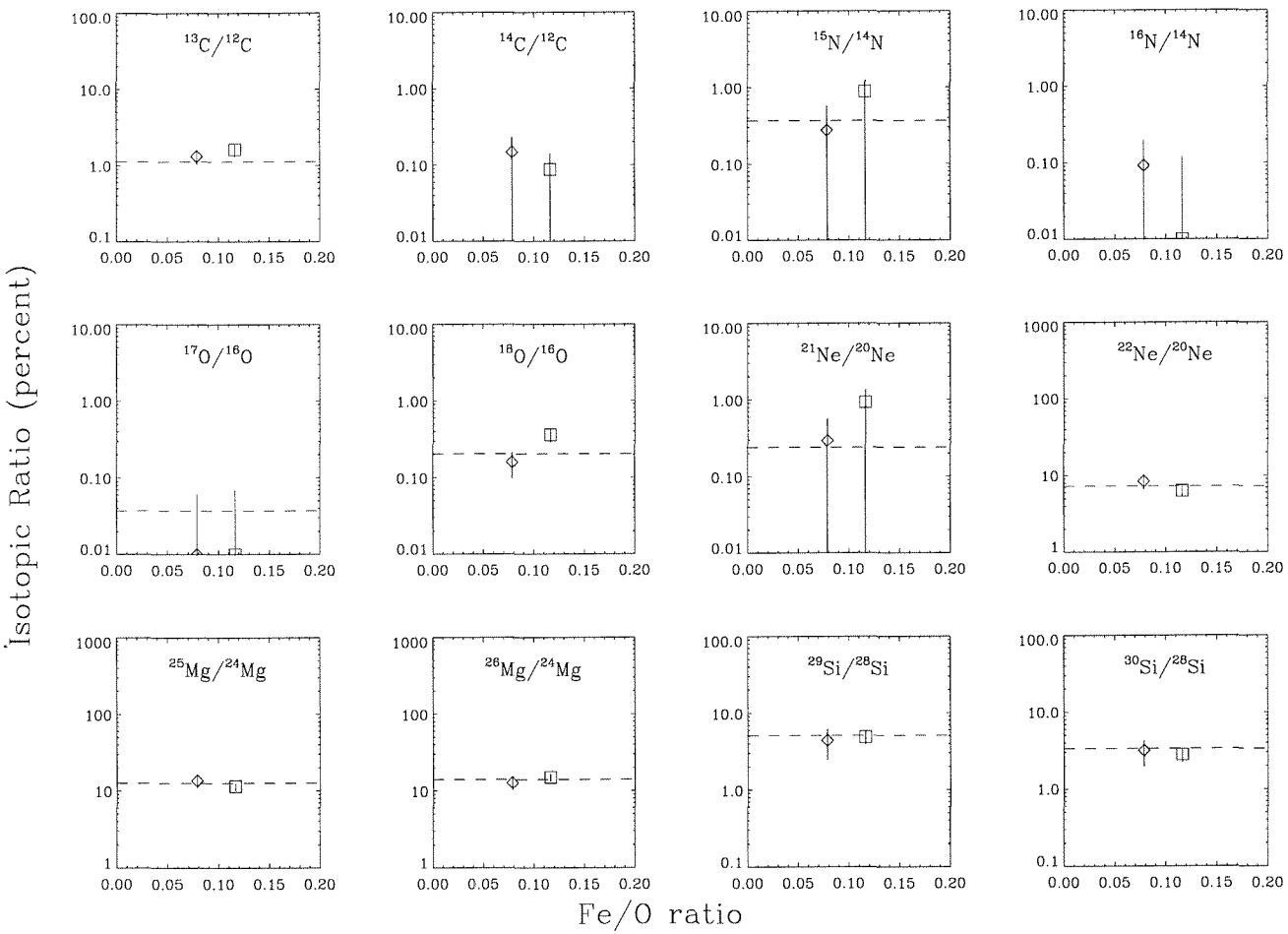

Figure 5.18: Isotopic abundance ratios for all the elements, plotted versus the iron to oxygen ratio in each SEP event. The diamond symbol marks the first SEP event, while the square marks the second SEP event. These measurements are taken with the ADCOR rate less than 50 thousand counts per second.

TABLE 5.11

Isotopic abundance ratios as measured by MAST. These numbers have been corrected for geomagnetic bias and range bias, and so should be representative of the isotopic abundances of the SEP material in interplanetary space at the Earth.

Mass	Isotopic Ratio (percent)			Std. Deviations from AG89	
Ratio	10/30 Event	11/02 Event	AG89	10/30 Event	11/2 Event
$^{13}C/^{12}C$	$1.34^{+0.27}_{-0.26}$	$1.63^{+0.24}_{-0.30}$	1.110	0.87	1.71
$^{14}C/^{12}C$	$< 0.15^{+0.08}$	$< 0.09^{+0.05}$	0.000	-	-
$^{15}N/^{14}N$	$< 0.28^{+0.30}$	$< 0.89^{+0.35}$	0.369	-	-
$^{17}O/^{16}O$	$< 0.01^{+0.05}$	$< 0.01^{+0.06}$	0.038	-	-
$^{18}O/^{16}O$	$0.16^{+0.05}_{-0.06}$	$0.36^{+0.06}_{-0.07}$	0.201	-0.76	2.41
$^{21}Ne/^{20}Ne$	$< 0.30^{+0.27}$	$< 0.93^{+0.41}$	0.243	-	-
$^{22}Ne/^{20}Ne$	$8.49^{+1.50}_{-1.66}$	$6.36^{+0.86}_{-0.82}$	7.310	0.71	-1.11
$^{25}Mg/^{24}Mg$	$13.71^{+2.33}_{-2.47}$	$11.46^{+1.11}_{-1.23}$	12.600	0.45	-1.03
$^{26}Mg/^{24}Mg$	$12.76^{+2.08}_{-2.19}$	$14.97^{+1.48}_{-1.48}$	13.900	-0.55	0.72
$^{29}Si/^{28}Si$	$4.42^{+1.69}_{-1.93}$	$4.90^{+0.83}_{-0.93}$	5.070	-0.38	-0.21
$^{30}Si/^{28}Si$	$3.19^{+1.10}_{-1.17}$	$2.81^{+0.51}_{-0.54}$	3.360	-0.15	-1.08

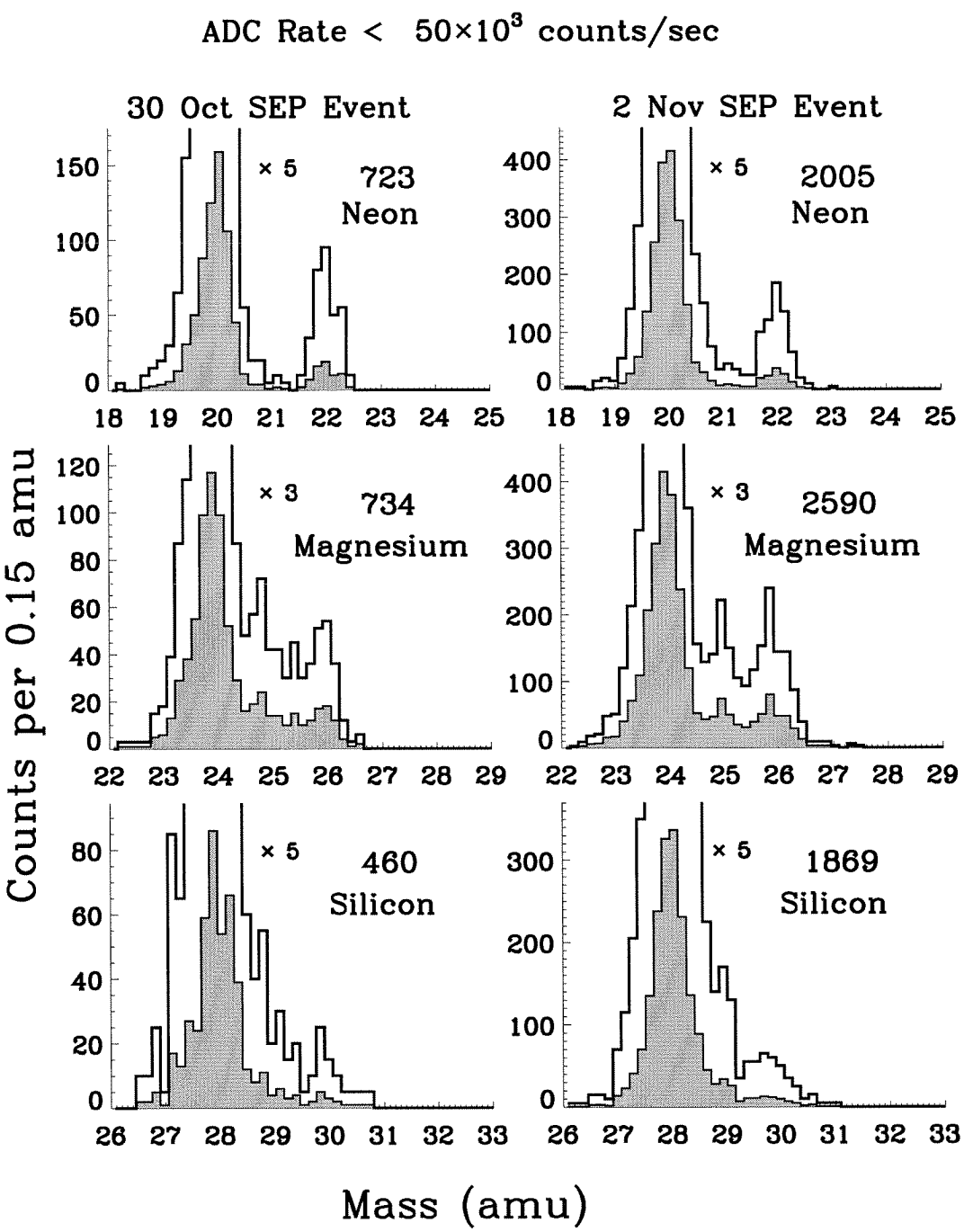

Figure 5.19: Histograms of the weighted average mass for neon, magnesium and silicon, selected with Λ >52°, χ^2_ν<4, $\mathcal{E}$<70 MeV/nucleon and ADCOR<50,000 counts per second.

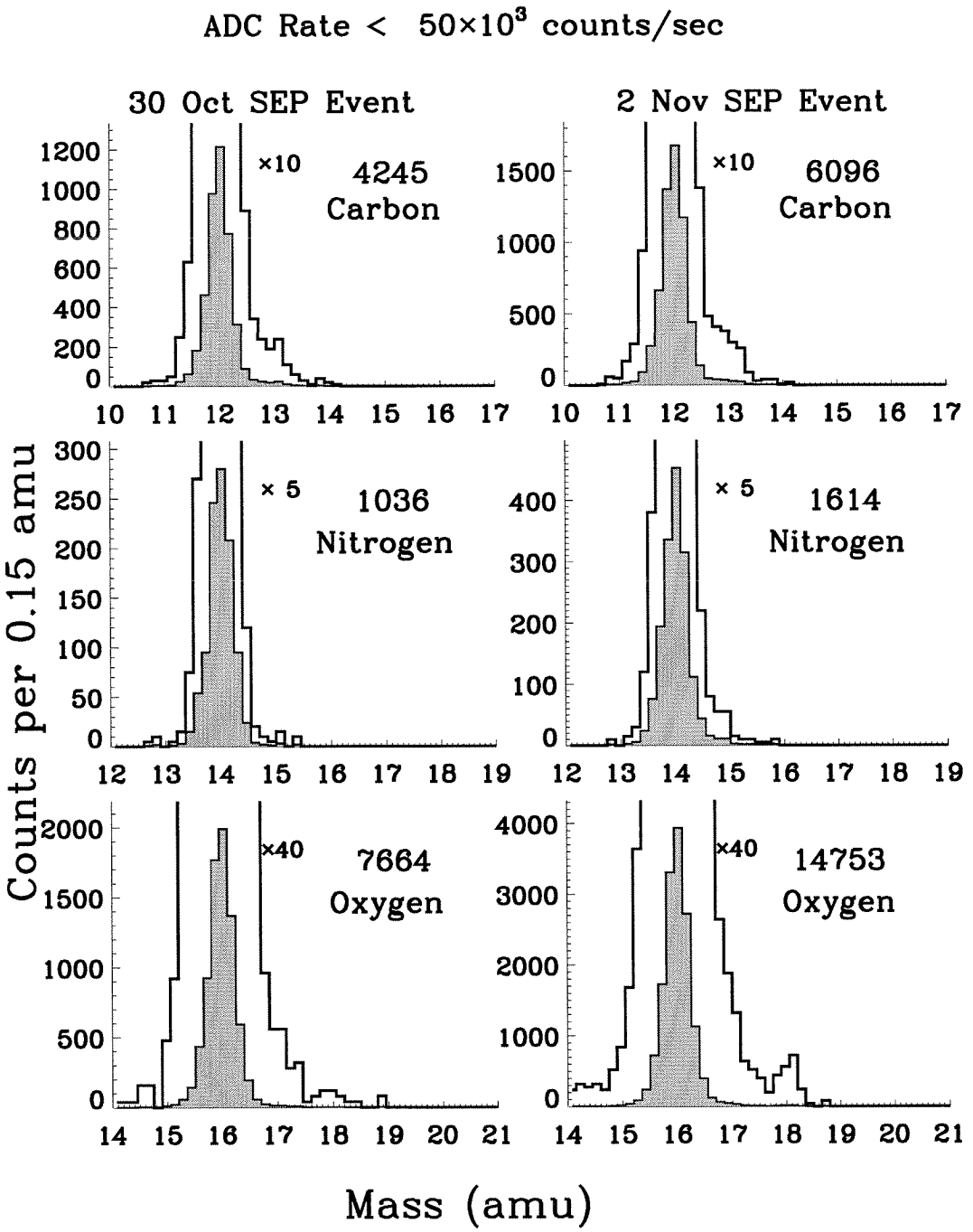

Figure 5.20: Histograms of the weighted average mass for carbon, nitrogen and oxygen particles, selected with Λ >52°, χ^2_ν<4, $\mathcal{E}$<70 MeV/nucleon and ADCOR<50,000 counts per second.

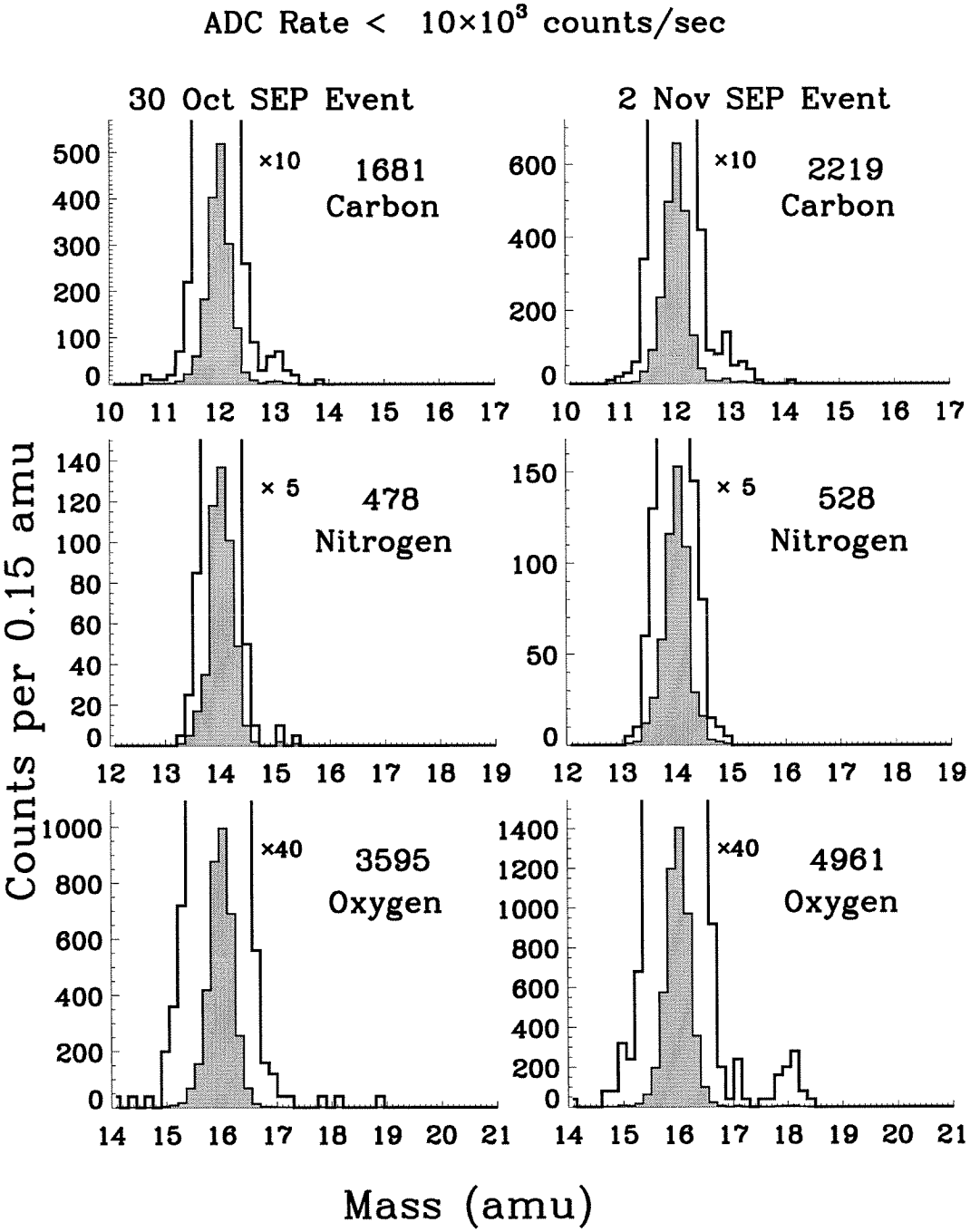

Figure 5.21: Histograms of the weighted average mass for carbon, oxygen and nitrogen, selected with $\Lambda > 52°$, $\chi^2_\nu < 2$, $\mathcal{E} < 70$ MeV/nucleon, and ADCOR<10,000 counts per second. This shows that ^{13}C is fairly well resolved when the data is greatly restricted, and that the $^{18}O/^{16}O$ ratio in the two SEP events is quite different, and not an artifact.

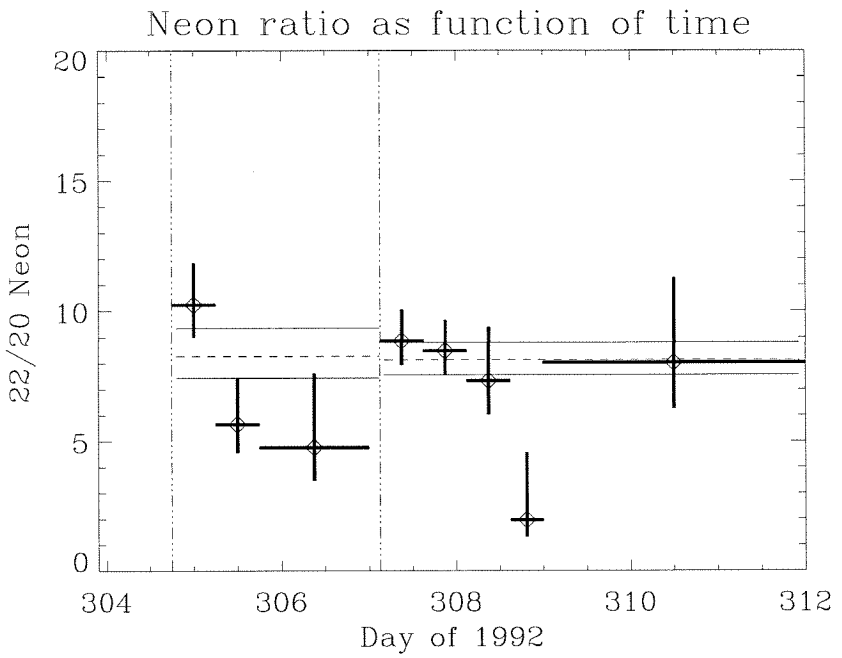

Figure 5.22: Neon ratio versus time for particles in the 19-70 MeV/nucleon energy interval. No ADCOR restriction is made on the data, nor any invariant latitude restriction. The χ^2_ν is less than 4. The dashed lines represent the average over all energies, and the solid lines represent the uncertainty.

behavior is similar to that of the Fe/O ratio, which also decreases with time, as shown in Figure 4.12 from Chapter 4. The reason should be the same — the ^{22}Ne has a higher rigidity than ^{20}Ne at the same value of $\mathcal{E}$, and so arrives earlier. Note that the geomagnetic bias is different in each of these time intervals. However, the bias is small compared to the uncertainties on the ratios, and does not alter the trend seen here.

We next examine the energy dependence of the isotope ratios. The behavior of the ^{22}Ne/^{20}Ne ratio as a function of energy is shown in Figure 5.23. In both events there is the suggestion that the isotopic ratio decreases with energy. This could be due to changing charge states of neon as a function of energy or perhaps due to changing source material for the particles as the source of acceleration moves outward from the Sun.

The elemental spectra from Chapter 4, Figure 4.11, however, show no sign

that the elemental abundances change with energy. If the spectra do change with energy, it might be expected that the effect would be organized by rigidity, and hence should be observed in other elements. To test this, we look at the oxygen to carbon ratio as a function of energy, as shown by the small asterisks in Figure 5.23. These elements show only a hint that the spectra decrease with energy. Thus, while a change in the neon isotope spectra with energy is a possibility, these data do not prove that in this case.

Fractionation in the isotopes might be expected to be a function of the isotope mass. To look for evidence of such fractionation, we have plotted each measured isotopic ratio divided by the isotopic ratios given by Anders and Grevesse (1989). These are plotted versus the ratio of the masses for the two isotopes compared in each ratio. For example, the ^{22}Ne ratio is plotted at $\frac{22}{20} = 1.1$. The resulting plots are shown in Figure 5.24. The weighted mean of the ratios is calculated, as is the standard deviation of the points. We find that the ratios are in good agreement with the solar system values. The apparently high abundances of ^{13}C and ^{18}O are seen to be within 2 sigma of the terrestrial values.

Yet we know that the elements are fractionated with respect to their charge to mass ratios. Such enhancements should also occur in the isotopic ratios. The expected fractionation of the isotopic ratios due to this effect is shown by the solid line.

5.7 SEP-Based Coronal Isotopic Composition

The composition measurements thus far have been corrected for geomagnetic bias and instrument bias, and thus represent the composition of the solar energetic particles as observed in interplanetary space at 1 AU. This composition can be related to that of the source coronal material if we assume that the rigidity-dependent fractionation discussed in Section 4.4, which is due to the acceleration and transport of the particles from the corona to the Earth, also applies to isotopes. Just as the elemental composition observed in interplanetary space can be related to the elemental composition of the corona, so too can the isotopic composition be related to

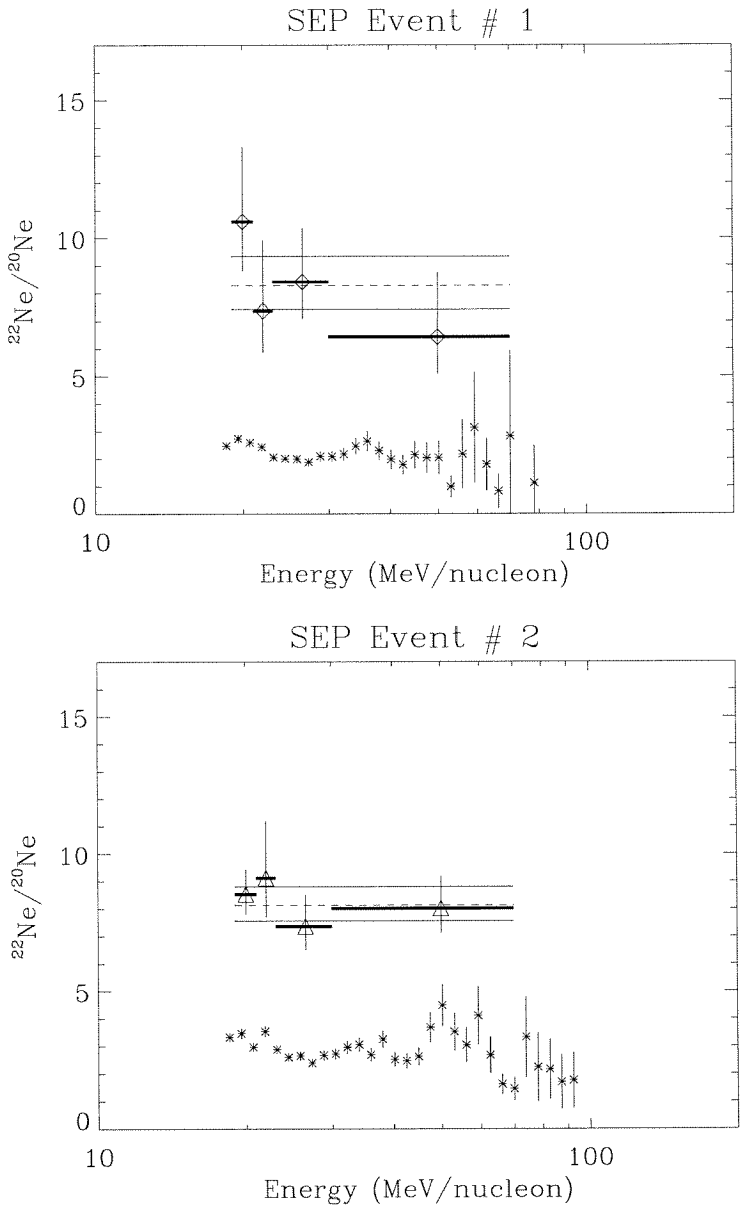

Figure 5.23: $^{22}Ne/^{20}Ne$ energy dependence. The $^{22}Ne/^{20}Ne$ ratio is shown by the triangle symbols for particles in each Range, 0 through 4. Each point is plotted at the average energy for that range, and the horizontal lines show the energy interval for particles in that range at average angle of incidence. No ADCOR restriction is made on the data, nor any invariant latitude restriction. The χ^2_ν is less than 2. The dashed lines represent the average over all ranges, and the solid lines represent the uncertainty. The asterisk symbols show the O/C ratio as a function of energy.

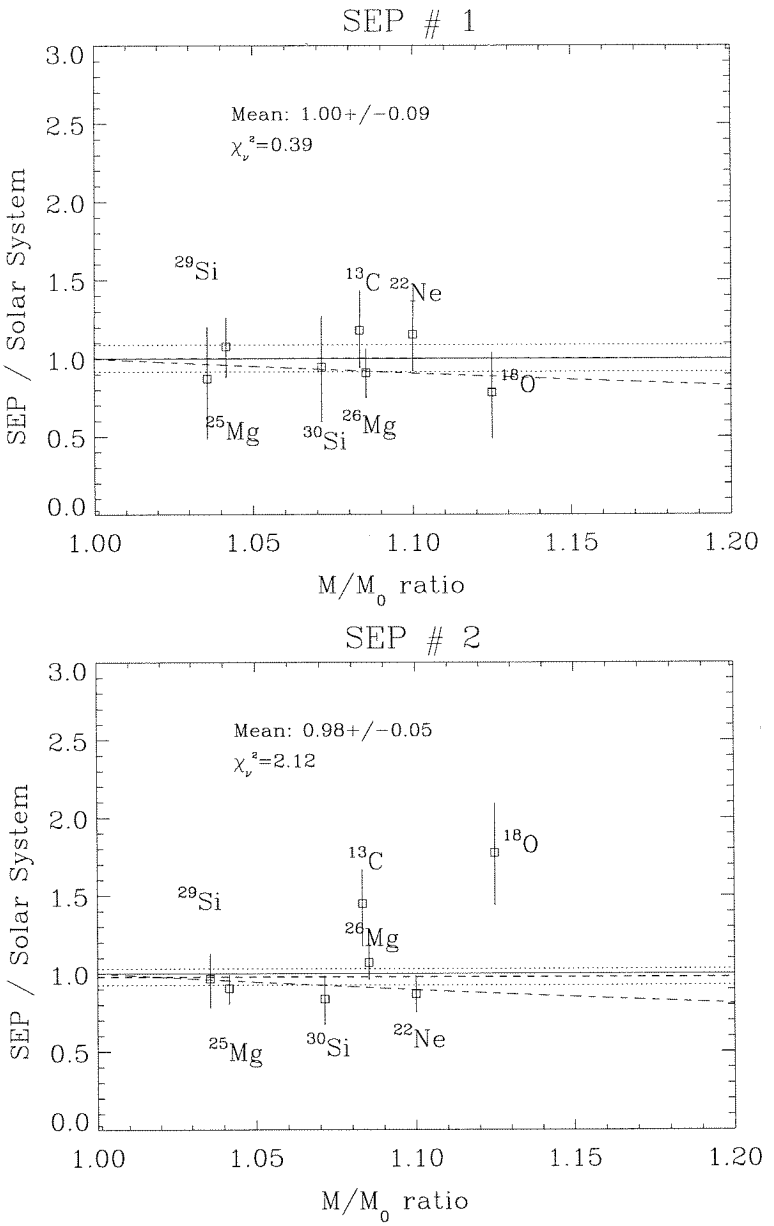

Figure 5.24: The ratio of the measured isotopic ratios at 1 AU to those listed in Anders and Grevesse (1989) plotted as a function of the ratio of the mass to the mass of the dominant isotope for each element. A solid line is drawn at a ratio equal to one. The weighted average ratio for all the measurements is listed, and is shown by upper the dashed line. The upper and lower uncertainties on the mean are shown by the dotted lines. The expected fractionation due to the Q/M effect, discussed in the next section, is shown by the lower dashed line.

that of the corona. The first attempt to infer coronal isotopic abundances from SEP measurements was made by Mewaldt and Stone (1989).

This correction for acceleration and transport for elements is a power-law in the charge-to-mass (Q/M) ratio, as discussed in Section 4.4. Since heavier isotopes have a lower charge to mass ratio than lighter ones, this affects the isotopic ratio measurements. Given an index, α, the enhancement of an isotope M_j with respect to a lighter isotope M_i is then:

$$f_{ij} = \left(\frac{M_i}{M_j}\right)^{\alpha} (M_i < M_j) \tag{5.25}$$

In Section 4.4 the value of α for each SEP event was calculated. The resulting correction factors are given in Table 5.12. The most significant correction to the measured ratios is for ^{18}O in the second event, which enhances the $^{18}O/^{16}O$ ratio by a factor of 1.15.

The inferred coronal isotopic ratios are listed in Table 5.13, along with the solar system ratios from Anders and Grevesse (1989). Also shown is the difference between the measured ratios and the AG89 values, normalized to the uncertainty in the measurements. These are rather large for $^{13}C/^{12}C$ and $^{18}O/^{16}O$ in the second SEP event. To explore the behavior of all the isotopes, our measured abundances are divided by the solar system abundances, and plotted versus the mass ratio in Figure 5.25. The weighted mean and the standard deviation of the measurements is also shown.

5.8 Chapter Summary

The isotopic ratios of six elements have been measured. The abundances in the first SEP event appear to be quite consistent with the solar system measurements, while ^{13}C and ^{18}O appear to be overabundant with respect to the solar system abundances of Anders and Grevesse (1989). How do these results compare to previous measurements of SEP composition? Can they reveal anything about the relation-

TABLE 5.12

Correction factors used to derive coronal isotopic abundance ratios from observed SEP isotopic abundance ratios.

Mass Ratio	30 Oct. Event	2 Nov. Event
$^{13}C/^{12}C$	1.076 ± 0.048	1.096 ± 0.025
$^{14}C/^{12}C^{*}$	1.152 ± 0.099	1.194 ± 0.053
$^{15}N/^{14}N^{*}$	1.066 ± 0.041	1.083 ± 0.022
$^{17}O/^{16}O^{*}$	1.057 ± 0.036	1.072 ± 0.019
$^{18}O/^{16}O$	1.114 ± 0.074	1.145 ± 0.039
$^{21}Ne/^{20}Ne^{*}$	1.046 ± 0.029	1.058 ± 0.015
$^{22}Ne/^{20}Ne$	1.092 ± 0.058	1.116 ± 0.031
$^{25}Mg/^{24}Mg$	1.038 ± 0.024	1.048 ± 0.012
$^{26}Mg/^{24}Mg$	1.076 ± 0.048	1.096 ± 0.025
$^{29}Si/^{28}Si$	1.033 ± 0.020	1.041 ± 0.011
$^{30}Si/^{28}Si$	1.066 ± 0.041	1.083 ± 0.022

*- Only upper limits to these ratios are measured.

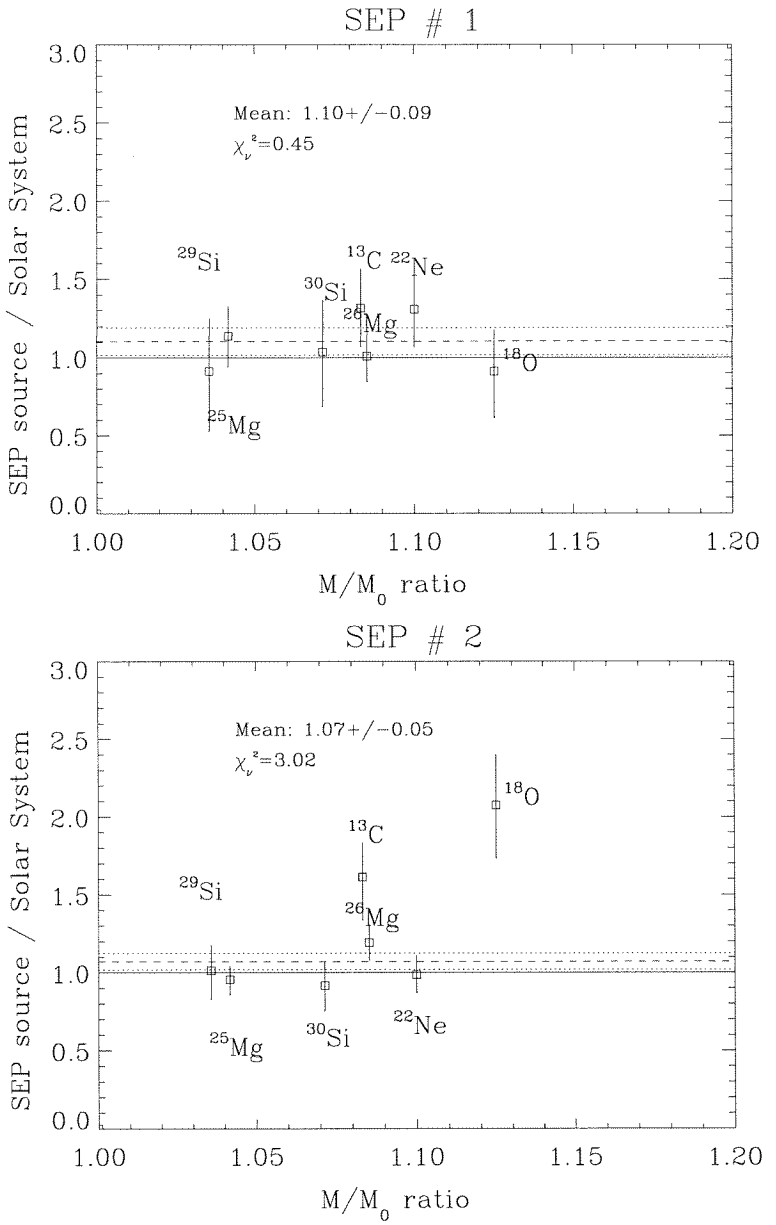

Figure 5.25: Ratios of the inferred coronal isotopic ratios to those listed in Anders and Grevesse (1989). A solid line is drawn at a ratio equal to one. The weighted average of all the ratios is listed, and shown by the dashed lines. Its uncertainties are shown by the dotted lines. The ratios are fairly consistent with the solar system values for the first SEP event, yet for the second event there are overabundances of ^{13}C and ^{18}O. Note that the ratios are not substantially different than the isotopic ratios at 1 AU (Figure 5.24), indicating that the effect of acceleration and propagation on the isotopes is not large.

TABLE 5.13

SEP isotopic ratios corrected to coronal composition. Also shown is the difference between each measurement and AG89 value, divided by the uncertainty in the measurement.

Mass	Isotopic Ratio (percent)			Std. Deviations from AG89	
Ratio	10/30 Event	11/02 Event	AG89	30 Oct. Event	2 Nov. Event
$^{13}C/^{12}C$	$1.44^{+0.28}_{-0.27}$	$1.79^{+0.25}_{-0.31}$	1.110	1.23	2.20
$^{14}C/^{12}C$	$< 0.17^{+0.08}$	$< 0.10^{+0.05}$	0.000	-	-
$^{15}N/^{14}N$	$< 0.29^{+0.30}$	$< 0.96^{+0.35}$	0.369	-	-
$^{17}O/^{16}O$	$< 0.06^{+0.06}$	$< 0.09^{+0.07}$	0.038	-	-
$^{18}O/^{16}O$	$0.18^{+0.05}_{-0.06}$	$0.42^{+0.07}_{-0.07}$	0.201	-0.40	3.12
$^{21}Ne/^{20}Ne$	$< 0.11^{+0.56}$	$< 0.99^{+0.41}$	0.243	-	-
$^{22}Ne/^{20}Ne$	$9.27^{+1.58}_{-1.73}$	$7.09^{+0.88}_{-0.85}$	7.310	1.13	-0.25
$^{25}Mg/^{24}Mg$	$14.24^{+2.35}_{-2.49}$	$12.01^{+1.11}_{-1.24}$	12.600	0.66	-0.53
$^{26}Mg/^{24}Mg$	$13.74^{+2.17}_{-2.28}$	$16.41^{+1.53}_{-1.53}$	13.900	-0.08	1.64
$^{29}Si/^{28}Si$	$4.56^{+1.70}_{-1.93}$	$5.10^{+0.83}_{-0.93}$	5.070	-0.30	0.03
$^{30}Si/^{28}Si$	$3.40^{+1.11}_{-1.17}$	$3.04^{+0.51}_{-0.54}$	3.360	0.04	-0.62

ship between solar wind and SEPs, or perhaps between particles implanted in lunar material and SEPs? We investigate these questions in the next chapter.

Chapter 6

Discussion

In this chapter we discuss how the isotopic ratios measured by MAST relate to other studies of isotopic composition. First, we compare our results to previous *in situ* measurements of solar energetic particles, and ask whether the measurements indicate any trends or fractionation effects. Next we compare our inferred solar energetic particle (SEP) source composition to that of the solar wind, both as measured using solar wind collection foils during the Apollo program, and as measured recently by instruments on spacecraft. We then address the question of how our measurements compare to standard isotopic ratios of the solar system, as established from measurements of terrestrial and meteoritic material, as well as from measurements of the solar wind.

As a final topic, we discuss past, present, and future instruments for measuring SEP isotopic composition in the ~10 to 100 MeV/nucleon energy range. We discuss the benefits of a SAMPEX-type mission, and suggest possibilities for future instruments.

6.1 SEP Isotopic Composition

In this thesis we have described the measurements of six heavy elements in two individual SEP events. While the composition of helium isotopes has been explored for many individual SEP events (see, e.g., Reames 1990), the only other

measurement of the isotopic composition of the Z>3 isotopes in a single gradual SEP event was made in 1979 with the ISEE-3 spacecraft (Mewaldt et al. 1984, 1989). Other reports of SEP isotopic composition used particles measured during several SEP events in order to build up sufficient statistics (Dietrich and Simpson, 1979, 1981; Simpson et al. 1984). The uncertainties on these measurements are all rather large; the isotopic ratios as reported by these groups are listed in Table 1.3. Our measurements utilize roughly five times more particles than all these previous measurements, and increase the SEP isotopic data set greatly, as shown in Table 6.1.

As noted by Mewaldt and Stone (1989), and discussed in Section 5.7, isotopic abundances should be fractionated as a function of their charge-to-mass ratio, just as the elements are. However, in our analysis we found that the size of this effect is much smaller than the uncertainties in our measurements (see Figure 5.25). Larger fractionation effects are expected in SEP events which have higher Fe/O ratios, and so a comparison of our results with the SEP isotopic measurements from other groups may show this fractionation better than our data set alone.

The Fe/O ratios from each SEP data set are listed in Table 6.1. Since the isotopic ratios measured by Dietrich and Simpson (1979,1981) are made over a number of SEP events, the Fe/O ratios listed are averages of the Fe/O ratio in each of the SEP events, weighted by the number of particles from each event used in the isotopic ratio. The measurements reported by Simpson et al. (1984) are an average over 4 SEP events which occurred from June through December of 1981.

Figure 6.1 shows all of the reported isotopic ratios as measured in interplanetary space. Each one is normalized to the AG89 solar system ratios, and plotted versus the Fe/O ratio as listed in Table 6.1. Note that no other group reported finite measurements of $^{30}Si/^{28}Si$.

The plots show that the ensemble of measurements are fairly consistent with the expected Q/M fractionation. There are a few statistically significant deviations in which the isotopic ratios are more than 1.5 sigma above the AG89 values. The $^{13}C/^{12}C$ and $^{18}O/^{16}O$ ratio in the MAST 11/2/92 SEP event are high by 1.6 and 2.3 sigma, respectively. The HIST measurement of $^{22}Ne/^{20}Ne$ is 1.8 sigma above the AG89 value.

TABLE 6.1

A comparison of the four analyses of SEP isotopic composition, ordered by the Fe/O ratios of the SEP events (see text). Also listed for comparison is the number of neon and magnesium nuclei used in each analysis.

Time Period	Fe/O ratio	Ne	Mg	Reference
1974-78	0.519	127	-	Dietrich and Simpson (1979)
9/23-9/27 1978	0.080	300	191	Mewaldt et al. (1979,1984)
1974-79	0.336	-	228	Dietrich and Simpson (1981)
5/10/82-12/5/82	0.004	~103	~112	Simpson et al. (1984)
10/31-11/2 1992	0.075	723	734	this work
11/2-11/7 1992	0.113	2005	2590	this work

When these ratios are corrected for Q/M effects, the HIST ratio rises to 2.4 sigma above the AG89 value, while the ^{13}C and ^{18}O ratios from the second MAST event rise to 1.8 and 3.1, respectively. Thus, the Q/M correction only increases the discrepancy with the AG89 ratios. In contrast, all the other isotopic ratios measured in the HIST event and in the second MAST event are all in good agreement with the AG89 values. And the isotopic ratios for the first MAST event agree quite well with the AG89 values. We are left to conclude that while the majority of the SEP isotopic ratios are consistent with AG89, there are three outliers which are statistically significant, indicating that some unknown fractionation is occurring.

Each of the isotopic ratios in Figure 6.1 can be corrected for Q/M fractionation using the technique described in Section 4.4. The values of the Q/M fractionation index, α, are only available for our two SEP events and the 9/23/78 SEP event. We approximate α for the other SEP events using the iron to oxygen ratio as a surrogate, as was done in Mewaldt and Stone (1989),

$$\alpha = \frac{\ln\left[(Fe/O)_f/(Fe/O)_c\right]}{\ln\left[(Q/M)_{Fe}/(Q/M)_O\right]} \tag{6.1}$$

The quantity $(Fe/O)_f$ is the observed value of the iron to oxygen ratio in

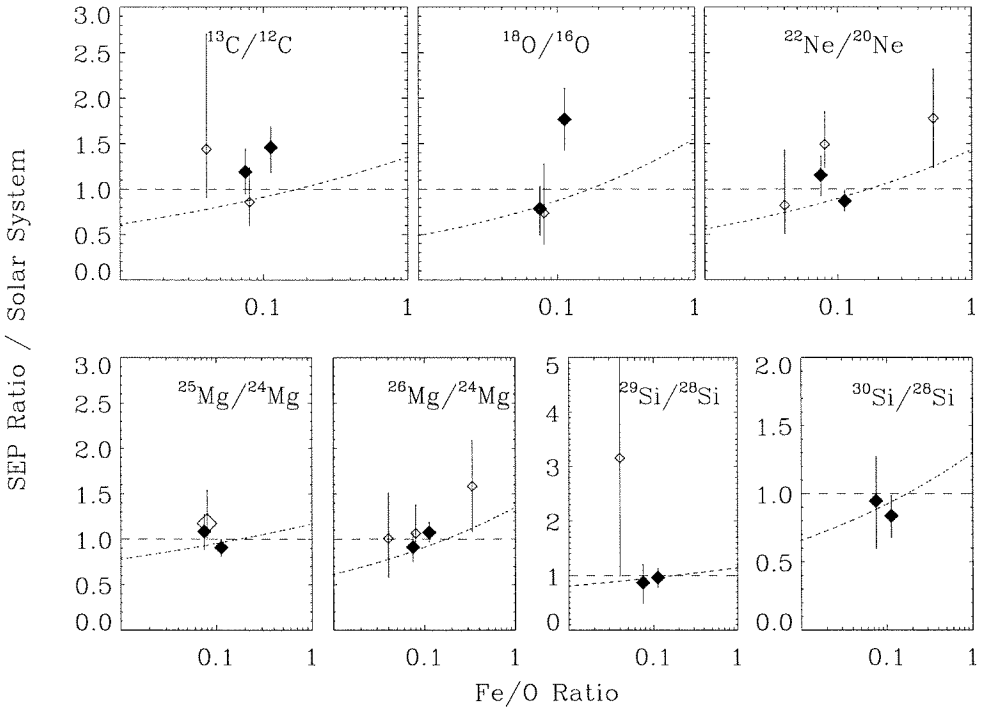

Figure 6.1: Comparison of the SEP isotopic ratios observed in interplanetary space as a function of the ratio of iron to oxygen for the SEP events. The filled symbols are from this study, while the open symbols are from earlier measurements of SEP isotopes. The measurements are ordered according to their Fe/O ratios, as listed in Table 6.1. The dotted lines show the expected Q/M fractionation, based on the Fe/O ratio of each SEP event.

the SEP event and $(Fe/O)_c$ is the coronal value of the iron to oxygen ratio (see Table 4.3). The quantity $(Q/M)_{Fe}$ is the charge to mass ratio of iron, and $(Q/M)_O$ is that ratio for oxygen (see Table 4.4). This represents the fractionation of low Q/M elements with respect to high Q/M elements. Since a heavy isotope has a lower Q/M value than a light isotope of the same elements, the heavy to light ratio will follow the Fe/O ratio, in that a Fe/O ratio lower than the coronal Fe/O ratio means that the observed heavy-to-light isotope ratio will be low also. Since both of the SEP events observed by MAST have a low Fe/O ratio as compared to the coronal Fe/O ratio, those isotopic ratios are increased by the Q/M correction.

Let the masses of a pair isotopes in an isotopic ratio be designated M_i and M_j, with $M_j > M_i$. The isotopic abundance ratio of the heavy isotope to the light one can then be corrected for Q/M fractionation using the formula

$$R_{\text{source}} = \left(\frac{M_i}{M_j}\right)^{\alpha} R_{\text{observed}} \tag{6.2}$$

where R_{observed} is the abundance ratio of the heavy isotope to that of the light isotope. The correction factor, $\left(\frac{M_i}{M_j}\right)^{\alpha}$, is plotted as the dotted line in Figure 6.1.

Each ratio can be corrected for the Q/M fractionation to yield the isotopic ratio at the source. The corrected ratios, normalized to the AG89 ratios, are shown in Figure 6.2 as a function of Fe/O. Many of the isotopic abundances shown in Figure 6.2 are greater than the solar system ratio. Compared to the AG89 ratios, there is an overall enhancement of $9 \pm 4\%$ in the heavy isotopes as a group, with a reduced chi-square equal to 1.21. If we assume that the average is equal to one (no enhancement of the source isotopes), the chi-square from that fit is equal to 1.38. Such a small difference in the chi-square indicates that the excess of heavy isotopes in the SEPs is not statistically significant, and thus we conclude that the overall composition of the SEP isotopes is consistent with the AG89 composition.

Since the differences between the interplanetary SEP isotopic ratios and the ratios corrected for Q/M effects are small, and since the elemental composition strongly indicates that the Q/M effect is present, we adopt the Q/M-corrected isotopic ratios, as listed in Table 5.13, when comparing our results to solar wind isotopic ratios.

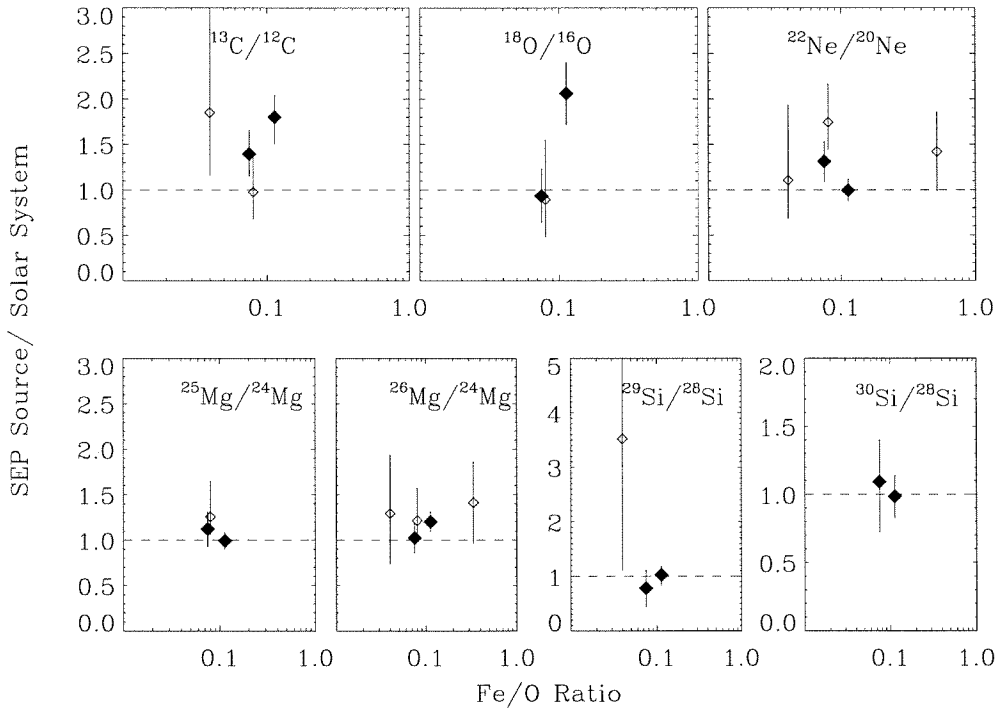

Figure 6.2: The SEP isotopic abundance ratios corrected for acceleration and propagation effects, normalized by the solar system isotopic ratios (AG89). These are plotted versus the iron to oxygen ratio in each SEP event. The filled triangles are the data from this study, and the unfilled triangles are results from other studies.

6.2 Solar Wind

The solar wind is composed of solar coronal material, as are solar energetic particles. Their composition should be similar, and studies have found that the relative abundances of solar wind and SEPs exhibit a similar fractionation with respect to FIP and FIT. The charge states of solar wind and SEPs are also similar, though the solar wind has a lower charge state in general. Also, slow solar wind exhibits a FIP depletion of ~4 to 5, as observed in SEPs, while fast wind has a much lower FIP depletion of ~1.5 to 2 (von Steiger et al. 1997).

According to models for solar wind acceleration, the isotopic composition of the solar wind can be affected by two processes. First, the transport of material from the photosphere to the corona can deplete heavy isotopes relative to light ones. This effect is quite small, however, and is at most a few parts per thousand for magnesium isotopes (Bochsler et al. 1996; von Steiger and Geiss 1989). There is also expected to be a fractionation of isotopes due to mass fractionation of the solar wind as it is accelerated out of the corona, due mainly to Coulomb drag of the ions. The size of this effect is a few percent per mass unit (Geiss 1973; Kallenbach et al. 1997).

Of the four elements whose isotopic composition has been studied in the solar wind, only three can be compared to our measurements: oxygen, neon, and magnesium. The MASS instrument on the WIND spacecraft has returned data on oxygen and magnesium isotopic composition (Collier et al. 1998; Bochsler et al. 1996). The oxygen measurements were made over a period of 17 months (12/94 though 6/96), and were obtained for solar wind only from solar quiet times when the solar wind speed was between 315-400 km/s. The magnesium results were obtained over eight months (12/94 through 7/95), and include observations at high (v >400 km/s) and low (v <400 km/s) solar wind speeds. No variation of the magnesium composition between the high and low speed solar wind samples was seen at the 10% level in the study by Bochsler et al. (1996). However, there have been recent claims of a somewhat smaller dependence on solar wind speed (Wimmer et al. ISSI conference poster, 1998).

The MTOF instrument on the SOHO spacecraft has made measurements

on the solar wind neon isotopic composition (Kallenbach et al. 1997). The data were collected over the first 200 days of 1996. MTOF can measure isotopes over a range of solar wind velocities. Currently, the measurements of solar wind from 350 to 600 km/s indicate no change in the isotopic composition with solar wind velocity. However, longer periods of data acquisition will improve the accuracy of the results.

The solar wind isotope measurements from Table 1.4 and our SEP measurements from Table 5.13 are compared to the isotopic ratios adopted by AG89 in Figure 6.3. Note that the AG89 value for $^{22}Ne/^{20}Ne$ composition is based on the Apollo measurements of the solar wind, and so the agreement between the SOHO measurement and the AG89 ratio is to be expected.

Our SEP measurements agree fairly well with the solar wind measurements, with the exception of $^{18}O/^{16}O$ in the 11/2/92 SEP event. That ratio is 3.1 sigma higher than the AG89 value. This deviation is much larger than can be explained by Q/M fractionation as derived from elemental composition. And as Figure 5.16 shows, the measurement of this ratio is consistent at all values of the ADCOR level.

SOHO and WIND are still collecting data, and instruments aboard the newly launched ACE spacecraft will join them in the analysis of solar wind isotopes. The uncertainties in both the SEP and solar wind data sets will undoubtedly decrease in the near future, leading to a better understanding of the relationship between solar wind and solar energetic particles.

6.3 Statistical Analysis of SEP Isotopic Ratios

Is it possible that the high ratio of $^{18}O/^{16}O$ in the 11/2/92 SEP event is simply a statistical outlier? This question is addressed by applying the chi-square test to the measurements,the results of which are shown in Table 6.2. In this table we consider two questions. First, are the isotopic measurements of a given isotope pair consistent when comparing the ratio from each of the two SEP events with their weighted average, i. e. are the measurements self-consistent? The weighted average of the pair, by definition should have the best possible value of chi-square for that set of measurements. The results of this test are shown in the second column of

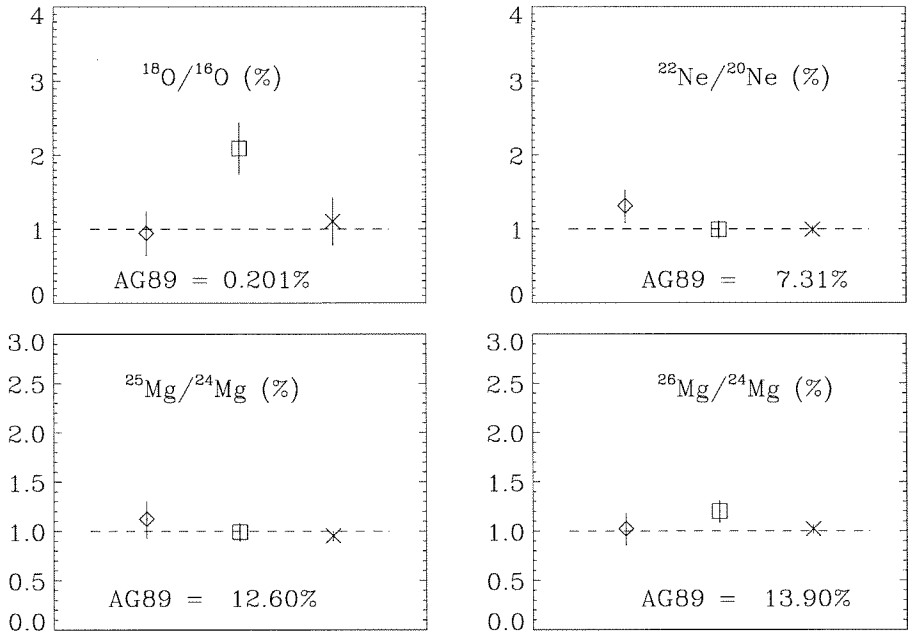

Figure 6.3: Comparison of *situ* measurements of solar wind and our measured SEP isotopic composition. Each measurement is normalized to the AG89 values, as given in Table 1.7. The symbols are: ◊- 31 October SEP Event, □- 2 November SEP Event, ×- solar wind. The neon values for the solar wind come from Kallenbach et al. (1997), the oxygen ratios are from Collier et al. (1998), and the magnesium ratios come from Bochsler et al. (1996). The horizontal dashed line at a value of one is drawn for reference.

Table 6.2. We find that all pairs are self-consistent, except for the $^{18}O/^{16}O$ ratio, which only has a 3.6% chance of arising from a distribution which has as its mean the weighted average of the pair. A second question to ask is whether any given pair of measurements is consistent with the AG89 values? This will naturally be as probable, or less probable than self-consistency between the pair. As shown in column three of Table 6.2, the measurements are for the most part consistent with the AG89 ratios. However, the ratios for $^{13}C/^{12}C$ and $^{18}O/^{16}O$ are quite unlikely.

Yet as more measurements are made, the chance of getting measurements which are outliers becomes more probable. There are 14 isotopic ratio measurements reported in this study, and so it is fair to ask how likely it would be to obtain this set of isotopic ratios when treated as a group. Again the ratios are probed for self-consistency and for consistency with the AG89 ratios. The result is that there is a 73% chance that the isotopic ratios are self-consistent. There is a 10% chance that the measurements are consistent with AG89. And so by considering the 14 measurements together, it is found that the apparent variations in the isotopic composition have a 10% chance of being due to statistical outliers in the data, and not to unknown fractionation effects.

6.4 Solar System Isotopic Standards

Deciding which sample of neon is most representative of the solar system has proven problematic in the past. Early measurements of SEP composition found high $^{22}Ne/^{20}Ne$ ratios (Dietrich and Simpson 1979; Mewaldt et al. 1979), which supported Cameron's choice of neon-A as representative of solar system neon in his compilation of solar system abundances (Cameron 1982). This ratio is much greater than the solar wind neon reported by Geiss et al. (1972), which Anders and Grevesse (1989) chose to use in their compilation of solar system composition. Our results are more in agreement with the $^{22}Ne/^{20}Ne$ values in neon-C and the solar wind, and not with neon-A. We interpret this to support the hypothesis that SEPs and the solar wind arise from the same reservoir of material, a reservoir which has a $^{22}Ne/^{20}Ne$ ratio more like that of the solar wind than neon-A. If SEPs are in general enhanced in

TABLE 6.2

The likelihood that each pair of ratios is self-consistent or consistent with the AG89 ratios. Also shown are the likelihoods that the full set of measurements is self-consistent or consistent with the AG89 ratios.

Isotope	Consistent with...	
Pair	...pair average	...AG89
$^{13}C/^{12}C$	69.2%	2.9%
$^{18}O/^{16}O$	3.6	1.1
$^{22}Ne/^{20}Ne$	52.1	50.2
$^{25}Mg/^{24}Mg$	71.0	70.0
$^{26}Mg/^{24}Mg$	63.4	28.0
$^{29}Si/^{28}Si$	96.8	96.4
$^{30}Si/^{28}Si$	95.8	83.3
As a group	72.8%	9.5%

neutron-rich nuclei, as suggested in Section 6.1, then neon-C may represent a long-term average of the SEP composition.

In summary, we have measured the isotopic composition of carbon, oxygen, neon, magnesium and silicon in two large SEP events. Both events are fairly normal gradual-type events, with well-organized energy spectra, and well-ordered elemental composition. The isotopic abundances that we have observed are generally in fair agreement with the solar system abundances as compiled by Anders and Grevesse (1989), and with the abundances in the solar wind. However, in two cases, we observe overabundances in both $^{13}C/^{12}C$ and $^{18}O/^{16}O$. While earlier measurements have found a high $^{22}Ne/^{20}Ne$ ratio, our measurements are in much better agreement with the solar wind neon composition. We interpret these results to support the idea that SEP isotopic composition can vary from event to event, yet there is presently no strong evidence that the overall SEP isotopic composition is significantly different from that of the solar wind.

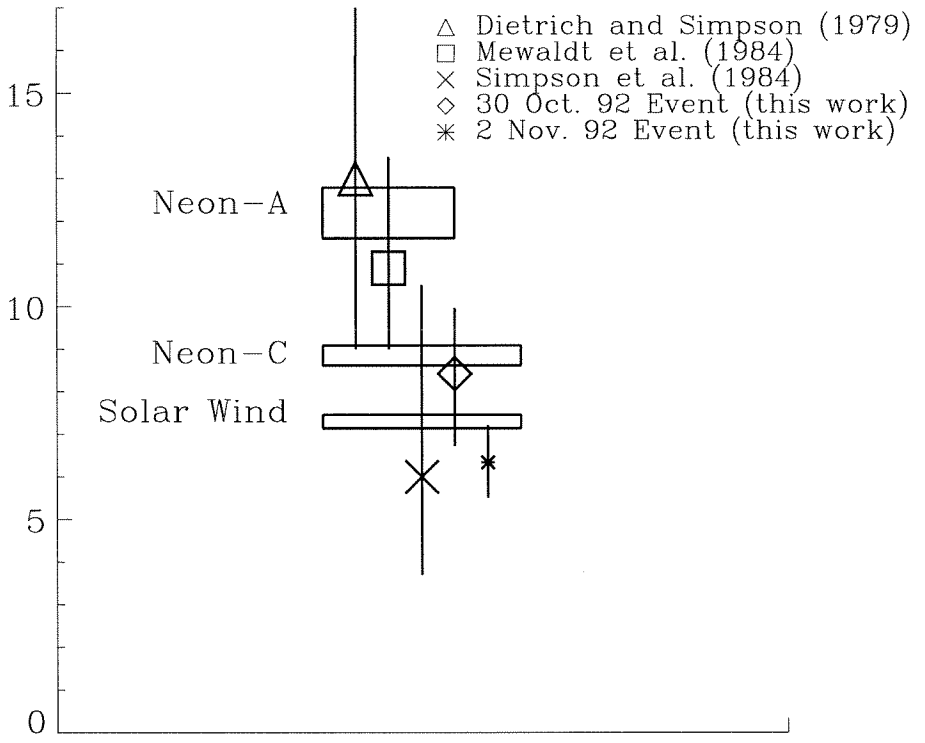

Figure 6.4: The isotopic $^{22}Ne/^{20}Ne$ as measured in solar energetic particles, compared to other samples of neon. Neon-A is the neon component trapped in carbonaceous chondrites. Neon-C is a component of neon observed first in meteorites, and more recently in lunar material by Wieler et al. (1986). Neon-C is attributed to the implantation of particles with energies of ~1 MeV/nucleon. The solar wind value is from Geiss et al. (1972).

6.5 MAST and Future SEP Experiments

The MAST instrument was designed in ~1980, using the best technology available at the time. MAST has a greater collecting power than similar instruments which have flown before (see Table 6.3). For SEP investigations there are three important factors which determine an instrument's relative collecting power: the geometry factor, the energy threshold, and the event rate, which is often limited by the rate allocation and telemetry. Of course, an underlying requirement in each of these is the ability to measure particle mass, and the ability to measure heavy ions efficiently during intense particle events. In the ensuing discussion, two instruments listed in Table 6.3 should be noted: HIST and SIS. The Heavy Isotope Spectrometer Telescope (HIST) was the Caltech experiment on the ISEE-3 spacecraft. Its hodoscope consisted of two two-sided matrix detectors. Each individual strip was connected to a discriminator, and the total signal from the device was connected to an ADC. This instrument flew in 1978, and lasted approximately 110 days until a component in the instrument logic failed. The Caltech Solar Isotope Spectrometer (SIS) was developed quite recently, using the latest technology, and is now in space aboard the Advanced Composition Explorer. Its hodoscope also consists of two two sided matrix detectors. However, in this case each matrix strip is individually pulse-height analyzed. The SIS instrument actually consists of two large-area solid state telescopes. In terms of collection power, MAST is more capable than HIST, yet less capable than SIS. Yet as will be discussed later, MAST has another unique capability which makes it presently irreplaceable.

An instrument's geometry factor, described in detail in Section 3.4.1, is more or less the effective area of the telescope in terms its physical size and field of view. Earlier instruments were limited in geometry factor mainly due to the size of sufficiently pure silicon wafers which could be manufactured at the time. That technology has been steadily improving due to the value of large pure silicon wafers to the semiconductor industry. Whereas HIST used detectors ~1.5 cm in radius, MAST has detectors which are 2.5 to 3 cm in radius. In more recent instruments such as SIS, the detector radii are large as ~4.6 cm, and SIS consists of two such telescopes. Since

TABLE 6.3

Comparison of experiments for measuring SEP isotopic composition in the ~10 to 100 MeV/nucleon energy range. The energy intervals are approximate.

Instrument/ Spacecraft	Launch Year	Geom. Factor (cm^2sr)	Duty Cycle	Energy Range (MeV/nuc.) ^{12}C	^{28}Si
HIST/ISEE-3	1978	0.70	1	6-39	12-40
Phoenix-1/S81-1	1982	1.5	0.33	11-24	17-38
MAST/SAMPEX	1992	11	0.33	15-90	20-220
SIS/ACE	1997	40	1	6-100	8-150

the geometry factor grows roughly as the fourth power of the radius, these advances have allowed the geometry factors of single charged-particle telescopes to increase by a factor of ~40 when comparing HIST to SIS.

Energy threshold is important because the intensity of particles in SEP events decreases quickly with increasing energy. For example, the flux of heavy nuclei in a typical SEP event falls as a power law with spectral index ~-2 to -4. If the threshold of an instrument can be lowered by a factor of 10, then the instrument will be sensitive to 10^2 to 10^4 times more particles. Yet the ΔE-E' technique for measuring mass requires that a particle penetrate at least two detectors, that the angle of incidence be measured, and that the thickness of the ΔE detector be known. This requires a hodoscope. In the MAST analysis, particles which did not have a well-defined signal in each of the four matrix detectors could not be used for obtaining mass.

Matrix detectors such as used in MAST can now be built as thin as ~50 μm. A MAST-type hodoscope could thus be 200 μm thick, as compared to the 460 μm thick hodoscope on MAST. One drawback, however, is that such a hodoscope would not be sensitive to carbon at high energies, due to the low amount of energy deposited in the matrix detectors by such nuclei. The MAST instrument had greatly simplified electronics thanks to the resistive-divider method for measuring particle position.

This was an important consideration, since complex electronics cost weight and power, which are two limited resources on spacecraft. On the SIS instrument, which has a greater amount of power (~17.8 W) allocated to it, each of the 64 strips on each matrix detector is individually biased and pulse-height analyzed. Each matrix detector has strips on both sides, enabling it to measure both X and Y positions. This means that only two detectors are required for its hodoscope, allowing the energy threshold to be much lower than that of MAST. Thus, the threshold for oxygen nuclei in SIS is ~8 MeV/nucleon, compared to ~17 MeV/nucleon in MAST. This factor of two decrease in threshold can become a factor of two to eight in terms of SEP particles measured, depending on the spectrum of the particles in a given SEP event.

The particle event rate must also be adequate. The HIST instrument could return pulse-height analyzed event data at a rate of ~1 per second. In normal operating mode, MAST can return about 48 PHA events per second, of which 12 are $Z \geq 3$ events. The main limitation to the SAMPEX data rate is the memory of the on-board solid-state recorder and the number of times the spacecraft can dump its data to a ground station each day. Currently SAMPEX dumps its data once per day, although the orbit sometimes allows up to three data dumps per day with the Wallops Flight Facility. With advances in ground-station technology, it may be possible to download data to ground much more frequently in the near future, using a network of mobile ground-stations scattered across the globe. The SIS instrument can return from 10-15 events per second. It sits at the L1 Lagrange point, and so requires time from the Deep Space Network in order to transmit its data to Earth.

Of course, a large area, low threshold, and high event rate are not sufficient if the instrument cannot sufficiently resolve particle mass. For example, the trajectory systems on both the Phoenix-I and MAST instruments are affected by chance coincidences. In order to measure mass, high counting-rate periods must be excluded from the data analysis in these instruments. There are two routes for solving this dilemma: reading out strips individually or adding redundancy to the hodoscope. For example, a six-element hodoscope could be made with 60 μm detectors which would still be less thick than the MAST hodoscope. Such redundancy might allow particles with poor trajectories to be identified and removed from the data.

It might seem that the best solution is to have two-sided matrix detectors as in the SIS instrument, with each strip individually biased and read out. So far this solution is working well, as the SIS instrument team finds that particles which have coincidences can be identified, and that the mass resolution of particles both with and without coincidences is of good quality since the strips are individually pulse-height analyzed. However, two-sided matrix detectors have a drawback in that the energy deposited in such detectors can be difficult to measure properly. The gain and offset of the electronics which read out each strip must be known, and these quantities can change over time. In order to take advantage of the lower energy threshold, the hodoscope must be used for ΔE-E' measurements, and so their energy resolution must be adequate.

A novel way to improve hodoscopes for charged-particle telescopes would be to use interdigitated pixel PIN detectors (IPPDs). These devices were developed and studied in a collaboration between the Center for Space Microelectronics at the Jet Propulsion Laboratory and the Space Radiation Laboratory at Caltech (Cook et al. 1994). In such devices, one side of the detector is divided into a two-dimensional array of pixels using photolithographic techniques. The pixels collect holes on both the pixel rows and columns, which are connected to simple discriminator circuits. The discriminator signals locate the particle position by row and column, and also indicate when chance coincidences occur. The other side of the detector has a flat electrode, from which the electrons are measured, yielding a total energy. The electronics for such a device are simple, requiring a chain of discriminators, and one pulse-height analyzer. These devices have been tested in the laboratory with pixel sizes of 40 μm, but are not yet fully developed for instruments on space missions.

Perhaps as important as the ability to measure particle mass is MAST's ability to measure the mean charge states of particles at SEP energies (Leske et al. 1995). This is due to the fact that SAMPEX is in low-Earth orbit, and can use the Earth's magnetic field to "filter" particles as a function of their rigidity. Rigidity is a vital concept for understanding the acceleration and propagation of SEPs, and so measurements of their charge states are essential. Until the SAMPEX mission, the only SEP charge state measurements were made at $\sim$0.4 to 4 MeV/nucleon (Luhn

et al. 1985), well below the SEP energies of ~10 to 100 MeV/nucleon, where isotope measurements have been made to date. SAMPEX changed all that, measuring for the first time the average charge states of SEPs at 10s of MeV/nucleon (Leske et al. 1995). The results showed that the charge states of most elements were consistent with the measurements of Luhn et al. (1985). However, iron differed in that its charge state appeared to increase with energy, from 11.04± 0.22 at ~0.5 to 5 MeV/nucleon, to 15.18± 0.73 at ~15 to 70 MeV/nucleon. This suggests that SEP charge states may vary with energy in typical events. If so, then having the ability to measure the high energy charge states in each event becomes essential to interpretation of the isotopic and elemental composition. In this respect, measuring charge states using the Earth's field is vital to the interpretation of the SEP isotopic composition measurements, and being in polar orbit is thus a benefit, in spite of the impact on the duty cycle for composition studies.

Of course, an instrument in low-Earth orbit (LEO) can only observe SEPs over the geomagnetic poles, which constitute approximately one-third of the spacecraft's orbit. In this respect, an instrument located outside of the Earth's magnetosphere can collect three times as many particles as one in low Earth orbit.

The ideal solution to the dilemma of providing both charge state measurements and a sufficient number of particles for isotope analysis would be to have a large area instrument such as SIS/ACE in interstellar space, and to have a similar instrument in low-Earth orbit measuring charge states. The LEO instrument would not be required to measure mass, only to clearly resolve elements and measure their kinetic energy. An instrument such as PET would also be useful on such a mission, since the large fluxes of protons and alphas allows one to measure the location of particle cutoffs on each orbit, allowing one to compensate for changing cutoffs as the geomagnetic field is disrupted by the interplanetary disturbances often associated with the SEP event.

Chapter 7

Summary/Conclusions

In this work we have presented measurements of the isotopic composition of solar energetic particles in the energy range of ~15 to 70 MeV/nucleon in two large SEP events which occurred in late 1992, including the elements carbon, nitrogen, oxygen, neon, magnesium and silicon. The data were obtained with the MAST instrument on the polar-orbiting satellite, SAMPEX, and result in improved statistical accuracy over any previous SEP isotopic measurements. The goal of this research has been to understand the nature of the SEP events, and to determine the composition of the SEP source material, for comparison with other measurements of solar system abundances.

This analysis has required a firm understanding of the MAST instrument, which is composed of a set of solid-state detectors that measure the energies deposited by incident particles. A hodoscope at the front of the instrument provides trajectory measurements, which are necessary for obtaining particle mass. The instrument was extensively calibrated before flight, and these calibrations aided in the analysis of flight data.

The theoretical mass resolution of the instrument has been studied, and the response of the instrument has been investigated through Monte Carlo techniques. These investigations included studies of the effect of charge state fluctuations on the mass measurements, of the instrument geometry factors for various nuclei, and of the effect of chance coincidences due to low-energy protons on the mass measurements.

The position measurements of the hodoscope and the energy resolution of the detectors make it possible to identify particle charge, mass and kinetic energy. Multiple, independent measurements of each particle's mass make it possible to achieve improved mass resolution over any single ΔE-E' measurement. Using standard statistical techniques, a chi-square quality was assigned to each particle, helping to identify background effects, such as particles exiting through the side of the telescope.

These studies have also required careful consideration of the nuances involved with an instrument in low-Earth orbit. Such an instrument has a relatively low duty cycle as the spacecraft is in regions of the magnetosphere inaccessible to interplanetary particles for approximately two-thirds of every orbit. The composition of the observed particles is affected by the Earth's magnetosphere, and is complicated by changes in the particle environment and the instrument livetime over the course of the orbit, so care must be taken to account for such geomagnetic biases to the elemental and isotopic composition.

Using observations over the geomagnetic polar regions, the instrument provided measurements of the interplanetary fluxes of particles. Two large SEP events began on 10/30/92 and 11/2/92. Each event was associated with a gradual rise in solar X-ray flux, Type II solar radio bursts, and a coronal mass ejection. The spectra of the heavy elements in each event was observed to follow an exponential in energy per nucleon, with the same e-folding energy for all observed elements, making it possible to measure the relative elemental abundances in these events. The elemental composition was found to be typical of gradual-type SEP events, and could be related to solar coronal and photospheric abundances in an organized manner, taking into account the charge to mass ratios of the elements in these SEP events, which were also measured by MAST. This is the first time that the charge states of >10 MeV/nucleon SEPs have been incorporated into the analysis of SEP elemental and isotopic composition. Observations of the elements also found a depletion of high-FIP elements as compared to the solar photosphere, which is a well-known characteristic of SEP material. The element abundances are also well-organized by the first-ionization time, a parameter which has been suggested for describing the fractionation of elements in the solar wind.

The isotopic abundances were measured using a maximum-likelihood technique in which the data itself serves as a template for the instrument response. This technique proved superior to the method of fitting histograms of the data to Gaussian shapes, as used in earlier studies of SEP isotopes. In particular, this approach made it possible to include a large fraction of the data, since the results of the maximum likelihood technique returned consistent values for a wider variety of selection criteria than was possible using an assumed Gaussian-shaped response function. The deduced isotopic ratios were consistent over a range of chi-square values. The dependence of the deduced isotopic ratios on the instrument counting rate was also explored, since a restraint on the counting rates was necessary to avoid the degradation of mass resolution due to chance coincidences of the heavy ions with low-energy protons. Although the isotopic ratios measured in the 11/2/92 SEP event were not greatly affected by counting rates, the data in the 10/30/92 event showed contamination at the highest counting rates. As a result, such periods of high counting rates were excluded from the final data set to avoid contamination.

Measurements of the elemental composition were used to test how various selection criteria could bias the isotopic composition, relying on the mean charge state measurements by Leske et al. (1995) to organize these effects by the charge to mass ratio. The elemental composition was found to be biased by geomagnetic effects and by the counting rate restrictions imposed on the data. The effect of acceleration and/or propagation on the elemental composition was also investigated, which allowed such effects to be corrected for in the isotopic abundances, yielding measurements of the SEP source material.

The isotopic ratios, $^{22}Ne/^{20}Ne$, $^{25}Mg/^{24}Mg$, $^{26}Mg/^{24}Mg$, $^{29}Si/^{28}Si$ and $^{30}Si/^{28}Si$ are in good agreement with the solar system values of Anders and Grevesse (1989) in both of the SEP events studied. This is the first time measurements of silicon isotopes in the SEPs have been made. Our measurements of $^{22}Ne/^{20}Ne$ are consistent with the $^{22}Ne/^{20}Ne$ ratio found in the solar wind and in neon-C. This is in contrast to previous studies of SEP composition which found larger $^{22}Ne/^{20}Ne$ ratios which were similar to the neon-A component which is found as gas trapped in certain classes of meteorites.

The ratios of $^{13}C/^{12}C$ and $^{18}O/^{16}O$ ratio in the 11/2/92 SEP event are higher than the AG89 values by a fator of about two. The reason for these high isotopic ratios is puzzling, considering the general agreement of the other measurements with the AG89 values. Taken as a whole, the probability that the isotopic ratios reported here are consistent with the AG89 values is 10%. This means that the high $^{13}C/^{12}C$ and $^{18}O/^{16}O$ measurements could simply be due to statistical fluctuations.

The SEP isotopic ratios reported here generally support both the assumption that SEPs and solar wind come from the same reservoir of material, and the assumption that the coronal isotopic composition is consistent with the standard solar system abundances. These measurements are still at an exploratory stage; the uncertainties are large; and the limited number of observations of heavy isotopes in gradual SEP events at present prevents us from making definite conclusions about possible event-to-event variations in the SEP isotopic composition, or the isotopic composition of coronal material. It is hoped that in the near future, the combination of further measurements of SEP isotopic composition, perhaps by the SIS instrument on ACE, and of SEP charge states by the instruments on SAMPEX, can shed new light on this subject as the increasing solar activity in Solar Cycle 23 brings forth new SEP events to explore.

Bibliography

Aguilar-Benitz, M., R. M. Barnett, C. Csao, G. Conforto, R. L. Crawford, R. E. Cutosky, R. A. Eichler, S. Eidelman, D. E. Groom, K. Hagiwara, K. G. Hayes, and J. J. Hernandez (1992). Review of Particle Properties. *Physical Review D D45*, S1–S584.

Althouse, W. E., A. C. Cummings, T. L. Garrard, R. A. Mewaldt, E. C. Stone, and R. E. Vogt (1978). A Cosmic Ray Isotope Spectrometer. *IEEE Trans. Geoscience Electronics 208*, 204.

Anders, E. and M. Ebihara (1982). Solar-system Abundances of the Elements. *Geochim. Cosmochim. Acta 46*, 2363.

Anders, E. and N. Grevesse (1989). Abundances of the Elements: Meteoritic and Solar. *Geochim. Cosmochim. Acta 53*, 197–214.

Baker, D. N., G. M. Mason, O. Figueroa, G. Colon, J. G. Watzin, and R. M. Aleman (1993). An Overview of the Solar, Anomalous, and Magnetospheric Particle Explorer (SAMPEX) Mission. *IEEE Trans. Geosci. Remote Sensing 31*, 531.

Baker, S. and R. D. Cousins (1984). Clarification of the Use of Chi-Square and Likelihood Functions in Fits to Histograms. *Nucl. Instr. and Meth. 221*, 437.

Becker, R. H. (1980). Evidence for a Secular Variation in the $^{13}C/^{12}C$ Ratio of Carbon Implanted in Lunar Soils. *Earth Plan. Sci. Lett. 50*, 189–196.

Black, D. C. (1983). The Isotopic Composition of Solar Flare Noble Gases. *Astrophys. J. 266*, 889–894.

Black, D. C. and R. O. Pepin (1969). Trapped Neon in Meteorites-II. *Earth Plan.*

Sci. Lett. 6, 395–405.

Bochsler, P., M. Gonin, R. B. Sheldon, T. Zurbuchen, G. Gloeckler, D. C. Hamilton, and M. R. Collier (1996). Abundances of Solar Wind Magnesium Isotopes Determined with WIND/MASS. In D. Winterhalter, J. T. Gosling, S. R. Habbal, W. S. Kurth, and M. Neugebauer (Eds.), *AIP Conference Proceedings 382, Solar Wind Eight*, Volume 382, Washington, D. C. AIP.

Boyer, R., J. C. Henoux, and P. Sotirovski (1971). Isotopes of Magnesium in the Solar Atmosphere. *Solar Physics 19*, 330–337.

Breneman, H. H. and E. C. Stone (1985). Solar Coronal and Photospheric Abundances from Solar Energetic Particle Mesurements. *Astrophys. J. Lett. 199*, L57–L61.

Brown, H. S. (1949). Table of Relative Abundances of Nuclear Species. *Rev. Mod. Phys. 21*(4), 625–634.

Cameron, A. G. W. (1982). Elemental and Nuclidic Abundances in the Solar System. In C. A. Barnes, D. D. Clayton, and D. N. Schramm (Eds.), *Essays in Nuclear Astrophysics*, pp. 23. Cambridge: Cambridge Univ. Press.

Cash, W. (1979). Parameter Estimation in Astronomy Through Application of the Likelihood Ratio. *Astrophys. J. 228*, 939.

Collier, M., D. C. Hamilton, G. Gloeckler, G. Ho, P. Bochsler, R. Bodmer, and R. Sheldon (1998). Oxygen 16 to Oxygen 18 Abundance Ratio in the Solar Wind Observed by WIND/MASS. *J. Geophys. Res. 103*(A1), 7–13.

Cook, W. R. (1981). *Elemental Composition of Solar Energetic Particles.* Ph.D. thesis, California Institute of Technology.

Cook, W. R., A. C. Cummings, J. R. Cummings, T. L. Garrard, B. Kecman, R. A. Mewaldt, R. S. Selesnick, E. C. Stone, and T. T. von Rosenvinge (1993). MAST: A Mass Spectrometer Telescope for Studies of the Isotopic Composition of Solar, Anomalous, and Galactic Cosmic Ray Nuclei. *IEEE Trans. Geosci. Remote Sensing 31*, 557.

Cook, W. R., A. C. Cummings, R. A. Mewaldt, D. L. Williams, T. J. Cunningham, M. Mazed, and E. R. Fossum (1994). *Two-Dimensional Interdigitated Pixel Detector for Energetic Particle Spectrometers*, Volume 2267, pp. 9408. Unknown.

Cook, W. R., E. C. Stone, and R. E. Vogt (1980). Elemental composition of solar energetic nuclei. *Astrophys. J. Lett. 238*, L97–L101. Provided by the NASA Astrophysics Data System.

Cook, W. R., E. C. Stone, and R. E. Vogt (1984). Elemental Composition of Solar Energetic Particles. *Astrophys. J. 279*, 827–838.

Cook, W. R., E. C. Stone, R. E. Vogt, J. H. Trainor, and W. R. Webber (1979). Elemental Composition of Solar Energetic Particles in 1977 and 1978. In *Proc. of the 16th Internat. Cosm. Ray Conf., Kyoto, Japan*, Volume 2, pp. 2.

Cummings, A. C. and E. C. Stone (1990). Elemental Composition of the Very Local Interstellar Medium as Deduced from Observations of Anomalous Cosmic Rays. In *Proc. of the 21st Internat. Cosm. Ray Conf., Dublin, Ireland*, Volume 6, pp. 202.

Cummings, J. R., A. C. Cummings, R. A. Mewaldt, R. S. Selesnick, E. C. Stone, and T. T. von Rosenvinge (1993). New Evidence for Geomagnetically Trapped Anomalous Cosmic Rays. *Geophys. Res. Lett. 20*(18), 2003–2008.

Dietrich, W. F. and J. A. Simpson (1979). The Isotopic and Elemental Abundances of Neon Nuclei Accelerated in Solar Flares. *Astrophys. J. Lett. 231*, L91–L95.

Dietrich, W. F. and J. A. Simpson (1981). The Isotopic Composition of Magnesium Nuclei in Solar Flares. *Astrophys. J. Lett. 245*, L41–L44.

Fichtel, C. E. and F. B. McDonald (1967). Energetic Particles from the Sun. *Ann. Rev. Astron. Astrophys. 5*, 351–398.

Fisk, L. A. (1978). He-3-rich flares - a possible explanation. *Astrophys. J. 224*, 1048–1055. Provided by the NASA Astrophysics Data System.

Foukal, P. (1990). *Solar Astrophysics*. New York: John Wiley and Sons.

Garrard, T. L. (1994). Tennis: A New Standard for Data Formatting, Input, and Output. *American Institute of Physics 283*, 648.

Garrard, T. L. and E. C. Stone (1993). New SEP-Based Solar Abundances. In *23rd International Cosmic Ray Conference, Calgary*, Volume 3, pp. 384–387.

Garrard, T. L. and E. C. Stone (1994). Composition of Energetic Particles from Solar Flares. *Adv. Space Res. 14*(10), 589–598.

Garrard, T. L., E. C. Stone, and R. E. Vogt (1973). Isotopes of H and He in Solar Cosmic Rays. In *Proc. Symposium on High Energy Phenomena on the Sun, NASA SP-342*, pp. 341.

Gehrels, N. (1986). Confidence Limits for Small Numbers of Events in Astrophysical Data. *Astrophys. J. 303*, 336–346.

Geiss, J. (1973). Solar Wind Composition and Implications about the History of the Solar System. In *13th International Cosmic Ray Conference Denver, CO, 1985*, Volume 5, pp. 3375–3398.

Geiss, J. (1982). Processed Affecting Abundances in the Solar Wind. *Space Science Reviews 33*, 201.

Geiss, J. and P. Bochsler (1985). Ion Composition in the Solar Wind in Relation to Solar Abundances. In *Rapports Isotopiques Dans Le System Solaire, Paris, 1984*, pp. 213.

Geiss, J., F. Buehler, H. Cerutti, P. Eberhardt, and C. Filleux (1972). Solar Wind Composition Experiment. In *Apollo-16 Prelim. Sci. Report, NASA SP-315*, Volume 231, pp. 14–1.

Geiss, J., G. Gloeckler, and R. von Steiger (1984). Solar and Heliospheric Processes from Solar Wind Measurements. *Phil. Trans. Roy. Soc. London A 349*, 213–226.

Gloeckler, G. (1990). Ion Composition Measurement Technique for Space Plasmas. *Rev. Sci. Instrum. 61*, 3613–3620.

Gosling, J. T. (1993). The Solar Flare Myth. *J. Geophys. Res. 98*, 18,937–18,949.

Grevesse, N. (1984). Abundance of Elements in the Sun. In R. Pallavicini (Ed.), *Seventh European Regional Astronomy Meeting, Florence, Italy, 12-16 December, 1983*, pp. 71–82. Italian Astronomical Society.

Hall, D. N. B. (1973). Detection of the ^{13}C, ^{17}0, and ^{16}0 Isotope Bands of CO in the Infrared Solar Spectrum. *ApJ 182*, 977–982. Provided by the NASA Astrophysics Data System.

Hoel, P. G. (1965). *Introduction to Mathematical Statistics, 3rd Edition*. New York: John Wiley and Sons.

Hovestadt, D. (1974). Nuclear Composition of Solar Cosmic Rays. In C. T. Russell (Ed.), *Solar Wind Three*, pp. 2. University of California.

Hsieh, K. C. and J. A. Simpson (1970). The Relative Abundances and Energy Spectra of ^{3}He and ^{4}He from Solar Flares. *Astrophys. J. Lett. 162*, L191–L196.

Humbert, F., R. Wieler, and B. Marty (1998). Nitrogen and Argon in Individual Mineral Grains of a Lunar Soil: Evidence for a Major Non-Solar Nitrogen Component. *Lunar and Planetary Institute 29*, 1034+. Provided by the NASA Astrophysics Data System.

Janni, J. F. (1966). Calculations of Energy Loss, Range, Pathlength, Straggling, Multiple Scattering, and the Probability of Inelastic Nuclear Collisions for 0.1- to 1000 MeV Protons. Technical report, USAF Weapons Laboratory technical report number AFWL-TR-65-150.

Kahler, S. W. (1984). Associations Between Coronal Mass Ejections and Solar Energetic Particle Events. *J. Geophys. Res. 89*, 9683–9693.

Kallenbach, R., F. M. Ipavich, P. Bochsler, S. Hefti, D. Hovestadt, H. Grunwaldt, M. Hilchenbach, W. I. Axford, H. Balsiger, A. Burgi, M. A. Coplan, A. B. Galvin, J. Geiss, G. Gloeckler, K. C. Hsieh, B. Klecker, M. A. Lee, S. Livi, G. G. Managadze, E. Marsch, E. Møbius, M. Neugebauer, N.-U. Reiche, M. Scholer, M. I. Verigin, B. Wilken, and P. Wurz (1997). Isotopic Composition of Solar Wind Neon Measured by CELIAS/MTOF on Board SOHO. *J. Geophys. Res. 102*(A12), 22,895–26904.

Kim, J. S., Y. Kim, K. Marti, and J. F. Kerridge (1995). Nitrogen Isotope Abundances in the Recent Solar Wind. *Nature 375*, 383–385. Provided by the NASA Astrophysics Data System.

Klecker, B. (1991). Particle Acceleration in Solar Flares. *Eos 71*(39), 1102.

Klecker, B. (1995). The Anomalous Component of Cosmic Rays in the 3-D Heliosphere. *Space Science Reviews 72*, 419.

Klecker, B., D. Hovestadt, M. Scholer, G. Gloeckler, F. M. Ipavich, C. Y. Fan, and L. A. Fisk (1984). Direct determination of the ionic charge distribution of helium and iron in He-3-rich solar energetic particle events. *Astrophys. J. 281*, 458–462. Provided by the NASA Astrophysics Data System.

Knoll, G. F. (1989). *Radiation Detection and Measurement, 2nd Edition.* New York: John Wiley and Sons.

Kox, S., A. Gamp, C. Perrin, J. Arvieux, R. Bertholet, J. F. Bruandet, M. Buenerd, R. Cherkaoui, A. J. Cole, Y. El-Masri, N. Longequeue, J. Menet, F. Merchez, and J. B. Viano (1987). Trends of total reaction cross sections for heavy ion collisions in the intermediate energy range. *Physical Review C 35*(5), 35.

Larimer, J. W. (1988). The cosmochemical classification of the elements. In *Meteorites and the Early Solar System (A89-27476 10-91)*, pp. 375–389. Tucson, AZ: Univ. of Arizona Press.

Lau, K. H. (1985). *A Cerenkov-ΔE-Cerenkov Detector for High-Energy Cosmic Ray Isotopes and an Accelerator Study of ^{40}Ar & ^{56}Fe Fragmentation.* Ph.D. thesis, California Institute of Technology.

Lee, M. A. and J. M. Ryan (1986). Time-dependent coronal shock acceleration of energetic solar flare particles. *ApJ 303*, 829–842. Provided by the NASA Astrophysics Data System.

Leske, R. A. (1995). SRL Internal Report #107: MAST/PET Livetime. Technical report, Caltech: Space Radiation Laboratory.

Leske, R. A., J. R. Cummings, R. A. Mewaldt, E. C. Stone, and T. T. von

Rosenvinge (1995). Measurements of the Ionic Charge States of Solar Energetic Particles Using the Geomagnetic Field. *Astrophys. J. Lett. 452*, L149–L152.

Leske, R. A., R. A. Mewaldt, A. C. Cummings, J. R. Cummings, E. C. Stone, and T. T. von Rosenvinge (1996). The Isotopic Composition of Anomalous Cosmic Rays from SAMPEX. *Space Science Reviews 78*, 149–154.

Longair, M. S. (1992). *High Energy Astrophysics*. Cambridge: Cambridge Univ. Press.

Looper, M. D., J. B. Blake, J. R. Cummings, and R. A. Mewaldt (1996). SAMPEX Observations of Energetic Hydrogen Isotopes in the Inner Zone. *Radiation Measurements 26*(6), 967–978.

Luhn, A., D. Hovestadt, B. Klecker, M. Scholer, G. Gloeckler, F. M. Ipavich, A. B. Galvin, C. Y. Fan, and L. A. Fisk (1985). The Mean Ionic Charges of N, Ne, Mg, Si, and S in Solar Energetic Particle Events. In *19th International Cosmic Ray Conference La Jolla, CA, 1985*, Volume 4, pp. 241.

Luhn, A., B. Klecker, D. Hovestadt, G. Gloeckler, F. M. Ipavich, M. Scholer, C. Y. Fan, and L. A. Fisk (1984). Ionic Charge States of N, Ne, Mg, Si, and S in Solar Energetic Particle Events. *Adv. Space Res. 4*(2), 161–164.

Luhn, A., B. Klecker, D. Hovestadt, and E. Mobius (1987). The Mean Ionic Charge State of Silicon in ^{3}He-Rich Solar Flares. *Astrophys. J. 317*, 951–955.

Mabry, D. J., S. J. Hansel, and J. B. Blake (1993). The SAMPEX Data Processing Unit. *IEEE Trans. Geosci. Remote Sensing 31*, 572.

Marsch, E., R. Von Steiger, and P. Bochsler (1995). Element Fractionation by Diffusion in the Solar Chromosphere. *A&A 301*, 261+. Provided by the NASA Astrophysics Data System.

Mason, G. M., J. B. Blake, R. A. Mewaldt, E. C. Stone, D. N. Baker, T. T. Vonrosenvinge, L. B. Callis, D. C. Hamilton, B. Klecker, D. Hovestadt, and M. Scholer (1997). Solar Cycle Dynamics of Solar, Magnetospheric, and Heliospheric Particles, and Long-Term Atmospheric Coupling: SAMPEX. In *Techni-*

cal Report, Maryland Univ. College Park, MD United States Dept. of Physics. Provided by the NASA Astrophysics Data System.

Mason, G. M., J. E. Mazur, and D. C. Hamilton (1994). Heavy-Ion Isotopic Anomalies in ^{3}He-Rich Solar Particle Events. *Astrophys. J. 425*, 843–848.

Mason, G. M., J. E. Mazur, M. D. Looper, and R. A. Mewaldt (1995). Charge State Measurements of Solar Energetic Particles Observed with SAMPEX. *Astrophys. J. 452*, 901–911.

Mazur, J. E., P. Walpole, and G. M. Mason (1998). *SAMPEX Master Data File Description, Version 1.2.* University of Maryland, College Park, MD: Space Physics Group.

McGuire, R. E. and T. T. von Rosenvinge (1986). The Composition of Solar Energetic Particles. *Astrophys. J. 301*, 938.

Mewaldt, R. A. (1980). Spacecraft measurements of the elemental and isotopic composition of solar energetic particles. In *The ancient sun: Fossil record in the earth, moon and meteorites; Proceedings of the Conference, Boulder, CO, October 16-19, 1979. (A81-48801 24-91) New York and Oxford, Pergamon Press, 1980, p. 81-101.*, pp. 81–48801. Provided by the NASA Astrophysics Data System.

Mewaldt, R. A. (1994). Galactic cosmic ray composition and energy spectra. *Advances in Space Research 14*, 737–747. Provided by the NASA Astrophysics Data System.

Mewaldt, R. A., A. C. Cummings, J. R. Cummings, E. C. Stone, B. Klecker, D. Hovstadt, M. Scholer, G. M. Mason, J. E. Mazur, D. C. Hamilton, T. T. von Rosenvinge, and J. B. Blake (1992). The Return of the Anomalous Cosmic Rays to 1 AU in 1992. *Geophys. Res. Lett. 20*(20), 2263–2266.

Mewaldt, R. A., J. D. Spalding, and E. C. Stone (1984). A High-Resolution Study of the Isotopes of Solar Flare Nuclei. *Astrophys. J. 280*, 892–901.

Mewaldt, R. A., J. D. Spalding, E. C. Stone, and R. E. Vogt (1979). The Isotopic Composition of Solar Flare Accelerated Neon. *Astrophys. J. Lett. 231*, 97–100.

Mewaldt, R. A. and E. C. Stone (1989). Isotope Abundances of Solar Coronal Material Derived from Solar Energetic Particle Measurements. *Astrophys. J. 337*, 959.

Meyer, J. P. (1981). A Tentative Ordering of All Available Solar Energetic Particles Abundance Observations. I - The Mass Unbiased Baseline. II - Discussion and Comparison with Coronal Abundances. *International Cosmic Ray Conference, 17th, Paris, France, July 13-25, 1981, Conference Papers. Volume 3. (A82-22580 09-92) Gif-sur-Yvette, Essonne, France, Commissariat a l'Energie Atomique, 1981, p. 145-152. 3*, 145–152. Provided by the NASA Astrophysics Data System.

Meyer, J.-P. (1985). The Baseline Composition of Solar Energetic Particles. *Astrophys. J. Supp. 57*, 151–171.

Moebius, E., M. Scholer, D. Hovestadt, B. Klecker, and G. Gloeckler (1982). Comparison of helium and heavy ion spectra in He-3-rich solar flares with model calculations based on stochastic Fermi acceleration in Alfven turbulence. *ApJ 259*, 397–410. Provided by the NASA Astrophysics Data System.

Mogro-Campero, A. and J. A. Simpson (1972a). Enrichment of Very Heavy Nuclei in the Composition of Solar Accelerated Particles. *Astrophys. J. Lett. 171*, L5–L9.

Mogro-Campero, A. and J. A. Simpson (1972b). The Abundances of Solar Accelerated Nuclei from Carbon to Iron. *Astrophys. J. Lett. 177*, L37–L41.

Neugebauer, M. and C. W. Snyder (1966). Mariner-2 Measurements of the Solar Wind. In M. Neugebauer and J. R. J. Mackin (Eds.), *The Solar Wind*. NASA.

Nichols, R. H., C. M. Hohenberg, and C. T. Olinger (1994). Implanted solar helium, neon, and argon in individual lunar ilmenite grains: Surface effects and a temporal variation in the solar wind composition. *Geochim. Cosmochim. Acta 58*, 1031–1042. Provided by the NASA Astrophysics Data System.

NOAA (1993). Monthly Report of Solar-Geophysical Data. Technical report, NOAA Environmental Data and Information Service, Boulder, CO.

Oetliker, M., D. Hovestadt, B. Klecker, M. R. Collier, G. Gloeckler, D. C. Hamilton, F. M. Ipavich, P. Bochsler, and G. G. Managadze (1997). The Isotopic Composition of Iron in the Solar Wind: First Measurements with the MASS Sensor on the WIND Spacecraft. *Astrophys. J. Lett. 474*, L69–L72.

Oetliker, M., B. Klecker, D. Hovestadt, G. M. Mason, J. E. Mazur, R. A. Leske, R. A. Mewaldt, J. B. Blake, and M. D. Looper (1997). The Ionic Charge State of Solar Energetic Particles with Energies of 0.3-70 MeV per Nucleon. *Astrophys. J. 477*, 495–501.

Ortec Incorporated (1980). *Instruction Manual: Surface Barrier Detectors.* Oak Ridge, Tennessee: Ortec Incorporated.

Parker, E. N. (1963). *Interplanetary dynamical processes.* New York, Interscience Publishers.

Pepin, R. O. (1967). Trapped Neon in Meteorites. *Earth Planet. Sci. Letters 2*, 13.

Pope, G. (1990). Program QSTATES. Technical report, Lawrence Berkeley Laboratories.

Press, W. H., S. A. Teukolsky, W. T. Vettering, and B. P. Flannery (1995). *Numerical Recipes in C, Second Edition.* Cambridge: Cambridge Univ. Press.

Priest, E. R., A. A. V. Ballegooijen, and D. H. McKey (1996). A Model for Dextral and Sinistral Prominences. *Astrophys. J. 460*, 530–543.

Pyle, K. R. (1998). University of Chicago Neutron Monitor Database, National Science Foundation Grant ATM-9613963. Technical report, University of Chicago.

Ramaty, R. and B. Kozlovsky (1974). Deuterium, Tritium, and Helium-3 Production in Solar Flares. *Astrophys. J. 193*, 729–740.

Reames, D. V. (1990). Energetic Particles from Impulsive Solar Flares. *Astrophys. J. Supp. 73*, 235–251.

Reames, D. V., S. W. Kahler, and C. K. Ng (1997). Spatial and Temporal Invariance in the Spectra of Energetic Particles in Gradual Solar Events. *Astrophys. J. 491*, 414–420.

Rossi, B. (1964). *Cosmic Rays*. New York: McGraw-Hill.

Rossi, B. and S. Olbert (1970). *Introduction to the Physics of Space*. New York: McGraw-Hill.

Ruffolo, D. (1997). Charge States of Solar Cosmic Rays and Constraints on Acceleration Times and Coronal Transport. *Astrophys. J. Lett. 481*, L119–L122.

Selesnick, R. S. (1992). SRL Internal Report #103: Droop in MAST Matrix Detectors. Technical report, Caltech: Space Radiation Laboratory.

Selesnick, R. S. (1996). SRL Internal Report #105: Confidence Limits in Poisson Statistics of Small Numbers. Technical report, Caltech: Space Radiation Laboratory.

Seltzer, S. M. and M. J. Berger (1964). Energy Loss Straggling of Protons and Mesons: Tabulation of the Vavilov Distribution. In *Studies in the Penetration of Charged Particles in Matter*, pp. 187–203. NAS/NRC publication 1133.

Shea, M. A. and D. F. Smart (1990). A Summary of Major Proton Events. *Solar Physics 127*, 297–320.

Sihver, L., C. H. Tsao, R. Silberberg, T. Kanai, and A. F. Barghouty (1993). Total reaction and partial cross section calculations in proton-nucleus ($Z_t \leq 26$) and nucleus-nucleus reactions (Z_p and $Z_t \leq 26$). *Physical Review C 47*(3), 1225.

Simpson, J. A. (1983). Elemental and Isotopic Composition of the Galactic Cosmic Rays. *Ann. Rev. Nuc. Phys. Sci. 33*, 323–381.

Simpson, J. A. (1995). The Anomalous Nuclear Component in the Three-Dimensional Heliosphere. *Adv. Space Res. 16*(9), 135–149.

Simpson, J. A., J. P. Wefel, and R. Zamow (1984). Isotopic and Elemental Composition of Solar Energetic Particles. In *Proc. 18th Internat. Cosmic Ray Conf.*, Volume 10, Bangalore, pp. 322–325.

Skryme, D. J. (1967). The Passage of Charged Particles through Silicon. *Nucl. Instr. and Meth. 57*, 61–73.

Spalding, J. D. (1981). SRL Internal Report #81: Energy Loss Fluctutaions in Thick Absorbers. Technical report, Caltech Space Radiation Laboratory.

Spalding, J. D. (1983). *The Isotopic Composition of Energetic Particles Emitted from a Large Solar Flare.* Ph.D. thesis, California Institute of Technology.

Spicer, D. S., U. Feldman, K. G. Widing, and M. Rilee (1998). The Neon-to-Magnesium Abundance Ratio as a Tracer of the Source Region of Prominence Material. *Astrophys. J. 494*, 450–452.

Stone, E. C., R. E. Vogt, F. B. McDonald, B. J. Teegarden, J. H. Trainor, J. R. Jokipii, and W. R. Webber (1977). Cosmic ray investigation for the Voyager missions: Energetic particle studies in the outer heliosphere - and beyond. *Space Science Reviews 21*, 355–376. Provided by the NASA Astrophysics Data System.

Suess, H. E. and H. C. Urey (1956). Abundances of the Elements. *Rev. Mod. Phys. 28*(1), 53–74.

Sullivan, J. D. (1971). Geometrical Factor and Directional Response of Single and Multi-Element Particle Telescopes. *Nucl. Instr. and Meth. 95*, 5–11.

Tascione, T. F. (1988). *Introduction to the Space Environment.* Malabar, Florida: Orbit Book Company.

Teegarden, B. J., T. T. von Rosenvinge, and F. B. McDonald (1973). Satellite Measurements of the Charge Composition of Solar Cosmic Rays in the $6 \leq Z \leq 26$ Interval. *Astrophys. J. 180*, 571.

Temerin, M. and I. Roth (1992). The production of He-3 and heavy ion enrichment in He-3-rich flares by electromagnetic hydrogen cyclotron waves. *ApJ 391*, L105–L108. Provided by the NASA Astrophysics Data System.

Veck, N. J. and J. H. Parkinson (1981). Solar Abundances from X-ray Flare Observations. *Mon. Not. R. Astr. Soc 197*, 41–55.

von Steiger, R. and J. Geiss (1989). Supply of Fractionated Gases to the Corona. *Astron. &Astrophys. 225*, 222–238.

von Steiger, R., J. Geiss, and G. Gloeckler (1997). *Composition of the Solar Wind*, pp. 581–616. Tucson: Univ. of Arizona Press.

Webber, W. R., J. C. Kish, and D. A. Schrier (1990). Individual isotopic fragmentation cross sections of relativistic nuclei in hydrogen, helium, and carbon targets. *Physical Review C 41*(2), 547.

Webber, W. R. and J. A. Lezniak (1974). The comparative spectra of cosmic-ray protons and helium nuclei. *Astrophys. Sp. Sci. 30*, 361–380. Provided by the NASA Astrophysics Data System.

Wiedenbeck, M. E. and D. E. Greiner (1980). A Cosmic-Ray Age Based on the Abundance of ^{10}Be. *Astrophys. J. Lett. 239*, 139–142.

Wielen, R. and T. L. Wilson (1997). The evolution of the C, N, and O isotope ratios from an improved comparison of the interstellar medium with the Sun. *A&A 326*, 139–142. Provided by the NASA Astrophysics Data System.

Wieler, R. and H. Baur (1995). Fractionation of Xe, Kr, and Ar in the Solar Corpuscular Radiation Deduced by Closed System Etching of Lunar Soils. *Astrophys. J. 453*, 987–997.

Wieler, R., H. Baur, and P. Singer (1986). Noble Gases From Solar Energetic Particles Revealed by Closed System Stepwise Etching of Lunar Soil Materials. *Geochim. Cosmochim. Acta 50*, 1997–2017.

Ziegler, J. F. (1985). *The Stopping and Ranges of Ions in Matter*, Volume 5. New York: Pergamon Press.

Zirin, H. (1989). *Astrophysics of the Sun.* New York: Cambridge Univ. Press.

Zombeck, M. V. (1992). *Handbook of Space Astronomy and Astrophysics.* Cambridge: Cambridge Univ. Press.

Zumberge, J. F. (1981). *A Balloon Measurement of the Isotopic Composition of Galactic Cosmic Ray Boron, Carbon, and Nitrogen.* Ph.D. thesis, California Institute of Technology.